ΕΘΝΙΚΟ ΜΕΤΣΟΒΙΟ ΠΟΛΥΤΕΧΝΕΙΟ
ΣΧΟΛΗ ΕΦΑΡΜΟΣΜΕΝΩΝ ΜΑΘΗΜΑΤΙΚΩΝ
ΚΑΙ ΦΥΣΙΚΩΝ ΕΠΙΣΤΗΜΩΝ

Αναζήτηση του μποζονίου Higgs του Καθιερωμένου Προτύπου με τον ανιχνευτή ATLAS στον LHC με αποτέλεσμα την παρατήρηση ενός νέου σωματιδίου συμβατού με το μποζόνιο Higgs

ΔΙΔΑΚΤΟΡΙΚΗ ΔΙΑΤΡΙΒΗ

ΕΛΕΝΗΣ Κ. ΜΟΥΝΤΡΙΧΑ

Διπλωματούχου Φυσικού Εφαρμογών Ε.Μ.Π.

ΕΠΙΒΛΕΠΩΝ:
Θ. ΑΛΕΞΟΠΟΥΛΟΣ
Καθηγητής Ε.Μ.Π.

ΑΘΗΝΑ, Σεπτέμβριος 2012

ΕΘΝΙΚΟ ΜΕΤΣΟΒΙΟ ΠΟΛΥΤΕΧΝΕΙΟ
ΣΧΟΛΗ ΕΦΑΡΜΟΣΜΕΝΩΝ ΜΑΘΗΜΑΤΙΚΩΝ
ΚΑΙ ΦΥΣΙΚΩΝ ΕΠΙΣΤΗΜΩΝ

Αναζήτηση του μποζονίου Higgs του Καθιερωμένου Προτύπου με τον ανιχνευτή ATLAS στον LHC με αποτέλεσμα την παρατήρηση ενός νέου σωματιδίου συμβατού με το μποζόνιο Higgs

ΔΙΔΑΚΤΟΡΙΚΗ ΔΙΑΤΡΙΒΗ

ΕΛΕΝΗΣ Κ. ΜΟΥΝΤΡΙΧΑ

Διπλωματούχου Φυσικού Εφαρμογών Ε.Μ.Π.

ΤΡΙΜΕΛΗΣ ΣΥΜΒΟΥΛΕΥΤΙΚΗ ΕΠΙΤΡΟΠΗ:

1. Θ. Αλεξόπουλος, Καθ. Ε.Μ.Π.
2. Ευ. Γαζής, Καθ. Ε.Μ.Π.
3. Γ. Τσιπολίτης, Αν. Καθ. Ε.Μ.Π.

ΕΠΤΑΜΕΛΗΣ ΕΞΕΤΑΣΤΙΚΗ ΕΠΙΤΡΟΠΗ:

1. Θ. Αλεξόπουλος, Καθ. Ε.Μ.Π.
2. Ευ. Γαζής, Καθ. Ε.Μ.Π.
3. Γ. Τσιπολίτης, Αν. Καθ. Ε.Μ.Π.
4. C. Guyot, Dir. of Research, CEA-Saclay
5. S. Hassani, Researcher, CEA-Saclay
6. Κ. Νικολόπουλος, Λέκτ. Univ. Birmingham
7. A. Schaffer, Dir. of Research, LAL

ΑΘΗΝΑ, Σεπτέμβριος 2012

To my family
and the people who stood by me

Contents

Introduction

Huge progress has been made in the field of particle physics after the middle of the 20^{th} century, including the development of the electroweak theory by Sheldon Glashow, Steven Weinberg and Abdus Salam and quantum chromodynamics by David Politzer, Frank Wilczek and David Gross. A theoretical framework that describes all known elementary particle interactions, except for gravity, has been established and is called the Standard Model of particle physics. A wide range of experiments have since then tested and confirmed most of the Standard Model predictions.

In this theoretical framework, the mass of the elementary particles could not be incorporated in a straight-forward way. For this reason, the so-called Higgs mechanism has been introduced, which postulates a scalar boson that gives rise to the mass components. Experiments have long ago aimed to the search of the Higgs boson, one of the largest being the LEP at CERN, followed by the Tevatron in Fermilab which ceased operation in 2011.

The search for the postulated Higgs boson that had not been experimentally confirmed by 2009/2010, was due to be continued by the promising LHC experiments. The LHC is the world's largest and highest-energy particle accelerator and is constructed at CERN. It is a proton-proton accelerator and collider and four main detectors have been built, designed according their physics program. ATLAS is one of the two general-purpose detectors whose main goal is to either confirm or reject experimentally the existence of the Higgs boson.

This thesis is aiming to include the work contributed by the author in the context of the ATLAS experiment and the search for the Standard Model Higgs boson using the proton-proton collision data recorded during the 2011 and 2012 LHC runs.

In Chapter 1, the basic elements of the Standard Model are described including the Higgs mechanism and the theoretical constraints on the Higgs boson mass. The results of direct and indirect searches are summarized. The Higgs production mechanisms and decay channels in the LHC are described.

In Chapter 2, the LHC and the ATLAS detector are introduced. The basic elements in the physics program of ATLAS are pointed out, including the search for the Higgs boson which is the subject of this thesis. The experimental setup is described, emphasizing the basic components of the detector.

Such a complicated detector requires a reliable system for its control and monitoring. On these grounds, the work of the author on the Detector Control System is described in Chapter 3. It involves the control system of the Power Supplies for the

Monitored Drift Tubes, which is the main component of the Muon Spectrometer. The software used is described including the developed tools and elements.

For the search of the Higgs boson electrons and muons are used. In Chapter 4, the experimental reconstruction and identification of these objects are described. In the second part of this chapter, three studies on muons, carried out by the author using data and Monte Carlo simulation, are presented. These consist of a study on the rate of muons originating from decays of other particles, a study on the effect of pileup on signal-like muon isolation and a study on the data-driven efficiency of Higgs boson analysis selection on signal-like muons.

In Chapter 5, the analysis for the Higgs boson search in its decay channel to two Z bosons, and subsequently to four leptons, is presented. Firstly, the signal and background topology is described as well as the data and the Monte Carlo simulation used. Secondly, the event selection for this Higgs decay channel is detailed resulting to the selection of a four-lepton final state. The background contribution to this final state is studied by the author and results using the 7 TeV collision data are presented along with the systematic uncertainties induced and the extracted upper limits for the Higgs search.

In Chapter 6, the analysis selection is revised towards an optimization for a low-mass Higgs boson search. The effect of the new analysis on the background processes is performed and its impact on the 7 TeV results and exclusion limits is presented.

In Chapter 7, $5.8\,\text{fb}^{-1}$ of 2012 collision data at $\sqrt{s} = 8\,\text{TeV}$, collected up to July, are analyzed and combined with the 2011 $\sqrt{s} = 7\,\text{TeV}$ data. Results of the background estimation are presented along with the results of the event selection and the exclusion limits. In addition, results on the combination of all ATLAS Higgs channels are shown.

In the conclusions, in Chapter 8, the main results of this thesis are summarized. The conclusive results from the ATLAS Higgs searches on the observation of a new boson consistent with the Standard Model Higgs boson are emphasized.

Περίληψη

Τεράστια πρόοδος σημειώθηκε στον τομέα της φυσικής στοιχειωδών σωματιδίων μετά τα μέσα του 20ού αιώνα, συμπεριλαμβανομένης της θεμελίωσης της ηλεκτρασθενούς θεωρίας από τους Sheldon Glashow, Steven Weinberg και Abdus Salam και της κβαντικής χρωμοδυναμικής από τους David Politzer, Frank Wilczek και David Gross. Μια συλλογή συσχετιζόμενων θεωριών που περιγράφουν τις αλληλεπιδράσεις μεταξύ των γνωστών στοιχειωδών σωματιδίων, εκτός της βαρυτικής, καθιερώθηκε και ονομάζεται το Καθιερωμένο Πρότυπο της σωματιδιακής φυσικής. Ένας μεγάλος αριθμός πειραμάτων έκτοτε έχει δοκιμάσει και επιβεβαιώσει τις προβλέψεις του Καθιερωμένου Προτύπου.

Σε αυτό το θεωρητικό πλαίσιο, η μάζα των στοιχειωδών σωματιδίων, δεν θα μπορούσε να εισαχθεί με ένα ευθύ τρόπο. Για αυτό το λόγο, ο λεγόμενος μηχανισμός Higgs εισήχθει, έχοντας ως αποτέλεσμα την πρόβλεψη ενός βαθμωτού σωματιδίου του οποίου η αλληλεπίδραση με τα στοιχειώδη σωματίδια οδηγεί στην εμφάνιση των μαζών τους. Τις τελευταίες δεκαετίες, διάφορα πειράματα αναζήτησαν το μποζόνιο Higgs, ανάμεσα αυτών το LEP στο CERN και το Tevatron στο Fermilab το οποίο σταμάτησε τη λειτουργία του το 2011.

Η αναζήτηση του μποζονίου Higgs που δεν είχε επιβεβαιωθεί πειραματικά μέχρι το 2009/2010, επρόκειτο να συνεχιστεί από τα πολλά υποσχόμενα πειράματα του LHC. Ο LHC είναι ο μεγαλύτερος και υψηλότερης ενέργειας επιταχυντής σωματιδίων στον κόσμο και είναι κατασκευασμένος στο CERN. Πρόκειται για έναν επιταχυντή δεσμών πρωτονίου με τέσσερις κυρίους ανιχνευτές που έχουν σχεδιαστεί ανάλογα με τα φαινόμενα φυσικής που προορίζονται να μελετήσουν. Ο ATLAS είναι ένας από τους δύο ανιχνευτές γενικής χρήσης των οποίων ένας από τους κύριους στόχους είναι είτε να επιβεβαιώσει είτε να απορρίψει πειραματικά την ύπαρξη του Higgs.

Η διδακτορική διατριβή αυτή έχει ως στόχο να συμπεριλάβει τη δουλειά της συγγραφέα, στα πλαίσια του πειράματος ATLAS και της αναζήτησης του μποζονίου Higgs του Καθιερωμένου Προτύπου, με τη χρήση των δεδομένων που καταγράφηκαν από τις συγκρούσεις πρωτονίων-πρωτονίων κατά τη διάρκεια των ετών 2011-2012.

Στο Κεφάλαιο 1 περιγράφονται τα βασικά στοιχεία του Καθιερωμένου Προτύπου συμπεριλαμβανομένου του μηχανισμού Higgs και των θεωρητικών ορίων σχετικά με την μάζα του μποζονίου Higgs. Αναφέρονται οι άμεσες και έμμεσες έρευνες που έχουν διεξαχθεί και τα αποτελέσματά τους, καθώς επίσης και οι μηχανισμοί παραγωγής και διάσπασης του μποζονίου στον LHC.

Στο Κεφάλαιο 2 γίνεται εισαγωγή στον LHC, καθώς και στον ανιχνευτή ATLAS. Τα βασικά στοιχεία του προγράμματος φυσικής του ATLAS επισημάνονται, συμπεριλαμβανομένης της αναζήτησης του μποζονίου Higgs, το οποίο αποτελεί το αντικείμενο

της παρούσας διατριβής. Η πειραματική διάταξη περιγράφεται τονίζοντας τα βασικά της στοιχεία.

Ένας τέτοιος περίπλοκος ανιχνευτής απαιτεί ένα καλά οργανωμένο σύστημα ελέγχου και παρακολούθησης. Η συνεισφορά της συγγραφέα στην ανάπτυξη του Συστήματος Ελέγχου του ανιχνευτή περιγράφεται στο κεφάλαιο 3. Αφορά την τροφοδοσία υψηλής και χαμηλής τάσης των ανιχνευτών της τεχνολογίας σωλήνων ολίσθησης, που αποτελούν ένα από τα βασικά στοιχεία του Μιονικού Φασματομέτρου του ATLAS. Περιγράφεται το λογισμικό που χρησιμοποιήθηκε και τα απαραίτητα εργαλεία.

Για την εργασία σχετικά με την αναζήτηση του μποζονίου Higgs τα βασικά αντικείμενα φυσικής που χρησιμοποιήθηκαν είναι τα ηλεκτρόνια και τα μιόνια. Στο Κεφάλαιο 4 αυτά τα αντικείμενα περιγράφονται όσον αφορά την ανακατασκευή και την ταυτοποίησή τους. Στο δεύτερο μέρος αυτού του κεφαλαίου, παρουσιάζονται τρεις μελέτες σχετικά με τα μιόνια που πραγματοποίησε η συγγραφέας με τη χρήση δεδομένων και προσομοίωσης Monte Carlo. Πρόκειται για μια μελέτη σχετικά με το ποσοστό των μιονίων που προέρχονται από διασπάσεις πιονίων και καονίων, μια μελέτη πάνω στην απομόνωση των μιονίων και μια μελέτη για την επίδραση των κριτηρίων επιλογής της ανάλυσης του μποζονίου Higgs σε μιόνια από διασπάσεις του μποζονίου Z, τα οποία είναι όμοια με αυτά της διάσπασης του μποζονίου Higgs που εξετάζεται στην παρούσα εργασία.

Στο Κεφάλαιο 5 παρουσιάζεται η ανάλυση για την αναζήτηση του Higgs στο κανάλι διάσπασης του σε δύο Z μποζόνια, τα οποία στη συνέχεια διασπώνται σε τέσσερα λεπτόνια. Αρχικά περιγράφεται η τοπολογία του σήματος και του υποβάθρου καθώς και τα δεδομένα και η προσομοίωση Monte Carlo που χρησιμοποιήθηκε. Στη συνέχεια αναφέρονται λεπτομερώς τα κριτήρια επιλογής για την ανάλυση του συγκεκριμένου καναλιού διάσπασης, τα οποία οδηγούν στην επιλογή των τεσσάρων λεπτονίων στην τελική κατάσταση. Η συνεισφορά του υποβάθρου σε αυτή την τελική κατάσταση μελετήθηκε από την συγγραφέα και τα αποτελέσματα, χρησιμοποιώντας τα δεδομένα συγκρούσεων από το έτος 2011, παρουσιάζονται μαζί με τις συστηματικές αβεβαιότητες και τα όρια που εξάχθηκαν στην αναζήτηση του Higgs.

Στο Κεφάλαιο 6 περιγράφονται τα κριτήρια επιλογής της ανάλυσης όπως αναθεωρήθηκαν για τη λήψη δεδομένων του 2012, στο πλαίσιο βελτιστοποίησης της αναζήτησης ενός μποζονίου Higgs χαμηλής μάζας. Το αποτέλεσμα της νέας ανάλυσης σχετικά με τις διαδικασίες υποβάθρου μελετάται με τη χρήση των δεδομένων του έτους 2011 ενώ παρουσιάζονται επίσης τα νέα αποτελέσματα της βελτιωμένης ανάλυσης για τα δεδομένα αυτά.

Στο Κεφάλαιο 7 τα δεδομένα σύγκρουσης σε $\sqrt{s} = 8\,\text{TeV}$, ολοκληρωμένης φωτεινότητας $5.8\,\text{fb}^{-1}$, που συλλέχθηκαν μέχρι τον Ιούλιο, αναλύονται και συνδυάζονται με τα δεδομένα του 2011 σε $\sqrt{s} = 7\,\text{TeV}$. Αποτελέσματα σχετικά με την εκτίμηση του υποβάθρου, τα κριτήρια επιλογής και τα όρια για την αναζήτηση του μποζονίου Higgs παρουσιάζονται. Επιπλέον, παρατίθενται τα αποτελέσματα του συνδυασμού όλων των καναλιών του Higgs στο ATLAS .

Στα συμπεράσματα, στο Κεφάλαιο 8, συνοψίζεται ο σκοπός αυτής της διατριβής και επισημαίνονται τα κύρια αποτελέσματα. Έμφαση δίνεται στα τελικά αποτελέσματα από τα κανάλια αναζήτησης του Higgs.

Résumé

La physique des particules a connu d'énormes progrès dans la deuxième moitiée du vingtième siècle avec l'élaboration de la théorie électrofaible de Sheldon Glashow, Steven Weinberg et Abdus Salam et la théorie de chromodynamique quantique de David Politzer, Frank Wilczek et David Gross. Une collection de théories qui décrivent toutes les interactions connues des particules élémentaires, à l'exception de la gravité, a été construite et est appelée le Modèle Standard de la physique des particules. Un grand nombre d'expériences a depuis testé et confirmé la plupart des prédictions du Modèle Standard.

Dans ce contexte théorique, la masse des particules élémentaires ne pouvait être simplement ajoutée dans les théories. Pour cette raison, le mécanisme de Higgs a été introduit, ce qui a conduit à la prédiction d'un boson scalaire dont l'interaction avec les particules élémentaires fait apparaître les composants de la masse. Beaucoup d' expériences dont la vocation est la recherche du boson de Higgs ont été réalisées, à commencer par le LEP au CERN et par la suite avec le Tevatron au Fermilab et récément avec le LHC au CERN.

Le LHC est l'accélérateur de particules, le plus grand et le plus puissant, construit à ce jour . C'est un collisionneur de faisceau proton-proton, mis en fonctionnement le 10 septembre 2008. Quatre détecteurs indépendants dont deux de très grande taille, sont installés sur cet accélérateur. Le détecteur ATLAS est l'un des deux détecteurs à usage général dont l'un des principaux objectifs est de confirmer ou d'infirmer expérimentalement l'existence du boson de Higgs.

Cette thèse retrace le travail effectué par l'auteur au sein de la collaboration ATLAS sur la recherche du boson de Higgs du Modèle Standard en utilisant les données des collisions proton-proton enregistrées en 2011-2012.

Dans le Chapitre 1, les éléments de base du Modèle Standard et le mécanisme de Higgs sont décrits . Les limites théoriques anisi que les résultats des recherches directes et indirectes sur la masse du boson de Higgs sont donnés. Enfin, les mécanismes de production et de désintégration de Higgs au LHC sont détaillés.

Dans le Chapitre 2, le LHC est introduit et le détecteur ATLAS, dont les données sont utilisées dans cette thèse, est décrit. Les éléments de base du programme de physique d'ATLAS sont mentionnées, incluant la recherche du boson de Higgs qui fait l'objet de cette thèse. Le dispositif expérimental du détecteur est décrit, en insistant sur les éléments de base du détecteur.

Un détecteur si compliqué, necéssite un système sophistiqué pour son contrôl et sa surveillance. Le travail de l'auteur sur le système de contrôl du détecteur est

décrit dans le Chapitre 3. Il s'agit des blocs d'alimentation des chambres à tubes de dérive du sectromètre à muon utilisé dans la détection des muons. Le logiciel utilisé est décrit et les outils et les éléments essentiels pour son fonctionnement sont présentés.

Pour la recherche du Higgs se désintégrant en quatre leptons, les objets de base utilisés sont les électrons et les muons. Dans le Chapitre 4, la reconstruction et l'identification de ces objets sont décrites. Dans la deuxième partie de ce chapitre, trois études de performance des objets muons effectuées par l'auteur à l'aide des données et des simulation de Monte Carlo, sont présentées. Celles-ci consistent en une étude sur le taux de faux muons provenant de la désintégration d'autres particules, une étude sur l'isolation des muons et une étude sur l'impact de la sélection de l'analyse du Higgs sur les muons provenant du boson Z, ces muons sont identiques à ceux provenant de la désintégration du Higgs considéré dans cette thèse.

Dans le Chapitre 5, l'analyse sur la recherche du boson de Higgs dans son canal de désintégration en deux bosons Z, se désintégrant en quatre leptons, est considérée. Premièrement, la topologie du signal et du bruit de fond est décrite ainsi que les données et la simulation de Monte Carlo utilisées. Deuxièmement, la sélection des événements dans ce canal est détaillée. La contribution du bruit de fond à cet état final a été étudiée par l'auteur et les résultats utilisant les données des collisions de 2011 ainsi que les incertitudes systématiques induites et les limites extraites sur la recherche de Higgs, sont présentés.

Dans le Chapitre 6, l'analyse a été révisitée avec les données de 2012 pour optimiser la recherche du boson de Higgs à basse masse. Les effets des nouvelles coupures sur les processus du bruits de fond ont été étudiés par l'auteur en utilisant les données de 2011. L'impact de cette optimisation sur les résultats de 2011 et les limites correspondantes sont présenté.

Dans le Chapitre 7, $5.8\,\mathrm{fb}^{-1}$ de données de 2012 à $\sqrt{s} = 8\,\mathrm{TeV}$, collectées jusqu'au mois de juillet, sont analysées et combinées avec les données de 2011 à $\sqrt{s} = 7\,\mathrm{TeV}$. Les résultats de l'estimation du bruit de fond, de la sélection des événements et les limites sur la recherche du boson de Higgs sont présentés. En plus, les résultats de la combinaison de tous les canaux pour la recherche du boson de Higgs avec l'expérience ATLAS sont discutés.

Dans le Chapitre 8, les objectifs de cette thèse sont résumée et les principaux résultats sont soulignés. L'accent est mis sur les résultats ayant permis la découverte d'une nouvelle particule compatible avec un boson de Higgs en ATLAS du Modèle Standard avec l'expérience ATLAS.

Chapter 1

Theory Elements

One of the main questions that has always puzzled the man since thousands of years ago, is "What is this world made of?". Having an intuition since the ancient years, Particle Physics proved with experiments that everything in the world is made of elementary particles. In the last centuries, both theoretical and experimental efforts driven by the need to explain the properties of these elementary particles and the interactions with each other. The Standard Model (SM) of Particle Physics is such a theoretical model which is widely-accepted and experimentally confirmed in a large extend.

1.1 Standard Model

According to the Standard Model there are three kinds of elementary particles: leptons, quarks and the force mediators, referred to as gauge bosons. The leptons and the quarks are spin-1/2 particles and hence obey to Fermi-Dirac statistics. Due to this, they are called fermions. According to the Fermi-Dirac statistics, the Pauli exclusion principle does not allow the occupation of any single quantum state by more than one particle of a given type. The force mediators are integer spin particles and thus obey to Bose-Einstein statistics. This is why they are called bosons. According to Bose-Einstein statistics the occupation of a single quantum state by a large number of identical particles is possible. An antiparticle corresponds to each of the elementary particles.

The leptons compose three generations. Every generation is composed by the charged lepton and its neutrino. The charged leptons differ only in their masses, which are increased in every generation with respect to the previous one. In Table 1.1 the lepton generations are presented along with their mass and charge. The second and third generation of charged leptons, the muon and the tau, are unstable and decay to other particles.

The quarks carry fractional charge and their world-average mass values or mass limits are shown in Table 1.2. There are six "flavors" of quarks forming three generations of increasing mass: "up" and "down", "charm" and "strange", "top" and "bottom", denoted by the first letter of their names. Every quark comes in three colors: "red", "blue", "green".

Table 1.1: There are three generations of leptons, each consisting of a charged and a neutral one. The quoted masses are the cited averages or limits set according to Reference [1].

Generation	lepton	mass [MeV]	charge
First	e	0.511	-1
	ν_e	$< 0.225 \cdot 10^{-3}$	0
Second	μ	105.7	-1
	ν_μ	< 0.19	0
Third	τ	1777	-1
	ν_τ	< 18.2	0

Table 1.2: The six quark flavors form three generations of increasing mass. The quoted masses are the cited averages or limits set according to Reference [1].

Generation	quark	mass [GeV]	charge
First	u	$< 2.3 \cdot 10^{-3}$	$+\frac{2}{3}$
	d	$< 4.8 \cdot 10^{-3}$	$-\frac{1}{3}$
Second	c	1.28	$+\frac{2}{3}$
	s	$95 \cdot 10^{-3}$	$-\frac{1}{3}$
Third	t	173.5	$+\frac{2}{3}$
	b	4.18	$-\frac{1}{3}$

The gauge bosons are the force carriers of the four kinds of fundamental interactions in nature: the gravitational, the electromagnetic, the weak and the strong. In Table 1.3 the gauge bosons are presented along with their mass, charge and the interaction type they correspond to. The gravitational interaction appears between all types of particles and is by far the weakest. The graviton (G), a purely theoretical spin-2 boson, is considered to be the gauge boson. The electromagnetic force is carried by spin-1 photons and acts between electrically charged particles. The weak interaction, responsible for nuclear β-decays, and absorption and emission of neutrinos, has three gauge bosons: $W^{\pm}$ and Z, which are massive with spin 1. The gauge bosons of the strong interaction acting between quarks are the eight massless, spin-1 gluons (g).

Effort has been made in the last century in order to describe the four fundamental interactions as different manifestations of a single field. This is partially achieved by the Standard Model which is a renormalizable quantum field theory describing the electromagnetic, weak and strong interactions based on a combination of local gauge symmetry groups $\mathrm{U}(1)_Y \bigotimes \mathrm{SU}(2)_L \bigotimes \mathrm{SU}(3)_C$. The indices refer to the conserved quantity in each transformation: weak hypercharge (Y), color (C) and for SU(2),

Table 1.3: There are six bosons for the four fundamental forces. The quoted masses are the cited averages or limits set according to Reference [1].

boson	mass [GeV]	charge	interaction
G	$< 7 \times 10^{-41}$ [2]	0	gravitational
γ	0	0	electromagnetic
$W^{\pm}$	80.4	± 1	weak
Z	91.2	0	weak
g	0	0	strong

although the weak isospin (I) is the conserved quantity, the L denotes the fact that it involves only left-handed fields. The two components of the Standard Model are the electroweak theory (EW) and quantum chromodynamics (QCD). The electroweak theory was developed by Sheldon Lee Glashow, Abdus Salam, and Steven Weinberg in the 1960s in order to describe the electromagnetic and weak interactions based on the $\mathrm{U}(1)_Y \bigotimes \mathrm{SU}(2)_L$ symmetry group. Quantum chromodynamics, developed by David Politzer, Frank Wilczek and David Gross, describe the strong interaction and is based on the $\mathrm{SU}(3)_C$ gauge symmetry group.

1.1.1 Quantum Field Theory

The Quantum Field Theories are theories that incorporate special relativity and quantum mechanics principles to describe the behavior of particles and their interactions.

In classic quantum mechanics, a system is described by its state represented by the wave function ψ whereas in the quantum field theories, each particle is described as excitation of the local field $\phi(x)$. From the Classical mechanics, the properties and the interactions of the field $\phi(x)$ are determined by the Lagrangian density $\mathcal{L}$, using the field and its space-time derivatives

$$\mathcal{L}(x) = \mathcal{L}(\phi, \partial_\mu \phi) \tag{1.1}$$

According to the principle of least action, the evolution of a system from an initial to a final state occurs along a path for which the action (S) is stationary

$$\delta S = \delta \int \mathcal{L}(\phi, \partial_\mu \phi) \mathrm{d}^4 x = 0 \tag{1.2}$$

which concludes to the Euler-Lagrange equation that describes the motion of the field

$$\partial_\mu \left[\frac{\partial \mathcal{L}}{\partial(\partial_\mu \phi)} \right] - \frac{\partial \mathcal{L}}{\partial \phi} = 0 \tag{1.3}$$

An important aspect in quantum field theory are the gauge symmetries. A symmetry is any continuous transformation of the field that does not change δS and

consequently, does not affect the equations of motion. These transformations form the gauge symmetry groups of the system.

Based on the Euler-Lagrange equation, a transformation

$$\phi \to \phi + \epsilon \Delta\phi \tag{1.4}$$

where ϵ is an infinitesimal parameter, can be a symmetry of the system if the Lagrangian density is invariant under this transformation up to a four-divergence

$$\mathcal{L} \to \mathcal{L} + \epsilon \partial_\mu J^\mu \tag{1.5}$$

According to Noether's Theorem, every symmetry of nature yields a conservation law and similarly, every conservation law reveals an underlying symmetry. Given this theorem, the current

$$j_\mu(x) = \frac{\partial \mathcal{L}}{\partial(\partial_\mu \phi)} \Delta\phi - J^\mu \tag{1.6}$$

is conserved, meaning

$$\partial_\mu j^\mu = 0 \tag{1.7}$$

1.1.2 Quantum Electrodynamics

Quantum electrodynamics (QED) is an abelian gauge theory describing a fermion field ψ and its electromagnetic field. The field's Lagrangian is required to satisfy the "local gauge invariance" principle, and therefore be invariant under the local gauge transformation,

$$\psi \to U\psi = \mathrm{e}^{\mathrm{i}\alpha(x)}\psi \tag{1.8}$$

where $\alpha(x)$ is an arbitrary parameter depending on the space and time coordinates. The family of such phase transformations forms a unitary abelian group known as the U(1) group.

The Dirac Lagrangian density for a spin-1/2 field of mass m is

$$\mathcal{L} = \mathrm{i}\bar{\psi}\gamma^\mu \partial_\mu \psi - m\bar{\psi}\psi \tag{1.9}$$

where $\bar{\psi} = \psi^\dagger \gamma^0$ and γ^μ are the 4×4 Dirac matrices satisfying the anticommutation relation $\{\gamma^\mu, \gamma^\nu\} = \gamma^\mu\gamma^\nu - \gamma^\nu\gamma^\mu = 2g^{\mu\nu}$ with $g^{\mu\nu}$ being the metric tensor. The Lagrangian density is not local gauge invariant since the first part transforms as

$$\partial_\mu \psi \to \mathrm{e}^{\mathrm{i}\alpha(x)}\partial_\mu \psi + \mathrm{i}\mathrm{e}^{\mathrm{i}\alpha(x)}\psi \partial_\mu \alpha \tag{1.10}$$

In order to satisfy the local gauge invariance, a term should be added in the Lagrangian density

$$\mathcal{L} = \left[\mathrm{i}\bar{\psi}\gamma^\mu \partial_\mu \psi - m\bar{\psi}\psi\right] + e\bar{\psi}\gamma^\mu A_\mu \psi \tag{1.11}$$

where e is later identified as the elementary charge and A_μ is a new field, called "gauge field" transforming as

$$A_\mu \to A_\mu + \frac{1}{e}\partial_\mu \alpha \tag{1.12}$$

The covariant derivative D_μ needs to be introduced

$$D_\mu \equiv \partial_\mu - \mathrm{i}eA_\mu \tag{1.13}$$

transforming as

$$D_\mu\psi \to \mathrm{e}^{\mathrm{i}\alpha(x)} D_\mu\psi \tag{1.14}$$

This introduces in the Lagrangian a term

$$e\bar{\psi}\gamma^\mu A_\mu\psi \tag{1.15}$$

which describes the interaction of the vector field A_μ with the electromagnetic current

$$J^\mu = e\bar{\psi}\gamma^\mu\psi \tag{1.16}$$

In order to finalize the Lagrangian density a kinematic part is needed for the vector field and using the Proca Lagrangian density,

$$\mathcal{L} = -\frac{1}{4}F^{\mu\nu}F_{\mu\nu} + \frac{1}{4}m^2 A_\mu A^\mu \tag{1.17}$$

where $F^{\mu\nu}$ is the electromagnetic field strength tensor, defined as $F^{\mu\nu} = \partial_\mu A_\nu - \partial_\nu A_\mu$. The first term in the Lagrangian is local gauge invariant while the second one is not. In order to satisfy the gauge principle, the gauge field is required to be massless and the full Lagrangian density is

$$\mathcal{L} = -\frac{1}{4}F^{\mu\nu}F_{\mu\nu} + \bar{\psi}(\mathrm{i}\gamma^\mu D_\mu\psi - m)\psi \tag{1.18}$$

Summing up, in order to satisfy the local gauge invariance a vector field A_μ has been introduced in the Lagrangian density of the spin-1/2 particle, which is the photon field obeying Maxwell's Lagrangian

$$\mathcal{L}_{\text{Maxwell}} = -\frac{1}{4}F^{\mu\nu}F_{\mu\nu} + e\bar{\psi}\gamma^\mu A_\mu\psi \tag{1.19}$$

1.1.3 Quantum Chromodynamics

In an analogous way, the structure of quantum chromodynamics is extracted from local gauge invariance, replacing the U(1) group with the group of phase transformations on the quark color fields, SU(3). The free Lagrangian density is

$$\mathcal{L} = \sum_j \bar{q}_j(\mathrm{i}\gamma^\mu\partial_\mu - m_j)q_j \tag{1.20}$$

where $q_j = (q_r, q_b, q_g)_j^T$, with $j = 1, \ldots, 6$ the color triplet corresponding to the six quark flavors. The equations will be given for one quark flavor hereafter but summation is implied.

Requiring the Lagrangian density to be invariant under

$$q(x) \to Uq(x) \equiv \mathrm{e}^{-\mathrm{i}g\alpha_a(x)T_a} q(x) \tag{1.21}$$

where U is an arbitrary 3×3 unitary matrix, g is the strong coupling constant which in analogy to the fine structure constant in QED is often expressed in terms of $a_s = \frac{g^2}{4\pi}$, α_a are arbitrary parameters, and $T_a = \frac{\lambda_a}{2}$ with $a = 1, ..., 8$, are the generators of the SU(3) group where λ_a the set of linearly independent traceless 3×3 matrices called Gell-Mann matrices. The generators satisfy the commutation relation $[T_a, T_b] = \mathrm{i} f_{abc} T_c$, where the real numbers f_{abc} are the structure constants of SU(3), manifesting the non-Abelian character of the theory. Summation is implied over a suffix.

Following the procedure as in the QED section, in order to satisfy SU(3) local gauge invariance eight gauge fields G^a_μ, the gluon fields, are introduced, transforming as

$$G^a_\mu \to G^a_\mu - \frac{1}{g}\partial_\mu \alpha_a - f_{abc}\alpha_b G^c_\mu \tag{1.22}$$

resulting to a Lagrangian density

$$\mathcal{L} = \bar{q}(\mathrm{i}\gamma^\mu \partial_\mu - m)q - g(\bar{q}\gamma^\mu T_a q)G^a_\mu \tag{1.23}$$

and the covariant derivative used is

$$D_\mu = \partial_\mu + \mathrm{i}g T_a G^a_\mu \tag{1.24}$$

where $T_a G^a_\mu$ is in analogy to A_μ and g to e from QED. In this way, a term has entered the Lagrangian describing the interaction of the

$$J^{a,\mu} \equiv g\bar{q}\gamma^\mu T_a q \tag{1.25}$$

currents with the gauge fields G^a_μ.

Adding the gauge invariant kinematic terms for each of the G^a_μ gauge fields, the final gauge invariant QCD Lagrangian density is

$$\mathcal{L} = -\frac{1}{4} G^a_{\mu\nu} G^{\mu\nu}_a + \bar{q}(\mathrm{i}\gamma_\mu D^\mu - m)q \tag{1.26}$$

where $G^a_{\mu\nu}$ the gluon field tensor

$$G^{\mu\nu}_a = \partial^\mu G^\nu_a - \partial^\nu G^\mu_a - g f^{abc} G^\mu_b G^\nu_c \tag{1.27}$$

Due to the non-Abelian character of the theory, resulting to the last term in Equation 1.27, the Lagrangian contains terms corresponding to self-interaction between the gauge boson fields forming three and four gluon vertices.

1.1.4 Electroweak Theory

The fact that the observed lifetimes of the pion and the muon are longer than the ones of particles that decay either through strong or electromagnetic interactions has pointed to another type of interactions with an even weaker coupling than the electromagnetic, the weak interaction. Weak interactions involve both charged and neutral currents. Charged currents are involved in transitions between up-type and

down-type quarks or charged leptons and the corresponding neutrinos whereas neutral currents conserve flavor.

Fermions are grouped into left-handed and right-handed

$$\psi_L = P_L\psi = \frac{1}{2}(1-\gamma^5)\psi \tag{1.28}$$

$$\psi_R = P_R\psi = \frac{1}{2}(1+\gamma^5)\psi \tag{1.29}$$

where $\gamma^5 = \mathrm{i}\gamma^0\gamma^1\gamma^2\gamma^3$ and $P_{L,R}$ the chirality operators. Left-handed fields, ψ_L, have $I = \frac{1}{2}$ and form doublets

$$\begin{pmatrix} u \\ d \end{pmatrix}_L, \quad \begin{pmatrix} \nu_e \\ e \end{pmatrix}_L, \qquad \begin{pmatrix} c \\ s \end{pmatrix}_L, \quad \begin{pmatrix} \nu_\mu \\ \mu \end{pmatrix}_L, \qquad \begin{pmatrix} t \\ b \end{pmatrix}_L, \quad \begin{pmatrix} \nu_\tau \\ \tau \end{pmatrix}_L \tag{1.30}$$

and the right-handed fields, ψ_R

$$u_R,\ d_R,\ e_R, \qquad c_R,\ s_R,\ \mu_R, \qquad t_R,\ b_R,\ \tau_R \tag{1.31}$$

are singlets with $I = 0$ and are invariant under the weak isospin transformations.

The Electroweak Theory is constructed based on the same principle of gauge invariance, as QED and QCD, and treats the weak and electromagnetic interactions as different manifestations of the same force. The gauge symmetry group is $\mathrm{U}(1)_Y \bigotimes \mathrm{SU}(2)_L$. $\mathrm{SU}(2)_L$ refers to the weak isospin (I) with the subscript L to remind that it involves only left-handed fields and U(1) refers to the weak hypercharge (Y) which involves both chiralities. The weak hypercharge is connected to the charge and the weak isospin by

$$Q = I_3 + \frac{Y}{2} \tag{1.32}$$

where I_3 is the third component of the weak isospin. For the left-handed doublets and right-handed singlets, the U(1) transformation corresponds to multiplication by a phase factor $\mathrm{e}^{\mathrm{i}\alpha^a(x)\frac{Y}{2}}$. The left-handed doublets additionally transform as

$$\psi_L \to \mathrm{e}^{\mathrm{i}\beta^a(x)\frac{\tau^a}{2}}\psi_L \tag{1.33}$$

where $a = 1, 2, 3$ and τ^a the Pauli matrices and $\frac{\tau^a}{2}$ the generators of the SU(2) group.

Four gauge fields are introduced when applying the gauge principle. One gauge field (singlet), B_μ, is associated to $\mathrm{U}(1)_Y$ and couples to both chiralities of the fermion fields and the rest (isotriplet), W^i_μ, are associated to $\mathrm{SU}(2)_L$ and couple only to the left-handed components. The Lagrangian density is

$$\mathcal{L} = -\frac{1}{4}W^a_{\mu\nu}W^{\mu\nu}_a - \frac{1}{4}B_{\mu\nu}B^{\mu\nu} + \bar{\psi}\mathrm{i}\gamma^\mu D_\mu\psi \tag{1.34}$$

where $W^a_{\mu\nu}$ and $B_{\mu\nu}$ the field tensors

$$W^i_{\mu\nu} = \partial_\mu W^i_\nu - \partial_\nu W^i_\mu - g\epsilon^{ijk}W^j_\mu W^k_\nu \tag{1.35}$$

$$B_{\mu\nu} = \partial_\mu B_\nu - \partial_\nu B_\mu \tag{1.36}$$

where ϵ^{ijk} the structure constants of SU(2) and D_μ the covariant derivative

$$D_\mu = \partial_\mu + \mathrm{i}gW_\mu^a I_a + \mathrm{i}g'\frac{1}{2}B_\mu Y \tag{1.37}$$

where g is the SU(2) and g' the U(1) coupling constants.

From the Lagrangian, the interaction terms between the fermions and the gauge fields is

$$\mathcal{L}_{\text{int}} = -\psi_L\gamma^\mu\left(g\frac{\tau_a}{2}W_\mu^a + g'\frac{Y}{2}B_\mu\right)\psi_L - \bar{\psi}_R\gamma^\mu\left(g'\frac{Y}{2}B_\mu\right)\psi_R \tag{1.38}$$

where the coupling of the W_μ^a only to the left-handed components is visible. In Equation 1.34 there are no fermion mass terms since $\bar{\psi}\psi = \bar{\psi}_L\psi_R + \bar{\psi}_R\psi_L$ would mix left- and right-handed fields and consequently, break gauge invariance. Therefore, fermion masses will be generated dynamically by gauge invariant Yukawa interactions with the Higgs field. The full electroweak Lagrangian will consist of the fermion and gauge terms included in Equation 1.34 in addition to the Yukawa and Higgs terms

$$\mathcal{L}_{\text{EW}} = \mathcal{L}_{\text{f,g}} + \mathcal{L}_H + \mathcal{L}_{\text{Yukawa}} \tag{1.39}$$

1.1.5 Higgs mechanism

In the Lagrangian densities described in the previous sections, there are no quadratic terms of the gauge fields which implies that the gauge bosons are massless. The vector bosons of the weak interaction are experimentally known to be massive, with $m_{W^\pm} = 80.4\,\text{GeV}$ and $m_{Z^0} = 91.2\,\text{GeV}$ [1], accordingly. However, adding a mass component leads to violation of the gauge invariance. The same stands for the fermion masses. The Higgs mechanism was introduced to solve these issue [3].

According to the Higgs mechanism, an additional $\text{SU}(2)_L$ isospin doublet of complex scalar fields with $Y = 1$

$$\phi = \begin{pmatrix}\phi^+\\ \phi^0\end{pmatrix} \tag{1.40}$$

is introduced with the corresponding contribution in the Lagrangian

$$\mathcal{L}_H = (D_\mu\phi)^\dagger(D^\mu\phi) - V(\phi) \tag{1.41}$$

where the potential term

$$V(\phi) = \mu^2\phi^\dagger\phi + \lambda(\phi^\dagger\phi)^2 = \mu^2\phi^2 + \lambda\phi^4 \tag{1.42}$$

To determine the ground state, ϕ_0, the potential is minimized

$$\frac{\partial V}{\partial\phi} = 2\phi(\mu^2 + 2\lambda\phi^2) = 0 \tag{1.43}$$

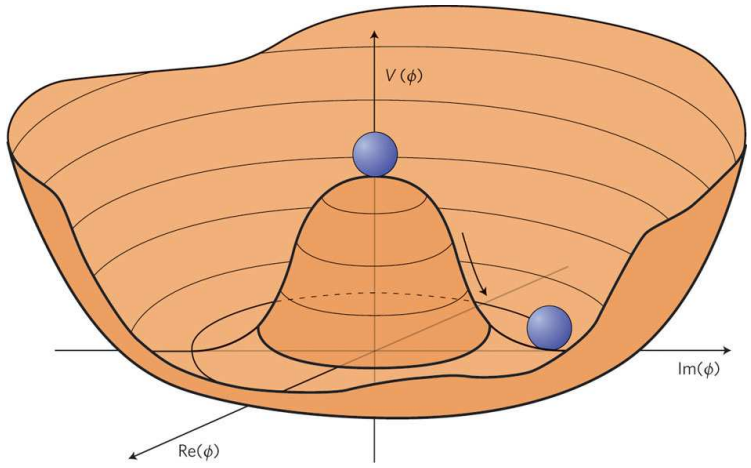

Figure 1.1: The shape of the Higgs potential $V(\phi) = \mu^2\phi^2 + \lambda\phi^4$ for $\mu^2 < 0$.

where μ is the mass parameter. For $\mu^2 > 0$, $\phi_0 = 0$. However, for $\mu^2 < 0$, the shape of the potential is shown in Figure 1.1 and

$$\phi_0^2 = -\frac{\mu^2}{2\lambda} \equiv \frac{u^2}{2} \tag{1.44}$$

The absolute value of the field at the minima of the potential is known as the vacuum expected value. For $\mu^2 < 0$ a non-vanishing vacuum expected value for ϕ^2 in the physical vacuum state has been obtained. The reference ground state for the local gauge transformation is chosen to be

$$\phi_0 = \frac{1}{\sqrt{2}}\begin{pmatrix} 0 \\ u \end{pmatrix} \tag{1.45}$$

which breaks the $\mathrm{SU}(2)_L$ symmetry while the Lagrangian remains invariant under $\mathrm{U}(1)_Y \bigotimes \mathrm{SU}(2)_L$ transformations. This behavior is called spontaneous symmetry breaking.

The fields are then expressed with quantum fluctuations about this minimum and the scalar doublet ϕ is redefined

$$\phi(x) = \mathrm{e}^{\frac{\mathrm{i}\xi_a(x)\tau^a}{2u}} \begin{pmatrix} 0 \\ \frac{u+H(x)}{\sqrt{2}} \end{pmatrix} \tag{1.46}$$

where $\xi_a(x)$, $a = 1, 2, 3$ real fields and $H(x)$ the real scalar Higgs field. The Lagrangian is locally SU(2) invariant and by using the freedom of gauge transformations, the $\xi_a(x)$ disappear from the Lagrangian and ϕ can be replaced by

$$\phi(x) = \frac{1}{\sqrt{2}}\begin{pmatrix} 0 \\ u + H(x) \end{pmatrix} \tag{1.47}$$

Taking into account that

$$D^\mu = \partial^\mu - \mathrm{i}gW_a^\mu \frac{\tau^a}{2} - \mathrm{i}g'\frac{1}{2}B^\mu \tag{1.48}$$

the kinetic part of the Lagrangian $\mathcal{L}_H$ component becomes

$$(D_\mu\phi)^\dagger(D^\mu\phi) \rightarrow \frac{1}{2}\partial^\mu H\partial_\mu H + \frac{1}{8}g^2(u+H)^2|W_\mu^1 + \mathrm{i}W_\mu^2|^2 + \frac{1}{8}(u+H)^2|g'W_\mu^3 - gB_\mu|^2 \tag{1.49}$$

The charged physical fields $W^\pm$ are then defined

$$W_\mu^\pm = \frac{1}{\sqrt{2}}(W_\mu^1 \mp \mathrm{i}W_\mu^2) \tag{1.50}$$

and the neutral physical fields of the Z and the photon are defined in a way as to be orthogonal to each other

$$Z_\mu = \frac{g'W_\mu^3 - gB_\mu}{\sqrt{g'^2+g^2}} \tag{1.51}$$

$$A_\mu = \frac{g'W_\mu^3 + gB_\mu}{\sqrt{g'^2+g^2}} \tag{1.52}$$

which, by introducing the "weak mixing angle" θ_w

$$\cos\theta_\mathrm{w} = \frac{g'}{\sqrt{g^2+g'^2}},\ \sin\theta_\mathrm{w} = \frac{g}{\sqrt{g^2+g'^2}} \tag{1.53}$$

become

$$Z_\mu = -B_\mu\sin\theta_\mathrm{w} + W_\mu^3\cos\theta_\mathrm{w} \tag{1.54}$$

$$A_\mu = B_\mu\cos\theta_\mathrm{w} + W_\mu^3\sin\theta_\mathrm{w} \tag{1.55}$$

The boson masses are extracted from the mass terms in Equation 1.49

$$M_W = \frac{gu}{2} \tag{1.56}$$

$$M_Z = \frac{\sqrt{g^2+g'^2}u}{2} \tag{1.57}$$

while the photon remains massless. The relation between the mass of the bosons and the weak mixing angle is

$$\frac{M_W}{M_Z} = \cos\theta_\mathrm{w} \tag{1.58}$$

Not only the masses of W and Z but also the fermion masses are generated by the spontaneous breaking of the $\mathrm{U}(1)_Y \bigotimes \mathrm{SU}(2)_L$ gauge symmetry. This is achieved by the Yukawa interactions between the Higgs and the fermion fields. For a single generation

$$\mathcal{L}_\mathrm{Yukawa} = -Y_\ell\bar{L}_L\phi\ell_R - Y_d\bar{Q}_L\phi d_R - Y_u\bar{Q}_L\tilde{\phi}u_R + \mathrm{h.c.} \tag{1.59}$$

where $L_L = (\nu_L, \ell_L)^T$ and $Q_L = (u_L, d_L)^T$ stand for the left-handed lepton and quark doublets, ℓ is the charged lepton and $\tilde{\phi} = -\mathrm{i}\tau_a\phi^*$ is the charge conjugate of the Higgs doublet. Written out in components, the Yukawa term of the Lagrangian becomes

$$\begin{aligned}\mathcal{L}_\mathrm{Yukawa} \quad = \quad & -Y_\ell(\bar{\nu}_L\phi^+\ell_R + \bar{\ell}_R\phi^-\nu_L + \bar{\ell}_L\phi^0\ell_R + \bar{\ell}_R\phi^{0*}\ell_L) \\ & -Y_d(\bar{u}_L\phi^+d_R + \bar{d}_R\phi^-u_L + \bar{d}_L\phi^0d_R + \bar{d}_R\phi^{0*}d_L) \\ & +Y_u(\bar{u}_R\phi^+d_L + \bar{d}_L\phi^-u_R - \bar{u}_R\phi^0u_L - \bar{u}_L\phi^{0*}u_R)\end{aligned} \tag{1.60}$$

The vacuum expectation value of ϕ gives rise to fermion mass terms.

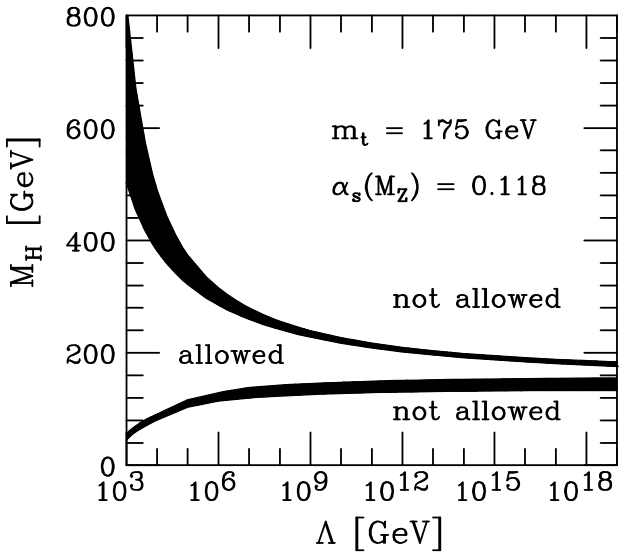

Figure 1.2: The allowed M_H range as set by the triviality (upper) bound and the vacuum stability (lower) bound as a function of the cut-off scale Λ. The bands correspond to the theoretical uncertainties.

1.1.6 Theoretical constraints on the Higgs boson mass

In the Higgs mechanism, the Higgs mass is a free parameter of the Standard Model but interesting theoretical constraints can be derived from assumptions on the energy range in which the SM is valid before perturbation theory breaks down and new phenomena emerge. These constraints are based on perturbative unitarity in scattering amplitudes, triviality, vacuum stability and fine-tuning.

Since interactions of the longitudinal components of the massive gauge bosons grow with their momenta, cross sections of processes involving W_L and Z_L, which increase with energy, would violate unitarity at some stage. From calculations of the amplitude for the scattering of W bosons involving the Higgs boson, it follows that $M_H^2 \leq 2\pi\sqrt{2}/G_F \sim (870\,GeV)^2$ [4]. In addition, large values of the Higgs mass can jeopardize perturbation theory in the SM. For instance, in the decays of Higgs into massive gauge bosons, assuming a very large Higgs mass $M_H > 1\,\text{TeV}$ leads to two-loop contributions at the same importance as one-loop contributions and the perturbative series is not convergent. Perturbative unitarity requires a Higgs boson mass well below 1 TeV.

Taking into account one-loop radiative corrections to the Higgs boson quartic coupling λ with contributions of the Higgs boson itself only, leads to a logarithmic dependence of λ on the squared energy scale, Q^2. At very small energies the quartic coupling vanishes making the theory trivial, non-interacting. On the other hand, for very large energies it can become infinite. The energy cut-off Λ_c can be established, below which the self-coupling λ remains finite. If the Λ_c is large, the Higgs mass should be small to avoid λ becoming infinite which can be translated into an upper

bound. Lattice simulations of gauge theories, including non-perturbative effects, have led to an upper limit for the Higgs mass of 710 GeV, for Λ_c set at the Higgs boson mass itself [5].

Furthermore, top quark loops tend to drive the Higgs quartic coupling λ to negative values, for which the vacuum is no more stable since it has no minimum. To avoid this instability, the Higgs boson mass must exceed a minimum value for a given top mass. This lower bound depends on the cut-off Λ. Therefore, requiring the Standard Model to be extended to the Great Unification Theory (GUT) scale, $\Lambda_{\mathrm{GUT}} \sim 10^{16}$ GeV, and including the effect of top quark loops on the running coupling, the Higgs boson mass should roughly lie in the range between 130 and 180 GeV. In Figure 1.2 the bounds are shown both for the triviality and vacuum stability as a function of the energy cut-off Λ_c [6].

The fine-tuning problem originates from the radiative corrections to the Higgs mass, according to which M_H diverges quadratically with scale Λ. Therefore, a fine arrangement is needed in order to have a physical Higgs boson mass at the electroweak symmetry breaking scale as required for the consistency of the Standard Model. For values of scales $\Lambda_c \leq 1$ TeV there is no fine-tuning problem but as the scale increases the range of Higgs masses becomes narrow and for $\Lambda_c = 10$ TeV only a narrow range around $M_H \sim 200$ GeV is allowed [7].

1.2 Searches for the Higgs boson

As the Higgs mass remains a free parameter of the Standard Model, various experiments over the last decades have aimed for either direct or indirect searches of the Higgs boson.

1.2.1 Direct searches

In 1989 the Large Electron Positron (LEP) collider became operational at CERN and the four experiments (ALEPH, DELPHI, L3 and OPAL) took data at a center-of-mass energy $\sqrt{s} = 89-93$ GeV in the first phase (LEP I) and $\sqrt{s} = 161-209$ GeV in the second phase (LEP II). At LEP the Standard Model Higgs boson was expected to be produced mainly in association with a Z boson through the Higgs-strahlung process, $e^+e^- \rightarrow HZ$. The searches were concentrated on four final state topologies:

- four-jet final state: $H \rightarrow b\bar{b}$ and $Z \rightarrow q\bar{q}$
- tau lepton production: $H \rightarrow \tau^+\tau^-$ and $Z \rightarrow q\bar{q}$, or $H \rightarrow b\bar{b}$ and $Z \rightarrow \tau^+\tau^-$
- missing energy final state: $H \rightarrow b\bar{b}$ and $Z \rightarrow \nu\bar{\nu}$
- leptonic final state: $H \rightarrow b\bar{b}$ and $Z \rightarrow e^+e^-$ or $Z \rightarrow \mu^+\mu^-$

The combination of the LEP data is shown in Figure 1.3 where a 95 % Confidence Level lower limit of 114.4 GeV is extracted [8]. The dashed line represents the median background expectation, the solid line represents the observation and the bands correspond to the 68 % and 95 % probability bands.

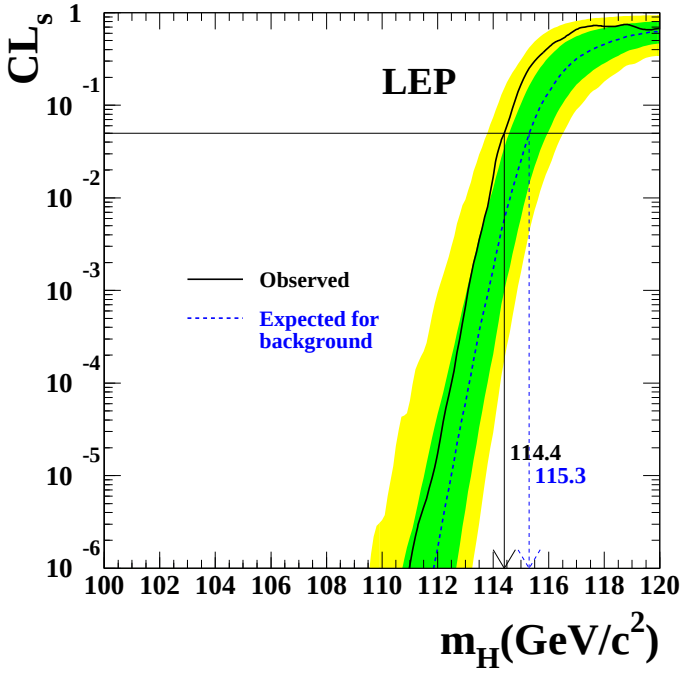

Figure 1.3: The ratio $\mathrm{CL}_s = \mathrm{CL}_{s+b}/\mathrm{CL}_b$ for the signal plus background hypothesis is presented for the combination of the LEP experiments. The dashed line represents the median background expectation and the solid line, the observation. The bands correspond to the 68 % and 95 % probability bands.

The Tevatron experiments, CDF and D0, at Fermilab, started taking data in 1985 up to 2011. Tevatron was a $p\bar{p}$ collider operating at center-of-mass energy $\sqrt{s} = 1.96\,\mathrm{TeV}$. The most important Higgs productions mechanisms in Tevatron were

- gluon fusion: $gg \to H$
- associated production with a vector boson: $q\bar{q} \to WH$ or $q\bar{q} \to ZH$
- vector boson fusion: $q\bar{q} \to q\bar{q}H$, where the quarks radiate weak gauge bosons which fuse to produce H.

The most sensitive channels are $H \to b\bar{b}$, $H \to WW^{(*)} \to \ell\nu\ell\nu$ and $H \to ZZ^{(*)} \to 4\ell$ for low Higgs masses ($m_H < 125\,\mathrm{GeV}$) and $H \to WW^{(*)} \to \ell\nu\ell\nu$ for higher masses. In Figure 1.4 the combination results presented in June 2012 are shown using $10.0\,\mathrm{fb}^{-1}$ [9]. The mass ranges $100 < m_H < 103\,\mathrm{GeV}$ and $147 < m_H < 180\,\mathrm{GeV}$ have been excluded at 95 % CL. There has been an excess of data events with respect to the background estimation in the mass range $115 < m_H < 140\,\mathrm{GeV}$. At $m_H = 120\,\mathrm{GeV}$, the p-value for a background fluctuation to produce this excess

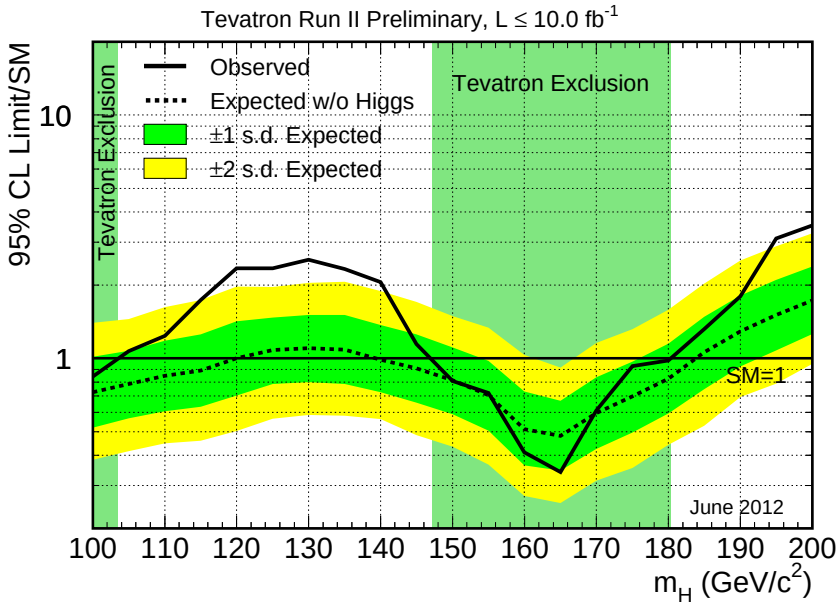

Figure 1.4: Observed and expected 95 % CL upper limits on the ratio of the Standard Model cross section as a function of the Higgs boson mass for the combined Tevatron analyses. The bands correspond to the 68 % and 95 % probability bands.

has been $\sim 1.5 \times 10^{-3}$, corresponding to a local significance of 3.0 standard deviations. The global significance for such an excess anywhere in the full mass range is approximately 2.5 standard deviations.

1.2.2 Indirect searches

Since the Higgs boson contributes to the radiative corrections in the electroweak sector, precision measurements of the electroweak observables are used to put indirect limits on the Higgs mass. The Standard Model predictions are calculated by GFITTER [10] based on a χ^2 minimization technique using the most recent experimental measurements as well as the latest theoretical predictions of electroweak observables and leaving free other parameters such as the M_Z and M_H.

In Figure 1.5 the $\Delta\chi^2 = \chi^2 - \chi^2_{\text{min}}$ is presented as a function of the M_H for the standard fit not including direct Higgs searches [11]. The fit yields

$$M_H = 96^{+31}_{-24}\, GeV \tag{1.61}$$

In Figure 1.6, the complete fit results are shown including results from Higgs direct searches in LEP, Tevatron and LHC. For the Higgs mass

$$M_H = 120^{+12}_{-5}\, GeV \tag{1.62}$$

In Figure 1.7, the compatibility between the complete fit results and the electroweak measurements is presented, where good agreement is observed.

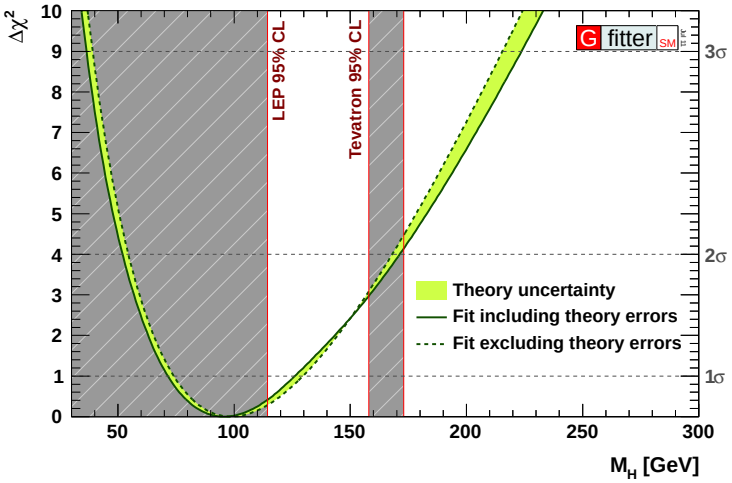

Figure 1.5: $\Delta\chi^2$ as a function of M_H for the standard fit, not including direct Higgs searches. The solid line gives the results when including theoretical errors while the dashed line gives the results ignoring the theoretical errors. The vertical bands correspond to excluded regions.

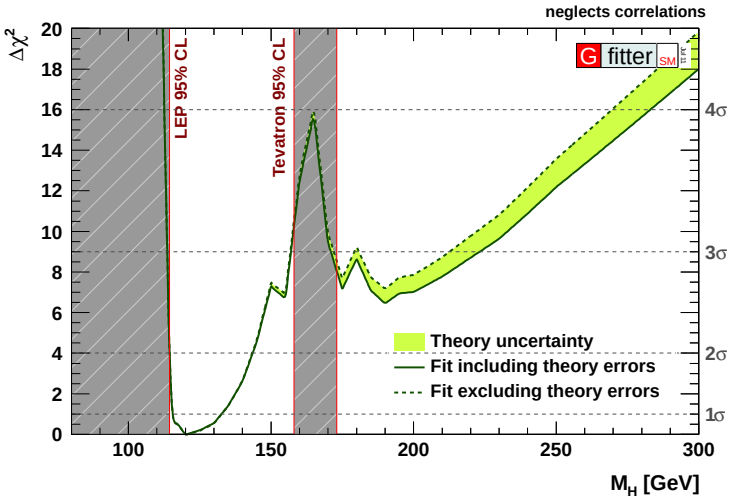

Figure 1.6: $\Delta\chi^2$ as a function of M_H for the complete fit including results from LEP, Tevatron and LHC. The solid line gives the results when including theoretical errors while the dashed line gives the results ignoring the theoretical errors. The vertical bands correspond to excluded regions.

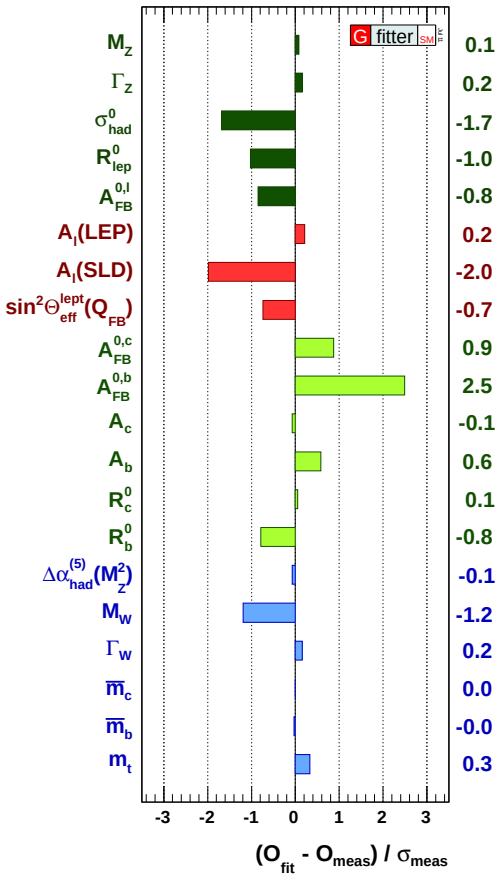

Figure 1.7: Pull values of the results of the complete fit, including direct Higgs searches, to the direct electroweak measurements are presented.

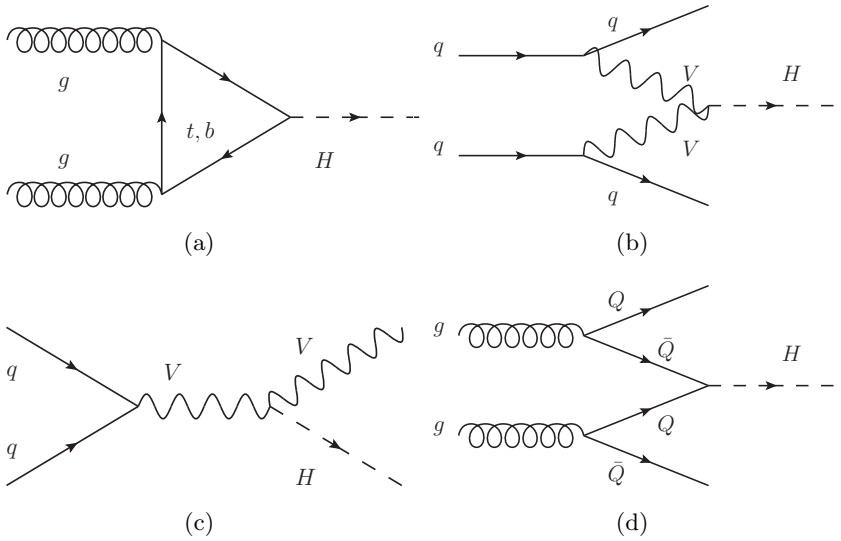

Figure 1.8: Main production mechanisms of the Standard Model Higgs at LHC: (a) gluon-gluon fusion, (b) vector boson fusion, (c) associated production with W/Z and (d) associated production with heavy quarks.

1.3 Higgs boson phenomenology at the LHC

The Higgs boson consists the Holy Grail of Particle Physics. After Tevatron, the LHC has joined this search in 2010. Due to the design performance of the collider and the detectors, a definite answer on the existence or not of the Higgs boson has been expected by the LHC.

1.3.1 Higgs production

At the LHC, the Higgs boson can be produced in the following ways:

- gluon fusion: $gg \to H$
- vector boson fusion (VBF): $q\bar{q} \to q\bar{q}H$
- associated production with vector bosons: $q\bar{q} \to WH$ or $q\bar{q} \to ZH$
- associated production with heavy quarks: $q\bar{q} \to Q\bar{Q}H$ or $gg \to Q\bar{Q}H$

some whose Feynman diagrams are presented in Figure 1.8.

In Figures 1.9 the inclusive Higgs production cross sections expected at the LHC are presented for the different production modes for $\sqrt{s} = 7\,\text{TeV}$ [12] and $\sqrt{s} = 8\,\text{TeV}$ [13]. The gluon-gluon fusion is the dominant production mode. It receives large contributions from higher order QCD corrections [14] and it is know at NNLO with 10 % uncertainty [15, 16]. The vector boson fusion is the next more important production mode. According to it, Higgs is produced in association with two quarks which will lead to two high energetic jets in the forward region. Higher

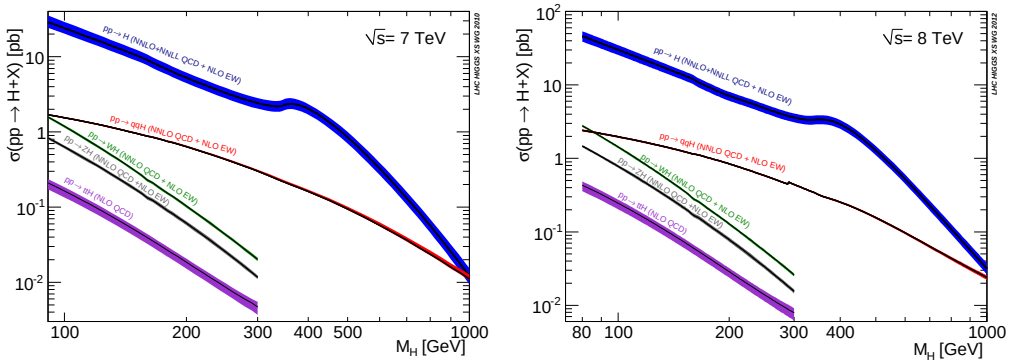

(a) (b)

Figure 1.9: The Higgs production cross sections are presented for (a) $\sqrt{s} = 7\,\text{TeV}$ and (b) $\sqrt{s} = 8\,\text{TeV}$ at the LHC as a function of the Higgs mass values.

order effects do not have a big contribution and the cross section is known at NLO with less than 10 % uncertainty. The associated production with vector bosons is known at NNLO in the QCD expansion and at NLO in the electroweak expansion with a uncertainty less than 5 %. The associated production with top quarks has very low cross section in the low masses that restricts the interest in this mode.

1.3.2 Higgs decays

The Higgs decays in different modes and the branching ratio of each depends on the Higgs mass. The branching ratios are known at NNLO [13, 17, 18], including both QCD and electroweak corrections and they are presented in Figure 1.10 as a function of the Higgs mass. One could divide the decay mode into two groups: the decays to fermions and the decays to bosons.

Concerning the Higgs decays to fermions, in the low mass region, $m_H \leq 130\,\text{GeV}$, the $H \to b\bar{b}$ is the dominant mode. Nevertheless, due to the huge background from jet production in QCD processes, this decay channel is not easily accessible. Another important channel in the low mass region is the decay to a τ pair, $qqH \to \tau^+\tau^-$. The taus can subsequently decay into pairs of leptons, hadrons or mixed (one lepton and one hadron). This process results to two relatively forward jets containing little hadronic activity. The basic sources of background for this decay channel are the Z+jets and the $t\bar{t}$ production but W+jets and single top production can also contribute.

Higgs can also decay into pairs of vector bosons. The $H \to ZZ^{(*)}/\gamma^{(*)} \to 4\ell$, where $\ell = \mu, e$, is also known as the "golden" channel due to the clean final state signature, the capability to fully reconstruct the Higgs mass and the coverage of a large mass range, from 120 GeV to 600 GeV. For $m_H < 180\,\text{GeV}$ one of the Z bosons is "off-shell" which results to leptons of lower transverse momentum which reduces the sensitivity. A decrease in sensitivity is also noticed for $m_H \approx 2M_W$, where the channel to two W bosons opens. The most dominant background is the $ZZ^{(*)} \to 4\ell$ while in the low masses where the leptons are softer, there are contributions from

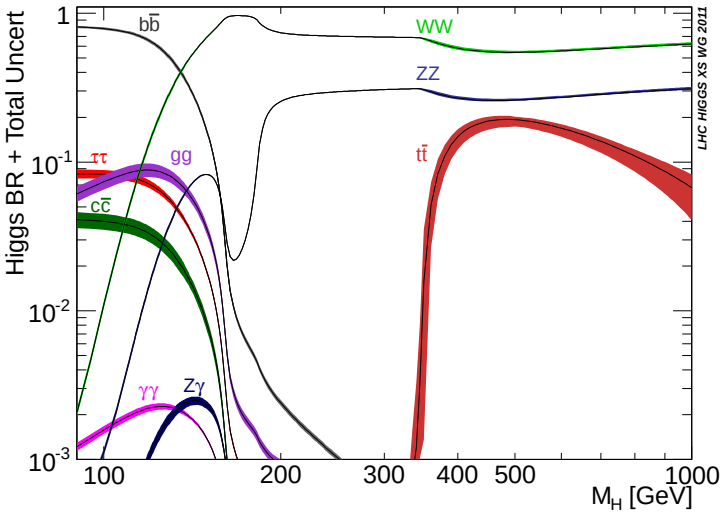

Figure 1.10: The decay branching ratios and their uncertainties are presented for the Standard Model Higgs boson.

$Zq\bar{q} \to 4\ell$ and $t\bar{t} \to 4\ell$.

The decay with the largest branching ratio is the $H \to WW^{(*)}$ which is dominant in the mass range $2M_W < m_H < 2M_Z$ and complements the $H \to ZZ^{(*)}/\gamma^{(*)} \to 4\ell$ searches. The final states considered are $\ell\nu\ell\nu$ and $l\nu q\bar{q}$. Due to the presence of high missing energy (high p_T neutrinos), only the transverse mass of the Higgs boson can be reconstructed. The dominant background processes are $WW^{(*)}$ and $t\bar{t}$ production with leptons and neutrinos in the final state.

Massless photons and gluons do not couple directly to the Higgs boson but through loops involving massive charged and/or colored particles which couple to the Higgs boson. In this sense $H \to \gamma\gamma$ and $H \to \gamma Z$ are mediated through the W boson and charged fermion loops while $H \to gg$ only through quark loops. The $H \to gg$ cannot be observed in a hadron collider due to the huge QCD background while the $H \to \gamma Z(\to e^+e^-/\mu^+\mu^-)$ channel is a demanding search channel since it needs separation from the huge Z+jets background.

The $H \to \gamma\gamma$ is a promising channel for the mass range from the LEP exclusion limit up to $m_H \approx 140\,\text{GeV}$ despite its low branching ratio. It has a very distinctive signature due to the two high energetic photons forming a narrow invariant mass peak. The main background is the direct photon production resulting to a smooth falling curve in the diphoton mass spectrum. However, the background can be estimated by a sideband fit with respect to the signal peak. Background contributions come also from dijet production and γj where at least one jet is misidentified as a photon.

Concerning the width of the Standard Model Higgs, Higgs is a very narrow resonance with $\Gamma(H) \leq 10\,\text{MeV}$ for low masses. For higher masses, the width rapidly increases and reaches $\sim 1\,\text{GeV}$ at the ZZ threshold. For even larger masses, the width is of the same order of magnitude as the Higgs mass. The behavior of the

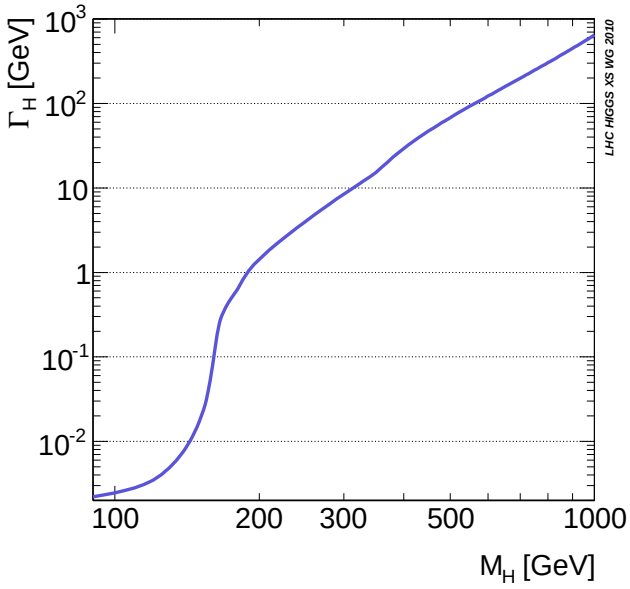

Figure 1.11: The Higgs total width is presented as a function of its mass. For low masses the Higgs is a narrow resonance while for high masses, the mass and the width are of the same order of magnitude.

decay width of the Higgs boson as a function of its mass is shown in Figure 1.11 [12].

Chapter 2

The ATLAS experiment at the LHC

The Large Hadron Collider (LHC) is an unprecedented technological achievement for the fields of High Energy and Accelerator physics. The ATLAS detector, built in one of the experimental caverns of the LHC, has been designed to provide physicists with the essential data to exploit the full physics potential of the accelerator.

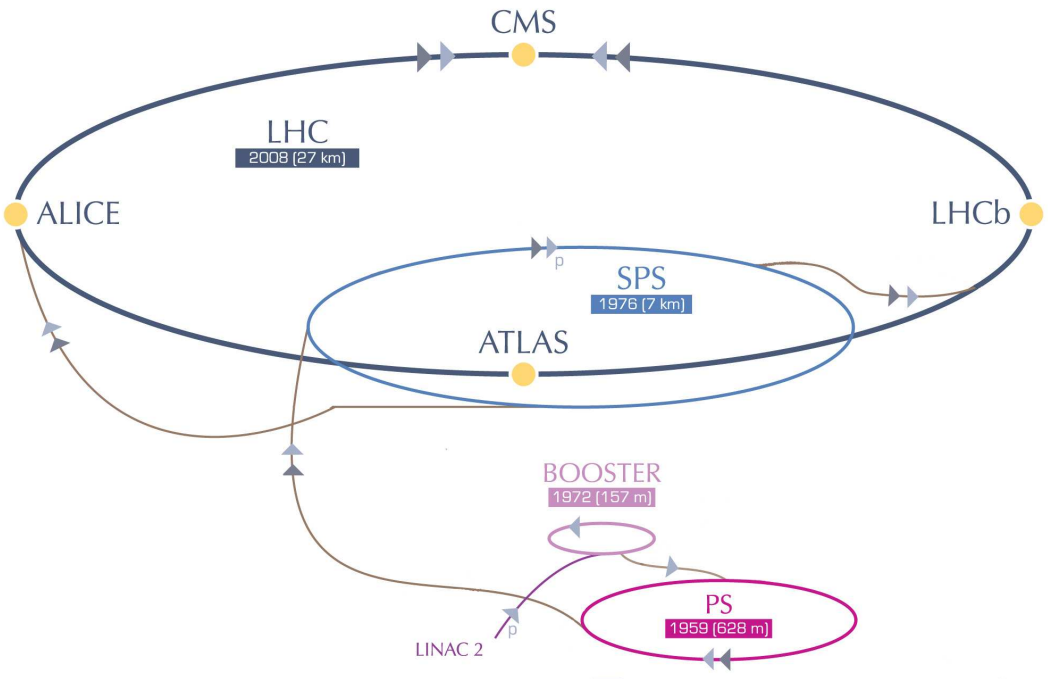

Figure 2.1: The full acceleration complex for the LHC proton-proton collisions along with the four main experiments (ALICE, ATLAS, CMS and LHCb).

2.1 The LHC complex

The LHC [19] is a two-ring superconducting hadron accelerator and collider installed in the existing Large Electron-Positron (LEP) accelerator tunnel. The LEP tunnel was built in the 1980's at the European Organization for Nuclear Research (CERN - Conseil Européen pour la Recherche Nucléaire) in the Franco-Swiss area near Geneva. It has a circumference of 26.7 km, consists of eight straight sections and eight arcs and lies between 45 m and 170 m below the surface, on an inclined plane of 1.4 % slope.

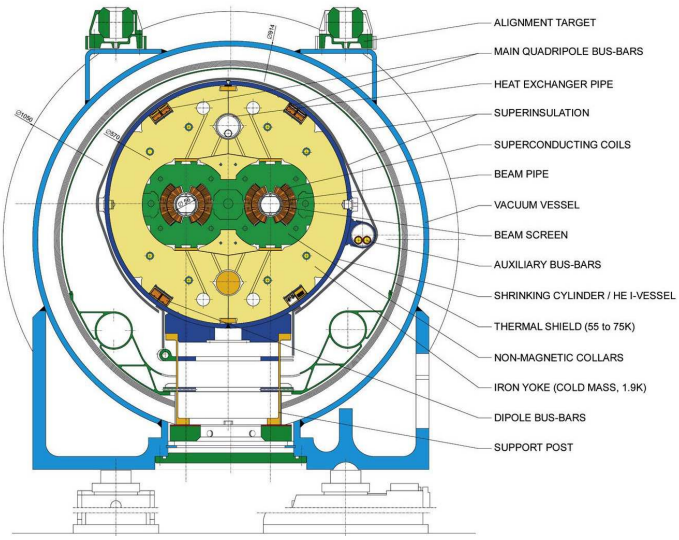

Figure 2.2: Diagram showing the cross-section of an LHC dipole magnet with its components including the coils and the vacuum vessel.

One of the main purposes of the LHC is to accelerate protons and heavy ions. Since it is a particle-particle accelerator, in contrast to the particle-antiparticle LEP, two separate beam lines are used for the counter-rotating beams. Due to space restrictions, a "two-in-one" superconducting magnet design [20, 21] has been applied as shown in Figure 2.2. The machine consists of 9593 magnets; 1232 dipole magnets responsible for bending the beams, 392 quadrupole magnets for beam focusing and higher multipole magnets aiming for beam correction. The acceleration of the beams is taken care of by 400 MHz Radio-Frequency (RF) cavities. The magnets have Niobium-Titanium (Nb-Ti) coils giving fields up to 8.33 T with a current of nearly 12 kA. The magnet and the beam lines are housed in the same cryostat and the system is cooled down to 1.9 K using super-fluid Helium (He).

The acceleration process starts at a very earlier stage. Protons remaining after stripping the electrons from Hydrogen atoms are firstly accelerated in LINAC2. The 50 MeV protons enter the Proton Synchrotron Booster where they form bunches and reach 1.4 GeV. The bunched protons are accelerated up to 26 GeV in the Proton Synchrotron (PS) and then up to 450 GeV in the Super Proton Synchrotron (SPS). The protons are then injected into the LHC and accelerated up to 7 or 8 TeV. The

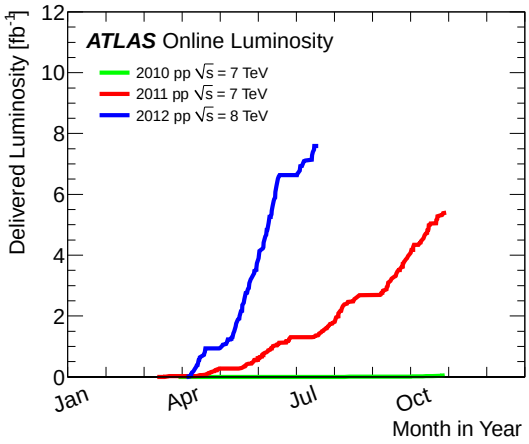

Figure 2.3: The cumulative luminosity versus day delivered to ATLAS during stable beams is shown for 2010 (green), 2011 (red) and 2012 (blue) running.

full acceleration complex is shown in Figure 2.1.

The second purpose of the LHC is to provide collisions to the four experimental caverns, built at different points of the tunnel. Four detectors have been built in these caverns. ATLAS (A Toroidal LHC ApparatuS) and CMS (Compact Muon Solenoid) are general purpose detectors with broad physics programs. Studies of the Standard Model and searches for evidence of New Physics are amongst their aims. ALICE (A Large Ion Collider Experiment) is dedicated to heavy ion physics and studies on the quark-gluon plasma and LHCb focuses on b-quark physics and CP violation measurements.

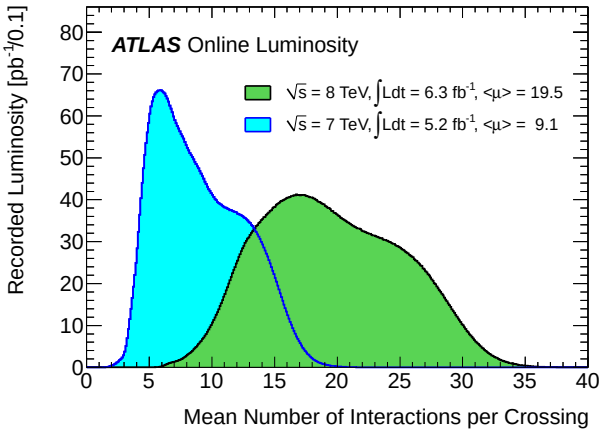

Figure 2.4: The luminosity-weighted distribution of the mean number of interactions per crossing is shown for the 2011 and 2012 data. This shows the full 2011 run and 2012 data taken between April 4th and June 18th.

The LHC has been designed to accelerate proton beams to a center-of-mass

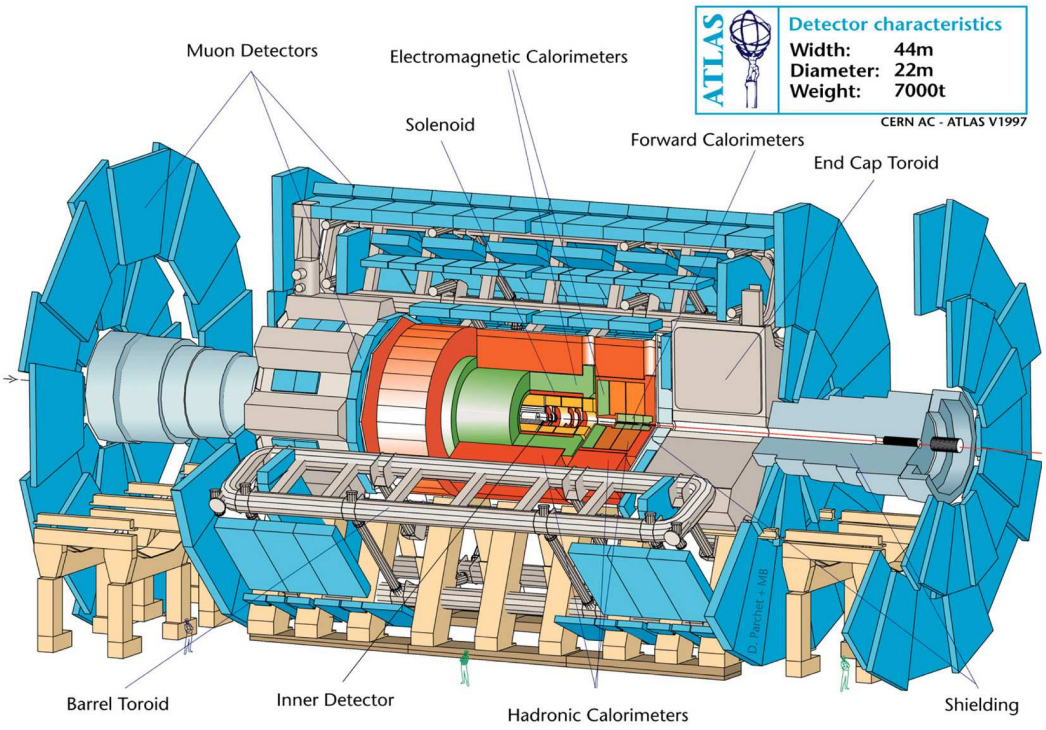

Figure 2.5: The ATLAS detector is one the two general purpose detectors at the LHC. It consists of three subdetector systems: the Inner Detector, the Calorimeters and the Muon Spectrometer.

energy $\sqrt{s} = 14\,\text{TeV}$ and lead (Pb) ion beams to $\sqrt{s} = 2.8\,\text{TeV}$. It should reach a luminosity of $10^{34}\,\text{cm}^{-2}\text{s}^{-1}$ and $10^{27}\,\text{cm}^{-2}\text{s}^{-1}$ respectively [22]. During 2011 the LHC has delivered $5.6\,\text{fb}^{-1}$ of proton-proton collisions at $\sqrt{s} = 7\,\text{TeV}$ and ATLAS has recorded $5.2\,\text{fb}^{-1}$ reaching a peak instantaneous luminosity of $3.65 \times 10^{33}\,\text{cm}^{-2}\text{s}^{-1}$. In 2012 the energy has been increased $\sqrt{s} = 8\,\text{TeV}$ and from April to June the LHC had delivered $6.6\,\text{fb}^{-1}$ and ATLAS has recorded $6.3\,\text{fb}^{-1}$. A peak luminosity record of $6.8 \times 10^{33}\,\text{cm}^{-2}\text{s}^{-1}$ has been reached during this period of 2012. In Figure 2.3 the cumulative luminosity is shown for 2010, 2011 and for 2012 until the end of June. In Figure 2.4 the distribution of the average number of interactions per bunch crossing is presented for 2011 and the above mentioned 2012 fraction of data taking.

2.2 The ATLAS detector

The ATLAS detector is 44 m in length and 25 m in height and it weights 7000 tons [23]. It is approximately forward-backward symmetric with respect to the Interaction Point (IP). It is divided in the barrel region, where the modules form cylindrical layers and two end-cap regions, where the detectors form disks to increase the detector coverage. ATLAS is mainly composed of six subsystems: the Inner Detector, the calorimeters, the Muon Spectrometer, the magnet system, the trigger

and the data acquisition system.

2.2.1 Physics program

The ATLAS experiment has been designed to exploit the full physics potential of the LHC. The high luminosity and the large center-of-mass energy of the proton-proton collisions enable high precision tests on the Standard Model as well as tests on various theoretical models.

One of the main tests on the Standard Model comes through studies on the electroweak bosons, W and Z, and their properties. The top quark is produced at sufficient rate which enables precise measurements on the top quark mass and its couplings. It is the heaviest known particle and plays an important role in constraining new physics phenomena. b-quark physics are also feasible where B-mesons properties and their decays, including some rare processes, can be studied as well as CP violation.

One of the main aims of the LHC physics program is to discover or exclude the Standard Model Higgs boson, which has also been a benchmark for the performance of the ATLAS detector. The Higgs mass is an unknown parameter of the Standard Model. For low Higgs masses the decay to two heavy quarks, two tau leptons or two photons are dominant. As explained in Section 1.3.2 the decays to $ZZ^{(*)}$ and $WW^{(*)}$ also start to become significant and for higher masses the decay to two real Z bosons is dominating, being the most clean channel.

A wide variety of phenomena and models beyond the Standard Model can be tested at the LHC. These include Supersymmetry, which is one of the theoretically favored candidates for physics beyond the Standard Model postulating the invariance of the theory under the symmetry which transforms fermions into bosons and vice versa, new heavy gauge bosons, W' and Z' with masses up to 6 TeV decaying to high p_{T} leptons and leptoquarks which are colored bosons carrying both lepton and quark quantum numbers [24].

Such physics program imposes stringent requirements in the design of the detector. Due to the experimental conditions, radiation hardness is required for the detector systems and their electronics. High granularity and quick response is also demanded to handle the particle fluxes. Good momentum resolution and reconstruction efficiency is important as well as large acceptance in pseudorapidity with almost full azimuthal coverage in the whole detector. Finally, highly efficient triggering on low transverse-momentum objects with sufficient background rejection, is a prerequisite to achieve an acceptable trigger rate for most physics processes of interest.

2.2.2 Coordinate system

ATLAS uses a right-handed coordinate system. The nominal Interaction Point (IP) is defined as the origin of the coordinate system, while the counter-clockwise beam direction defines the z-axis and the x-y plane is transverse to the beam direction. The positive x-axis is pointing to the center of the LHC ring and the positive y-axis upwards. The side-A of the detector is defined as that with positive z and side-C

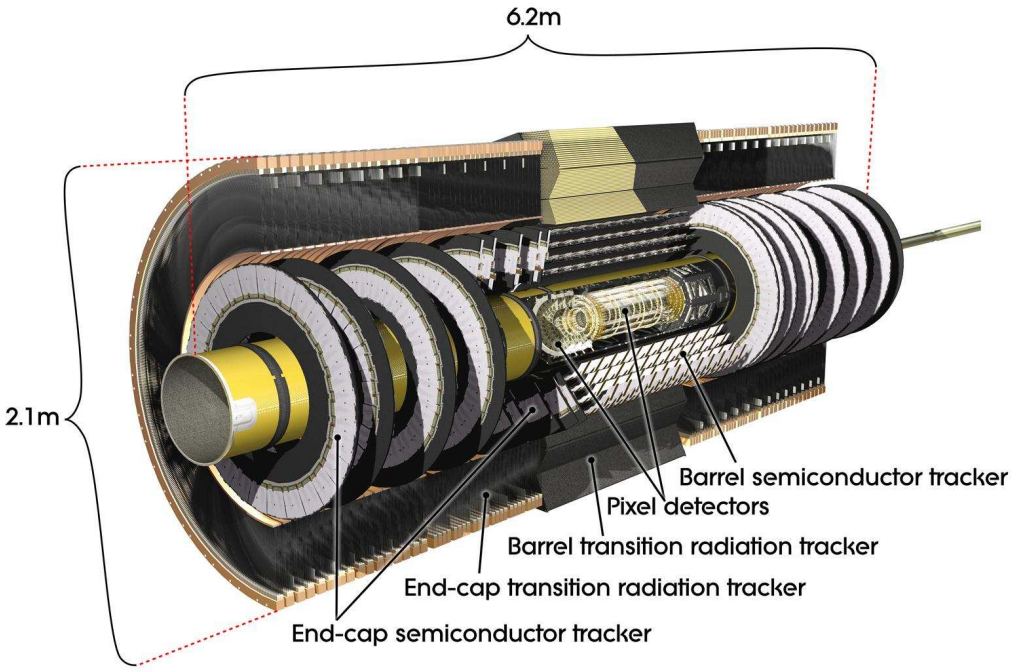

Figure 2.6: The ATLAS Inner Detector is a tracker consisting of three subdetectors: the Pixel Detector, the SemiConductor Tracker and the Transition Radiation Tracker.

is that with negative z. The pseudorapidity is defined as $\eta = -\ln(\tan(\theta/2))$. The transverse momentum p_T and the transverse energy E_T are defined in the x-y plane. The distance ΔR in the pseudorapidity-azimuthal angle space is defined as

$$\Delta R = \sqrt{\Delta\theta^2 + \Delta\phi^2} \tag{2.1}$$

2.2.3 Inner Detector

The ATLAS Inner Detector (ID) is designed to provide hermetic and robust pattern recognition, excellent momentum resolution and both primary and secondary vertex measurements for charged tracks within the pseudorapidity range of $|\eta| < 2.5$. The ID consists of three independent but complementary subdetectors: the Pixel Detector, the SemiConductor Tracker (SCT) and the Transition Radiation Tracker (TRT), pointed out in Figure 2.6. The Pixel Detector and the SCT are arranged in concentric cylinders around the beam axis, in the barrel, and on disks perpendicular to the beam axis, in the endcaps.

Pixel Detector

The highest granularity is achieved around the vertex region using silicon pixel detectors. It consists of three barrel layers and two three-layer endcaps. The pixel

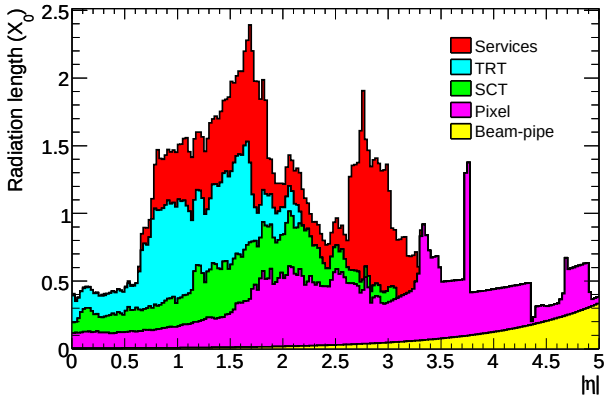

Figure 2.7: The material distribution is presented in radiation lengths at the exit of the ID envelope as a function of η and averaged over ϕ.

sensors have a minimum pixel size in r-ϕ×z of 50×400 µm^2. The intrinsic resolution in the barrel is 10 µm in the plane transverse to the beam line and 115 µm in the longitudinal coordinate. Since this subdetector is the closest to the beam (down to 5.05 cm from the Interaction Point in the radial direction), there are stricter requirements on the radiation hardness, occupancy and precision. The pixel detector is operated at between -5° C and -10° C to reduce the damage caused by radiation.

SemiConductor Tracker

The middle subdetector system is a silicon strip detector which provides high-quality tracking at lower cost than silicon pixels. It should satisfy though similar radiation hardness and precision requirements since its innermost barrel layer is placed at 299 mm away from the Interaction Point in the radial direction. It consists of four double sided barrel layers and two nine-layer endcaps. The strip sensors have a width that varies between 56.9 µm and 94.2 µm.The resolution is expected to be 17 µm in the r-ϕ plane and 580 µm in the z direction. The SCT operates at the same conditions as the pixels, so they share the same thermal enclosure.

Transition Radiation Tracker

The TRT is the outermost part of the Inner Detector. It uses thin drift tubes to provide, on average, 36 additional measurements per track up to $|\eta| = 2.0$ that improves the pattern recognition of the tracking algorithms and consequently the precision of the momentum measurement. It also provides pion-electron discrimination based on transition radiation foils and fibers. It consists of 73 layers of tubes placed parallel to the beam direction in the barrel and 160 layers placed radially in each of the endcaps. Therefore, the TRT provides limited information on the pseudorapidity of the tracks. The two-dimensional design resolution is 130 µm. The TRT can be operated at room temperature.

In Figure 2.7 the material distribution in radiation lengths at the exit of the ID envelope is shown as a function of pseudorapidity. The contribution of the beampipe, the services and the subdetectors is indicated.

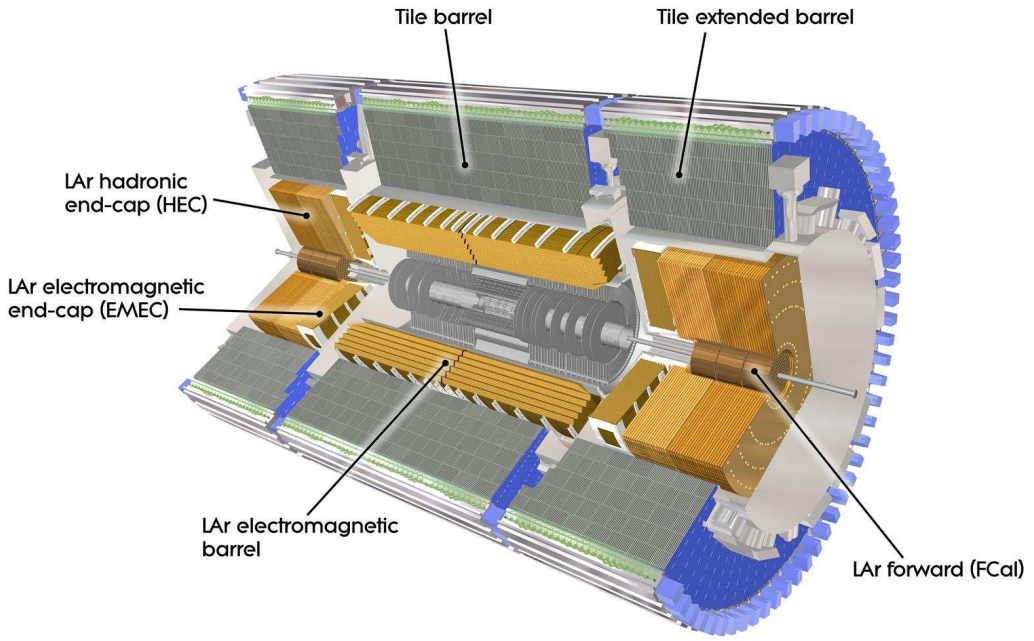

Figure 2.8: The calorimeter system measures the energy and the position of particles by sampling the energy deposit in them. It comprises the Electromagnetic and the Hadronic Calorimeters.

2.2.4 Calorimeters

The calorimeters, depicted in Figure 2.8, measure the energy and position of the particles by sampling the energy deposit in them. They are designed to identify photons, electrons and jets with energies from 10 GeV to 1 TeV as well as for the determination of the missing energy. For the latter, an hermetic coverage is required. The calorimetric system consists of an electromagnetic calorimeter dedicated to electron and photon detection and their energy measurement, and a hadronic calorimeter assigned to detect and measure hadrons.

Electromagnetic Calorimeter

The Electromagnetic (EM) Calorimeter makes use of the interaction of electrons and photons with matter to provide excellent performance in terms of energy and position resolution. The most important energy loss mechanism for electrons at high energies is the bremsstrahlung effect which results to the emission of a photon, while high-energy photons produce electron pairs via pair production. Both cases lead to a

cascade of electrons and photons detected by the lead–liquid argon (Pb–Ar) detectors with accordion shaped absorbers and electrodes. This calorimeter consists of three layers in the barrel and two in the endcaps (EMEC) up to $|\eta| = 3.2$. The total thickness is more than $22\,X_0$ and $26\,X_0$ in the barrel and the endcaps, respectively. The resolution of the EM calorimeter is expected to be σ(E)/E=10 %/$\sqrt{E}\oplus$0.7 % and the angular one $\sigma_\theta = 55\,\text{mrad}/\sqrt{E\,(GeV)}$. The barrel EM calorimeter is housed in the same cryostat as the solenoid magnet, to be described in Section 2.2.6, while the two endcap calorimeters are housed in their own. The first module of the Forward calorimeter is an electromagnetic one, too, starting from $|\eta| = 3.1$. It is made of copper plates with embedded copper rods and tubes through them with LAr between the rods and the tubes with a total thickness of more about $27\,X_0$.

Hadronic Calorimeter

The purpose of the Hadronic Calorimeter is the identification, reconstruction and energy measurement of particle jets and the measurement of the missing transverse energy in an event. As presented in Figure 2.8, it consists of the Tile calorimeter placed outside the barrel EM calorimeter ($|\eta| < 1.7$), the Liquid Argon Hadronic Endcap Calorimeter (LArHEC) placed behind the EMEC ($1.5 < |\eta| < 3.2$) and the two modules of the Forward Calorimeter (FCal) dedicated to detection and measurement of forward jets with $3.1 < |\eta| < 4.9$. The Tile calorimeter is a sampling calorimeter with alternate layers of steel (absorber) and plastic scintillator tiles (active material). The LArHEC uses copper (Cu) plates as the absorber and liquid argon (Ar) as the active material, while the FCal modules use tungsten (W) as absorbers. The total thickness of the hadronic calorimeter is approximately 9.7 interaction lengths in the barrel at $|\eta| = 0$ and 10 in the FCal. The resolution in the barrel is expected to be $\sigma(E)/E = 50\,\%/\sqrt{E}\oplus 3\,\%$ and $\sigma(E)/E = 100\,\%/\sqrt{E}\oplus 10\,\%$ in the endcap. The endcap hadronic calorimeter parts are housed with the EMEC in the same cryostat.

2.2.5 Muon Spectrometer

The aim of the Muon Spectrometer (MS) [25] is to identify, measure and trigger muons. The MS is even designed to provide standalone measurement of muons independently to the measurements of the Inner Detector. As shown in Figure 2.9, it consists of two subdetectors for precision measurements, the Monitored Drift Tubes (MDT) and the Cathode Strip Chambers (CSC), and two triggering technologies, the Resistive Plate Chambers (RPC) and the Thin Gap Chambers (TGC).

Monitored Drift Tubes

The MDT system covers both the barrel and the endcap regions. Each chamber comprises layers made of aluminium tubes of 30 mm diameter filled with Ar–CO_2 (93–7 %) gas at a pressure of 3 bar. A 50 µm diameter tungsten–rhenium (W–Re) wire is used as an anode, positioned at the center of the tube. The wire is kept at

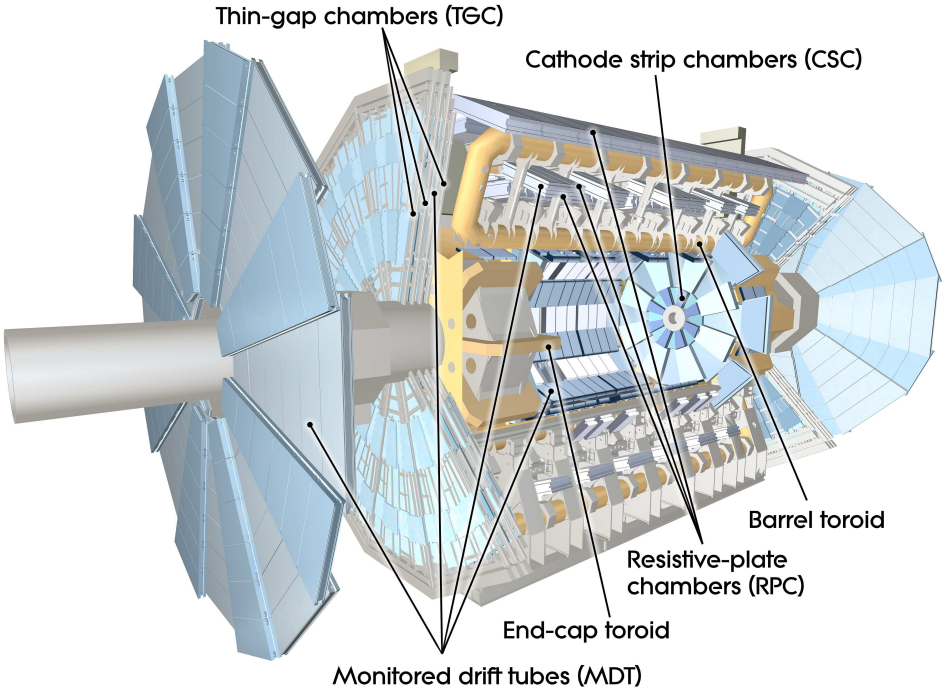

Figure 2.9: The Muon Spectrometer intends to identify, measure and trigger muons. It contains four detector technologies: the Monitored Drift Tubes, the Cathode Strip Chambers, the Resistive Plate Chambers and the Thin Gap Chambers.

3080 V creating avalanches from the ionization electrons. The overall precision on the plane transverse to the tube wire is of the order of 40 µm.

In the MDT chambers, multiple rows of drift tubes are used in different configurations depending on the position requirements. There are two multilayers in each chamber[1], each consisting of either three or four rows of tubes[2]. Each row may comprise 30–72 tubes while the length of the tubes can variate from 0.7 m to 6.3 m depending on the position in the MS.

The layers are separated by a mechanical spacer and mounted on an aluminum support frame as shown in Figure 2.10 in order to maintain the inherent resolution of the drift tubes. Since deformations are still expected, an internal chamber optical alignment system, RASNIK [26], has been implemented. The relative position of the chambers in the consecutive layers are also monitored by a projective alignment system while the chambers within a layer are referenced to each other by chamber-to-chamber alignment sensors.

There are 1150 MDT chambers, 592 of which are located in the barrel and 558 at the endcap regions. The chambers form three layers[3]: Inner, Middle and Outer

[1]Except for all 'BIS8' and 'BEE' chambers that contain only one.

[2]It had been decided to use four rows of tubes in each multilayer for the innermost chambers and three rows for the rest of the chambers.

[3]In the Endcaps a fourth layer (EE) is unofficially used in the Power Supplies Detector Control

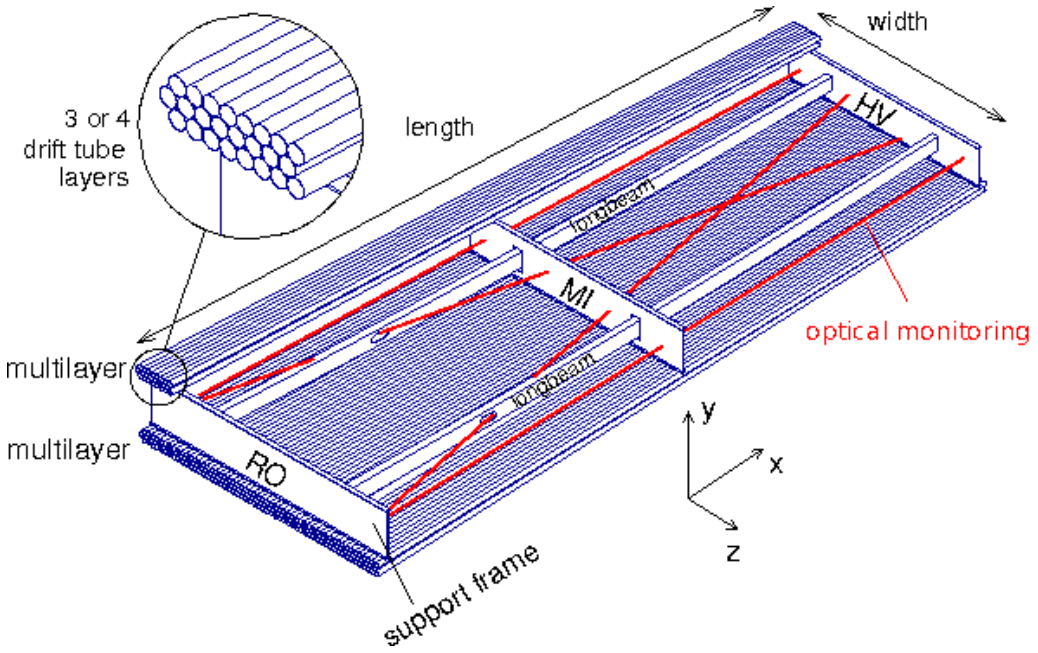

Figure 2.10: The MDT chambers form two layers (multilayers) of two or three rows of tubes, glued on a support frame and monitored from the internal alignment point of view through an optical system.

according to their distance from the IP. In the barrel they form layers of co-axial cylindrical shells whereas in the endcap regions, consecutive concentric disks: the Small Wheel (Inner), the Big Wheel (Middle) and the Outer Wheel. The MDT chambers cover[4] up to $|\eta| = 2.7$.

Every layer is divided in a number of stations. For the barrel, the stations indicate the position of the chambers with respect to the IP in the direction parallel to the beam axis, being numbered from 0 to 8, while for the endcap regions, the stations indicate the position of the chamber with respect to the radial coordinate, being numbered from 1 to 6. According to the azimuthal coordinate, the chambers form 16 sectors of which the odd sectors contain the "Large" chambers and the even sectors the "Small" ones which have indeed a difference in size for better azimuthal coverage.

All the above information is summarized in the name of the chamber, e.g. EIL2A01 is an endcap-region ("E") large ("L") chamber in the inner layer ("I"), in station 2 ("2") in side A ("A") and sector 1 ("01").

Cathode Strip Chambers

In the very forward region where the flux of the muons is higher, the MDT have been replaced by CSC which combine high spatial, time and double-track resolution

System for better granularity.

[4]The Inner layer chambers in the endcap regions cover up to $|\eta| = 2.0$

with high rate capability. They are multi-wire proportional chambers filled with Ar–CO_2 (80–20 %) gas mixture with a cathode strip readout orthogonal to the anode wires. The wires are kept at 1800 V. The spatial resolution is 60 µm for the strips coordinate and 5 mm for the wire coordinate. They are composed of four layers in each endcap region covering $2.0 < |\eta| < 2.7$.

Resistive Plate Chambers

The precision chambers have long charge-collection time, of the order of 20 ns, and therefore cannot be used for triggering. In the barrel region RPC are used instead, which provide a fast momentum estimation for the hardware-based trigger and necessary timing information for the MDT chambers. These chambers are composed of two parallel resistive plates forming a gap filled with $C_2H_2F_4$–Iso-C_4H_{10}–SF_6 (94.7–5–0.3 %) gas mixture. The plates are covered with readout strips at their back which are orthogonal to each other so that an $\eta - \phi$ measurement is possible. The electric field between the plates is of about 9800 V. They have a spatial resolution of 1 cm and timing resolution of 2 ns. There are three layers of RPC covering up to $|\eta| = 1.05$.

Thin Gap Chambers

For the muon trigger for $1.05 < |\eta| < 2.4$ the TGC have been used. Apart from the triggering, their second functionality is the determination of the second, azimuthal, coordinate to complement the measurement of the MDT chambers in the radial direction. They are multi-wire proportional chambers with two cathode plates, filled with a gas mixture of CO_2 and n-C_5H_{12}, n-pentane, (55–45 %). A voltage of 2900 V is applied on the anode wires. Including the variation of the propagation time on wires and strips, signals arrive with 99 % probability inside a time window of 25 ns. There are four layers of TGC at each end-cap region.

2.2.6 Magnets

The ATLAS detector contains two types of superconducting magnet systems in order to provide the bending power needed for the momentum measurement of the charged particles: the solenoid magnet surrounding the Inner Detector and the toroid magnet system embedded in the Muon Spectrometer.

The central superconducting solenoid, presented in Figure 2.11(a), is aligned on the beam axis and is designed to provide a 2 T axial magnetic field for the momentum measurements of the Inner Detector, minimizing the radiative thickness in front of the barrel EM calorimeter. The single-layer coil is wound with a high-strength aluminium-stabilized niobium-titanium (NbTi) conductor inside a 12 mm thick support cylinder. The inner and outer diameters of the solenoid are 2.46 m and 2.56 m and its axial length is 5.8 m. It is housed in a cryostat which is shared with the calorimeter to minimize the usage of material and operates at 4.5° K.

The air-core toroid magnet system provides the magnetic field for momentum measurement in the Muon Spectrometer and has an average field strength of 0.5 T.

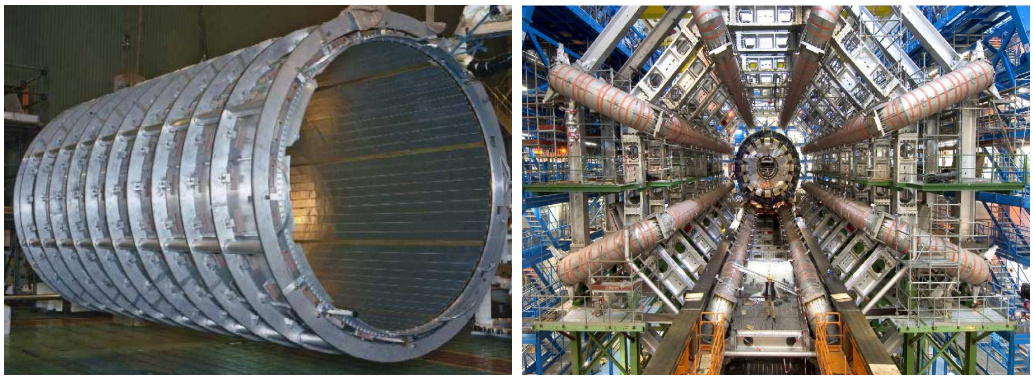

(a) (b)

Figure 2.11: The solenoid magnet (a) provides the magnetic field required for the Inner Detector momentum measurements and the toroid magnet system, consisting of coils in the barrel (b) and coils in both endcap regions, fulfills the requirements for the Muon Spectrometer.

The magnetic field which is toroidal and perpendicular to the one of the solenoid, is created by eight superconducting coils in the barrel, shown in Figure 2.11(b), and by two toroids with eight coils each in the endcap regions. The magnet coils are not placed in iron, which would increase the magnetic field strength, but are surrounded by air to minimize multiple scattering effects. The coil winding technology is the same as in the solenoid and is operating at a nominal current of 20.5 kA.

The magnetic field strength varies with pseudorapidity for the barrel toroid and exhibits a maximum of 3.9 T, while for the endcap toroids the peak value is 4.1 T. In Figure 2.12 the expected magnetic field integral is presented as a function of η. In the transition region between the barrel and the endcap regions, where the field integral is low, the momentum resolution is increasing.

2.2.7 Trigger and Data Acquisition

The Trigger and Data AcQuisition (collectively TDAQ) systems are the main components for the data readout. The trigger system has three distinct levels: Level-1 (L1), Level-2 (L2), and the Event Filter (EF) as described in Figure 2.13. Each trigger level refines the decisions made at the previous level and, where necessary, applies additional selection criteria. The data acquisition system receives and buffers the event data from the detector-specific readout electronics, at the L1 trigger accept rate.

Since bunch crossings occur with a rate of 20 MHz, a trigger system is required to reduce the rate of candidate collisions without the loss of interesting physics events. The first trigger level (L1), which is hardware based, uses information from the calorimeters, with reduced granularity, and the muon trigger chambers to make a decision in less than 2.5 μs, reducing the rate to about 75 kHz. It also defines the so-called Regions of Interest (RoI), information which is then passed on to Level-2.

Level-2 trigger is software-based and uses the full granularity of the RoI and

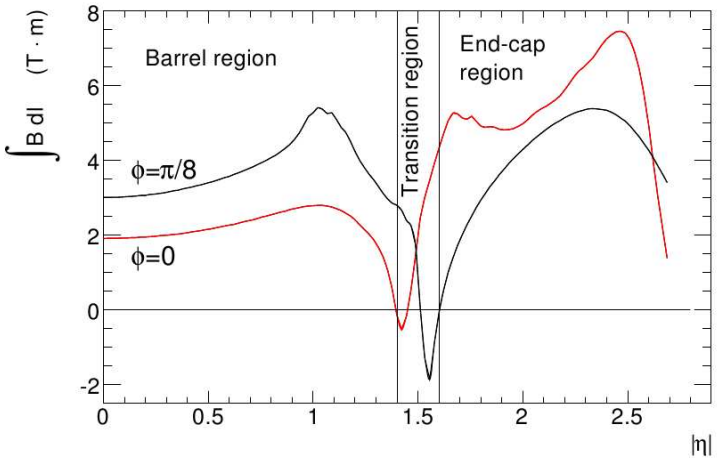

Figure 2.12: The predicted field integral as a function of η inside the Muon Spectrometer is decreased in the transition region resulting to degraded momentum resolution.

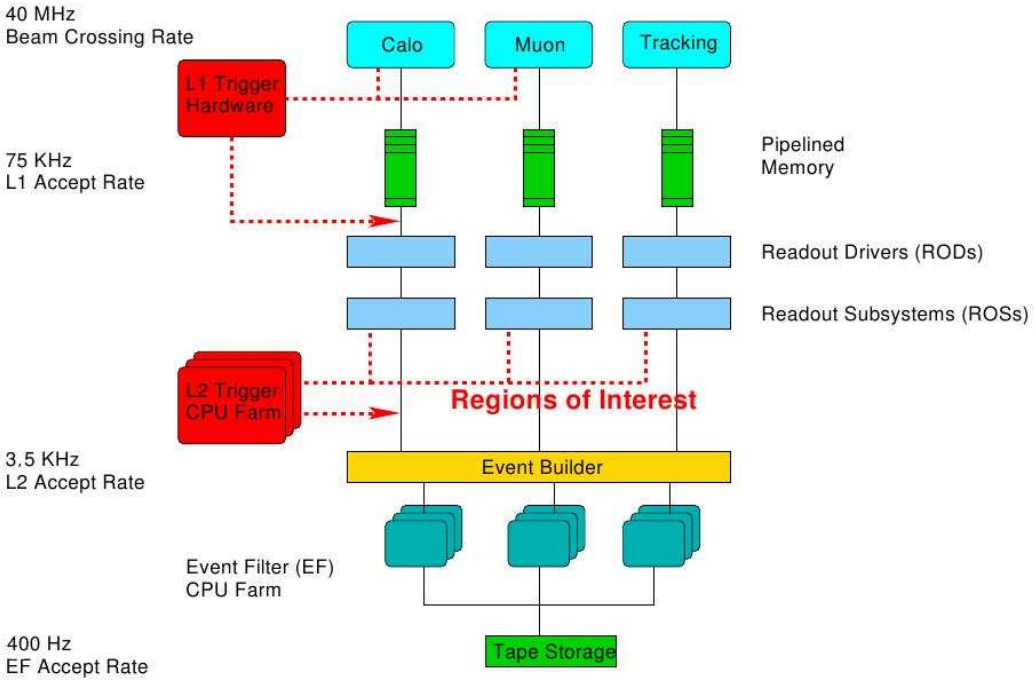

Figure 2.13: The ATLAS three-level trigger has achieved a final rate of about 400 Hz from the 40 MHz proton-proton collision rate.

the Inner Detector to refine the trigger selection. It is designed to reduce the rate down to approximately 3.5 kHz with an event processing time of an average of 40 ms, depending on the complexity of the event. If an event passes the L2 requirements, all information of the event is then passed to the Event Filter.

The Event Filter is also software based and has access to the event information in full granularity. It is designed to reduce the rate down to the final roughly 400 Hz with an event size of approximately 1.3 Mbyte. The events passing the EF are then recorded for further analysis.

Chapter 3

Detector Control System

Such compound detectors require a well designed framework for their control and monitoring. At the end of December 1997 the Joint COntrol Project (JCOP) was established with the aim to construct the framework to be used in all four experiments of the LHC [27]. The task of the JCOP Framework is to select, develop and the support the tools and the components to be used for the Control System of the detectors. Consequently, it was decided to use the PVSS (Prozess Visualisierungs- und Steuerungs-System) SCADA (Supervision Control And Data Acquisition) system and the State Management Interface (SMI++) [28] for the Finite State Machine (FSM) hierarchy.

3.1 The SCADA system - PVSS

PVSS is a software used to develop control systems. It is used to connect to hardware or software devices, acquire their parameter values and use them for supervision. It can also provide some other functions such as archiving of values and alarm handling.

3.1.1 PVSS tools

In order to fulfill the aim to monitor, configure and operate the devices, PVSS provides the following tools:

Database The device data are stored in the PVSS internal database in a structure consisting of 'Datapoints'. The datapoints are grouped into various 'Datapoint Types' which are similar to the 'Classes' in the Object Oriented terminology. All information is stored in the so-called 'Datapoint Elements' which are the parameters of the datapoints. All this structure is user-defined and can be as complex as required. In order to enable specific configuration such as alarming or archiving, every datapoint element can contain various 'Configs'.

Graphical Editor The Graphical EDItor (GEDI) allows the user to build their own User Interfaces, also known as 'Panels', in a "drag and drop" mode. GEDI provides the developer various widgets such as buttons, tables, text fields and

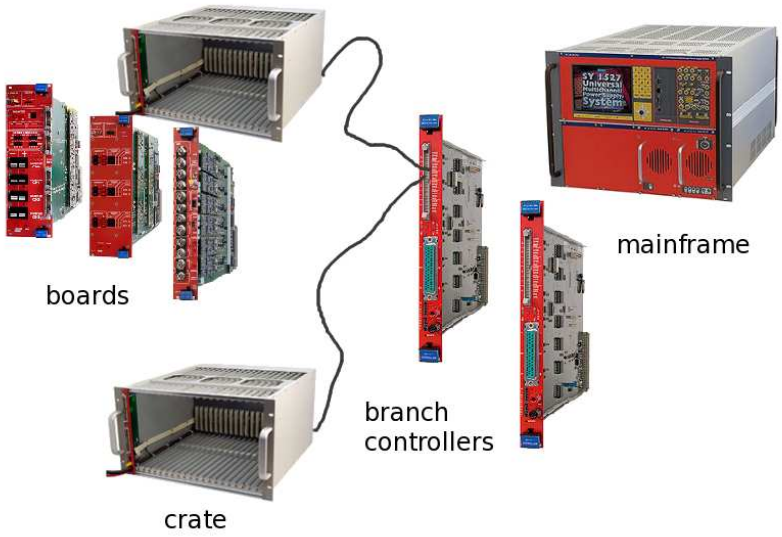

Figure 3.1: The hierarchy of the Power Supplies hardware for the MDT chambers.

"drop-down" lists which can be placed anywhere in the panel and configured by scripting.

Control scripting The control scripting enables the developers to write code which can be used standalone and run as a "background" process. The scripting language is based on 'C' and PVSS provides a large library of functions to be used.

Drivers In order to acquire the devices' data, a connection must be established between them and the project. This connection mechanism is accomplished by the Drivers and depends on the type of the devices being used. For this reason PVSS provides several Drivers with different communication protocols such as OPC (Open Process Control) and DIM (Distributed Information Management).

Alert screen One of the basic features of PVSS is the Alert handling. The word 'alert' is the PVSS word for the alarm. The alarms are configured to the datapoints or the elements through the corresponding config. The panel used for the display of all active and triggered alarms is called the Alert Screen and comprises one of the two main tools for the shifter. On the Alert screen there is one line for each activated alarm providing information.

3.2 Power Supplies Hardware and Datapoints

For the MDT chambers, one of the main systems to be monitored and controlled is the Power Supplies (PS) system. As described in Section 2.2.5 every tube requires a High Voltage (HV) supply of 3080 V and in addition, the chamber electronics require a Low Voltage (LV) supply of approximately 5 V. Therefore, both HV and LV supply modules are being used (CAEN A3540P, A3025B and A3016B). These boards are placed in crates (EASY 3000S) in racks located in the experimental cavern. Each crate has 21 slots[1] and can be filled with both HV and LV boards. Each crate is connected with (up to five) others in a chain belonging to one 'Branch Controller' board (A1676). All Branch Controllers are housed in and controlled by the 'Mainframe' (SY1527) located outside and close to the experimental cavern. This hardware hierarchy is depicted in Figure 3.1.

In the whole MDT system there are two Mainframes used, containing 14 Branch Controllers, eight of which control the barrel hardware and six of them the endcap regions, with a total of 68 crates, 339 boards (177 for the barrel and 162 for the endcap regions) and 2820 used channels. 1485 channels correspond to the barrel chambers and 1335 to the endcap regions.

The datapoints are the basic parts of a project in PVSS. The PS project uses datapoints corresponding to the chambers, the hardware modules described above and other necessary elements for the system operation [29].

3.2.1 Chamber datapoints

The datapoints corresponding to the chambers of the system contain information like the connection mapping, meaning the three channels connected to the chamber: the LV channel for the electronics and the HV ones for the two multilayers. There are also some more information for every channel concerning trip handling and flags.

The flags provide information on whether a channel can be turned on due to various errors, e.g. concerning the gas system of the chambers, the temperature of the power supply modules or the electronics for the readout. There are also elements concerning trips in the chambers datapoints. They involve the temporary automatic increase in the trip limit when the voltage is ramping up, since more current is drawn, and trip recovery. If the recovery process is activated, in the case of tripping, the channel is automatically reset and ramped up again. This recovery process is attempted a few times according to a predefined value.

3.2.2 Datapoints corresponding to PS hardware

As described above, there is a structure for the PS hardware which includes the SY1527 mainframe, the Branch Controllers, the Easy Crates and the Easy Boards. For all of the previously mentioned hardware units there is a corresponding datapoint. Each of them has elements referring to general information such as the model, the serial number and the firmware release.

[1] Only 20 are available since the first one is used for the control of the crate.

The datapoints that are mostly used in the PS projects are the ones corresponding to the channels and the Easy Board modules. In the case of the boards, information is provided about the status of the power and the clock synchronization as well as about the temperature of the module which is a very important element to monitor. On the channel datapoint the elements are grouped into:

'settings' They include all the elements that must be set by the user such as the voltage of the channel ('v0'), the trip limit ('i0') and the steps in which voltage ramps up or down('rUp'-'rDwn').

'readBackSettings' They contain the values that the hardware "sees" as settings.

'actual' They correspond to the online values of the channels such as the voltage ('vMon'), the current ('iMon') and the 'status' . The status is a 16-bit word containing all information about the state of the channel and boolean errors, such as 'Trip' and 'OverCurrent'.

3.2.3 Other datapoints

There are many more datapoints, most of which are internal such as the ones concerning all nodes of the FSM tree, the groups in which communication between the hardware and the software is accomplished and recipes which are used to configure massively the whole system and are saved in a database.

3.3 Datapoint configuration

For each datapoint element, apart from the value there are various configurations that can be stored ('configs'). Some of them, used in the PS DCS are described in the following paragraphs.

3.3.1 Periphery address

This configuration is used to connect to peripherals and thus establish communication between the hardware and the software. The OPC application has been used to obtain all the information from the channels and the other hardware units. The OPC server, the OPC group the element belongs to, the item, the driver's number, the direction of the communication and the activation status of the datapoint element can be stored in this 'config'. If the address is not active, information for the specific element cannot be updated. The activation of the addresses as well as the creation and handling of the OPC groups is managed by a corresponding Expert panel.

3.3.2 Alert handling

Since one of the main aims of the PS project is to monitor the values of the power supplies, it is essential to point out any case in which a value exceeds some predefined limits. In this case an alert which is stored in the '_alert_hdl' configuration is raised

in the alert screen, described in Section 3.4. The severity of the alarm ('Warning', 'Error', 'Fatal') as well as the ranges corresponding to each severity are set in this part. Whether an alarm has to be acknowledged by an expert or not, is also defined in this 'config'. In the case of an acknowledgeable alarm this will appear in the alert screen until it is acknowledged, even after it is no longer in an erroneous state. In the case of multiple activated alarms of the same type, the list in the alert screen can be narrowed down to one using 'summary alerts'. All the alarms are configured through the corresponding Expert panel, described in Section 3.6.

3.3.3 Archive settings

There is the need to archive values of the datapoint and alerts for more efficient monitoring of the system. This can be done using either the RAIMA DB or Oracle archiving. In both cases, in order to archive the values, an '_archive' 'config' is essential in which it is defined where the value will be archived, if the archiving will be smoothed and the parameters of the smoothing. Smoothing is a process through which the amount of data stored is reduced. The users of the system can manage the configuration of the archiving for all elements and activate or deactivate it through a panel, as will be shown in Section 3.6.

3.4 Alert screen

Provided that an element has an alert configuration which is activated, if the "OK" range limits are exceeded a new entry is created in the 'Alert Screen'. As shown in Figure 3.2, the following properties for every alarm are listed by default in the alert screen : the alarm class (severity of the alarm), the direction ('CAME', 'WENT'), the description of the alarm, the alarm text of the error range, the online value, the acknowledgment situation, the time when the alarm appeared at the alert screen and the comment of the alarm.

In the 'Filter settings' frame at the bottom of the window the systems whose alarms are to be monitored can be defined while filters can be placed also concerning the severity of the alarms as well as their description, alert text, datapoint element name and their acknowledgment situation. There is also the option to mask any alarms that are understood and are not wanted to appear in the alert screen anymore ('Masked Alerts').

By right-clicking on an alarm in the alert screen you get other options such as the possibility to insert an entry in the electronic logbook of the experiment where all subdetectors' abnormal situations are recorded. Another option is to acquire a trend plot of the datapoint element's values with respect to time, provided that there is archiving for this element. There is also the option to insert a comment, view the details of the alarm which in the case of a summary alert lists the individual alarms behind the summary one, view the description of the alarm and the alarm ranges defined by the Experts.

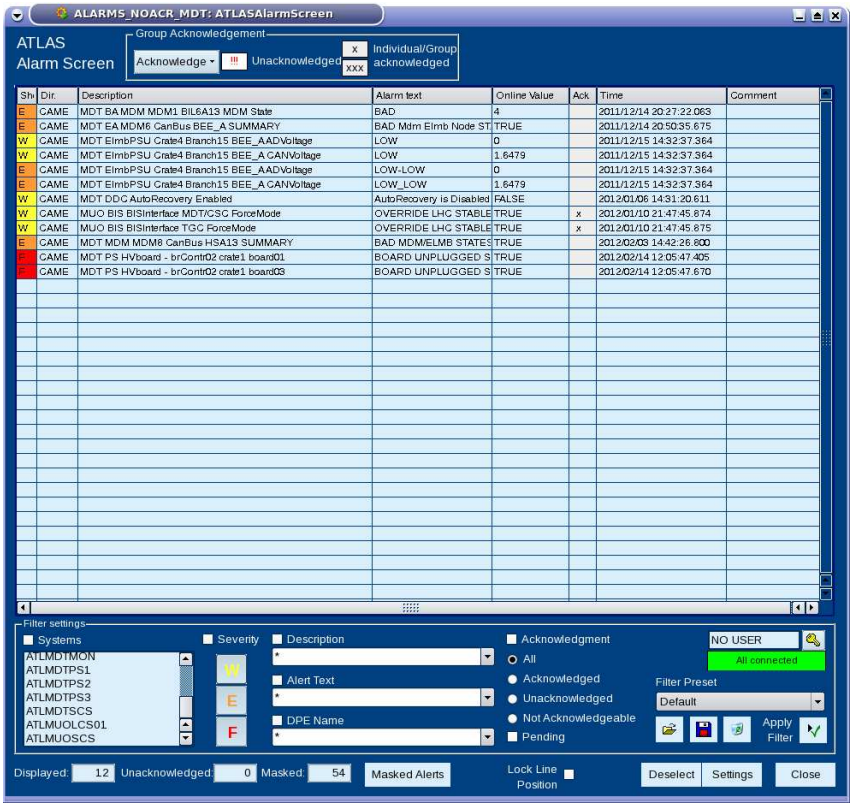

Figure 3.2: The Alert Screen contains all the errors of the system along with many information to track them down and how to react to them. It is one of the main shifter tools.

3.5 Finite State Machine - SMI++

Since PVSS offers neither an abstract behavior monitoring nor automation and error recovery, a Finite State Machine (FSM) is required. In this case the JCOP Framework has decided to use SMI++ (State Management Interface) which has been developed for the Delphi experiment. The SMI provides the tool to build an FSM and an Expert System which is vital for controlling and recovering in complicated systems.

3.5.1 FSM hierarchy

The FSM is based on a strict hierarchical structure with parent-children relations. In this tree-like structure commands propagate from the parents down to the children whereas the states propagate from the children up to the parent on a "most-severe" priority. In this way, when an action is required on all children it is sufficient to give the command to the very top node and correspondingly, the state of the top node summarizes the state of all children nodes of any generation. All nodes can be found in predefined states and can take predefined commands as defined in their FSM type. The nodes can be of one of the following types:

Device Unit (DU) The nodes of this type usually correspond to a device instance and are used to interface to this device. Commands coming from their parents are translated to values' settings of the devices' parameters and accordingly, the parameters' values define the nodes' state which propagates to the highest nodes. A Device Unit node cannot contain any children.

Logical Unit (LU) The Logical Unit nodes cannot interface devices but can contain Device Units as children and control them.

Control Unit (CU) An FSM tree should contain at least one such node. This node can have children of all three types but its parent, if any, can only be a Control Unit, too. Control Units have absolute control over the subtree below in the sense that it can be detached from the rest of the system and function independently as long as the top node is a Control Unit.

3.5.2 FSM User Interface

Panels created using the Graphical Editor with particular specifications comprise the FSM User Interface which together with the alert screen compose the shifter's tools for the monitoring and the control of the detector. Such a panel is presented in Figure 3.3. At the left top of the panel the navigation, the Log-in and the FSM module are located. At the bottom left space the 'Secondary' module is placed and on the center-right part of the panel the 'Main' module dominates except for the top part where a table with the system error messages can be found.

Navigation and Log-in modules In this part there are several buttons to navigate "Back" and "Forth" in the FSM. There is also the Log-in module for the

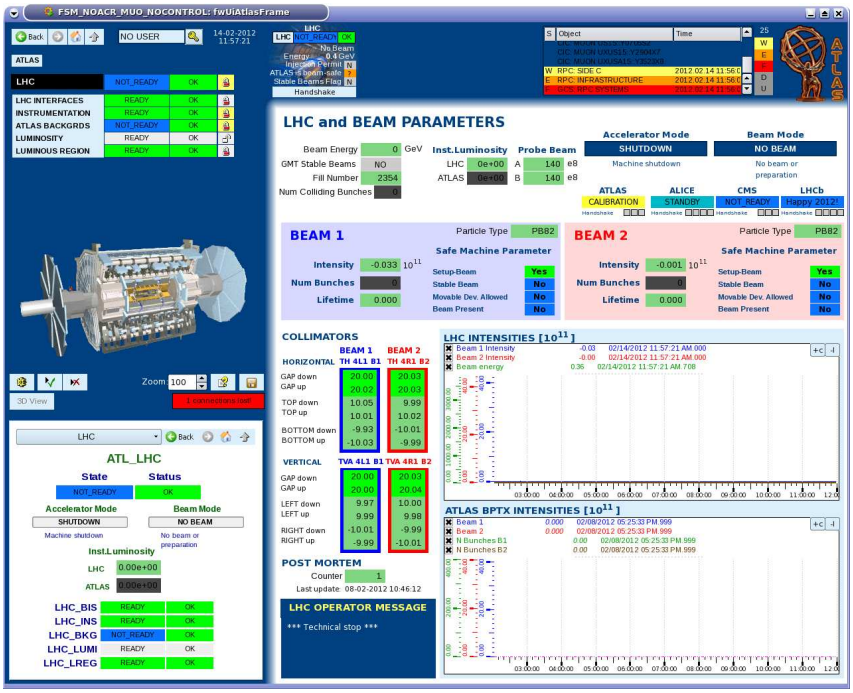

Figure 3.3: The FSM panels are one of the main shifter tools in order to control and monitor the detectors. There are panels for every node of the FSM tree providing the necessary information.

shifter to sign in. All the panels in the FSM are protected and contain the so-called Access Control which enables usage of the FSM panel features for users that have logged in successfully.

FSM module The FSM module (black box) shows the current node in the hierarchy that the FSM panel belongs to. The parents up to the top node of the whole tree are provided above it and below it, all its children. Next to the current node and its children three kinds of information are shown:

State The first box shows the 'state' which defines the operational mode of the node and has the corresponding color. When clicking on a 'state' button, a menu with all the available actions on the corresponding node opens.

Status The second box refers to the 'status' which shows how well the node is working in the current state.

Control The last button next to the nodes is the Control Button. It provides information on if a node is enabled in the system and if it can be controlled by the specific panel.

Main module Every FSM node has an FSM panel where information is provided concerning either parameters of the node itself or information on the children.

Secondary module Similar to the Main panel, there is a Secondary panel for each node of the FSM tree which is located in the bottom left part of the panel. It provides additional information of the current node or its children or a summary of the information shown on the node's Main module.

3.6 Expert panels

In order to make it easy for the the people who maintain the system to control and configure it, various Expert panels have been created. These panels can manipulate the values of the datapoint elements, add, configure and remove 'config's, configure the structure and the actions/commands in the FSM or even get read-write access to a database (DB). In the following paragraphs only three examples of the Expert panels used in the PS project are described.

3.6.1 Alarm handling panel

The Expert panel in Figure 3.4 is used to configure, activate, deactivate or delete all the alarms of the system. Firstly, the part of the system is chosen (barrel and/or endcap regions) and then different elements can be selected. The channel alarms can either be selected by chamber or by channel. In order not to flood the alert screen with individual alarms, there is also the possibility to create summary alerts for various elements of the system. Apart from the alarms set on the channels, the boards, the branch controllers and the mainframes corresponding to erroneous status, temperature, synchronization and power supply, there are also alarms for the hardware communication and the database connection (OPC, RDB).

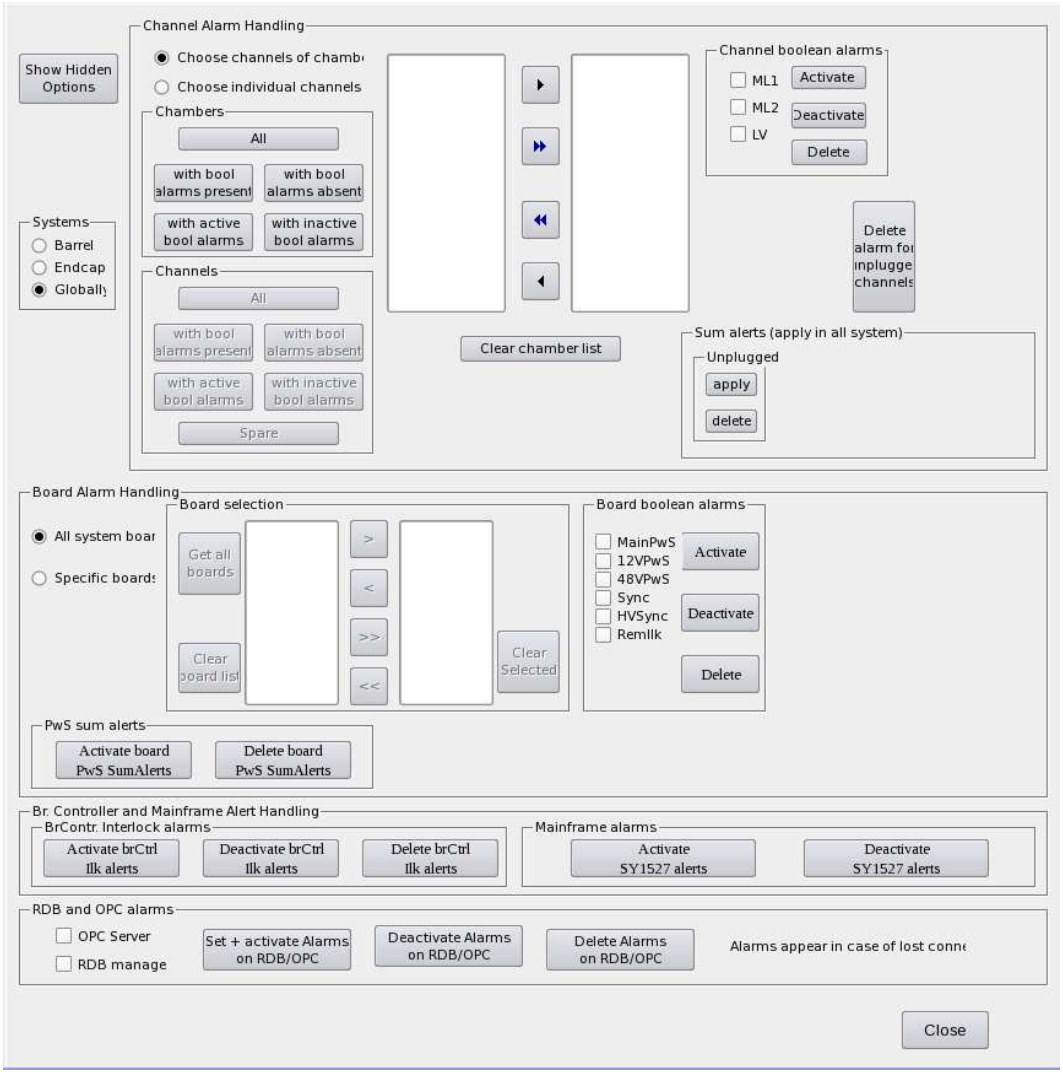

Figure 3.4: The alarm handling Expert panel is used for the configuration, activation and deactivation of all the alarms of the system.

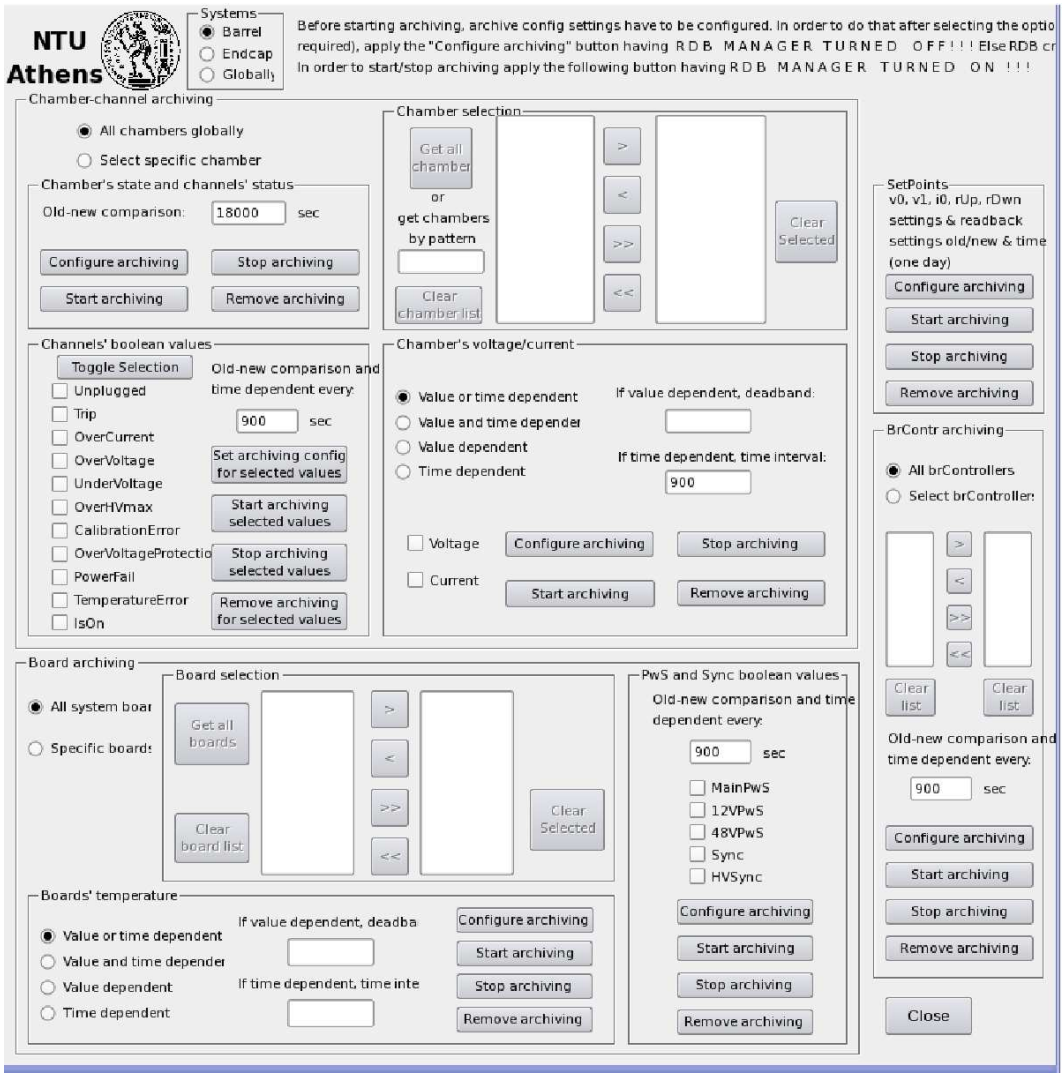

Figure 3.5: The Expert can configure the archiving of elements of the system using the archiving handling panel.

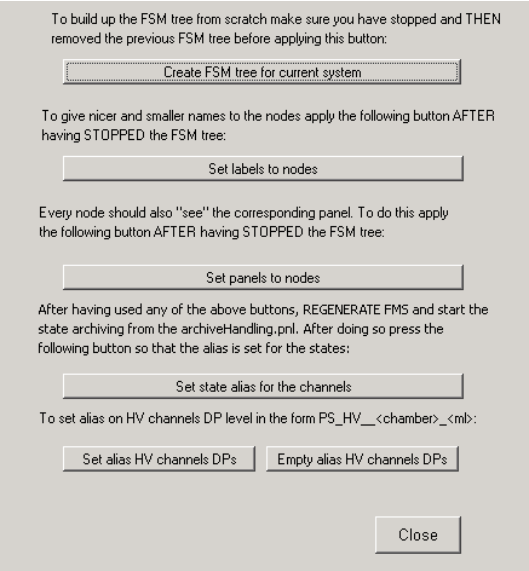

Figure 3.6: The FSM handling Expert panel builds and configures the whole FSM structure of the system.

3.6.2 Archive handling panel

The panel in Figure 3.5 is used to record several values of the system using the archive 'config'. The first step is to configure the archiving and then activate it. This expert panel is also divided in the configuration for the channels/chambers, the boards and the branch controllers. There are options as to which elements to archive in each case as well as fields for the desired smoothing. Smoothing can be value and/or time dependent. The value dependent smoothing archives an element value as soon as its value changes by a predefined value while the time dependent one archives it as soon as a predefined time is elapsed.

3.6.3 FSM handling panel

The FSM, as described in Section 3.5, is one of the main components of the DCS and one of its crucial elements is the FSM tree. In the FSM tree the hierarchy of the logical components of the system is set and as a consequence the way the commands and the states propagate is defined. The panel in Figure 3.6 is dedicated to the configuration of the FSM tree. This involves building the FSM tree for the whole system, setting the labels of every node, specifying the Main and Secondary panel corresponding to each node and setting aliases to its nodes.

3.7 Script libraries

The code needed for any part of the project refers repeatedly to the basic components that the system is made of. In order to avoid repeating code, functions have been

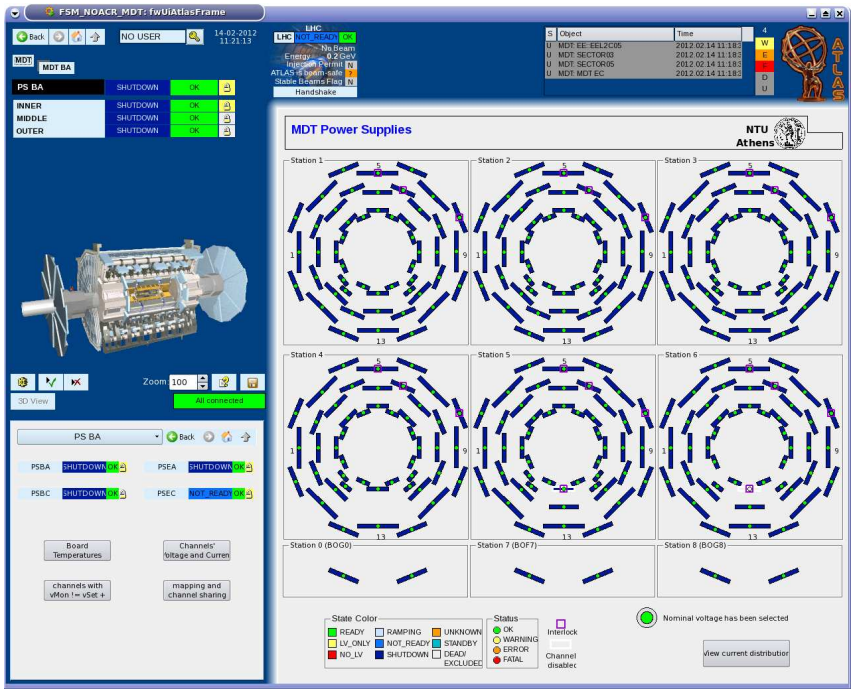

Figure 3.7: The partition FSM panel corresponding to the barrel region, side-A.

developed located in global libraries. There are various library functions used in the PS project categorized according to what they serve for: datapoint handling, alarm setting, communication and FSM configuration.

3.8 The FSM tree for the Power Supplies system

As already mentioned in Chapter 3.5, the FSM is an essential part of the Detector Control System, defining the hierarchy of the system through the FSM tree. At the top of the tree there are the four partition CUs, side-A and side-C for the barrel and the endcap regions. Below them, there are the three layer CUs per partition, containing 16 sector LUs each. The children of the sector nodes are the chamber LU nodes and at the bottom of the tree there are the DUs corresponding to the channels. Each node type belongs to an FSM type which is defined with respect to which states it can be found at and what actions can be applied on it.

The channel nodes can be found in various states: 'ON', 'OFF', 'RAMP_UP' and 'RAMP_DOWN' (only for the HV channels), 'STANDBY' (only for the HV channels, too), 'UNPLUGGED' and 'UNKNOWN'. The 'STANDBY' state corresponds to a lower set voltage than the nominal one, used for the chambers' protection until "stable beams" are declared. The 'UNKNOWN' state is set in the case of communication problems. The actions to be applied on the channel nodes are: 'SWITCH_ON', 'SWITCH_OFF', 'RESET_TRIP' and 'REFRESH'.

Accordingly, the chamber nodes can be found in the following states: 'ON' when

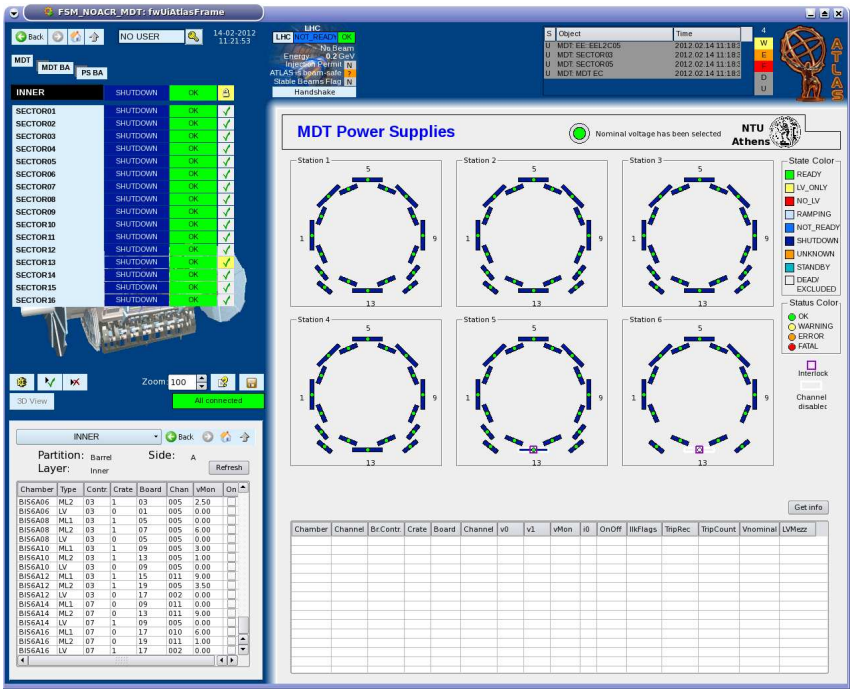

Figure 3.8: The FSM panel for the Inner layer of the barrel side-A.

all channels are on, 'OFF' when all channels are off, 'ON50' when the LV and only one of the two HV channels are on, 'STANDBY' when only the LV channel is on, 'NO_LV' when any HV channel is on while the LV one is off, 'RAMPING' when any HV channel is either ramping up or down and 'UNKNOWN' when there are communication problems. The actions configured for this type are actions concerning the channels: 'SWITCH_HV_ON', 'SWITCH_HV_OFF', 'SWITCH_ONLY_ML1_ON', 'SWITCH_ONLY_ML2_ON', 'SWITCH_LV_ON', 'SWITCH_LV_OFF', 'REFRESH' and 'RESET_TRIP'.

Similar actions to the above can be applied on the higher nodes in the tree and propagate down to the chamber nodes while the states of the channels are reflected in the states of the chamber, sector, layer and partition nodes accordingly.

3.9 FSM panels for the Power Supplies system

By means of the FSM panels the system is overall monitored and controlled providing various information through the Main and the Secondary panels described in Section 3.5.2. In Figure 3.7 the Main panel for the side-A barrel partition is shown as well as the Secondary one on the bottom left part. The Main panel contains all chambers as viewed in the transverse plane. As in all PS FSM panels the colors of the chambers show their state and status, explained in Section 3.5.2, and are defined at the bottom part of the panel. The state of the chambers is given by the color of the rectangles whereas the color of the circle in the middle of the chambers indicates

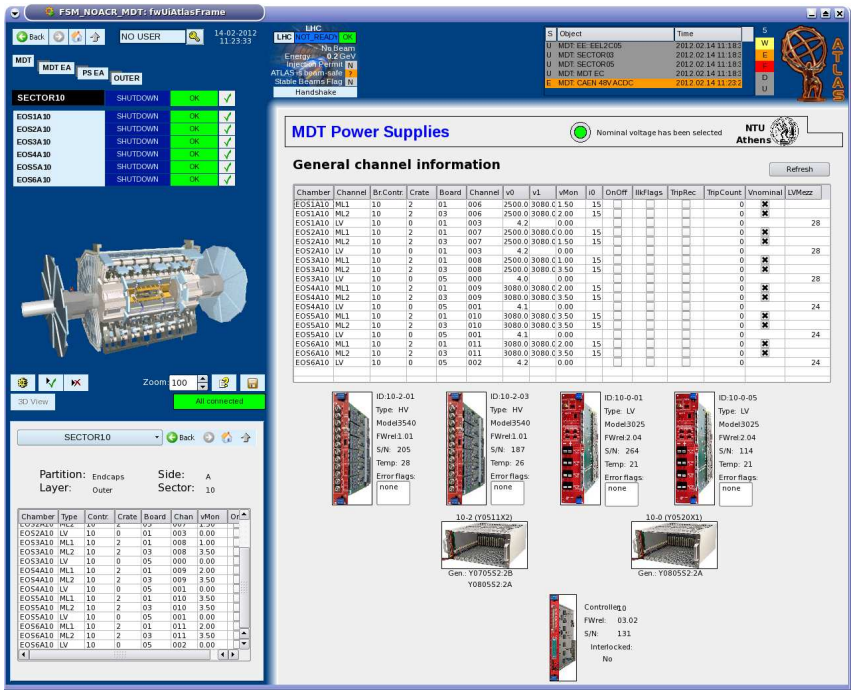

Figure 3.9: The sector FSM panel corresponding to sector 10 of the Outer layer of the endcap region side-A.

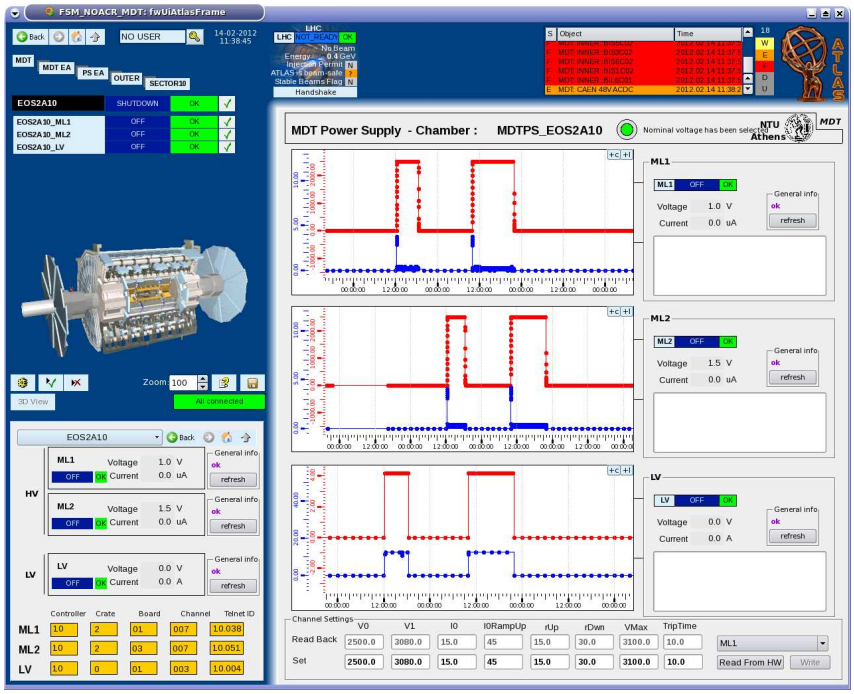

Figure 3.10: The chamber FSM panel contains information on the three channels.

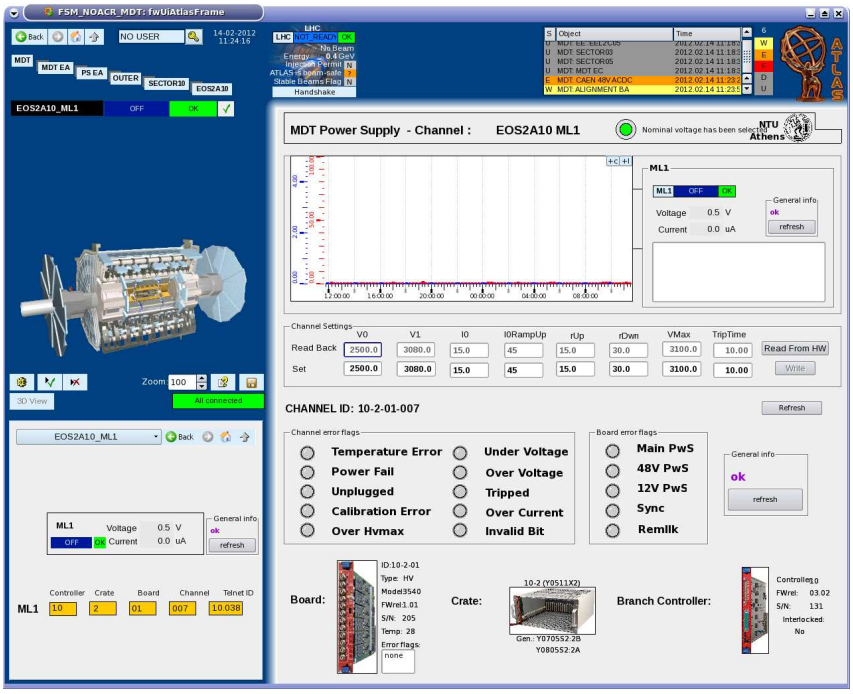

Figure 3.11: The FSM panel corresponding to a HV channel.

the status.

The panel in Figure 3.8 corresponds to the Inner layer node. The state and status of the chambers in this layer are available again and at the bottom of the panel, there is a table to provide information on the mapping and the conditions of all channels in the current node. In the Secondary panel, there is again a list of all channels providing their mapping, their voltage and their state. In Figure 3.9, an example sector panel is shown, where a table with the information of all channel is provided as well as figures with the involved hardware and some basic information. In the chamber panel, depicted in Figure 3.10, plots of the corresponding channels' voltage and current are shown. These plots are also shown in the individual channel panels along with the set values and the channel error flags. Figure 3.11 and Figure 3.12 correspond to a HV and a LV channel correspondingly.

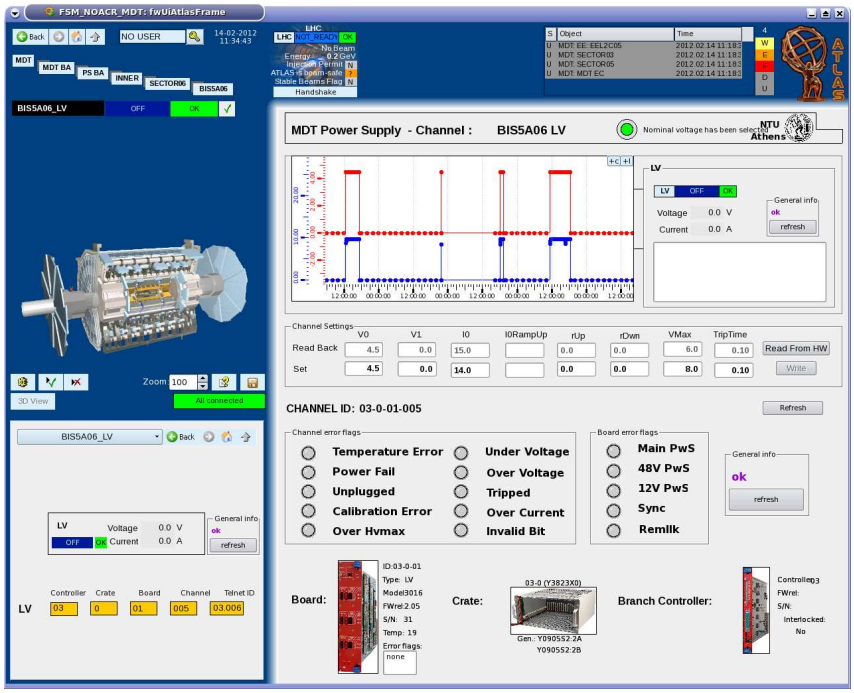

Figure 3.12: The FSM panel corresponding to a LV channel.

Chapter 4

Physics Objects : Electrons and Muons

In the proton-proton collisions, outcoming particles have electromagnetic or nuclear interactions in the detectors they pass through. These interactions usually create analog signals which are measured or converted into standardized pulses. Hits or energy deposits are formed, which are then combined using reconstruction algorithms into tracks or clusters of particles. Combining the information of the different subdetectors, it is possible to identify the kind of the passing particle. With this procedure physics objects are created which are then used in the physics analyses.

4.1 Electron Reconstruction and Identification

Electrons leave a track in the Inner Detector and deposit their energy in the electromagnetic calorimeter. There are three reconstruction algorithms for electrons. In the main algorithm, reconstruction is seeded by a reconstructed cluster in the electromagnetic calorimeter. The second one is dedicated mostly to electrons in jets (non-isolated electrons) and is seeded by a track in the Inner Detector. The third algorithm is available for the reconstruction of forward electrons outside the acceptance of the Inner Detector ($|\eta| > 2.5$) and therefore no track matching is possible.

For the clusterization, a "sliding-window" algorithm is used. According to this algorithm, a window of fixed size $\Delta\eta \times \Delta\phi = 0.075 \times 0.125$ is moved in the $\eta \times \phi$ space of the calorimeter. If the transverse energy of the window is a local maximum, above a threshold $E_{\mathrm{T,thres}} = 2.5\,\mathrm{GeV}$, a seed-cluster is formed.

The main electron reconstruction algorithm uses the before-mentioned reconstructed clusters and searches for Inner Detector tracks to match the clusters [30,31]. The tracks are extrapolated taking into account the magnetic field and the material and are required to loosely match the seed clusters. More specifically, a $\Delta\eta < 0.05$ selection is applied as well as an asymmetric $-0.10 < -q\Delta\phi < 0.05$ in order to account for possible bremsstrahlung energy losses. The clusters which are successfully matched to at least one track are electron candidates. Afterwards, a cluster is built

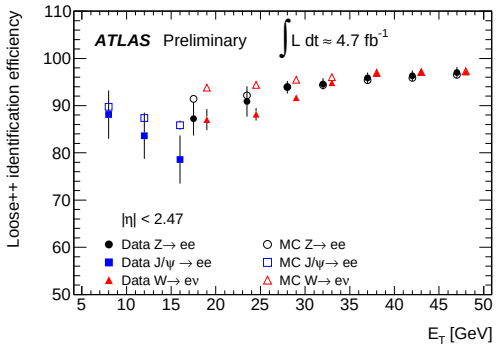

Figure 4.1: The identification efficiency measurement for electrons with transverse energy between 7 and 50 GeV is presented with respect to the E_{T}.

by taking into account all cells inside a fixed-size rectangle, $\Delta\eta \times \Delta\phi = 0.075 \times 0.175$ for electrons in the barrel and $\Delta\eta \times \Delta\phi = 0.125 \times 0.125$ for electrons in the endcap regions. The electron energy is given by the cluster energy while the rest of the parameters are taken from the best associated track.

The electron identification in ATLAS is based on requirements on variables that provide good separation between isolated electrons and jets faking electrons. Jets can deposit a large fraction of their energy in the Hadronic calorimeter in contrast to electrons that deposit most of their energy in the electromagnetic calorimeter. The comparison between the transverse energy in the hadronic and the electromagnetic calorimeter is a powerful discriminant against jets. Selections are also applied on the second sampling of the EM calorimeter where most of the electron energy is deposited. The cluster isolation in η and the η shower width are expected to be narrow for electrons due to the small lateral leakage while for the jets tails are expected. Requirements made in the hadronic and the second sampling of the EM calorimeters reject jets with highly energetic pions and wide shower. After these requirements, jets with single or multiple neutral particles decaying to photons, mainly π^0 mesons, leading to electromagnetic-like showers become an important contribution to the electron background. In order to reject these jets, the fine granularity of the first layer of the EM calorimeter can be exploited. An electron shower is expected to be narrow in pseudorapidity with no second maximum compared to a jet which can contain several particles that cause a possible significant second maximum. After the calorimeter requirements, the background from charged hadrons is greatly reduced and the remaining background is dominated by photon conversions and low multiplicity jets containing mainly π^0 mesons. These backgrounds are rejected by requiring the presence of a good quality Inner Detector track consistent with the EM cluster. This consistency is imposed by requirements on the $\Delta\eta$ and $\Delta\phi$ between the track and the cluster. The above selections are typically optimized in bins of η and E_{T}. In the ATLAS experiment several working points can be employed (Loose, Medium, Tight, MultiLepton) depending on the particular requirements of each analysis.

Electrons in ATLAS lose on average between 20 and 50 % of their energy de-

pending on $|\eta|$ by the time they leave the SCT [24]. The bremsstrahlung emission introduces, in general, non-Gaussian contributions to the event-by-event fluctuations of the calorimetry and tracking measurements. By fitting electron tracks in such a way as to allow for proper modeling of the energy loss due to bremsstrahlung, it is possible to improve the reconstructed track parameters. The Gaussian-sum filter (GSF), which was used in order to account for energy losses due to bremsstrahlung, is a non-linear generalization of the Kalman filter [32, 33], which takes into account non-Gaussian noise by modeling it as a weighted sum of Gaussian components and therefore acts as weighted sum of Kalman filters operating in parallel [34]. By allowing for changes in the curvature of the track, the bremsstrahlung recovery algorithms follow the track better and correctly associate more of the hits.

The identification efficiency with respect to the electron E_{T} for the loose electron definition is shown in Figure 4.1. Electrons from W and Z decays provide measurements from 15 to 50 GeV, while the transverse energy region from 4 to 20 GeV is probed by the J/ψ decays. Kinematical differences between the three decay channels account for the small observed channel-to-channel efficiency variations in a given E_{T} range. The reconstruction and track quality efficiency has been measured with $Z \to e^+e^-$ decays to be approximately 95 % in the range from 15 to 50 GeV. It is well modelled by the simulation with a $\sim 1\,\%$ uncertainty.

4.2 Muon Reconstruction and Identification

The ATLAS detector is designed to detect and measure muons in the Muon Spectrometer, while measurements in the Inner detector and the calorimeters are meant to improve the muon identification efficiency and momentum resolution. There are two independent reconstruction algorithms: Muonboy [35] and MOORE [36]. Both of them are based on reconstructing trajectories both locally, at the level of individual chambers, and globally, at the level of the Muon Spectrometer. The trajectories at the chamber level are approximated by straight lines, called track segments, due to the small effect of the bending, and are combined within multiple chambers in order to form full tracks.

In a first step, Regions Of Activity (ROA) are identified in the Muon Spectrometer using information from the trigger muon chambers. These ROA are used in order to reconstruct local track segments in the muon layers. The segments are then combined to form muon track candidates using three-dimensional tracking in the magnetic field. The last step is to combine all available information through the full system.

There are four muon categories defined by the systems involved in their reconstruction and identification:

Combined Muons (CB) Independent track reconstruction is performed both in the Muon Spectrometer and the Inner Detector and after the two are combined into a single track. This combination improves the momentum resolution of low momentum muons due to the use of the high quality Inner Detector information. More precisely, the momentum where the Muon Spectrometer measurement is more precise than the Inner Detector one is at $p_{\mathrm{T}} = 80$ GeV in the

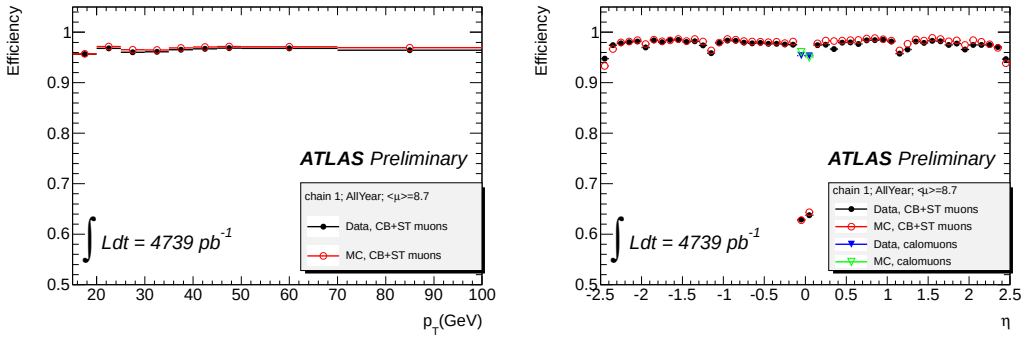

(a) (b)

Figure 4.2: Muon efficiency with respect to the (a) p_{T} and (b) η of the muons for combined and segment-tagged muons with the addition of the calorimeter-tagged muons in the second case.

barrel region and at $p_{\mathrm{T}} = 20\,\mathrm{GeV}$ in the endcap regions. The combined muon is the type with the highest purity.

Segment-Tagged Muons (ST) Low momentum muons which do not have enough energy to transverse all muon layers can still be reconstructed if there is successful association of their Inner Detector tracks with one reconstructed track segment in the Muon Spectrometer. segment-tagged muons are also used to recover efficiency loss in specific regions where coverage is limited to less than three muon layers, e.g. $|\eta| \sim 1.3$, where the EE chambers' installation has not been completed yet.

Standalone Muons (SA) Muons of high pseudorapidity ($|\eta| > 2.5$), outside the Inner Detector acceptance, can still be reconstructed by the Muon Spectrometer which extends up to $|\eta| = 2.7$. Only the hits in the muon system are taken into account in the reconstruction and extrapolation to the beam axis is performed through the calorimeters and the Inner Detector as in all other categories, by taking into account the energy losses.

Calorimeter-Tagged Muons (CT) This type of muons uses the pattern of the energy deposition in the calorimeter in combination with the Inner Detector measurement in order to reconstruct muons. This is accomplished by requiring the presence of a minimal energy deposit in all calorimeter layers along the track's projected trajectory. Calorimeter-tagged muons are expected to improve the muon identification efficiency the region $|\eta| < 0.1$, where there is no coverage in the Muon Spectrometer.

Combined, segment-tagged and calorimeter-tagged muons have associated Inner Detector tracks. To obtain good muon candidates, requirements have to be applied on these tracks. At least one hit in the B-layer is required unless the extrapolated muon track has passed an uninstrumented or dead area of the B-layer. The number of crossed dead silicon modules are added to the number of hits and are required to

be greater than 1 and 5 for the pixel detector and SCT, respectively. if the Like in the release 16 guidelines for 2010 data, the cuts are constructed such that detector conditions are taken into account for the silicon systems: if e.g. a passed module is dead, it is added to the hit count, ignored in the hole count and (if applicable) the b-layer expectation canceled. The number of silicon holes [1] is restricted to two. Finally, a successful extension to the TRT is expected within the TRT acceptance. The sum of TRT hits and outliers [2] should be greater than five, the TRT outliers being less than 90 % of this sum. These compose the basic muon selection for the combined, segment-tagged and calorimeter-tagged muons.

In Figure 7.2(a)(a) the muon reconstruction efficiency as a function of p_{T} and in 7.2(a)(b) as a function of η are presented. The efficiency is presented for combined and segment-tagged muons, while in the distribution with respect to η the calorimeter-tagged muons are also included to restore the efficiency at $\eta \sim 0$ which is dropped due to the lack of coverage in order to provide space for the services of the ID and the calorimeters.

4.3 Muon studies using data and Monte Carlo simulation

Studies are performed for the muons using either Monte Carlo (MC) simulation or MC in comparison to the data. The first study is a data-driven estimation of the rate of non-prompt muons originating from decays in flight or punch-through and the results are compared to the MC simulation. The second study focuses on the effect of the multiple interactions taking place in each bunch crossing on the isolation of the muons using MC simulation. This study was important before analyzing the data in order to tune accordingly the isolation selection criteria. Finally, the calculation of the efficiency of the isolation and impact parameter selection criteria on muons from $Z \to \mu\mu$ decays is performed, both in data and MC. In this way the minimal effect of these selections on isolated signal-like muons can be checked for the $H \to ZZ^{(*)} \to 4\ell$ analysis.

4.3.1 In-Situ estimation of muon fake rates for low p_{T} muons

The ATLAS detector will be used to look for evidence of new physics in various processes with muons in the final state. Thus, it is necessary to understand and eliminate the sources of background due to the misidentification of prompt muons. One of the fake muons categories is the one where muons are coming from long-living mesons (K and π) that have decayed in the detector. Charged pions decay to muons

[1] A hole is an expected measurement given the track trajectory that has not been assigned to the track. Holes can result from material interactions, silicon inefficiency or problems within the pattern recognition. Inactive modules are excluded from the definition of holes.

[2] TRT outliers appear in two forms in the track reconstruction: as a straw tube with a signal but not crossed by the nearby track or as a set of TRT measurements in the prolongation of a track which, however, failed to form a smooth trajectory together with the pixel and SCT measurements.

with a branching ratio of 99.99 % and charged kaons decay leptonically to muons at more than 67 % and hadronically to pions at more than 28 % [37].

In this study the aim is the in-situ estimation of low p_{T} muon fake rates from K and π mesons using the decay channel

$$\begin{aligned} D^* \rightarrow & D^0 + \pi_s^+ \\ & \big\lfloor\!\!\longrightarrow \quad K^- + \pi^+ \end{aligned}$$

Its charge conjugate decay is implied throughout this section. Low p_{T} muons are defined as muons with transverse momentum less than 10 GeV. The advantage of using this decay is that muons coming from K mesons can be separated from the ones coming from π mesons according to their charge and in this sense, the fake rates from both kaons and pions can be studied separately. In order to extract the fake rates, the association of the kaon and pion tracks with muon objects is studied.

Data and Monte Carlo

Collision data at $\sqrt{s} = 7$ TeV recorded in ATLAS from July 29$^{\mathrm{th}}$ to October 29$^{\mathrm{th}}$ 2010 are considered. This period corresponds to the ATLAS data taking periods E to I. The collected data are organized in segments, called Luminosity Blocks, which cover short time intervals of the order of few minutes of approximately constant instantaneous luminosity and data taking conditions such as detector status and trigger menu. In all runs, the luminosity blocks that are retained for analysis are only the ones for which the LHC operators had declared the beams to be stable. Furthermore, data are included only if they qualify to be suitable for physics analysis, from the point of view of the Inner Detector, the Muon Spectrometer and the magnet systems.

Muon triggers with the lowest thresholds have been used (L1_MU0, EF_mu4, EF_mu6, EF_mu10, EF_mu13, EF_mu15 and EF_mu20). To remove biases, care is taken so that the ID tracks of the trigger muons are not taken into account so that the trigger is not activated by the same part of the $b\bar{b}/c\bar{c}$ decay as the one used for the D^* reconstruction.

A MC simulation sample dedicated to D mesons and prepared by PYTHIAB, which is a generator dedicated to B-Physics [38], was used to compare data results with the simulated ones. The sample takes into account the bunch train pileup effect and in addition, reweighting is applied in order to reflect the pileup conditions in the corresponding data. The MC sample is also reweighed with respect to the track p_{T} spectrum.

Decay channel reconstruction

D^* mesons are reconstructed in the kinematic range of $p_{\mathrm{T}}(D^*) > 3.5$ GeV and $|\eta(D^*)| < 2.1$ [39]. For the reconstruction, tracks measured in the ATLAS Inner Detector tracking system are used but the $\mathrm{d}E/\mathrm{d}x$ particle identification was not used since it was not effective in the kinematic range used. In order to reconstruct

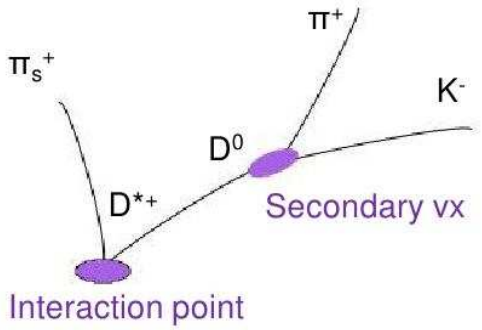

Figure 4.3: The decay of D^* to D^0 and a "soft" pion, with D^0 decaying to a kaon and a pion, is reconstructed in order to study the muon fakes from kaons and pions.

D^0, two Inner Detector tracks are combined (a kaon and a pion track) and then a third one is added to reconstruct D^* as depicted in Figure 4.3.

The selection criteria for the ID tracks of the two daughters (K and π) of D^0 are the same while the ones for the third track (soft π) are similar. The latter track is constrained to have low momentum by the small mass difference between D^* and D^0 and thus it is called the "soft" pion. So, the two D^0 tracks are required to have $p_{\mathrm{T}} > 1\,\mathrm{GeV}$ while the soft track is required to have $p_{\mathrm{T}} > 250\,\mathrm{MeV}$. The pseudorapidity for all three tracks is required to be within the acceptance of the Inner Detector ($|\eta| < 2.5$). To ensure high reconstruction efficiency and good momentum resolution, each of the reconstructed tracks should have at least one hit in the Pixel Detector and at least four hits in the SCT.

In addition, requirements are applied for all tracks on their transverse and longitudinal impact parameters with respect to the Primary Vertex (PV). For the two tracks forming D^0, $d_0^{\mathrm{PV}} < 1.5\,\mathrm{mm}$ and $z_0^{\mathrm{PV}} \sin\theta < 1.5\,\mathrm{mm}$ cuts are applied while for the soft pion $d_0^{\mathrm{PV}} < 0.8\,\mathrm{mm}$ and $z_0^{\mathrm{PV}} \sin\theta < 1.5\,\mathrm{mm}$. These cuts are loose enough for both prompt charm and charm from beauty contributions and intent to remove fake-vertex and no-vertex combinations.

After having selected the track candidates for the kaon and the pion forming the D^0, pairs of oppositely charged tracks are created and vertexing is used to fit them to a common vertex. Only pairs for which the fit is successful with $\chi^2 < 5$ are taken into account. Also, a cut on the transverse decay length of D^0 is applied ($L_{\mathrm{xy}} > 0.2\,\mathrm{mm}$). To calculate the invariant mass of D^0, kaon and pion masses were assumed in turn for each track.

After having reconstructed D^0 and selected the π_{soft} candidates, D^* is reconstructed. For this, three different methods can be used:

Simple combination Every D^0 candidate is simply combined with every π_{soft} candidate without applying any vertexing.

1-vertex approximation All three tracks are simultaneously fit to one common vertex. D^0 time of flight is considered negligible. This method is used to

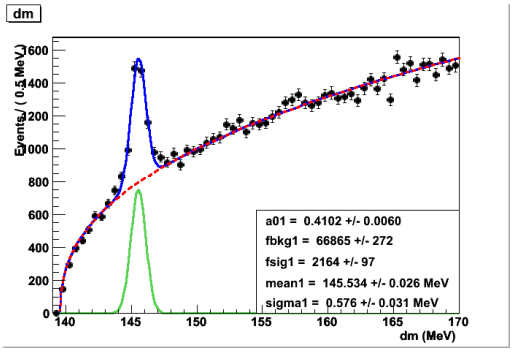

Figure 4.4: The distribution of the mass difference $m_{K\pi} - m_{K\pi\pi}$ is shown fitted with a powered threshold function, $\mathrm{a}(\Delta\mathrm{mass} - m_\pi)^{\mathrm{b}}$.

extract the following results as it provides the best resolution in the invariant mass distribution.

Cascade vertexing Vertexing is applied taking into account that the time of flight of D^0 is not negligible, so the tracks are fitted in two vertices, in two steps; first the two tracks in the D^0 vertex and then the vertex track with the third one in the D^* vertex. This method although promising, needed further validation and its usage had been postponed.

Having selected the D^* candidates, various selection criteria are applied on them in order to reduce the combinatorial background. Firstly, in the track triplet candidate forming the D^*, the soft pion track should have opposite charge to the kaon track. Only successful fits are taken into consideration with $\chi^2 < 5$. The most discriminant and important cut is the one on the Δmass variable. Δmass is defined as the difference between the invariant mass of D^* and the invariant mass of D^0 and it is required to be within $144.5\,\mathrm{MeV} < \Delta\mathrm{mass} < 146.5\,\mathrm{MeV}$. In Figure 4.4 the Δmass distribution is presented and is fitted with a powered threshold function, $\mathrm{a}(\Delta\mathrm{mass} - m_\pi)^{\mathrm{b}}$.

In order to subtract further combinatorial background a cut based on the hard nature of charm fragmentation is applied. It is required that $p_{\mathrm{T}}(D^*)/E_{\mathrm{T}} > 0.02$, where $p_{\mathrm{T}}(D^*)$ is the transverse momentum of D^* and E_{T} is the sum of the transverse energy deposits in the ATLAS calorimeters and the muon system.

Fake rate definition and estimation method

Before proceeding with describing the method used to estimate muon fake rates, it is important to define when a muon is called prompt or fake. Prompt is a muon produced directly in the Interaction Point (IP) or a muon coming from interesting Physics decays such as H, W, Z decays and SUSY. Fake muons are considered the ones that are not prompt but can be actually real. So, fakes are muons coming from short-living mesons (D, B) and baryons with decay length less than 1 mm, muons coming from long-living mesons (K, π) which have decayed in the detector, as in this study, misidentified hadrons and reconstruction ghosts.

The fake rate depends on the fragmentation model, the detector performance, the detector simulation model and on the reconstruction algorithms. That is why it is essential to develop a data driven calibration of fakes from the first data and in this sense the $D^{*+} \to D^0(K^-\pi^+)\pi_s^+$ decay channel is used to extract the fake rates for the kaon and the pion.

As the first step, the D^* decay is reconstructed as described previously using the Inner Detector tracks. Using a background subtraction method the number of the reconstructed D^* mesons is extracted. There are two methods used in this study for background subtraction: the fit method and the "*s*Plot" technique. In the next step, it is checked if any of the daughters of D^0 is associated to a muon and then, with the same background subtraction method, the number of D^0 daughters associated to muons is extracted. The fraction of the latter over the former one provides the muon fake rate:

$$\text{muon fake rate} = \frac{D^0 \text{ daughters associated to a muon}}{\text{all } D^0 \text{ daughters}} \tag{4.1}$$

The fit method The subtraction of the background in this case is simply based on modeling the invariant mass distribution of the D^0 candidates with two probability density functions, one for the signal (f_{sig}) and one for the background (f_{bkg}) shape. For f_{sig} a double Gaussian is selected while the f_{bkg} shape is considered as exponential. The fit applied is an unbinned maximum likelihood fit with the likelihood function defined as

$$L = \prod_{i=1}^{N} [f_{sig}(m_i) + f_{bkg}(m_i)] \tag{4.2}$$

where N is the total number of D^0 candidates and m_i the invariant mass of the two tracks forming the D^0 candidate. The fit is performed using RooFit and the number of D^0 signal (background) events is obtained from the f_{sig} (f_{bkg}) integral. The fitting range is constrained in the region above 1.7 GeV due to contributions from other D^0 decays.

The *s*Plot technique The *s*Plot technique [40] is a statistical method which performs likelihood analysis of a data sample in which several species of events are merged. The species in this case are the signal and background components. This method allows to reconstruct the distributions for the so-called control variables (p_{T}, η and ϕ) without making use of any *a priori* knowledge on these variables but based on the knowledge available for a discriminating variable (D^0 invariant mass). An essential assumption for the *s*Plot technique is that the control variables are uncorrelated with the discriminating variable. This is checked for the variables in this study and the correlation is found to be less than 7% for all cases, which is considered negligible.

The log-likelihood is expressed as

$$L = \sum_{e=1}^{N} \left\{ \sum_{i=1}^{N_s} N_i f_i(y_e) \right\} - \sum_{i=1}^{N_s} N_i \tag{4.3}$$

Table 4.1: Integrated Kaon fake rates for data and MC.

Chain	Data ($\times 10^{-3}$)	Monte Carlo ($\times 10^{-3}$)
Chain 1	8.7 ± 1.3	7.5 ± 1.3
Chain 2	14.8 ± 1.6	11.1 ± 1.0

where N is the total number of events in the data sample, N_s is the number of species of events populating the data sample, N_i is the number of events expected on the average for the i-th species, y is the set of discriminating variables, f_i is the Probability Density Function (PDF) of the discriminating variables for the i-th species, y_e denotes the value taken by the PDFs f_i for event e. The yields N_i of the various species are determined by maximizing the above log-Likelihood. The method calculates event weights for the unfolded signal and background distributions and using these weights on the events, histograms of the control variable are filled.

Results

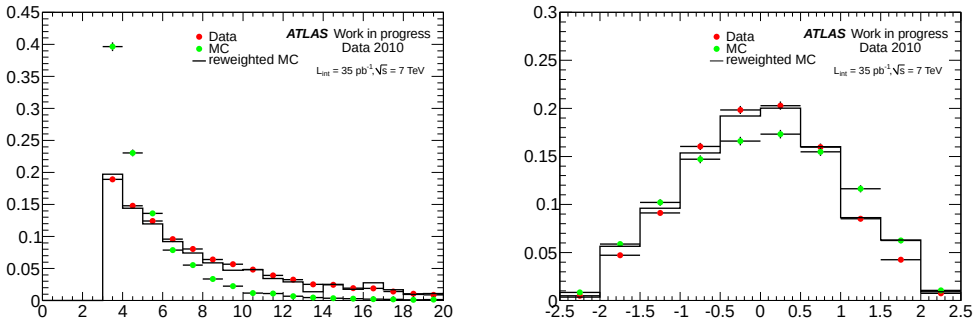

(a) p_{T} (b) η

Figure 4.5: p_{T} and η distributions for data and MC before and after reweighting.

Following the procedure described above, the fake rates are extracted. In Table 4.1 the integrated values are presented for Data and MC for the two muon reconstruction chains. In MC the statistics are very limited, so only the Kaon integrated numbers could be extracted. To account for difference in the p_{T}-η spectrum of the tracks between data and MC as well as the different pileup conditions, the MC is reweighted. In Figure 4.5 the p_{T} and η distributions can be seen for data and MC before and after reweighting.

In Figure 4.6 the D^0 invariant mass distribution using the 1-vertex approximation method is presented. The mean value is 1864.67 ± 0.34 MeV which is compatible with the world average value 1864.86 ± 0.13 [37] while the widths of the double Gaussian are of 18.48 MeV and 34.39 MeV for the tails. The yield from the fit is 11304 ± 204.

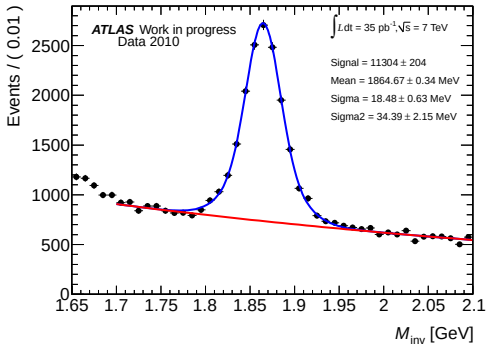

Figure 4.6: The invariant mass distribution for D^0 using the 1-vx approximation method for all tracks.

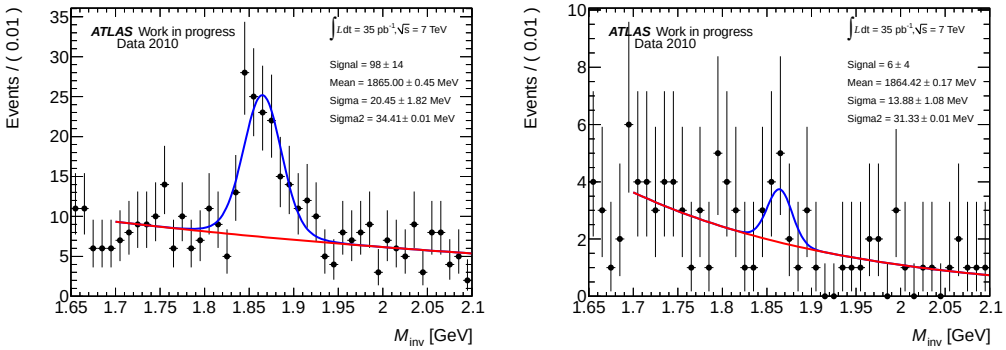

(a) Kaon tracks associated to muons.

(b) Pion tracks associated to muons.

Figure 4.7: The invariant mass distribution for D^0 provided that one of the D^0 daughters is associated to a muon for Chain 1.

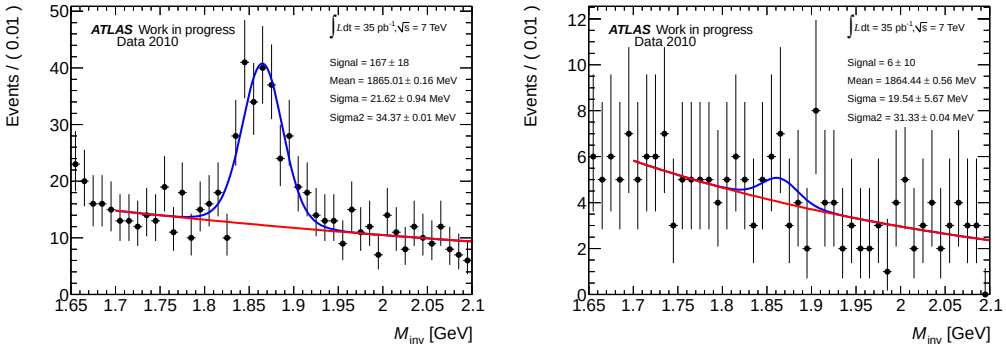

(a) Kaon tracks associated to muons.

(b) Pion tracks associated to muons.

Figure 4.8: The invariant mass distribution for D^0 provided that one of the D^0 daughters is associated to a muon for Chain 2.

Table 4.2: Fake rates for combined and segment-tagged muons from both chains associated to the kaon and pion hadrons.

Hadron	Muon type	Chain 1 ($\times 10^{-3}$)	Chain 2 ($\times 10^{-3}$)
Kaon	Combined or ST	8.7 ± 1.3	14.8 ± 1.6
	Segment-tagged	5.0 ± 1.0	4.5 ± 0.9
	Combined	3.5 ± 0.8	9.8 ± 1.3
Pion	Combined or ST	0.6 ± 0.4	0.5 ± 0.9
	Segment-tagged	0.5 ± 0.3	0.1 ± 0.3
	Combined	0.1 ± 0.3	0.4 ± 0.5

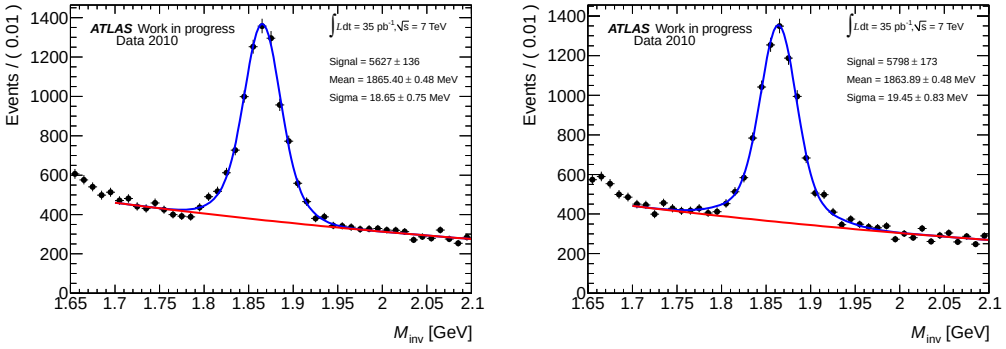

(a) D^0 coming from D^{*-}. (b) D^0 coming fromD^{*+}.

Figure 4.9: The invariant mass distribution for D^0 coming from D^{*+} and D^{*-} separately.

It is also important to separate the cases where the track associated to a muon is either the kaon daughter or the pion one, so that the muon fake rate for both particles can be extracted. This is possible using this decay channel since the kaon has a charge opposite to the soft pion whereas the pion has the same charge as the soft pion, and in this way one can identify the two tracks. The D^0 invariant mass distributions for these two cases are presented in Figure 4.7 for Chain 1 and in Figure 4.8 for Chain 2.

In both kaon cases a clear peak can be seen in the expected range while in the pion cases there are no clear peaks and the study cannot be conclusive with the available statistics. Nevertheless, the rates are evaluated for completeness. The fits in Figure 4.7 give a yield of 98 ± 14 for the kaon case and 6 ± 4 for the pion case. In Figure 4.8 the corresponding ones are 167 ± 18 for the kaon and 6 ± 10 for the pion. Taking into account these yields and the yield given in Figure 4.6, a fake rate of $8.7 \pm 1.3 \times 10^{-3}$ for the kaon and $0.6 \pm 0.4 \times 10^{-3}$ for the pion is extracted using Chain 1 while a fake rate of $14.8 \pm 1.6 \times 10^{-3}$ for the kaon and $0.5 \pm 0.9 \times 10^{-3}$ for the pion is extracted in the case of Chain 2.

For the distributions in Figures 4.7 and 4.8 combined and segment-tagged muons are used. In a further step, the type of the muons are considered separately and the

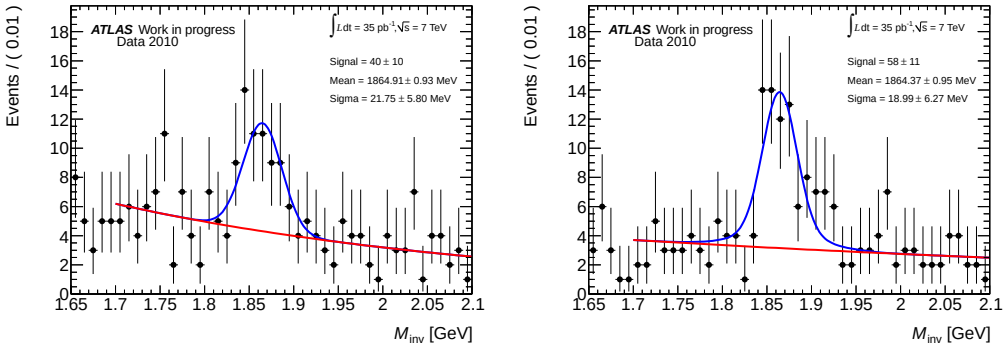

(a) K^+ (b) K^-

Figure 4.10: The invariant mass distribution for D^0 provided that the K daughter (K^+ and K^- separately) is associated to a muon for Chain 1.

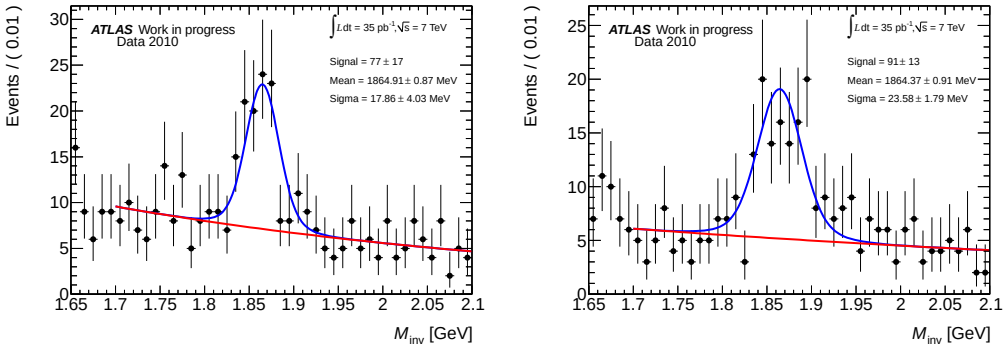

(a) K^+ (b) K^-

Figure 4.11: The invariant mass distribution for D^0 provided that the K daughter (K^+ and K^- separately) is associated to a muon for Chain 2.

extracted fake rates are provided in Table 4.2 for both chains. It is notable that in Chain 1 there is a larger contribution to the fake muons from segment-tagged muons and in Chain 2 from the combined ones.

D^{*+} and D^{*-} are reconstructed separately and the outcoming D^0 invariant mass distributions are shown in Figure 4.9. The yields from the fit are 5798 ± 173 for D^{*+} and 5627 ± 136 for D^{*-}. Plotting only the D^0 candidates for which the K^+ and K^- separately are associated to a muon from Chain 1, the distributions in Figure 4.10 are extracted. The yields are 40 ± 10 and 58 ± 11, correspondingly. The equivalent distributions for Chain 2 are shown in Figure 4.11 and the yields in this case are 77 ± 17 and 91 ± 13, correspondingly. The results are summarized in Table 4.3 and the values are consistent within their errors.

Using the *s*Plot technique, signal and background can be unfolded using the D^0 invariant mass distribution as the discriminating variable, so that the distributions of the hadrons' p_{T}, η and ϕ for the signal can be plotted. Applying this both for

Table 4.3: Summary table for the kaon fake rates for both chains.

Chain	Kaon fake rate ($\times 10^{-3}$)		
	$K^{\pm}$	K^{+}	K^{-}
Chain 1	8.7 ± 1.3	7.2 ± 1.9	9.9 ± 2.0
Chain 2	14.8 ± 1.6	13.6 ± 3.1	15.7 ± 2.4

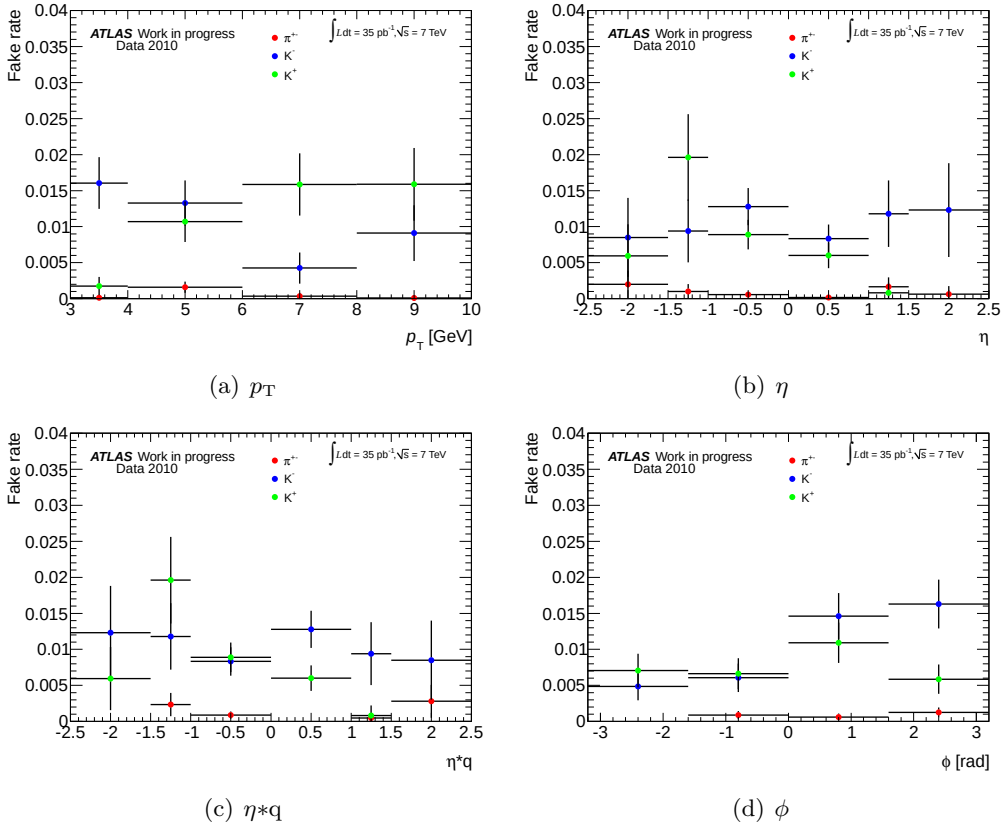

(a) p_{T} (b) η

(c) η*q (d) ϕ

Figure 4.12: Fake rates versus the p_{T}, η, η*q and ϕ of the K^{+}, K^{-} and pion tracks associated to either a combined or a segment-tagged muon from Chain 1.

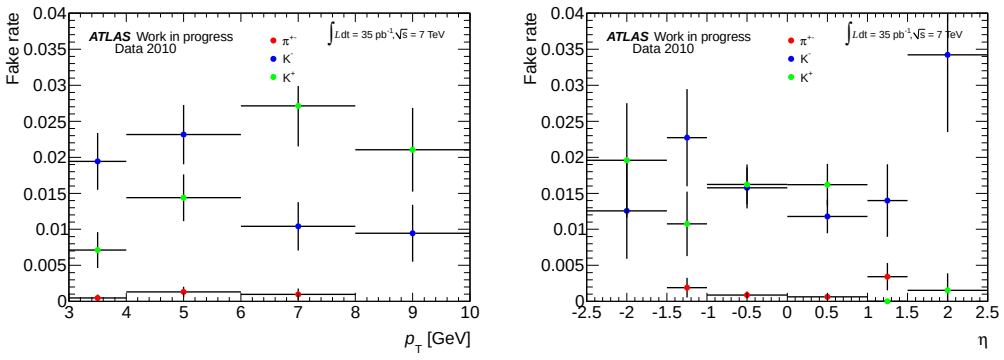

(a) p_{T} (b) η

(c) η*q (d) ϕ

Figure 4.13: Fake rates versus the p_{T}, η, η*q and ϕ of the K^+, K^- and pion tracks associated to either a combined or a segment-tagged muon from Chain 2.

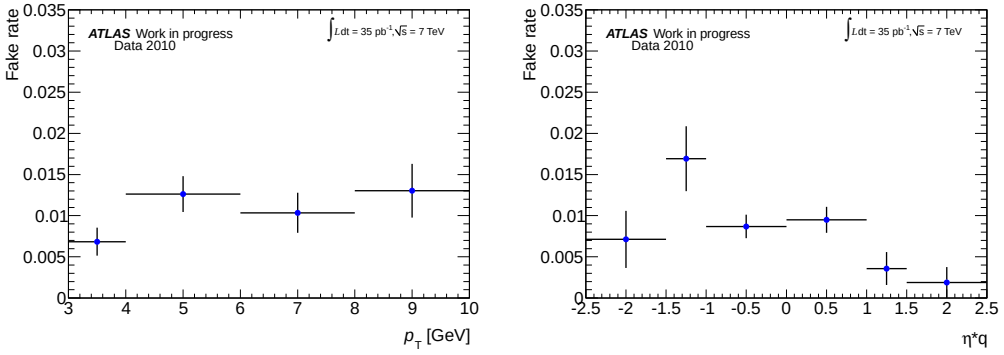

(a) p_{T} (b) η∗q

Figure 4.14: Fake rates with respect to the p_{T} and η∗q of the K for Chain 1.

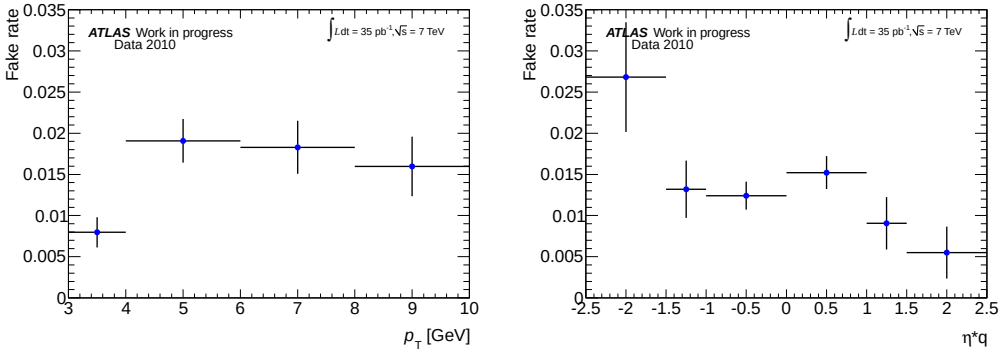

(a) p_{T} (b) η∗q

Figure 4.15: Fake rates with respect to the p_{T} and η∗q of the K for Chain 2.

the case of all tracks and for the case of tracks associated to muons, it is possible to extract the muon fake rates versus the hadrons' p_{T}, η and ϕ. In Figure 4.12 the fake rates with respect to the p_{T}, η, η∗q and ϕ of the K^+, K^- and the pion hadrons are presented for Chain 1 using the sPlot technique. The equivalent results for Chain 2 are presented in Figure 4.13.

The decision to also plot the fake rates with respect to η∗q is taken due to the fact that there is charge dependence of the efficiency with respect to pseudorapidity. The efficiency for positively (negatively) charged muons is larger for $\eta < 0$ ($\eta > 0$) than for $\eta > 0$ ($\eta < 0$) since in the former case the magnetic field bents the muons away from the beamline in the first case and towards the beamline in the latter case. In Figure 4.14 (Figure 4.15) the fake rates with respect to the p_{T} and η∗q of the K are presented for Chain 1 (Chain 2). The previous effect is well presented in the η∗q plots.

Table 4.4: Differential fake rates for the kaon hadrons in four p_{T} and four η bins for Chain 1.

p_{T} range (GeV)	η integrated ($\times 10^{-3}$)	$-2.5 < \eta < -1.0$ ($\times 10^{-3}$)	$-1.0 < \eta < 0.0$ ($\times 10^{-3}$)	$0.0 < \eta < 1.0$ ($\times 10^{-3}$)	$1.0 < \eta < 2.5$ ($\times 10^{-3}$)
$3 < p_{\mathrm{T}} < 4$	8.4 ± 4.5	21.5 ± 13.7	4.9 ± 6.7	9.2 ± 5.7	17.1 ± 9.5
$4 < p_{\mathrm{T}} < 6$	10.9 ± 2.9	16.5 ± 12.6	14.8 ± 5.1	6.5 ± 4.0	8.9 ± 8.5
$6 < p_{\mathrm{T}} < 8$	8.2 ± 2.6	8.0 ± 8.5	8.6 ± 5.6	13.6 ± 5.0	5.6 ± 6.1
$8 < p_{\mathrm{T}} < 10$	12.7 ± 3.5	24.9 ± 11.9	14.7 ± 6.8	8.6 ± 4.9	8.9 ± 11.5

Table 4.5: Differential fake rates for the kaon hadrons in four p_{T} and four η bins for Chain 2.

p_{T} range (GeV)	η integrated ($\times 10^{-3}$)	$-2.5 < \eta < -1.0$ ($\times 10^{-3}$)	$-1.0 < \eta < 0.0$ ($\times 10^{-3}$)	$0.0 < \eta < 1.0$ ($\times 10^{-3}$)	$1.0 < \eta < 2.5$ ($\times 10^{-3}$)
$3 < p_{\mathrm{T}} < 4$	15.2 ± 4.8	10.3 ± 14.0	22.5 ± 9.6	12.5 ± 8.1	16.9 ± 10.7
$4 < p_{\mathrm{T}} < 6$	16.3 ± 3.5	24.9 ± 11.3	21.4 ± 6.3	15.0 ± 5.3	1.7 ± 10.0
$6 < p_{\mathrm{T}} < 8$	17.3 ± 3.7	18.9 ± 12.6	19.5 ± 6.5	19.8 ± 6.0	13.2 ± 10.0
$8 < p_{\mathrm{T}} < 10$	15.9 ± 4.6	21.0 ± 12.0	14.5 ± 7.8	18.4 ± 7.9	8.3 ± 14.9

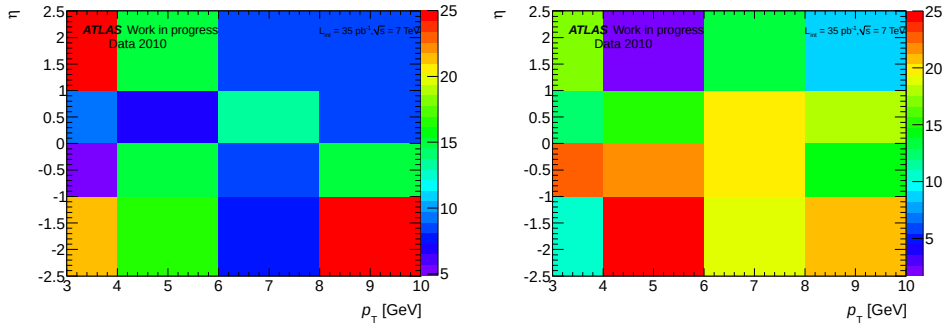

(a) Chain 1 (b) Chain 2

Figure 4.16: Fake rate color maps for the kaons in 4 p_{T} and 4 η bins for both chains.

It is important for many physics analyses to provide the differential fake rates, meaning the fake rates in the various p_{T} and η bins. In Tables 4.4 and 4.5 this information is provided for the kaons along with the integrated rates for every p_{T} bin. The errors in most cases are large due to the little statistics when dividing the data in p_{T} and η bins.

In Figure 4.16 the color map for the fake rates of the kaon hadrons is shown in four p_{T} and four η bins for both chains while in Figure 4.17 the integrated values over η are shown for every p_{T} bin. For both Chains the estimation with respect to the Kaon p_{T} is at the same level.

In this study the fake rate is calculated as the fraction of the signal for which one of the tracks is associated to a reconstructed muon to the total signal. Since the variable under study is a ratio of similar quantities, most systematic uncertainties cancel and the remaining sources of systematics are the models used to describe the signal and the background contribution when fitting the invariant mass distribution as well as the efficiency of the background subtraction method.

For the first case, a modified Gaussian[3], which was giving a very good description during the first periods of data taking, is used for the signal description, and a linear function to describe the non-resonant background, in turn.

For the second case, a stricter cut is applied in order to reduce further the background with minimal effect on the signal. For this reason the $144.75 < \Delta m < 146.25\,\mathrm{MeV}$ cut is used. The whole analysis is repeated and the difference in the fake rates is taken into account in the systematic errors.

The systematics from all above mentioned sources are summarized in Table 4.6 for both Chain 1 and Chain 2 for the different types of muons. The statistical errors are also included for comparison. In Tables 4.7 and 4.8 the systematic errors are presented in the different p_{T} and η bins for the two chains. In both tables, it can be noted that the systematic errors are smaller than the statistical ones.

[3]The modified Gaussian used is:

$$\propto \exp\left[-\frac{1}{2}x^{1+\frac{1}{1+0.5x}}\right] \tag{4.4}$$

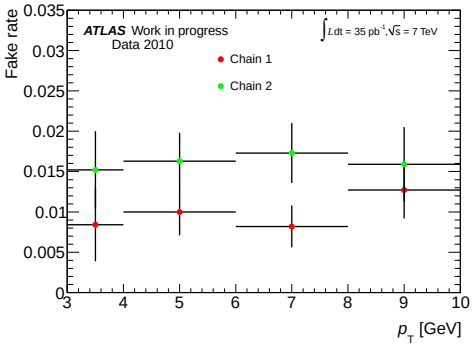

Figure 4.17: Fake rates integrated over η for every p_{T} bin for both chains.

Table 4.6: Systematic errors for the various muon types for Chain 1 and 2.

	$(\times 10^{-3})$	mod Gaussian signal	linear background	Δm cut	statistical error
Chain 1	Combined or ST	0.8	0.1	0.1	1.3
	Segment-tagged	0.6	0.1	0.8	1.0
	Combined	0.3	0.1	0.3	0.8
Chain 2	Combined or ST	1.2	0.2	1.8	1.6
	Segment-tagged	0.6	0.0	0.6	0.9
	Combined	0.9	0.1	1.1	1.3

Table 4.7: Systematic errors in the different p_{T} and η bins for Chain 1.

($\times 10^{-3}$)		mod Gaussian	linear	Δm	statistical
p_{T} bins	η bins	signal	background	cut	error
	$-2.5 < \eta < 2.5$	2.9	0.2	0.5	4.5
$3.0 < p_{\mathrm{T}} < 4.0$	$-2.5 < \eta < -1.0$	0.4	0.2	3.5	13.7
	$-1.0 < \eta < 0.0$	2.6	0.4	0.9	6.7
	$0.0 < \eta < 1.0$	0.2	0.1	1.0	5.7
	$1.0 < \eta < 2.5$	3.1	0.9	3.0	9.5
	$-2.5 < \eta < 2.5$	0.8	0.1	0.0	2.9
$4.0 < p_{\mathrm{T}} < 6.0$	$-2.5 < \eta < -1.0$	2.2	0.1	2.9	12.6
	$-1.0 < \eta < 0.0$	1.1	0.4	1.5	5.1
	$0.0 < \eta < 1.0$	0.3	0.1	0.1	4.0
	$1.0 < \eta < 2.5$	0.6	0.0	3.8	8.5
	$-2.5 < \eta < 2.5$	0.6	0.1	0.6	2.6
$6.0 < p_{\mathrm{T}} < 8.0$	$-2.5 < \eta < -1.0$	0.7	0.1	3.3	8.5
	$-1.0 < \eta < 0.0$	1.6	0.1	0.7	5.6
	$0.0 < \eta < 1.0$	0.1	0.3	0.2	5.0
	$1.0 < \eta < 2.5$	0.5	0.1	2.0	6.1
	$-2.5 < \eta < 2.5$	0.4	1.0	0.8	3.5
$8.0 < p_{\mathrm{T}} < 10.0$	$-2.5 < \eta < -1.0$	3.5	0.3	6.6	11.9
	$-1.0 < \eta < 0.0$	1.1	0.0	0.3	6.8
	$0.0 < \eta < 1.0$	0.2	0.1	1.6	4.9
	$1.0 < \eta < 2.5$	4.0	0.2	1.7	11.5

Table 4.8: Systematic errors in the different p_{T} and η bins for Chain 2.

($\times 10^{-3}$)		mod Gaussian	linear	Δm	statistical
p_{T} bins	η bins	signal	background	cut	error
	$-2.5 < \eta < 2.5$	3.6	0.9	1.3	4.8
$3.0 < p_{\mathrm{T}} < 4.0$	$-2.5 < \eta < -1.0$	2.6	0.6	8.2	14.0
	$-1.0 < \eta < 0.0$	2.1	0.9	1.5	9.6
	$0.0 < \eta < 1.0$	3.0	0.1	5.2	8.1
	$1.0 < \eta < 2.5$	0.7	0.8	4.4	10.7
	$-2.5 < \eta < 2.5$	0.7	0.2	1.2	3.5
$4.0 < p_{\mathrm{T}} < 6.0$	$-2.5 < \eta < -1.0$	0.8	0.3	0.8	11.3
	$-1.0 < \eta < 0.0$	0.7	0.5	2.8	6.3
	$0.0 < \eta < 1.0$	0.8	0.2	1.1	5.3
	$1.0 < \eta < 2.5$	0.7	0.7	0.9	10.0
	$-2.5 < \eta < 2.5$	0.0	0.1	0.3	3.7
$6.0 < p_{\mathrm{T}} < 8.0$	$-2.5 < \eta < -1.0$	2.0	0.1	7.7	12.6
	$-1.0 < \eta < 0.0$	2.3	0.1	2.7	6.5
	$0.0 < \eta < 1.0$	2.3	0.6	0.8	6.0
	$1.0 < \eta < 2.5$	0.0	0.2	0.5	10.0
	$-2.5 < \eta < 2.5$	2.1	1.2	2.5	4.6
$8.0 < p_{\mathrm{T}} < 10.0$	$-2.5 < \eta < -1.0$	0.1	0.2	0.6	12.0
	$-1.0 < \eta < 0.0$	2.3	0.1	2.9	7.8
	$0.0 < \eta < 1.0$	1.7	0.2	3.8	7.9
	$1.0 < \eta < 2.5$	3.4	8.3	1.5	14.9

Table 4.9: Fake rates in the different data taking periods for both chains having subtracted the background using the RooFit yield.

period	Chain 1 ($\times 10^{-3}$)	Chain 2 ($\times 10^{-3}$)
E-I	7.5 ± 1.1	11.5 ± 1.4
E	10.1 ± 4.9	12.5 ± 3.8
F	8.1 ± 2.0	16.8 ± 3.5
G	6.5 ± 2.5	9.5 ± 4.7
H	10.1 ± 5.1	11.6 ± 6.6
I	10.7 ± 5.1	11.4 ± 4.6

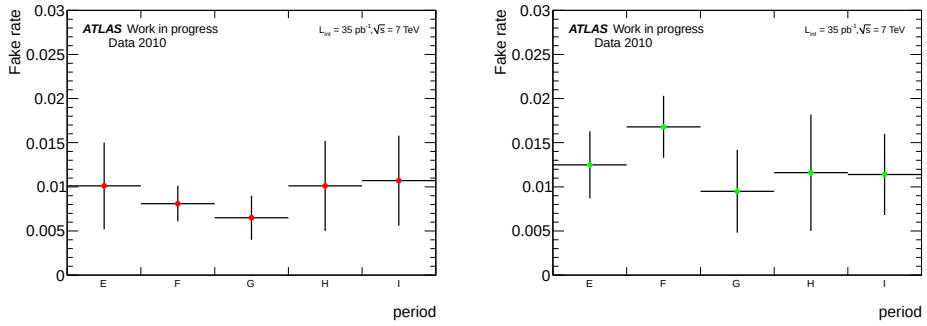

(a) Chain 1 (b) Chain 2

Figure 4.18: Kaon fake rates with respect to the different data taking periods for both chains.

Due to the various Trigger and the beam configurations during data recording, it is important to extract the fake rates in the different data taking periods. In Table 4.9 the extracted numbers for the Kaon are shown. In the first row, the integrated numbers are presented and below, the numbers for every period individually. Since the p_{T} spectra in the different periods was different, the distributions are reweighted with respect to the p_{T} distribution of period F. The results are also shown in Figure 4.18 where it can be seen that numbers are at the same level.

The muon fake rates have been studied using the decay $D^* \to D^0\pi_s \to (K\pi)\pi_s$. The extracted integrated K fake rates for Chain 1 and Chain 2 are $8.7 \pm 1.3 \times 10^{-3}$ and $14.8 \pm 1.6 \times 10^{-3}$, correspondingly. For π, the study could not be conclusive with the available statistics.

4.3.2 Study on the effect of pileup on muon isolation

As the parameters of the LHC evolve towards the designed values, the average number of interactions per bunch crossing increase. In Figure 2.4, it is shown how the average number of interactions has evolved during 2011 and 2012 data. This increase in the pileup is making the reconstruction of physics objects and the physics

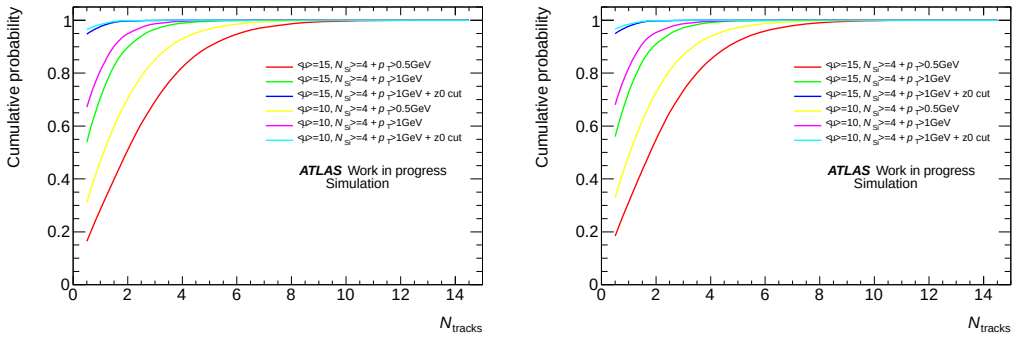

(a) (b)

Figure 4.19: The cumulative probability of the muons is presented as a function of the number of tracks included in a cone of $\Delta R = 0.4$ taking into account a bunch spacing configuration of (a) 50 ns and (b) 75 ns, applying different selection on the tracks to be considered in the cone size. The curves correspond to 10 and 15 average number of reconstructed vertices.

analysis more complicated. Therefore, it is important to study the effect of pileup on the physics objects and more specifically on their isolation.

In order to perform this study in expectation of the 2011 data, generated events with single muons of 100 GeV are used with different pileup and bunch spacing conditions. Samples with average number of interactions of 10 and 15, with bunch spacing of 50 ns and 75 ns and with or without cavern background are compared to each other and to a sample with no pileup.

Both the tracking and the calorimetric isolation of muons is studied. The tracking isolation is defined as the sum of the transverse momenta of all tracks greater than 500 MeV within a cone around the muon ($\sum p_{\mathrm{T}}$) and the calorimetric isolation is respectively defined as the sum of the transverse energy deposits in the calorimeter within a cone ($\sum E_{\mathrm{T}}$). The definition of the cone size is

$$\Delta R \equiv \sqrt{\Delta\phi^2 + \Delta\eta^2} \tag{4.5}$$

In Figures 4.19 the cumulative probability is presented for the muons to have as many tracks as indicated in the x axis within their cones, considering a cone of $\Delta R = 0.4$ which gives the worst case scenario concerning isolation. The cumulative probability is shown for a bunch spacing of 50 ns in 4.19(a) and of 75 ns in 4.19(b). Three of the curves correspond to an average μ value of 10 considering different selection for the tracks to be taken into account within the cone and three curves to an average μ value of 15. Additional selection on the tracks to be considered within the muon cones are encouraged in order to rely on well reconstructed tracks originating from the same vertex as the muon. These include requirements to have at least four silicon hits, p_{T} greater than 1 GeV and a longitudinal impact parameter within 10 mm the one of the muon. It can be noted that these selections for the tracks lead to better determination of isolated leptons and the difference between various μ values is decreased. Finally, there is little difference between the two bunch

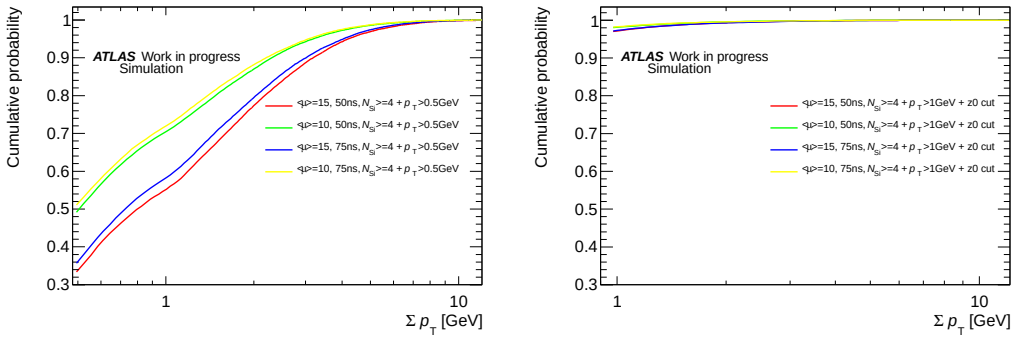

(a) (b)

Figure 4.20: The cumulative probability of the muons is presented with respect to the track isolation for different pileup and bunch spacing conditions applying (a) the basic selection and (b) additional selection on the tracks to be considered in the cone size of $\Delta R = 0.3$.

spacing configurations. For the rest of the plots a bunch spacing of 50 ns, as in the configuration of the 2011 data, will be implied unless stated otherwise.

In Figure 4.20(a) only the basic selection for the tracks inside the muon cone is considered for different pileup and bunch spacing conditions using an intermediate cone of $\Delta R = 0.3$. In Figure 4.20(b) the additional selections are applied. The effect on the muon isolation is huge and it enables to clearly point out the isolated muons and distinguish them from the non-isolated ones. For an average number of interactions per bunch crossing of 10 and bunch spacing of 75 ns about 52 % of the muons are well isolated using the basic selection while 98 % are well isolated using the additional selection.

In Figures 4.21 the cumulative probability is shown with respect to the isolation using different cone sizes around the muons. Therefore, the percentage of the muons having isolation equal or less than the value on the x axis is presented for each number of reconstructed vertices. The additional selections on the tracks included in the muon cones are applied. For 17 reconstructed vertices more than 88% of the muons are completely isolated using $\Delta R = 0.4$, more than 91% using $\Delta R = 0.3$ and more than 95% using $\Delta R = 0.2$.

For the calorimetric isolation there is a double effect of the pileup. The first is due to the contribution of tracks from other interaction vertices, known as the in-time pileup and the second is due to the shape of the calorimetric bipolar pulse which at its end extends to negative values up to about 600 ns. If the bunch spacing is small signals can be added up resulting to the out-of-time pileup. In Figures 4.22 the cumulative probability of the muons as a function of the calorimetric isolation is presented for different pileup and bunch spacing conditions and for three cone sizes. The case where no pileup is considered is also included. It can be noted that the effect of the bunch spacing is considerable in calorimetric isolation as well as the effect of the average number of interactions and evidently the selected cone size.

In Figure 4.23(a) the percentage of the muons with calorimetric isolation greater

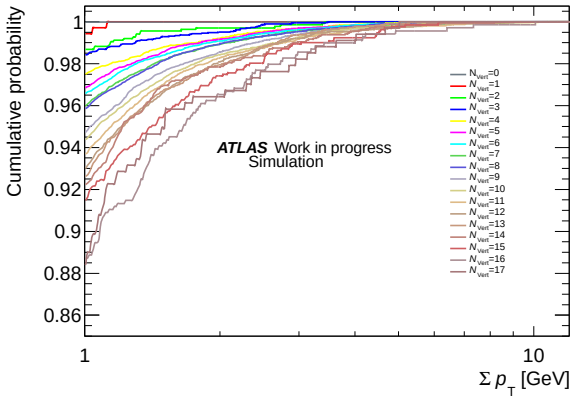

(a)

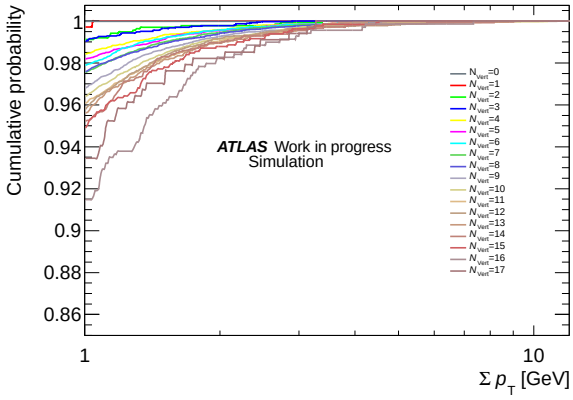

(b)

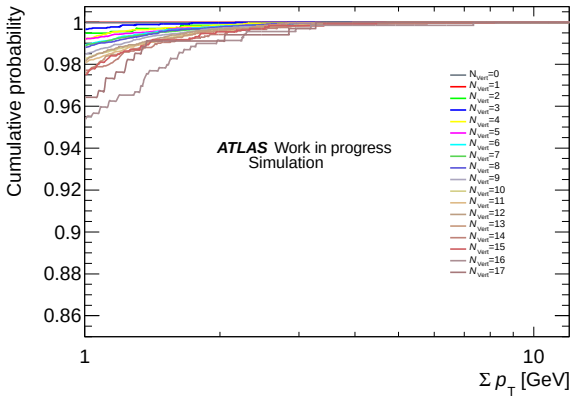

(c)

Figure 4.21: The cumulative probability of the muons is presented as a function of the track isolation using a cone of (a) $\Delta R = 0.4$, (b) $\Delta R = 0.3$ and (c) $\Delta R = 0.2$ after applying the selection on the tracks included in the cone for different numbers of reconstructed vertices. A bunch spacing configuration of 50 ns is considered.

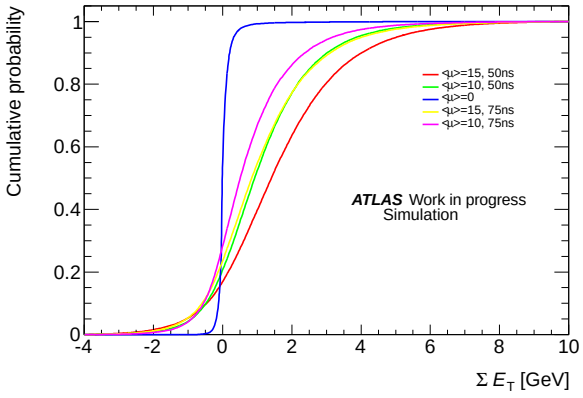

(a)

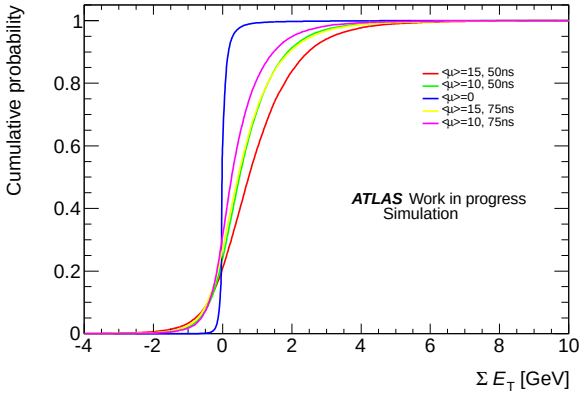

(b)

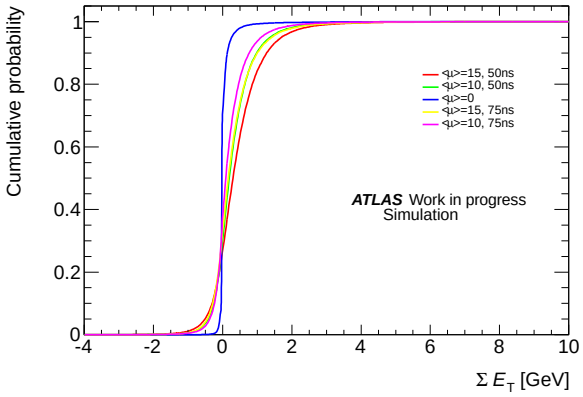

(c)

Figure 4.22: The cumulative probability of the muons is presented as a function of the calorimetric isolation using a cone of (a) $\Delta R = 0.4$, (b) $\Delta R = 0.3$ and (c) $\Delta R = 0.2$. Different pileup and bunch spacing conditions are considered.

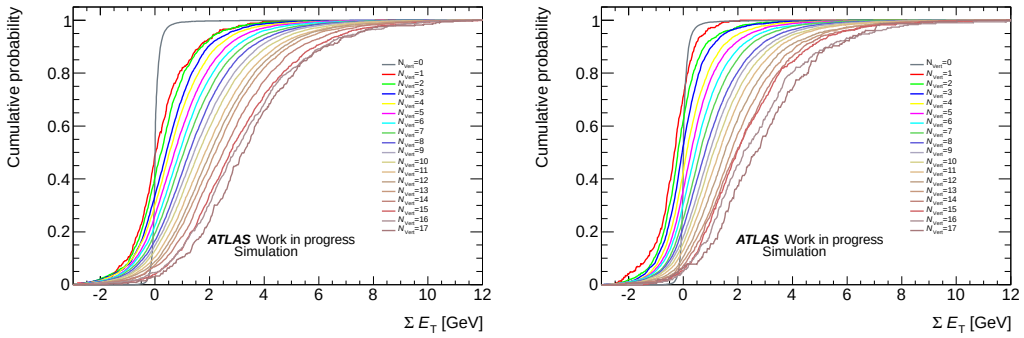

(a) (b)

Figure 4.23: The cumulative probability of the muons is presented as a function of the calorimetric isolation for different numbers of reconstructed vertices using a cone of $\Delta R = 0.4$ and a bunch spacing of (a) 50 ns and (b) 75 ns.

or equal to the value on the x axis is shown for various numbers of reconstructed vertices assuming a cone of $\Delta R = 0.4$ and a bunch spacing configuration of 50 ns. The effect of the in-time pileup can be seen as the number of reconstructed vertices increases compared to the "no pileup" scenario. In Figure 4.23(b), a bunch spacing of 75 ns is considered. Comparing with 4.23(a) the effect of out-of-time pileup can be assessed. Assuming 17 reconstructed vertices, all muons are isolated when considering isolation at about 10 GeV for 50 ns and 9 GeV for 75 ns.

In general, the pileup is affecting both tracking and calorimetric isolation due to the contribution of particles from other reconstructed vertices (in-time pileup) in the sense that the larger the average number of reconstructed vertices, the less isolated the muons. The effect of pileup is suppressed in tracking isolation by applying additional selection on the tracks to be considered in the momenta sum and the effect of bunch spacing is minimal. The effect of pileup is considerable in the case of the calorimetric isolation due to both the in-time and out-of-time pileup. The bunch spacing configuration has also a large effect on calorimetric isolation due to the out-of-time pileup but it can be mitigated by using a smaller cone size.

4.3.3 Muon efficiencies for isolation and impact parameter selection criteria using $Z \to \mu^-\mu^+$ events

The $Z \to \mu\mu$ decay results in well isolated muons from the primary vertex giving a clean signature in the same way as the muons coming from the $H \to ZZ^{(*)} \to 4\ell$. In order to study the efficiency of the isolation and impact parameter cuts used in the $H \to ZZ^{(*)} \to 4\ell$ analysis on the muons, one can use the signal-like muons from $Z \to \mu\mu$ decays. The main background processes to these decays are the $Z \to \tau^+\tau^-$ where both tau leptons decay to a muon and the $t\bar{t}$ production where each t quark decays to W and b and the each of the two muons comes either from the hadronization of the quark or the leptonic decay of the W.

The relative tracking isolation is defined as the sum of the transverse momenta

of the tracks included in a cone of defined size around the muon over the transverse momentum of the track

$$\text{relative tracking isolation} \equiv \frac{\sum p_{\mathrm{T}}}{p_{\mathrm{T}}} \tag{4.6}$$

and the relative calorimetric isolation is accordingly defined as the sum of the energy deposited in the calorimeters included in a cone of defined size around the muon over the energy deposited by the muon in the calorimeters

$$\text{relative calorimetric isolation} \equiv \frac{\sum E_{\mathrm{T}}}{p_{\mathrm{T}}} \tag{4.7}$$

Finally, the significance of the transverse impact parameter of the track

$$\text{significance of the transverse impact parameter} \equiv \frac{d_0}{\sigma_{d_0}} \tag{4.8}$$

is also used in the analysis selection, where d_0 is the distance of closest approach on the transverse plane and σ_{d_0} the corresponding uncertainty. The selection criteria under study are $\Sigma p_{\mathrm{T}}/p_{\mathrm{T}} < 0.15$, $\Sigma E_{\mathrm{T}}/E_{\mathrm{T}} < 0.3$ and transverse impact parameter significance $\mathrm{d}_0/\sigma_{d_0} < 3.5$. For both the tracking and calorimetric isolation a cone of 0.2, defined in Equation 4.5, around the muon is used.

This study was performed on the total $4.8\,\mathrm{fb}^{-1}$ 2011 data and several Monte Carlo samples both for the signal, $Z \to \mu^+\mu^-$ generated by ALPGEN-JIMMY, and the backgrounds: $Z \to \tau^+\tau^-$ also generated by ALPGEN-JIMMY and $t\bar{t}$ generated by MC@NLO. All Monte Carlo samples correspond to 50 ns of bunch spacing configuration as in data.

The "Tag and Probe" method is a data-driven method used for efficiency estimation. According to this method, a well defined muon, called "tag", is required, satisfying strict selections described below and a "probe" muon is searched for satisfying the requirements under study. The efficiency is extracted by studying the percentage of the probes that satisfy the selection under consideration. The highest p_{T} muon selected as the tag is required to be a combined muon satisfying further Inner Detector hits requirements, to have $p_{\mathrm{T}} > 20\,\mathrm{GeV}$ and longitudinal impact parameter with respect to the primary vertex less than 10 mm in order to reduce cosmics and cavern background contribution. It should also be well isolated with a relative tracking isolation less than 0.05.

The Probe muon is the remaining highest-p_{T} muon, either combined or segment-tagged, satisfying basic muon requirements described in Section 4.2. It is also required to have $p_{\mathrm{T}} > 7\,\mathrm{GeV}$ and longitudinal impact parameter with respect to the primary vertex less than 10 mm for background rejection. Dimuon pairs (tag-probe) are formed with an opposite charge requirement and their invariant mass distribution is used in order to estimate the selection criteria efficiency on the probe muon. Consequently, the efficiency is defined as

$$\text{efficiency} \equiv \frac{\text{number of probes satisfying the selection}}{\text{total number of probes}} \tag{4.9}$$

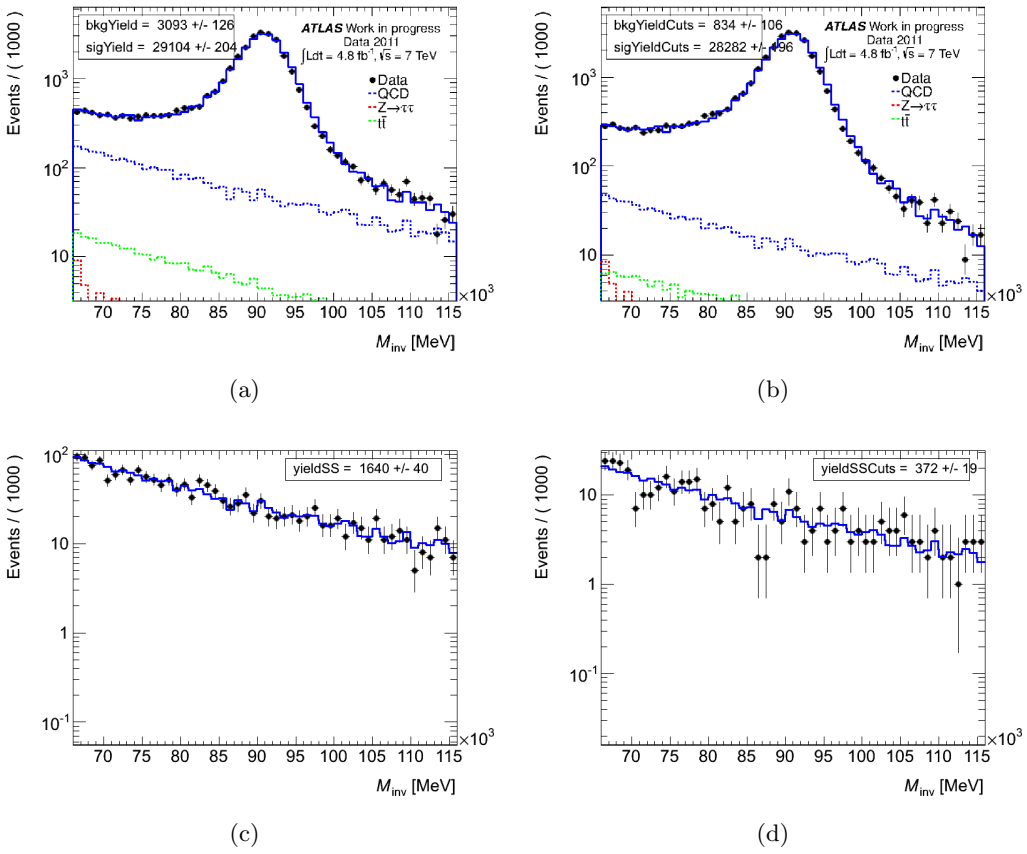

Figure 4.24: The invariant mass distribution for the tag and probe pair in data is presented for (a) opposite charge combinations before and (b) after applying the tracking isolation cut, (c) for the same charge combinations before and (d) after the tracking isolation cut, where the probe has a transverse momentum within 12 and 15 GeV.

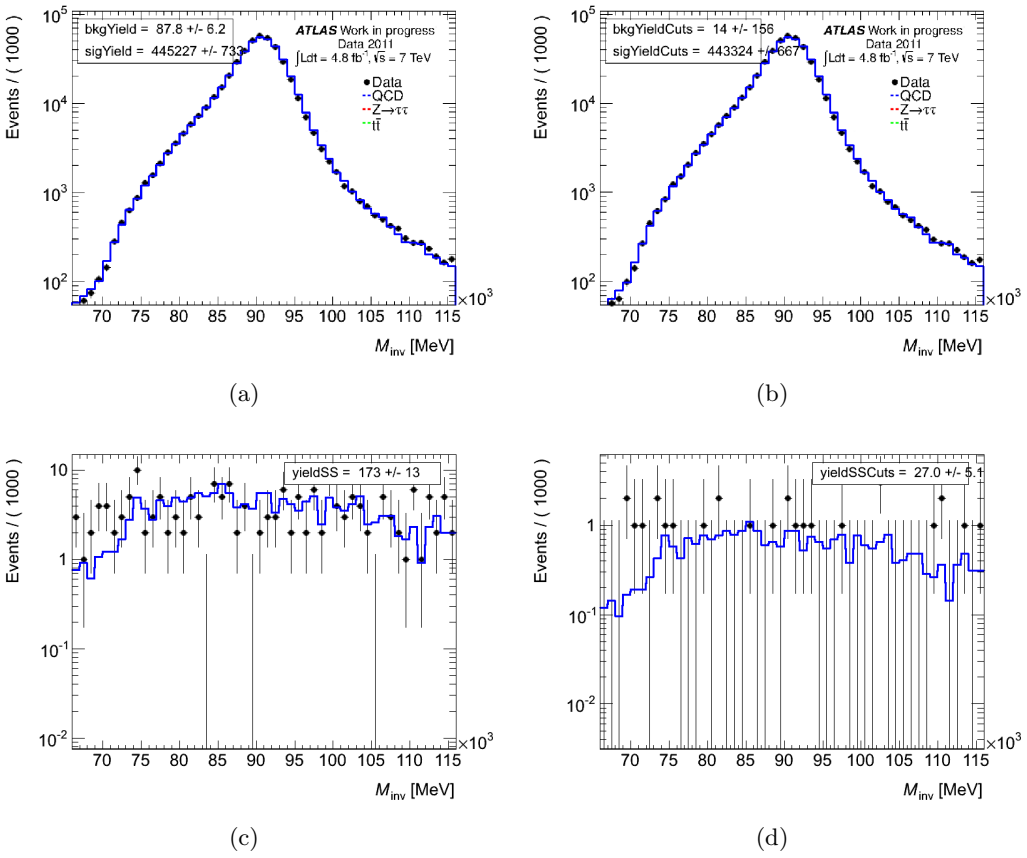

Figure 4.25: The invariant mass distribution for the tag and probe pair in data is presented for (a) opposite charge combinations before and (b) after applying the tracking isolation cut, (c) for the same charge combinations before and (d) after the tracking isolation cut, where the probe has a transverse momentum within 35 and 40 GeV.

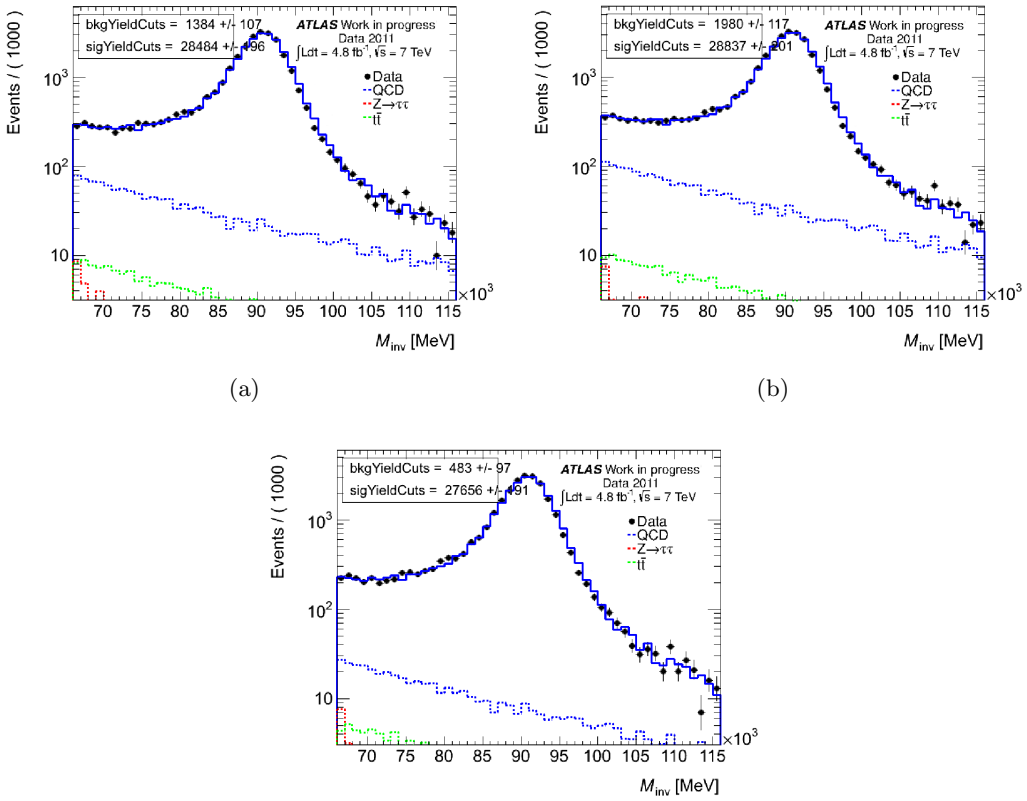

Figure 4.26: The invariant mass distribution for the tag and probe pair in data is presented for the opposite charge combinations after applying (a) calorimetric isolation, (b) d_0 significance and (c) all three cuts simultaneously, for the probe p_{T} interval of 12 and 15 GeV.

The estimation is performed both in the total phase space and in different p_{T} intervals for the probe muons down to 7 GeV.

For the data, the resulting mass distributions for every probe p_{T} bin are fitted using a shape template from the $Z \to \mu^+\mu^-$ Monte Carlo sample to describe the signal, including the smearing corrections to be applied on the Monte Carlo samples. To describe the QCD background, templates from the data same charge combination invariant mass distribution are being used while templates from the $Z \to \tau^+\tau^-$ and $t\bar{t}$ MC simulation are also taken into account. The latter background contributions are normalized to the luminosity used, before and after applying the selection criteria separately and the QCD normalization is left free in the combined fit in the mass range 66-116 GeV. In order to estimate the efficiency, only a mass range of 3 GeV around the Z mass peak is considered in order to introduce as less as possible uncertainties due to the background estimation.

In Figures 4.24 and 4.25 the invariant mass distributions are shown for the probe p_{T} intervals of 12-15 GeV and 35-40 GeV, respectively. The results of the fits on the

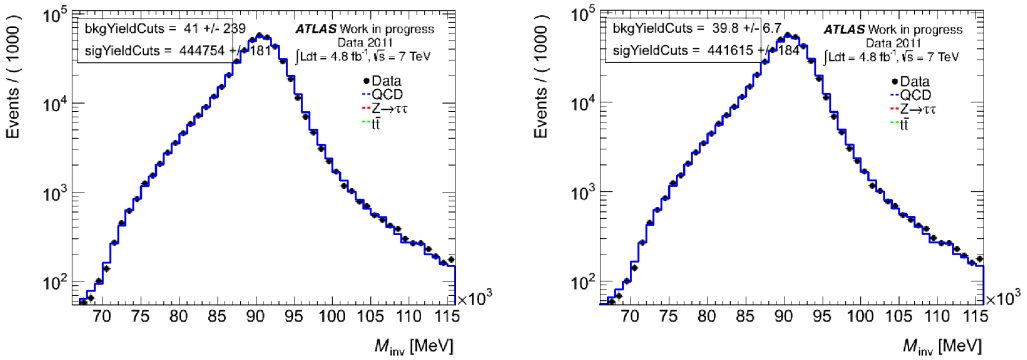

Figure 4.27: The invariant mass distribution for the tag and probe pair in data is presented for the opposite charge combinations after applying (a) calorimetric isolation, (b) d_0 significance and (c) all three cuts simultaneously, for the probe p_{T} interval of 12 and 15 GeV.

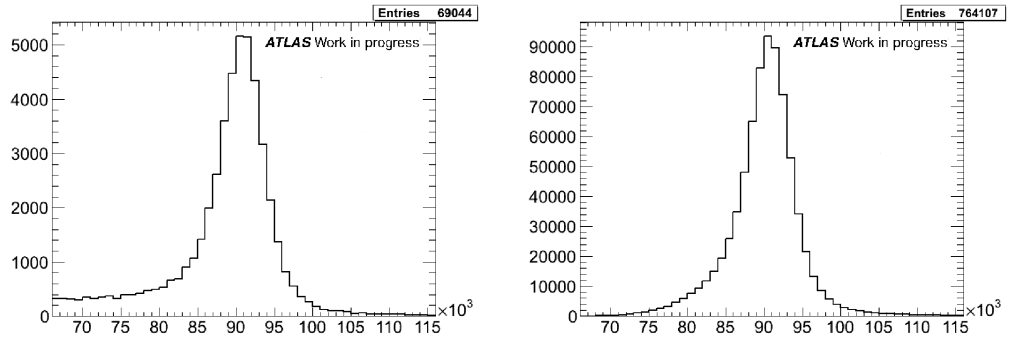

(a) (b)

Figure 4.28: The invariant mass distributions for the tag and probe pair in $Z \rightarrow \mu^+\mu^-$ Monte Carlo are presented after applying all three cuts in the p_{T} interval of (a) 12-15 GeV and (b) 35-40 GeV.

opposite and same charge combination distributions are presented before and after applying the tracking isolation cut. The blue dashed lines correspond to the QCD estimation using the same charge templates from data. The red dashed lines correspond to the estimated $Z \rightarrow \tau^+\tau^-$ and the green ones to the $t\bar{t}$ contribution. The combination of all the templates is shown with the continuous blue lines. Logarithmic scale is used to illustrate the tails. The rest of the p_{T} intervals are presented in Appendix A.

The corresponding invariant mass distributions for the opposite charge combinations after applying the calorimetric isolation cut, the transverse impact parameter significance cut and all three cuts simultaneously for the p_{T} intervals of 12-15 GeV and 35-40 GeV are presented in Figures 4.26 and 4.27, respectively. The combination of the templates is in agreement with the data in all probe p_{T} bins (Appendix A). It is noticeable that the backgrounds and mainly the QCD one are small for low probe transverse momenta and even smaller after applying the selection criteria while they vanish as the momenta increase.

For the Monte Carlo, the yields are extracted directly from the invariant mass distributions before and after the cuts and for the calculation of the efficiency only the yields in the window of 3 GeV around the Z mass peak are considered, for consistency to the data efficiency estimation. In Figures 4.28 the invariant mass distribution for the Monte Carlo $Z \rightarrow \mu\mu$ signal is presented for the probe p_{T} intervals of 12-15 GeV and 35-40 GeV after applying all selections. It can be noted that there is a non-negligible radiation tail to the distribution in the low probe momenta that decreases as the probe momenta increase. All distributions before and after the tracking isolation cut for all p_{T} intervals are shown in Appendix A.

The systematic uncertainties arealso studied. In order to estimate them, a range of 5 and 8 GeV around the Z peak are considered, in turn, for the efficiency estimation. Also, the fitting range is expanded to the broader 56-126 GeV, compared to the standard 66-116 GeV. Finally, a PYTHIA generated $Z \rightarrow \mu^+\mu^-$ Monte Carlo

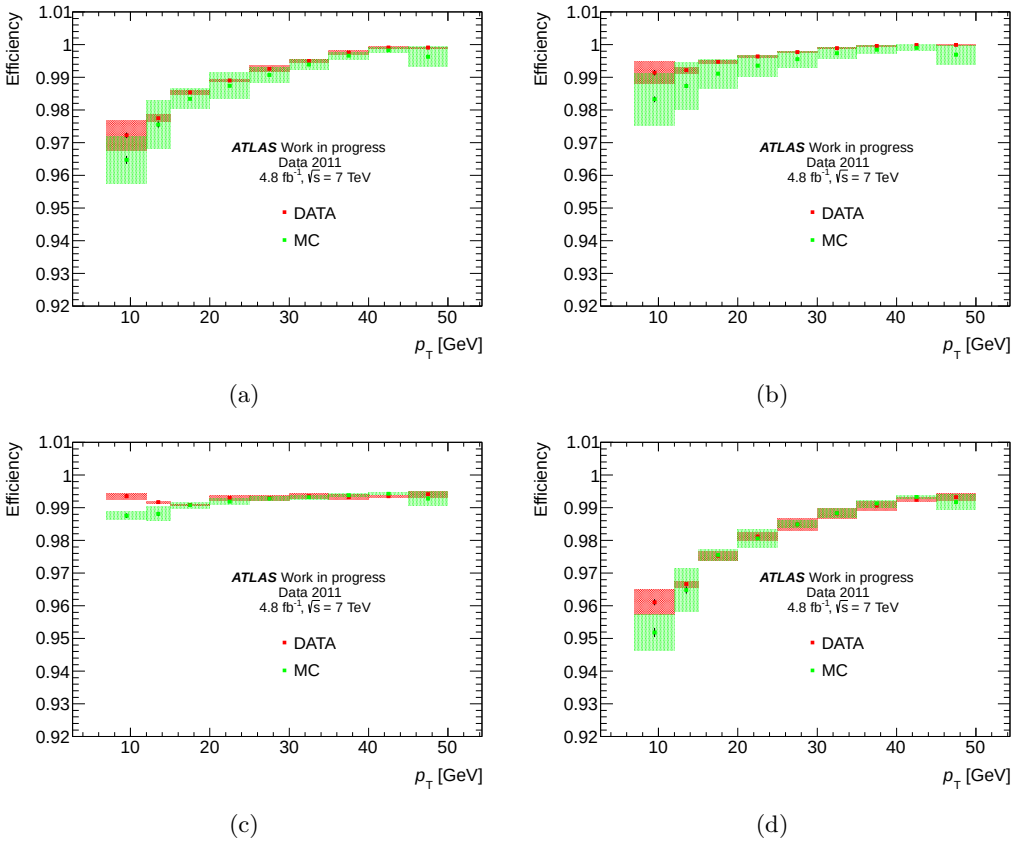

Figure 4.29: Probe muon efficiencies as function of the transverse momentum of the probe muon for both data and Monte Carlo for (a) the track isolation cut of 0.15 using a cone of 0.2, (b) the calorimeter isolation cut of 0.3 using a cone of 0.2, (c) the d_0 impact parameter cut of 3.5 and (d) all three cuts combined ($4.8\,\mathrm{fb}^{-1}$).

sample is taken into account. Using different generators proves to be the source of the largest systematics. The efficiencies of the cuts along with the efficiency ratios for data and Monte Carlo are calculated for every case considered for the systematics in Appendix A and the systematic uncertainties are found to be less than 8 per mil.

The resulting efficiency estimation of the tracking isolation can be seen in Figure 4.29(a) for both data and Monte Carlo while for the calorimetric isolation and the d_0 significance, the results are shown in Figures 4.29(b) and 4.29(c), and in Figure 4.29(d) for the simultaneous application of all three cuts. The effect of the selection criteria is minimal for the well isolated muons from $Z \to \mu^+\mu^-$ decays, as the effect is less than 5 %, even for low-p_{T} muons. In Table 4.10 the efficiencies of the cuts along with the efficiency ratios for data and Monte Carlo are calculated and in Figure 4.30 the ratio of the efficiency in data over Monte Carlo are shown including statistical and systematic uncertainties. As can be easily noted, all scale factors are compatible with unity. Finally, the integrated efficiency and scale factors

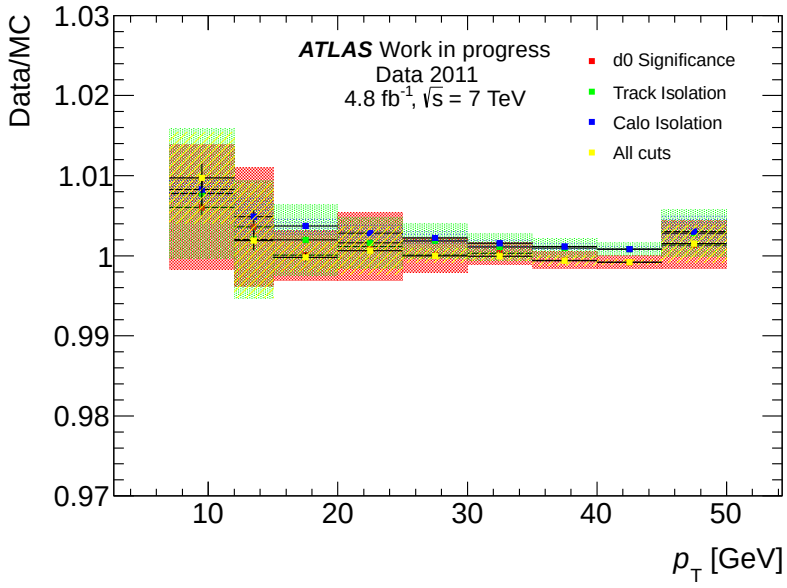

Figure 4.30: Scale factors for the efficiency as a function of the transverse momentum of the probe muon for both data and Monte Carlo and for all three individual cuts and all cuts simultaneously.

are provided in Table 4.11.

Table 4.10: The lepton selection criteria efficiencies and their ratio between data ($4.8\,\mathrm{fb}^{-1}$) and Monte Carlo are presented in the various probe p_{T} bins.

probe p_{T}	Track Isolation			Calorimeter Isolation			d_0 significance			all three		
(GeV)	Data	MC	ratio	Data	MC	ratio	Data	MC	ratio	Data	MC	ratio
7 - 12	0.972	0.965	1.008	0.991	0.983	1.008	0.994	0.988	1.006	0.961	0.952	1.010
12 - 15	0.978	0.976	1.002	0.992	0.987	1.005	0.992	0.988	1.004	0.967	0.965	1.002
15 - 20	0.985	0.983	1.002	0.995	0.991	1.004	0.991	0.991	1.000	0.975	0.975	1.000
20 - 25	0.989	0.987	1.002	0.996	0.994	1.003	0.993	0.992	1.001	0.981	0.981	1.001
25 - 30	0.993	0.991	1.002	0.998	0.996	1.002	0.993	0.993	1.000	0.985	0.985	1.000
30 - 35	0.995	0.994	1.001	0.999	0.997	1.002	0.993	0.993	1.000	0.988	0.988	1.000
35 - 40	0.998	0.997	1.001	1.000	0.998	1.001	0.993	0.994	0.999	0.991	0.991	0.999
40 - 45	0.999	0.998	1.001	1.000	0.999	1.001	0.993	0.994	0.999	0.992	0.993	0.999
45 - 50	0.999	0.996	1.003	1.000	0.997	1.003	0.994	0.993	1.001	0.993	0.992	1.002

Table 4.11: The integrated lepton selection criteria efficiency and the ratio between data ($4.8\ \mathrm{fb}^{-1}$) and Monte Carlo. The error corresponds to the systematic uncertainty.

Selection variable	Efficiency in Data [%]	Efficiency in MC [%]	Ratio
$d_0/\sigma_{d_0} < 3.5$	99.3	99.3	1.000 ± 0.001
Norm. Calo. isolation < 0.3	99.9	99.7	1.002 ± 0.002
Norm. Track isolation < 0.15	99.5	99.4	1.002 ± 0.002
All cuts	98.8	98.8	1.000 ± 0.001

Chapter 5

Search for the $H \to ZZ^{(*)} \to 4\ell$ using 4.8 fb^{-1} of 7 TeV data

One of the objectives of the ATLAS detector is the search for the Higgs boson. As stated in Section 1.3.2, the $H \to ZZ^{(*)} \to \ell^+\ell^-\ell'^+\ell'^-$, where $\ell, \ell' = e, \mu$, is the "golden" channel for the Higgs discovery due to the clean final state signature, the sensitivity in a wide mass range, from 110 GeV to 600 GeV, and the ability to fully reconstruct the Higgs mass accompanied by the excellent detector resolution. However, it has a relatively low branching ratio especially in the lower masses as already pointed out in Figure 1.10. This analysis has been published in Phys. Lett. B710.

5.1 Signal and background topology

Due to the excellent momentum and energy resolution in ATLAS, the channel $H \to ZZ^{(*)} \to \ell^+\ell^-\ell'^+\ell'^-$, where ℓ, ℓ' are muons or electrons, is experimentally the cleanest one. Firstly, the Higgs boson decays into two Z bosons, as shown in Figure 5.1, which can be off-shell. The Z boson decays to electrons and muons at a small branching ratio of 6.7 % in contrast to 69.9 % of its decays to hadrons [1]. In the leptonic channel $H \to ZZ^{(*)} \to \ell^+\ell^-\ell'^+\ell'^-$ where, $\ell, \ell' = e, \mu$, there are three possible final states: $4e$ (two electron pairs), 4μ (two muon pairs) and one electron and $2e2\mu$ (one electron and one muon pair).

The same final state particles can also come from other physics processes which are background sources for the $H \to ZZ^{(*)} \to 4\ell$ search. The major contribution comes from $ZZ^{(*)}/\gamma^*$ production, referred to as $ZZ^{(*)}$ hereafter. The diagrams for this background process are presented in Figure 5.2. The most challenging region is the low mass one up to $2\,m_Z$ where one of the Z bosons is off-shell giving low transverse momentum leptons. In this regime there is also important background contribution from Z production accompanied by jets and $t\bar{t}$ production. In the first case, the charged leptons arise either from decays of hadrons with b- or c-quark content as in Figure 5.3 or from misidentification of light jets. In the second case, shown in Figure 5.4, each top quark decays mainly to a W boson and a b quark,

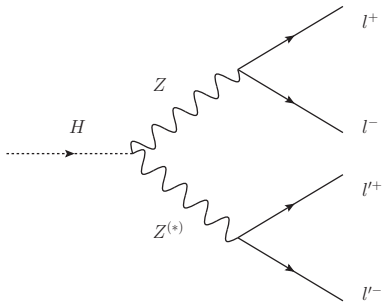

Figure 5.1: The $H \to ZZ^{(*)} \to 4\ell$ channel is presented.

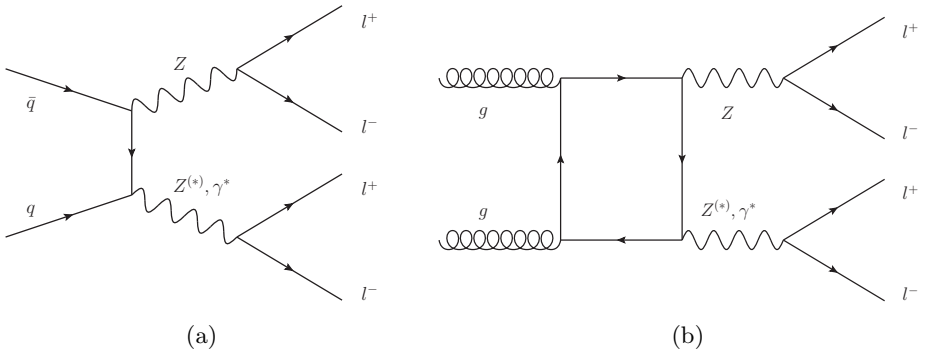

Figure 5.2: The production of a pair of Z bosons which decay leptonically is the major background in the $H \to ZZ^{(*)} \to 4\ell$ channel.

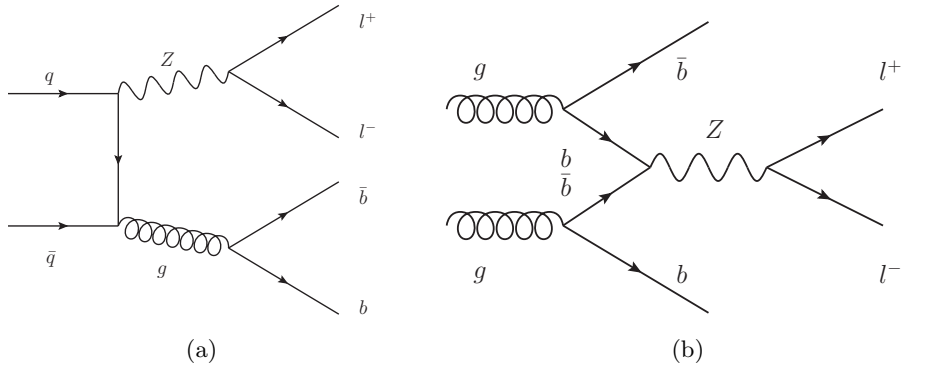

Figure 5.3: In the low m_H region there is background contribution from Z boson production accompanied by heavy quark jets.

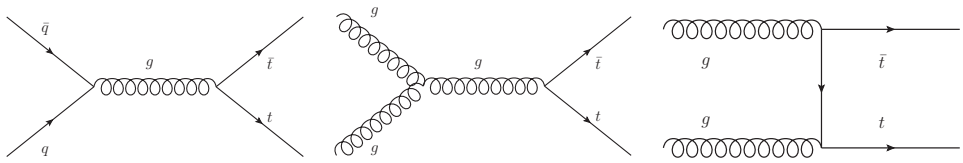

Figure 5.4: The pair production of top quarks is another background contribution for the $H \to ZZ^{(*)} \to 4\ell$ channel.

where W gives a lepton and a neutrino at 33 % and the b quark can result to a lepton from hadrons.

The Z production accompanied by jets has a larger cross section than the top-quark pair and the $ZZ^{(*)}$ background. However the b quarks produced in the $t\bar{t}$ decays are more energetic resulting in leptons with higher transverse momenta. Furthermore, the presence of jets in the Z+jets background makes the process more distinguishable than the $ZZ^{(*)}$ background. Other background processes with negligible contribution after applying the selections of the analysis are the WZ production, resulting to three leptons and considering a fourth lepton from an accompanying jet, and the various QCD processes producing multiple jets. The control and the estimation of the background contributions is essential in order to achieve high Higgs discovery potential. So the analysis is directed and aiming to an as more precise background estimation as possible.

5.2 Data and MC simulation samples

The data used in this section were recorded with the ATLAS detector during the 2011 LHC run involving pp collisions at $\sqrt{s} = 7\,\text{TeV}$. During this year, the LHC has delivered $5.61\,\text{fb}^{-1}$ and the ATLAS detector has recorded $5.25\,\text{fb}^{-1}$ divided in periods A-M. The evolution of the delivered and recorded luminosity was shown in Figure 2.3. A number of quality requirements are imposed on the data in order to ensure that all essential components of the ATLAS detector are working as expected. The integrated luminosity is then calculated per final state channel and the values extracted are: $4.8\,\text{fb}^{-1}$, $4.8\,\text{fb}^{-1}$ and $4.9\,\text{fb}^{-1}$ for the 4μ, $2e2\mu$ and $4e$ final states, respectively.

The $H \to ZZ^{(*)} \to 4\ell$ signal is modeled in the range 110 to 600 GeV using the POWHEG Monte Carlo event generator [41,42], which calculates separately the gluon and vector-boson fusion production mechanisms of the Higgs boson with matrix elements up to next-to-leading order (NLO). The Higgs boson transverse momentum, p_{T}, spectrum in the gluon fusion process is reweighted [43] to include QCD corrections up to NLO and QCD soft-gluon resummations up to next-to-next-to-leading logarithm (NNLL). POWHEG is interfaced to PYTHIA [38] for showering and hadronization, which in turn is interfaced to PHOTOS [44] for QED radiative corrections in the final state and to TAUOLA [45] for the description of τ decays. PYTHIA is used to simulate the production of a Higgs boson in association with a W or a

Table 5.1: Higgs boson production cross sections are quoted for gluon fusion, vector-boson fusion and associated production with a vector boson in pp collisions at $\sqrt{s} = 7\,\text{TeV}$. The quoted uncertainties correspond to the total theoretical systematic uncertainty. The branching ratio of $H \to 4\ell$, with $\ell = e, \mu$, is reported in the last column.

m_H [GeV]	$\sigma(gg \to H)$ [pb]	$\sigma(qq \to Hqq)$ [pb]	$\sigma(qq \to WH)$ [pb]	$\sigma(qq \to ZH)$ [pb]	$\text{BR}(H \to 4\ell)$ $\times 10^{-3}$
125	$15.3^{+3.0}_{-2.3}$	1.21 ± 0.03	$0.57^{+0.02}_{-0.03}$	0.32 ± 0.02	0.13
130	$14.1^{+2.7}_{-2.1}$	1.15 ± 0.03	0.50 ± 0.02	0.28 ± 0.01	0.19
190	$5.9^{+1.0}_{-0.9}$	0.69 ± 0.02	0.125 ± 0.005	0.074 ± 0.004	0.94
400	$2.03^{+0.32}_{-0.33}$	$0.162^{+0.009}_{-0.005}$	–	–	1.21
600	0.37 ± 0.06	$0.058^{+0.005}_{-0.002}$	–	–	1.23

Z boson. The contribution of the associated production with a top quark pair is negligible.

The cross sections for the Higgs boson production, the corresponding branching fractions, as well as their uncertainties, have been calculated by the LHC Higgs Cross Section Working Group [46]. The cross sections for the exclusive production mechanisms and the branching ratios for some generated m_H are listed in Table 5.1 for pp collisions at $\sqrt{s} = 7\,\text{TeV}$. They correspond to next-to-next-to-leading order (NNLO) in QCD for the gluon fusion [47–52] and vector boson fusion [53] and the associated production with a W or Z boson [54] processes. In addition, QCD soft-gluon resummations up to next-to-next-to-leading log (NNLL) are available for the gluon fusion process [55], while the NLO electroweak corrections are applied to the gluon fusion [56, 57], the vector-boson fusion [58, 59] and the associated production with a W or Z boson [60] processes. These cross section calculations do not take into account the width of the Higgs boson, which is implemented through a Breit-Wigner line shape applied at the event generator level. The Higgs boson decay branching ratio to the four-lepton final state is predicted by PROPHECY4F [18,61], including the complete NLO QCD and EW corrections with all interference and leading two-loop heavy Higgs boson corrections to the four-fermion width.

The irreducible $ZZ^{(*)} \to 4\ell$ background is generated using PYTHIA, implementing the $q\bar{q}$ initial state and taking into account the Z-γ interference, while the inclusive total cross section and the shape of the $m_{ZZ^{(*)}}$ spectrum is calculated using MCFM [62, 63]. MCFM v6.1 computes the cross section at LO and NLO for the process $q\bar{q} \to ZZ$ including ZZ, $Z\gamma^*$ and their interference, for the double resonant (or t-channel) and single resonant (or s-channel) diagrams, and for the process $gg \to ZZ$ including both quark-antiquark annihilation at QCD NLO and gluon fusion.

The inclusive Z boson and $Zb\bar{b}$ production is modeled using ALPGEN [64], while for the $t\bar{t}$ production MC@NLO [65–67] is employed. Both ALPGEN and MC@NLO generators are interfaced to HERWIG [68] for parton shower and hadronization, and

JIMMY [69] for simulation of the underlying events. For the inclusive Z boson and $Zb\bar{b}$ processes, overlaps between the two samples are removed. Namely, $b\bar{b}$ pairs with separation $\Delta R = \sqrt{\Delta\phi^2 + \Delta\eta^2} \geq 0.4$ between the jets are taken from the matrix-element calculation, while for $\Delta R < 0.4$ the parton-shower jets are used. The total inclusive cross section for Z boson production is normalized to the QCD NNLO prediction by FEWZ [70,71], while $Zb\bar{b}$ is normalized to the MCFM prediction [62,63]. The $t\bar{t}$ background is normalized to the approximate NNLO cross section calculated using HATHOR [72]. Finally, the WZ background was produced with HERWIG and was interfaced to JIMMY for simulation of the underlying events. In Table 5.2 the cross sections are quoted for the MC samples used.

During the 2011 data taking the parameters of the LHC machine were continuously evolving resulting in increasing values for the average number of interactions in every bunch crossing. In order to depict this effect on the MC samples used, a pileup reweighting procedure had become necessary in order to compare data and MC in all analyses.

5.3 Event selection

Good quality data are selected for the $H \to ZZ^{(*)} \to 4\ell$ analysis and trigger requirements are applied. Event candidates are retained if they have a reconstructed primary vertex with at least three tracks. On these events, leptons are selected in order to form quadruplets satisfying specific requirements. Finally, additional selections are applied to reject most of the reducible background processes. The requirements are detailed in the following sections.

5.3.1 Data quality requirements

The collected data are divided into Luminosity Blocks (LB), which consist of one or two minutes of approximately constant instantaneous luminosity and data taking conditions, such as detector status and trigger menu. Only LB where the LHC has declared "stable beams" have been used as well as LB where the involved components of the detector were declared to be operating as expected.

5.3.2 Trigger

Events within the surviving LB are then selected on single- or di-lepton triggers. For the single muon trigger, the p_{T} threshold is 18 GeV while for the single electron trigger the transverse energy, E_{T}, threshold varies from 20 to 22 GeV. For the dilepton triggers the thresholds are 12 GeV in the dielectron trigger and 10 for the dimuon one. The corresponding triggers are applied on the MC simulation, too. The trigger selection is evolving into using higher thresholds as the machine parameters tunings result to higher instantaneous luminosity. Finally, the efficiency of these triggers on $m_H = 125$ GeV signal events with is 98.2 % for the 4μ final state, 98.1 % for $2e2\mu$ and 99.8 % for $4e$.

Table 5.2: Background processes and their corresponding cross sections.

Process	Cross section [fb]
$Z \to ee$, no gen. partons	827375
$Z \to ee$, 1 gen. parton	166625
$Z \to ee$, 2 gen. partons	50375
$Z \to ee$, 3 gen. partons	14000
$Z \to ee$, 4 gen. partons	3375
$Z \to ee$, 5 gen. partons	1000
$Z \to \mu\mu$, no gen. partons	822125
$Z \to \mu\mu$, 1 gen. parton	166000
$Z \to \mu\mu$, 2 gen. partons	49500
$Z \to \mu\mu$, 3 gen. partons	13875
$Z \to \mu\mu$, 4 gen. partons	3500
$Z \to \mu\mu$, 5 gen. partons	1000
$Z \to \tau\tau$, no gen. partons	828125
$Z \to \tau\tau$, 1 gen. parton	167375
$Z \to \tau\tau$, 2 gen. partons	50375
$Z \to \tau\tau$, 3 gen. partons	13750
$Z \to \tau\tau$, 4 gen. partons	3500
$Z \to \tau\tau$, 5 gen. partons	1000
$Z \to ee + bb$ ($m_{ee} > 30\,\text{GeV}$), no gen. partons, $m_{\ell\ell} > 60/12\,\text{GeV}$	20.701
$Z \to ee + bb$ ($m_{ee} > 30\,\text{GeV}$), 1 gen. parton, $m_{\ell\ell} > 60/12\,\text{GeV}$	18.8029
$Z \to ee + bb$ ($m_{ee} > 30\,\text{GeV}$), 2 gen. partons, $m_{\ell\ell} > 60/12\,\text{GeV}$	10.505
$Z \to ee + bb$ ($m_{ee} > 30\,\text{GeV}$), 3 gen. partons, $m_{\ell\ell} > 60/12\,\text{GeV}$	7.30463
$Z \to \mu\mu + bb$ ($m_{\mu\mu} > 30\,\text{GeV}$), no gen. partons, $m_{\ell\ell} > 60/12\,\text{GeV}$	21.516
$Z \to \mu\mu + bb$ ($m_{\mu\mu} > 30\,\text{GeV}$), 1 gen. parton, $m_{\ell\ell} > 60/12\,\text{GeV}$	19.6674
$Z \to \mu\mu + bb$ ($m_{\mu\mu} > 30\,\text{GeV}$), 2 gen. partons, $m_{\ell\ell} > 60/12\,\text{GeV}$	10.516
$Z \to \mu\mu + bb$ ($m_{\mu\mu} > 30\,\text{GeV}$), 3 gen. partons, $m_{\ell\ell} > 60/12\,\text{GeV}$	7.93834
$Z \to ee + bb$ ($m_{ee} > 30\,\text{GeV}$), no gen. partons, 3ℓ, veto $m_{\ell\ell} > 60/12\,\text{GeV}$	1058.848
$Z \to ee + bb$ ($m_{ee} > 30\,\text{GeV}$), 1 gen. parton, 3ℓ, veto $m_{\ell\ell} > 60/12\,\text{GeV}$	605.15
$Z \to ee + bb$ ($m_{ee} > 30\,\text{GeV}$), 2 gen. partons, 3ℓ, veto $m_{\ell\ell} > 60/12\,\text{GeV}$	246.4
$Z \to ee + bb$ ($m_{ee} > 30\,\text{GeV}$), 3 gen. partons, 3ℓ, veto $m_{\ell\ell} > 60/12\,\text{GeV}$	135.45
$Z \to \mu\mu + bb$ ($m_{\mu\mu} > 30\,\text{GeV}$), no gen. partons, 3ℓ, veto $m_{\ell\ell} > 60/12\,\text{GeV}$	1022.336
$Z \to \mu\mu + bb$ ($m_{\mu\mu} > 30\,\text{GeV}$), 1 gen. parton, 3ℓ, veto $m_{\ell\ell} > 60/12\,\text{GeV}$	605.15
$Z \to \mu\mu + bb$ ($m_{\mu\mu} > 30\,\text{GeV}$), 2 gen. partons, 3ℓ, veto $m_{\ell\ell} > 60/12\,\text{GeV}$	251.02
$Z \to \mu\mu + bb$ ($m_{\mu\mu} > 30\,\text{GeV}$), 3 gen. partons, 3ℓ, veto $m_{\ell\ell} > 60/12\,\text{GeV}$	129.35468
$t\bar{t}$, at least one lepton	91550.6
$t\bar{t}$, (with $m_{\ell\ell} > 60$ GeV filter and $m_{\ell\ell} > 12$ GeV)	515.2
$ZZ \to 4\ell$ 3LepFilter	91.54
WZ	5735

Table 5.3: The subleading dilepton invariant mass (m_{34}) is required to exceed a threshold based on the reconstructed four-lepton invariant mass ($m_{4\ell}$). The actual cut value is obtained by linear interpolation between the following mass points.

$m_{4\ell}$ (GeV)	$\leq$120	130	140	150	160	165	180	190	$\geq$200
threshold (GeV)	15	20	25	30	30	35	40	50	60

5.3.3 Lepton selection

After the events are selected concerning good quality data and trigger, an additional requirement that the reconstructed primary vertex has at least three tracks is applied to assure good vertex quality, and then individual leptons are selected. As far as muons are concerned, combined and segment tagged muons are selected satisfying the basic requirements explained in Section 4.2. Concerning electrons, loose quality electrons, described in Section 4.1, are required while the Gaussian-sum filter (GSF) has been applied to account for energy losses due to bremsstrahlung.

The muons should have a transverse momentum of $p_{\mathrm{T}} > 7\,\mathrm{GeV}$ and a pseudorapidity $|\eta| < 2.7$ limited by the acceptance of the Muon Spectrometer and the electrons, $E_{\mathrm{T}} > 7\,\mathrm{GeV}$ and $|\eta| < 2.47$, respectively. In order to reject cosmic muons, the transverse impact parameter of the muons with respect to the primary vertex is required to be within 1 mm ($|d_0| < 1\,\mathrm{mm}$). A requirement on the longitudinal impact parameter of the lepton Inner Detector tracks, $|z_0| < 10\,\mathrm{mm}$, is applied to assure association to the primary vertex.

Care is also taken to remove overlaps concerning lepton tracks. When two electron candidates are sharing the same Inner Detector track, the electron with the highest E_{T} is kept. When an electron shares the same track with a muon, the electron is removed from the selection.

5.3.4 Lepton quadruplet selection

All four-lepton combinations satisfying the lepton flavor requirements of the final states, four muons for the 4μ channel, four electrons for the $4e$ channel, and two muons and two electrons for the $2\mu 2e$ channel, are retained for the analysis. In this way quadruplets are formed consisting of two same flavor, opposite charge pairs. In addition, they should contain at least two high p_{T} leptons, satisfying $p_{\mathrm{T}} > 20\,\mathrm{GeV}$. Within the quadruplet the same flavor, opposite charge pair with invariant mass closer to the $m_Z = 91.1876\,\mathrm{GeV}$ [1] is called the "leading" dilepton and the other one, the "subleading" dilepton.

All dileptons are required to satisfy $m_{\ell\ell} > 15\,\mathrm{GeV}$ and additionally, the leading dilepton is required to have an invariant mass (m_{12}) close to m_Z, within 15 GeV and the subleading pair invariant mass (m_{34}) should exceed a threshold, depending on the reconstructed four-lepton invariant mass ($m_{4\ell}$) as described in Table 5.3, but not 115 GeV. The actual cut value for the lower threshold of m_{34} is obtained by linear interpolation between the mass points in Table 5.3. The leptons are required

to be well separated to each other, satisfying $\Delta R > 0.1$. Finally, only the quadruplet with m_{12} closer to m_Z and with the most energetic off-shell m_{34} within the event is considered.

5.3.5 Additional lepton selection

The leptons coming from the $H \to ZZ^{(*)} \to 4\ell$ channel are expected to be well isolated and directly associated to the primary vertex. Based on this, additional selections are applied on the leptons in order to reject the background contributions that produce non-isolated leptons and leptons from secondary vertices. These requirements concern the relative tracking isolation, the relative calorimetric isolation and the significance of the transverse impact parameter.

The relative tracking isolation discriminant is defined as the sum of the transverse momenta of tracks, $\sum p_{\mathrm{T}}$, inside a cone of $\Delta R = 0.20$ around the lepton, divided by the lepton p_{T}. The tracks considered in the sum are of good quality, having at least four silicon hits, and satisfy $p_{\mathrm{T}} > 1\,\mathrm{GeV}$. All leptons in the quadruplet are required to have a relative tracking isolation smaller than 0.15.

The relative calorimetric isolation discriminant is defined as the sum of the transverse energy deposit in the calorimeter cells, $\sum E_{\mathrm{T}}$, inside an isolation cone of 0.20 around the lepton, divided by the lepton p_{T}. In case of electromagnetic showers, the corresponding cells are excluded from the sum. Each lepton is required to have a relative calorimetric isolation less than 0.30.

Since leptons originating from b or c quarks are associated to displaced vertices, the impact parameter significance of the leptons, d_0/σ_{d_0}, is a good discriminant for this case. The transverse impact parameter, d_0, is defined as the distance of closest approach on the transverse plane, and σ_{d_0} is the corresponding uncertainty. For the muons, the significance is required to be lower than 3.5 while for the electrons lower than 6, since bremsstrahlung smears the impact parameter distribution and therefore reduces the discriminating power of this selection.

The performance of the isolation and impact parameter criteria are studied using $Z \to \ell\ell$ decays for signal-like leptons and $b, c \to \mu$ events for background-like leptons. The efficiency of the selection criteria in simulation was found to be in close agreement with that observed in the data. For the signal-like leptons, this can be seen in Figures 5.5, where the efficiency ratio is presented, as well as in Table 5.4 where the integrated efficiencies and ratios are quoted. The Tag and Probe method had been used for these results and the study on the signal-like muons is extensively described in Section 4.3.3. For the background-like leptons the results can be seen in Tables 5.9 and 5.15 of the following sections.

In Figures 5.6 the efficiency of the additional selection is presented from simulation for each individual final state channel and for the inclusive $H \to ZZ^{(*)} \to 4\ell$ with respect to m_H. In all cases the efficiency is higher than 85 %. In Table 5.5 the percentage of the background events failing the additional requirements is quoted.

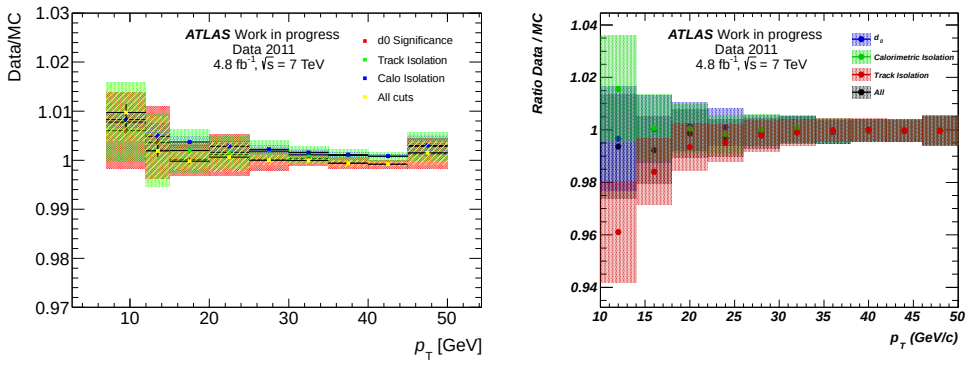

(a) (b)

Figure 5.5: The ratio of the efficiency of the additional selection criteria in data and MC simulation is shown as a function of the transverse momentum of the (a) muons and (b) electrons.

Table 5.4: The efficiency of the additional lepton selection requirements imposed in the analysis are quoted for data and MC as well as their ratio using $Z \to \ell\ell$ events.

Selection variable	Data efficiency [%]	MC efficiency [%]	Ratio
Electrons			
$d_0/\sigma_{d_0} < 6.0$	99.4	99.5	0.999 ± 0.002
Norm. Calo. isolation < 0.3	99.7	99.7	0.999 ± 0.002
Norm. Track isolation < 0.15	99.4	99.5	0.998 ± 0.002
All requirements	98.6	98.8	0.997 ± 0.002
Muons			
$d_0/\sigma_{d_0} < 3.5$	99.3	99.3	1.000 ± 0.001
Norm. Calo. isolation < 0.3	99.9	99.7	1.002 ± 0.002
Norm. Track isolation < 0.15	99.5	99.4	1.002 ± 0.002
All requirements	98.8	98.8	1.000 ± 0.001

Table 5.5: The percentage of the background events failing the additional selection requirements is quoted.

Background process	Tracking isolation [%]	Calorimetric isolation [%]	d_0 significance [%]	All additional selection [%]
$ZZ^{(*)}$	2.60	2.52	0.70	5.10
$Z+$ light jets	63.91	71.22	6.92	82.94
$Zb\bar{b}$	87.61	72.43	62.83	96.15
$t\bar{t}$	97.24	91.54	59.40	99.82

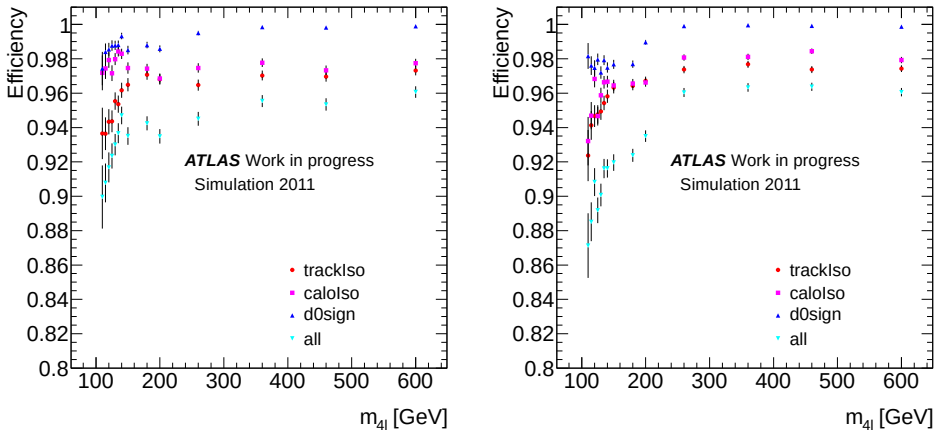

(a) $H \to ZZ^{(*)} \to 4\mu$ (b) $H \to ZZ^{(*)} \to 2e2\mu$

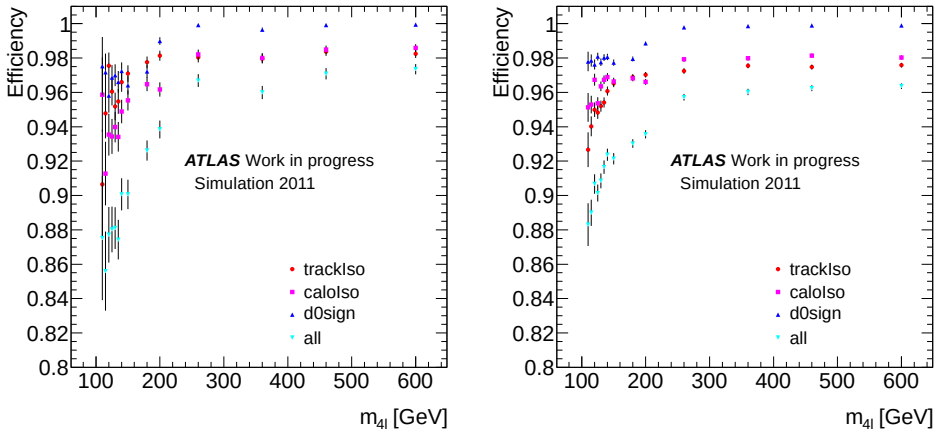

(c) $H \to ZZ^{(*)} \to 4e$ (d) $H \to ZZ^{(*)} \to 4\ell$

Figure 5.6: The efficiency of the isolation and impact parameter criteria on the signal is shown with respect to m_H on the three final states separately and on the inclusive $H \to ZZ^{(*)} \to 4\ell$ channel. The efficiencies are shown for every individual requirement and for applying simultaneously all three of them.

Table 5.6: Efficiency of reconstructing the Higgs signal after the analysis selection criteria.

Analysis efficiency in %			
Higgs mass	4μ	$2e2\mu$	$4e$
110	10.5	6.12	3.55
115	23.4	14.7	8.68
120	32.2	21.5	14.8
125	39.5	25.9	18.5
130	44.5	29.9	21.4
135	47.4	33.1	23.0
140	49.0	35.3	27.9
145	52.4	36.4	28.7
150	54.0	39.3	30.0
180	70.2	54.1	44.5
200	71.8	58.0	47.4
260	69.7	59.1	49.7
360	70.0	61.0	52.8
460	69.5	63.2	56.0
600	68.9	64.1	59.8

5.4 Selection efficiency and mass resolution

Applying the previously described selection criteria to generated samples of Higgs decays to ZZ^* at different masses one evaluates the global analysis efficiency to reconstruct the $H \to ZZ^{(*)} \to 4\ell$ final states. Table 5.6 quotes the efficiency on selected Higgs masses. Final state electrons and muons with $p_{\mathrm{T}} > 5.5\,\mathrm{GeV}$ and $|\eta| < 2.7$ were required in the truth events in addition to the $m_Z, m_{Z*} > 12\,\mathrm{GeV}$ requirement.

The resolution of the reconstructed Higgs mass is dominated by experimental performance at low m_H values and by the natural Higgs boson width at high m_H with a full-width at half-maximum of approximately $35\,\mathrm{GeV}$ at $m_H = 400\,\mathrm{GeV}$. Figures 5.7 show the invariant mass distribution for a simulated signal sample with $m_H = 130\,\mathrm{GeV}$ for the four final states. The resolution is obtained from an unbinned maximum likelihood fit of a Gaussian model to the $m_{4\ell}$ distribution.

5.5 Data-driven background estimation

As already mentioned, the control and the estimation of the background contributions is essential in order to achieve high Higgs discovery potential. The QCD background is expected to have negligible effect while the $t\bar{t}$ and Z+jets backgrounds will need to be estimated with data-driven studies. The major contribution will remain the irreducible $ZZ^{(*)}$. The Z+jets background will be handled separately for

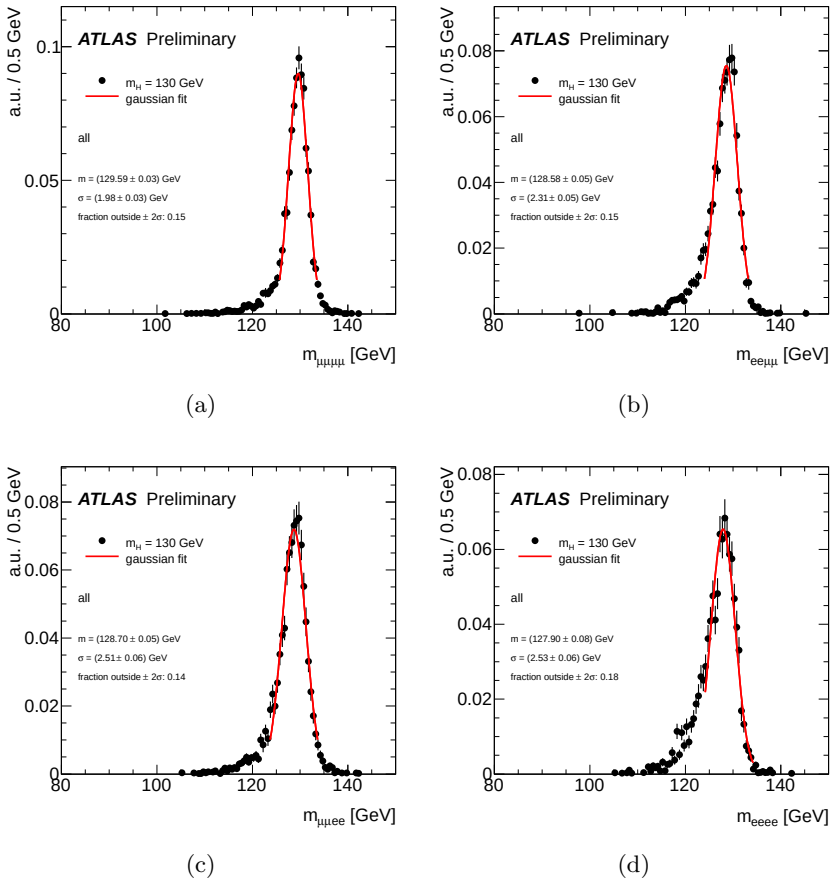

Figure 5.7: The invariant mass distribution for a simulated MC sample with $m_H = 130\,\text{GeV}$, in the (a) 4μ, (b) $2e2\mu$, (c) $2\mu2e$ and (d) $4e$ final state channels is presented. The Gaussian fit to the $m_{4\ell}$ peak is superimposed (red line).

Table 5.7: The number of events in the QCD control region in data are in agreement with Monte Carlo simulation after applying all the selection criteria of the 4ℓ analysis confirming that the QCD jet production has a negligible contribution to the analysis. MC includes $ZZ^{(*)}$, Z+jets and $t\bar{t}$.

Selection	4μ		$2e2\mu$		$4e$	
	Data	MC	Data	MC	Data	MC
Lepton quadruplet, kinematic req., charge requirement, dilepton mass requirements, $\Delta R(\ell,\ell') > 0.10$	13	5.53	6	4.24	10	7.68
Application of additional req. independently						
Tracking isolation on leading dilepton	1	0.43	1	1.43	5	3.76
Tracking and calorimeter isolation on leading dilepton	1	0.36	1	1.33	4	3.37
Tracking isolation on all leptons	0	0.04	1	0.48	1	2.66
Tracking and calorimeter isolation on all dileptons	0	0.04	1	0.39	1	1.47
Isolation on all leptons and d_0 significance	0	0.02	0	0.38	1	1.39

heavy quark jets and for light quarks due to the different source and behavior.

5.5.1 QCD multijet background

In this analysis, where the presence of four isolated leptons with low impact parameter significance is required in the final state, the possible contributions from QCD multijet production is expected to be minimal. However, since the production cross section of these processes are several orders of magnitude higher than the signal and other major backgrounds considered in this channel, it is important to check the contribution in a data-driven method.

The control region for the QCD background study is constructed by selecting events where the primary dilepton is formed by same sign leptons and fulfill all the other criteria of the analysis. One should also take into account the expected number of events in this control region from other processes like $ZZ^{(*)}$, Z+jets and $t\bar{t}$, especially for the electrons where the charge mis-identification rate is non-negligible. From MC, the ratio of same-sign to opposite-sign QCD events is expected to be O(50 %).

The event yields in the QCD control region are summarized in Table 5.7 where the MC includes $ZZ^{(*)}$, Z+jets and $t\bar{t}$. By applying relative tracking isolation selection on the leptons, all QCD-like events are rejected in the leading dilepton mass window. In the $4e$ final state one event survives in data which is compatible with the expectation from $ZZ^{(*)}$, Z+jets and $t\bar{t}$. Thus, no QCD events are expected after the application of the full analysis selection.

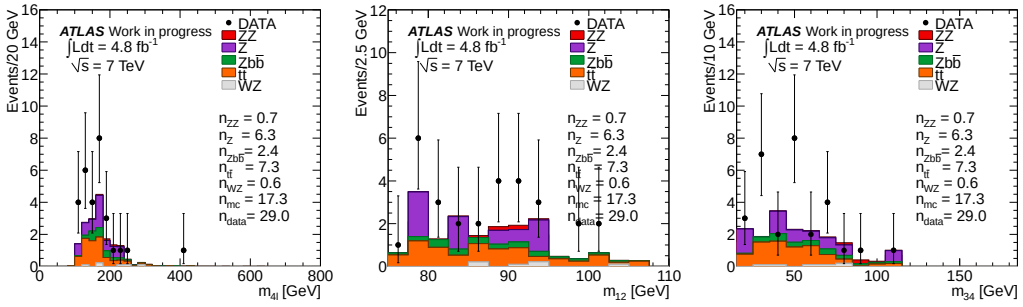

(a) (b) (c)

Figure 5.8: The invariant mass distribution of (a) $m_{4\ell}$, (b) m_{12} and (c) m_{34} are presented for the measured and expected events in the QCD control region after applying the analysis selection criteria with the exception of the isolation and impact parameter requirements.

In Figures 5.8 the four lepton invariant mass distributions are shown for the measured and expected events in the QCD control region after applying all the requirements of the analysis except for the additional selection on isolation and impact parameter. The discrepancy between data and MC provide an estimation of the QCD contribution at this level of the analysis.

5.5.2 $t\bar{t}$ background

In $t\bar{t}$ production each top quark decays mainly to a W boson, which decays leptonically with a branching ratio of about 11 % per lepton flavor, and a b quark which hadronizes resulting to multiple leptons. The b quarks produced are considerably energetic resulting in leptons with relatively high transverse momenta.

The control region for $t\bar{t}$ is constructed by selecting events with an $e\mu$ opposite charge dilepton, with an invariant mass within 15 GeV from m_Z, and two additional same flavor, opposite charge leptons. Events with a same-flavor opposite-charge pair with $m_{\ell\ell}$ within 15 GeV from m_Z are vetoed from the study. The leptons should satisfy the identification criteria of the $H \to 4\ell$ analysis up to the level before the additional lepton selection, requiring the $e\mu$ pair leptons to satisfy $p_{\mathrm{T}} > 20$ GeV. Finally, isolation requirements are only applied on the leptons of the $e\mu$ pair. The invariant mass distributions are presented in Figures 5.9 and 5.10, where agreement between data and MC simulation can be noted. Extrapolation to the signal region for the estimation of the $t\bar{t}$ background can be based on the MC simulation using the transfer factors from the control region to the signal region.

5.5.3 $Z + (QQ \to \mu\mu)$ background

One of the reducible backgrounds are the Z+jets events, contributing in the low mass region ($m_{4\ell} < 2m_Z$). For the $ee/\mu\mu + \mu\mu$ final state the main contribution comes from Z+QQ, where Q refers to heavy flavor jets originating from mainly b but

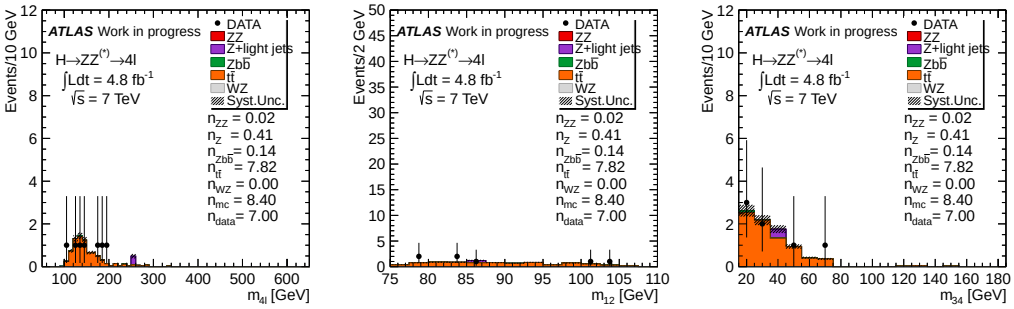

(a) (b) (c)

Figure 5.9: The invariant mass distribution of (a) $m_{4\ell}$, (b) m_{12} and(c) m_{34} are presented for the measured and expected events in the $t\bar{t}$ control region, reconstructing $e\mu+\mu\mu$ events. Only isolation and no impact parameter requirements are applied on the $e\mu$ pair. On the additional lepton pair no isolation or impact parameter criteria are required.

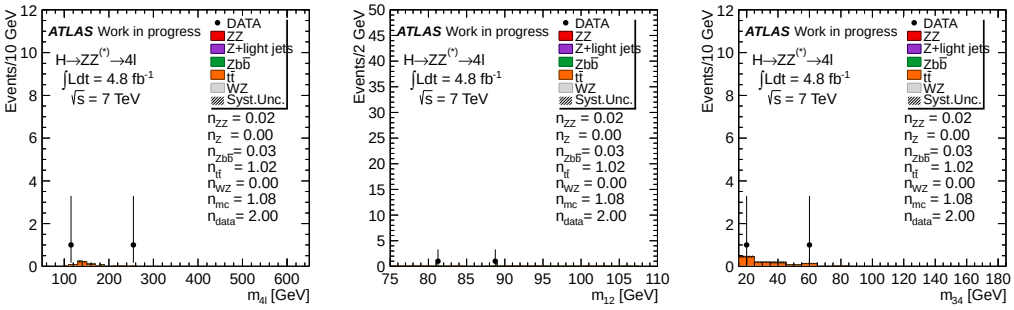

(a) (b) (c)

Figure 5.10: The invariant mass distribution of (a) $m_{4\ell}$, (b) m_{12} and(c) m_{34} are presented for the measured and expected events in the $t\bar{t}$ control region, reconstructing $e\mu+ee$ events. Only isolation and no impact parameter requirements are applied on the $e\mu$ pair. On the additional lepton pair no isolation or impact parameter criteria are required.

Table 5.8: The total number of observed $Z + \mu^+\mu^-$ events with $m_{34} < 72\,\text{GeV}$ are presented along with the expected ones from $ZZ^{(*)}$, WZ and $t\bar{t}$ decays and the data-driven estimated ones from $P(\pi/K \to \mu)$ in light jets. The true $Z(QQ \to \mu^+\mu^-)$ events are also derived for comparison.

	$Z + \mu^+\mu^-$
Observed	34
ZZ	8.2 ± 0.2
WZ	0.2 ± 0.1
$t\bar{t}$	6.4 ± 0.4
Total MC	14.8 ± 0.5
Z+light jets	7 ± 2
Total without $Z(QQ \to \mu^+\mu^-)$	22 ± 2
Estimated $Z(QQ \to \mu^+\mu^-)$	12 ± 7
True $Z(QQ \to \mu^+\mu^-)$	13.3 ± 1.8

also c quarks, usually denoted simply as $Z + b\bar{b}$. The MC prediction of the $Z(QQ \to \mu^+\mu^-)$ background contribution is affected by the theoretical uncertainty on the ZQQ production cross section and by uncertainties related to lepton reconstruction within b-jets. Therefore, the control and estimation of this background can be carried out by selecting suitable control regions where the signal is negligible and the $Z + b\bar{b}$ background is favored. Extrapolating the background yield from the control region to the signal region gives an estimation of this background contribution.

A control region is formed by requiring the selection criteria of the analysis but applying the isolation and impact parameter requirements only on the leading dilepton. For the subleading dilepton two additional muons are requested with an invariant mass $m_{34} > 15\,\text{GeV}$ without applying any isolation and impact parameter selection. In order to suppress the $ZZ^{(*)}$ contribution $m_{34} < 72\,\text{GeV}$ is required. The contribution in this final state are muons from heavy quark decays, $Q \to \mu$, produced in association with a Z boson, muons from $ZZ^{(*)}$, WZ and $t\bar{t}$ decays, and muons from pion and kaon decays in-flight and punch-through hadrons in events with a Z candidate.

The contamination due to pion and kaon decays is estimated through a track weighting procedure and is therefore subtracted. Each charged track, satisfying the analysis selection requirements, is assigned a p_{T}- and η-dependent probability $P(\pi/K \to \mu)$ to be reconstructed as a muon [73]. In events with a Z boson and one additional muon, the probability $P(\pi/K \to \mu)$ is applied to each of the additional tracks in the event. The systematic uncertainty on $P(\pi/K \to \mu)$ is 20 %.

The results are presented in Table 5.8 where the observed events are quoted along with the expected contributions from $ZZ^{(*)}$, WZ and $t\bar{t}$. The data-driven estimation for the muons from pion and kaon decays in-flight are denoted as Z+light jets. The $Z(QQ \to \mu^+\mu^-)$ contribution is then derived by subtracting all the expected

Table 5.9: The efficiency of the isolation and impact parameter criteria on the additional muon of the $Z + \mu$ events are shown.

	Data (%)	MC (%)
Norm. Track isolation < 0.15	31.9 ± 0.9	32.6 ± 0.24
Norm. Calo. isolation < 0.3	43.0 ± 0.8	44.01 ± 0.23
All isolation requirements	25.0 ± 1.0	25.3 ± 0.25
$d_0/\sigma_{d_0} < 3.5$	82.6 ± 0.5	81.8 ± 0.13
All requirements	20 ± 1	20.3 ± 0.4

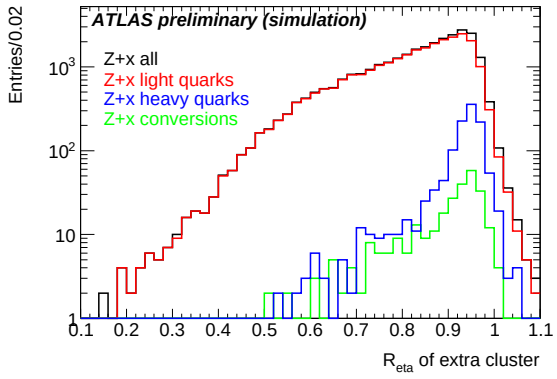

Figure 5.11: The R_η shower shape distributions for electron candidates, after track and electromagnetic cluster matching, in $Z + X$ events are shown including light quark, heavy quark and conversion contributions. These candidates are not associated with the Z boson.

contributions from the observed yield. The estimation is in agreement with the one from the MC simulation.

A check on the efficiency of the additional lepton selection on background-like muons is also studied by reconstructing $Z + \mu$ events. The results are presented in Table 5.9 for both data and MC and good agreement is noted.

5.5.4 $Z + (XX \to ee)$ background

For the $ee/\mu\mu + ee$ final state the main Z+jets contribution comes from light jets where the additional electrons can originate from hadrons in jets faking an electron denoted by j, photons, e.g. from π_0 decays, denoted by γ, or from heavy quark mesons decaying semi-leptonically denoted by Q. For this study, a control region is chosen composed by a reconstructed Z and two reconstructed Loose electron candidates. Then, the relative composition of the background sources for the Loose electron candidates is extracted and extrapolation to the signal region is performed by using the efficiency of each component predicted by simulation [74].

The first step is to extract the yields in the control region. In the case of a

Table 5.10: The predicted $Z + qX$ yields at different cut levels for the additional electrons in reconstructed $Z \to \ell\ell$ events using the R_η method. The yields are shown separately for the $4e$ and $2\mu 2e$ final states. The quoted uncertainties are statistical. The systematic uncertainties of these predictions are of the order of 20 %.

Selection level	Predicted $ZjX \to 4e$	Predicted $ZjX \to 2\mu 2e$	Predicted
Loose, m_{34} >15 GeV	20 ± 4	32 ± 6	
Loose, final m_{34} selection	11 ± 3	12 ± 3	
Loose, final selection	3 ± 2	1.7 ± 0.7	

subleading electron pair, the main contribution for $Z + 2e$(Loose) are the $Z + jX$ events. Since the MC is not reliable as far as the description of fake electrons is concerned, a data-driven method to normalize the expected $Z + jX$ events is used. In order to estimate this component, $Z + ee$ events are selected without the Loose quality requirement for the additional electrons. In order to select events dominated by jets, the R_η variable is used, which is defined as the ratio of the energy sum in 3×7 ($\eta\times\phi$) over 7×7 cells in the calorimeter. Figure 5.11 shows the simulated distribution of the R_η variable for electron candidates (X) in $Z + X$ events, and separately the contribution from light quarks, heavy quarks and photon conversions. One can thus acquire the normalization for the Z inclusive MC sample (N^{CR}_{ZjX}) to the data using the region $R_\eta < 0.7$ ($N^{Data}_{R_\eta<0.7}$, $N^{MC}_{R_\eta<0.7}$) and then, considering the scaled MC, predict the $Z + jX$ yields after Loose quality requirement using the efficiency ϵ_{MC}(Loose). The predicted $Z + jX$ yields are given by the following formula:

$$N_{jX}(\text{Loose}) = N^{CR}_{ZjX} \times \frac{N^{Data}_{R_\eta<0.7}}{N^{MC}_{R_\eta<0.7}} \times \epsilon_{MC}(\text{Loose}), \tag{5.1}$$

In Table 5.10 the predictions for the above method are quoted for the data, separately for the $4e$ and $2\mu 2e$ final states, and at different cut levels. From simulation, 19 $Z + jX$ events ($ee + XX = 8 \pm 2$, $\mu\mu + XX = 11 \pm 3$) are expected at the level of the final m_{34} selection and is to be compared to 23 events predicted in Table 5.10. A scale factor of 1.2 ± 0.2 is derived and used in order to normalize the MC prediction in the control region.

The total systematic uncertainty of these expectations is of the order of 20 %, arising mainly from the variation of the shower-shapes ($\simeq 15$ %), the available statistics in the normalization region ($\simeq 1.5$ %) and the intrinsic accuracy of the normalization method (< 3 %).

The next step is the break-down of the composition of XX. The expected $Z + XX$ composition after the Loose requirement and final m_{34} selection is divided into the $4e$ and $2\mu 2e$ final states, as shown in Table 5.11. The leading dilepton is firstly selected using the analysis criteria and then truth matching is applied on the additional leptons.

The last step is to use the appropriate efficiencies and extrapolate to the signal region. A method which is based on pixel and silicon hits requirements is used to

Table 5.11: The $Z + XX$ composition is quoted after the Loose requirement and final m_{34} selection.

[%]	$+jj$	$+j\gamma$	$+ej$	$+\gamma\gamma$	$+jQ$	$+\gamma Q$	$+\gamma e$
$Z \to ee$	25	25	21	7	7	7	7
$Z \to \mu\mu$	35	57	-	8	-	-	-

Table 5.12: Percentage of jet-like and photon-like additional electron candidates in $Z + ee$ events based on Pixel and B-Layer requirements. Results are provided before and after the application of the isolation and impact parameter significance requirements.

	Before requirements (%)	After requirements (%)
	Both Jets	
Data	65 ± 9	73 ± 25
Z+jets MC	57 ± 6	58 ± 13
	Both Conversions	
Data	1.0 ± 1.0	0.0 ± 7
Z+jets MC	0.8 ± 0.2	0.0 ± 7
	Jet - Conversion	
Data	34 ± 8	27 ± 15
Z+jets MC	42 ± 6	42 ± 20

Table 5.13: The efficiency of the isolation and impact parameter criteria are presented when applied to the jet-like additional electron of $Z + e$ events.

	Data (%)	Monte Carlo (%)	Truth light Hadrons (%)
Norm. Track isolation < 0.15	48.3 ± 0.6	48.57 ± 0.23	
Norm. Calo. isolation < 0.3	47.4 ± 0.6	46.91 ± 0.22	
All isolation requirements	32.4 ± 0.7	31.80 ± 0.26	
$d_0/\sigma_{d_0} < 6$	91.4 ± 0.3	92.92 ± 0.10	
All requirements	28.7 ± 0.7	28.5 ± 0.3	26 ± 2

Table 5.14: The efficiency of the isolation and impact parameter criteria are presented when applied to the photon-like additional electron of $Z + e$ events.

	Data (%)	Monte Carlo (%)	Truth photons (%)
Norm. Track isolation < 0.15	71.6 ± 0.7	68.2 ± 0.4	
Norm. Calo. isolation < 0.3	59.4 ± 0.9	59.88 ± 0.5	
All isolation requirements	50.4 ± 1.0	48.98 ± 0.6	
$d_0/\sigma_{d_0} < 6$	67.7 ± 0.8	62.12 ± 0.4	
All requirements	34.1 ± 1.1	33.9 ± 0.3	34.5 ± 1.3

Table 5.15: The efficiency of the isolation and impact parameter criteria are presented when applied to the additional electron of $Z + e$ events.

	Data (%)	Monte Carlo (%)
Norm. Track isolation < 0.15	54.6 ± 0.5	54.3 ± 0.3
Norm. Calo. isolation < 0.3	50.6 ± 0.5	50.0 ± 0.3
All isolation requirements	37.3 ± 0.6	36.5 ± 0.3
$d_0/\sigma_{d_0} < 6$	84.5 ± 0.3	85.6 ± 0.2
All requirements	29.9 ± 0.6	30.4 ± 0.4

separate jet-like and photon-like electron candidates. Jets are expected to have B-Layer hits or, in cases where the B-layer module is dead, at least an extra Pixel hit in addition to that of the Loose quality definition. In this selection, jets include all non-photon contribution. The purity, estimated using Z inclusive MC simulation, is 92.3 % for the jet category and 90.7 % for the photon category.

Table 5.12 presents the composition of the additional electrons in $Z + ee$ events using the definition above before and after the isolation and impact parameter significance selection. To suppress the $ZZ^{(*)}$ background, $m_{34} < 72\,\text{GeV}$ is applied. In Tables 5.13 and 5.14 the efficiencies of the tracking and calorimetric isolation and of the impact parameter significance are quoted for the two categories using $Z + e$ events. The results both in data and MC are in agreement with the ones extracted from MC truth. In Table 5.15 the efficiencies are quoted for the additional electron in the $Z + e$ events without taking into account the categorization.

Taking into account all the calculated efficiencies and purities it is possible to extrapolate to the $H \to 4\ell$ signal region. The final estimates are 1.5 ± 0.7 and 1.2 ± 0.5 events for the $4e$ and $2\mu 2e$ final states, respectively.

5.6 Data and simulation comparison in control regions

In order to check that the estimation of the background processes is well controlled, control regions are used with a four-lepton final state selected as in the standard

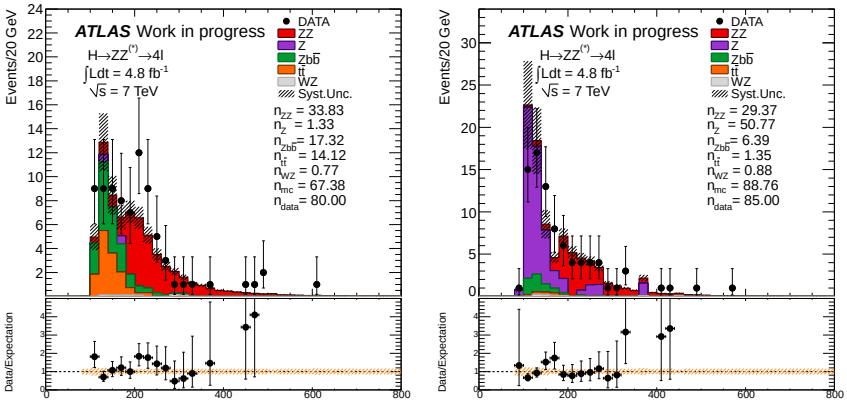

(a) $Z + \mu\mu \quad m_{4\ell}$

(b) $Z + ee \quad m_{4\ell}$

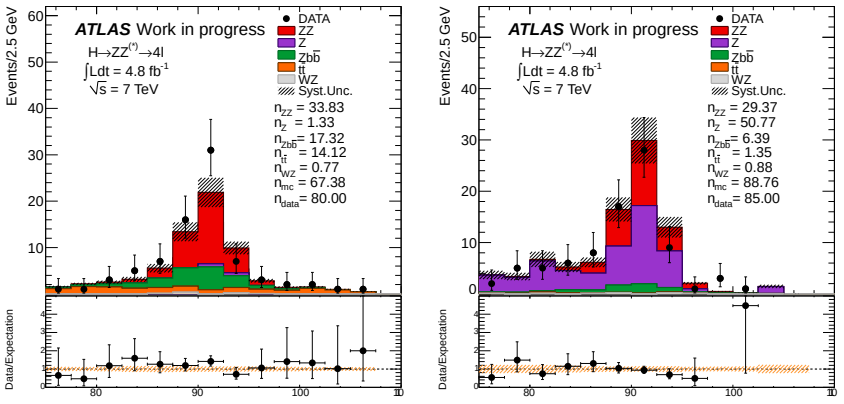

(c) $Z + \mu\mu \quad m_{12}$

(d) $Z + ee \quad m_{12}$

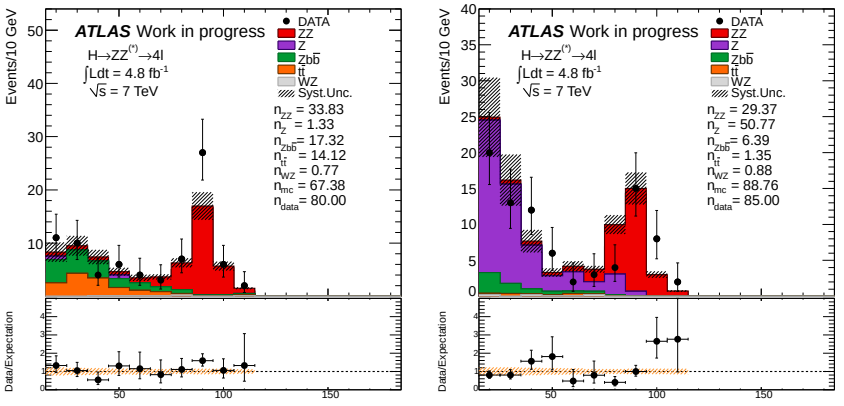

(e) $Z + \mu\mu \quad m_{34}$

(f) $Z + ee \quad m_{34}$

Figure 5.12: The invariant mass distributions are shown when applying the analysis selection but relaxing the charge, isolation and impact parameter requirements on the subleading dilepton.

analysis, but relaxing the additional lepton requirements on isolation and impact parameter significance and the charge requirement on the subleading dilepton. For all the plots in this section the ZjX contribution in simulation is scaled by ~ 1.2 as indicated in Section 5.5.4.

Relaxed selection control region

The invariant mass distributions for data and the simulation background samples are shown in Figures 5.12 for $\mu\mu/ee+\mu\mu$ and $\mu\mu/ee+ee$ in this control region, where the selection of the standard analysis is applied apart from the impact parameter selection on the leading dilepton, and the charge, isolation and impact parameter requirements for the subleading dilepton. The ratio of data over MC simulation is also added in the bottom part of the plots. In this region, the irreducible contribution from the $ZZ^{(*)}$ background is visible as well as the main reducible background contributions, $Zb\bar{b}$ for the $\mu\mu/ee + \mu\mu$ and Z+jets for the $\mu\mu/ee + ee$ final state. The data are described well by the MC simulation.

Inverted impact parameter criteria control region

Inverting the requirement on the transverse impact parameter significance selects leptons coming from displaced vertices, such as muons coming from b hadronization. In this control region the selection described in the previous paragraph is used and in addition, the impact parameter requirement is inverted for the subleading dilepton. The effect of this selection on data and the various MC samples can be seen in Figures 5.13. The number of events in the data and the expected ones from the various backgrounds are quoted on the plots. No significant contribution of the $Z + ee$ background is shown in this control region and in the $Z + \mu\mu$ case the data are found in agreement with the expectation.

Inverted isolation criteria control region

In Figures 5.14 the requirements of the relaxed selection control region are applied. In addition the standard selection for the impact parameter significance is required on the subleading dilepton while the tracking isolation is inverted. This selection favors non-isolated leptons as the ones coming from jets and jets faking leptons. General agreement is observed between data and Monte Carlo.

5.7 Results of event selection

Applying the selection criteria of the analysis as described in Section 5.3 on the 2011 7 TeV data, corresponding to an integrated luminosity of $4.8\,\text{fb}^{-1}$, 71 candidate events are selected presented in Tables 5.17, 5.18 and 5.16 for the three different final states, 4μ, $2e2\mu$ and $4e$, respectively. The corresponding expected events from the background processes are 62 ± 9 events.

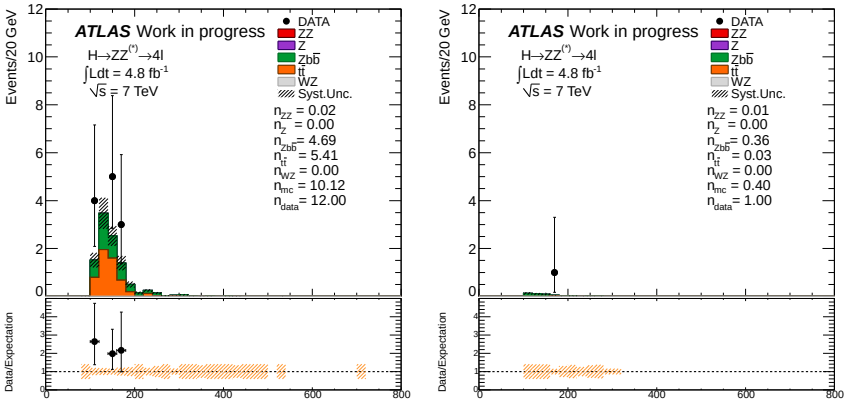

(a) $Z + \mu\mu \quad m_{4\ell}$

(b) $Z + ee \quad m_{4\ell}$

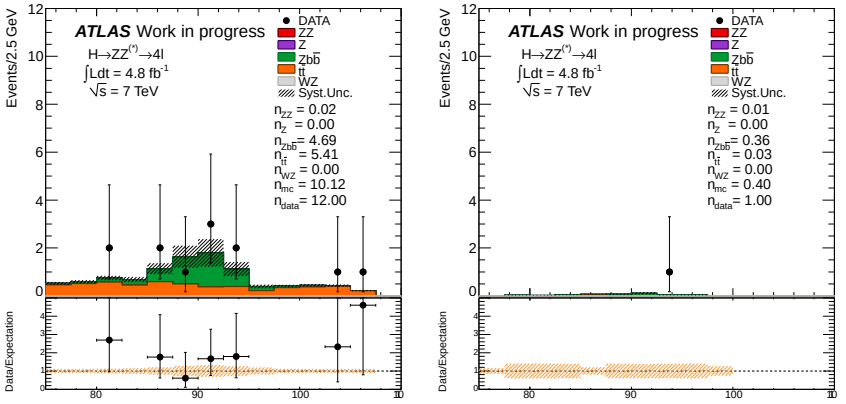

(c) $Z + \mu\mu \quad m_{12}$

(d) $Z + ee \quad m_{12}$

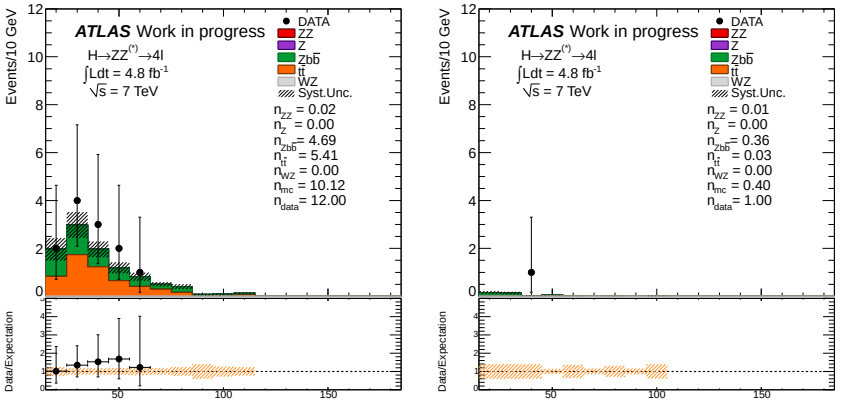

(e) $Z + \mu\mu \quad m_{34}$

(f) $Z + ee \quad m_{34}$

Figure 5.13: The invariant mass distributions are shown when applying the analysis selection but relaxing the charge and isolation requirements while inverting the impact parameter requirement on the subleading dilepton.

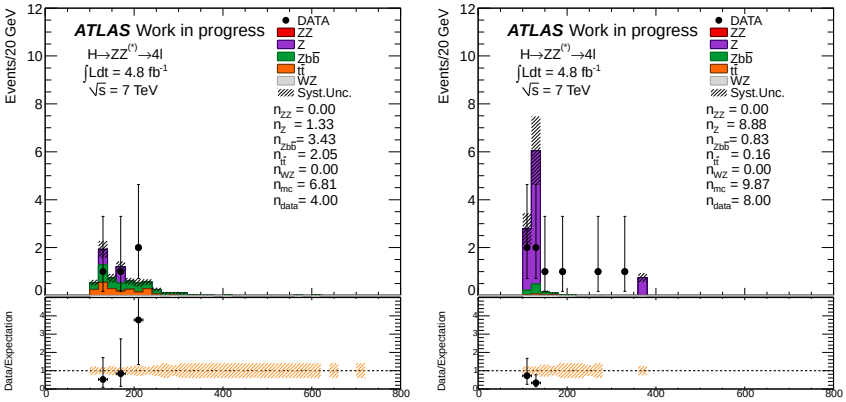

(a) $Z + \mu\mu \quad m_{4\ell}$

(b) $Z + ee \quad m_{4\ell}$

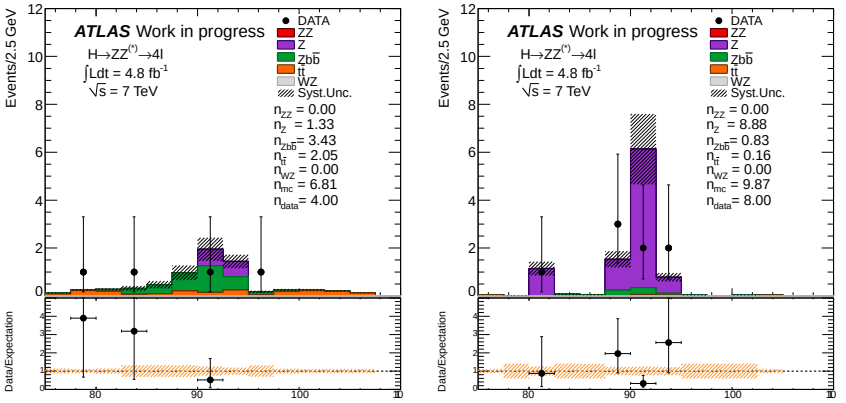

(c) $Z + \mu\mu \quad m_{12}$

(d) $Z + ee \quad m_{12}$

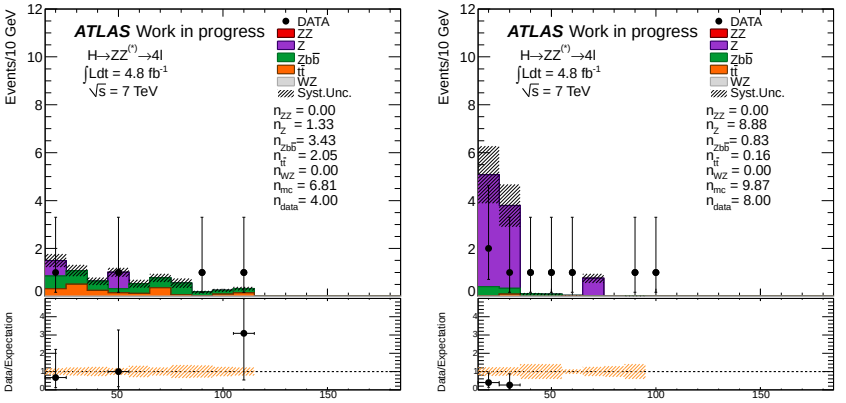

(e) $Z + \mu\mu \quad m_{34}$

(f) $Z + ee \quad m_{34}$

Figure 5.14: The invariant mass distributions are shown when applying the analysis selection but relaxing the charge requirement while inverting the isolation requirement on the subleading dilepton. The impact parameter requirements are only applied on the subleading dilepton.

Table 5.16: List of the $4e$ candidates passing the full selection using $4.9\,\text{fb}^{-1}$ of 7 TeV data.

N	Run Number	Event Number	LB	$m_{4\ell}$ [GeV]	m_{12} [GeV]	m_{34} [GeV]
1	182787	35518831	265	196.0	93.2	85.8
2	183216	75692579	371	270.3	85.0	111.5
3	184022	20046902	320	245.4	92.2	99.8
4	184022	78541915	625	496.1	92.5	85.5
5	186216	10253640	49	264.4	91.1	90.1
6	186216	36894463	176	157.6	81.3	36.1
7	186729	203362752	1004	200.4	89.5	84.4
8	186934	65787798	649	230.7	90.0	87.8
9	187453	34960141	622	226.0	90.2	93.8
10	187552	3744932	16	331.2	91.1	87.0
11	187763	83732606	528	172.0	89.8	76.9
12	189483	33468656	145	238.4	86.7	68.4
13	189751	51800361	355	184.9	90.5	88.6
14	190933	99272087	804	426.2	91.6	94.2
15	191138	17388332	70	194.6	90.5	100.2
16	191139	5871977	305	202.3	84.3	99.2
17	191635	2200900	568	315.0	89.5	102.0

Table 5.17: List of the 4μ candidates passing the full selection using $4.8\,\text{fb}^{-1}$ of 7 TeV data.

N	Run Number	Event Number	LB	$m_{4\ell}$ [GeV]	m_{12} [GeV]	m_{34} [GeV]
1	182284	91584073	745	277.7	90.9	98.3
2	182486	33852510	282	208.6	83.8	76.9
3	182766	5404925	213	243.0	91.1	85.3
4	183003	44433120	385	222.2	93.8	100.6
5	183003	121099951	723	603.5	85.9	99.7
6	183391	19834577	303	204.9	97.5	82.5
7	183426	47756740	317	455.3	89.6	94.3
8	183602	282919	20	239.7	89.2	88.0
9	184130	194694606	1304	182.9	93.3	76.8
10	186156	65491657	381	234.4	89.9	86.3
11	187219	88203394	476	372.2	89.1	94.0
12	189207	79774710	330	250.7	89.7	88.0
13	189207	81313827	338	171.9	83.9	62.1
14	189280	82801561	439	208.7	87.9	85.3
15	189280	128083498	640	220.6	91.1	92.6
16	189280	143576946	713	124.6	89.7	24.6
17	189561	20659041	117	207.3	91.9	73.4
18	189693	10714212	266	209.6	92.2	87.4
19	189822	75634934	460	217.0	102.4	71.6
20	190116	60445481	341	199.8	91.9	88.8
21	190300	60554334	325	145.8	94.3	29.7
22	190872	52781235	212	264.2	91.0	91.5
23	191426	60906769	447	225.5	91.9	92.2
24	191676	1888359	380	487.4	92.4	96.5

Table 5.18: List of the $2e2\mu$ candidates passing the full selection using $4.8\,\mathrm{fb}^{-1}$ of 7 TeV data.

N	Run Number	Event Number	LB	$m_{4\ell}$ [GeV]	m_{12} [GeV]	m_{34} [GeV]
1	179710	25946709	422	234.5	90.5	92.8
2	180636	71391739	407	242.9	90.9	86.1
3	180710	37143864	561	247.3	92.6	94.2
4	182747	63217197	281	209.2	85.6	85.5
5	182796	74566644	413	124.3	76.8	45.7
6	183407	136901836	930	188.9	90.0	93.3
7	183426	50303812	330	251.9	84.4	104.8
8	183462	75344317	798	486.8	92.4	86.9
9	186399	14250520	331	325.1	91.3	93.1
10	186877	12509901	232	191.0	90.1	94.0
11	186877	84622334	602	123.6	89.3	30.0
12	186923	96974859	507	238.7	86.0	82.8
13	187014	105211056	963	292.2	91.4	89.7
14	189242	7233912	57	158.2	102.4	46.9
15	189483	1021987	10	460.1	92.5	105.1
16	189561	105481981	570	214.2	88.6	87.1
17	189719	37988693	382	314.8	89.1	88.6
18	189781	8619753	57	568.1	91.7	90.1
19	190046	8638208	105	267.0	87.8	87.2
20	190300	17344710	114	321.7	91.5	92.0
21	190878	50034828	274	210.9	90.2	92.2
22	190878	57044890	309	200.2	91.5	92.8
23	190975	20471852	272	281.4	90.6	89.1
24	190975	62905396	449	268.2	90.2	101.9
25	191138	15762515	64	199.4	88.1	80.2
26	191150	5742674	170	244.1	92.21	92.28
27	191150	45707611	308	222.34	90.63	97.19
28	191190	76273161	513	218.6	87.9	87.9
29	191218	1072214	9	249.71	87.1	93.16
30	191428	25718643	213	236.4	92.1	97.8

Table 5.19: The expected number of signal and background events, with their systematic uncertainty, separated into "low mass" ($m_{4\ell} < 180$ GeV) and "high mass" ($m_{4\ell} \geq 180$ GeV) regions. The observed numbers of events are also presented.

	$\mu\mu\mu\mu$		$ee\mu\mu$		$eeee$	
	Low mass	High mass	Low mass	High mass	Low mass	High mass
Int. Luminosity	$4.8\,\text{fb}^{-1}$		$4.8\,\text{fb}^{-1}$		$4.9\,\text{fb}^{-1}$	
$ZZ(*)$	2.1 ± 0.3	16.3 ± 2.4	2.8 ± 0.6	25.2 ± 3.8	1.2 ± 0.3	10.4 ± 1.5
Z+jets and $t\bar{t}$	0.16 ± 0.06	0.02 ± 0.01	1.4 ± 0.5	0.17 ± 0.08	1.6 ± 0.7	0.18 ± 0.08
Total Background	2.2 ± 0.3	16.3 ± 2.4	4.3 ± 0.8	25.4 ± 3.8	2.8 ± 0.8	10.6 ± 1.5
Data	3	21	3	27	2	15
$m_H = 130$ GeV	1.00 ± 0.17		1.22 ± 0.21		0.43 ± 0.08	
$m_H = 150$ GeV	2.10 ± 0.40		2.90 ± 0.40		1.12 ± 0.18	
$m_H = 200$ GeV		4.9 ± 0.7		7.7 ± 1.0		3.1 ± 0.4
$m_H = 400$ GeV		2.0 ± 0.3		3.3 ± 0.5		1.49 ± 0.21
$m_H = 600$ GeV		0.34 ± 0.04		0.62 ± 0.10		0.30 ± 0.06

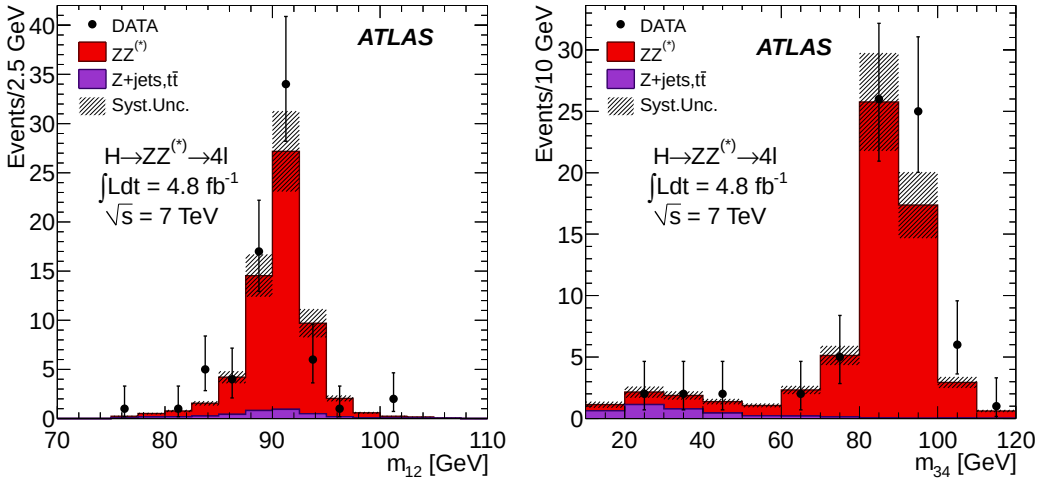

(a) (b)

Figure 5.15: The invariant mass distributions for (a) m_{12} and (b) m_{34} are shown for the 7 TeV candidates. All plots show comparisons with background expectation from the dominant ZZ^* and the sum of $t\bar{t}$, $Zb\bar{b}$ and Z+jets processes. Error bars represent 68.3 % central confidence intervals.

As already explained, particular interest is focused in the "low mass" region defined as $m_{4\ell} < 180$ GeV. In Table 5.19 the observed and expected number of events are quoted for the different final states in the low ($m_{4\ell} < 180$ GeV) and high ($m_{4\ell} \geq 180$ GeV) mass region separately. The expected numbers from various m_H signal samples are also added.

In Figures 5.15 the invariant mas distributions for m_{12} and m_{34} are shown. The expected background is also added in two components: the dominant ZZ^* and the sum of the $t\bar{t}$, $Zb\bar{b}$ and Z+jets backgrounds. In Figures 5.16 the m_{4l} distribution of the candidates is superimposed to the total background expectation. The Higgs signal corresponding to various m_H is also added. In Figures 5.17 the three final state channels of the analysis are presented separately.

Figure 5.18 shows the η and p_{T} distributions of the leptons in the 71 candidates. In Figure 5.19(a)-(d) the p_{T} distributions of the leptons, from the highest-p_{T} to the lowest-p_{T} one, are presented. In Figure 5.20 the distribution of m_{12} versus m_{34} for the selected candidates together with the background expectation is shown.

5.8 Systematic uncertainties

As in every analysis an important component is to extract the systematic uncertainties either theoretical, related to the cross sections used, or experimental, related to the methods implemented in the measurement. All the systematic uncertainties taken into account in the $H \to 4\ell$ analysis are summarized below.

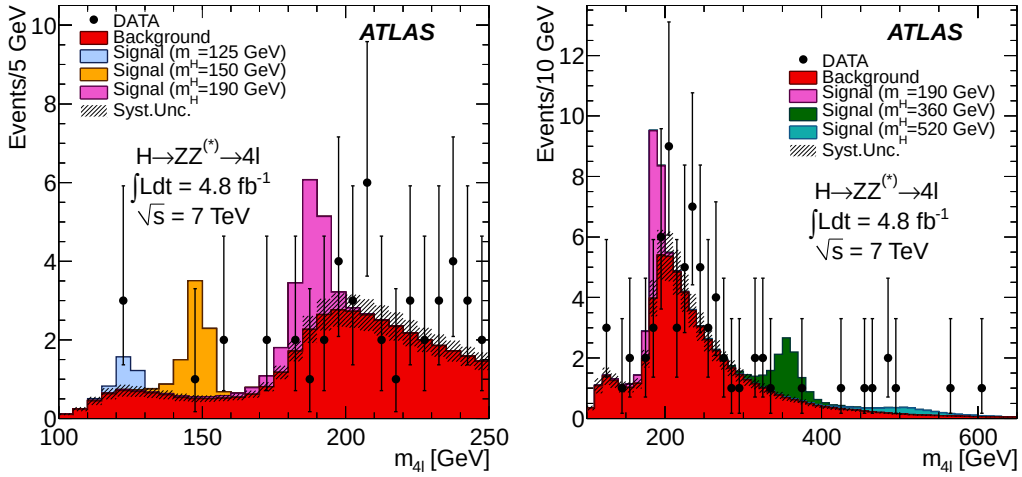

(a) (b)

Figure 5.16: The $m_{4\ell}$ distribution of the selected candidates is compared to the background expectation (a) in the low mass region and (b) in the whole mass spectrum of the analysis. Error bars represent 68.3 % central confidence intervals. The signal expectation for several m_H hypotheses is also shown.

5.8.1 Theoretical uncertainties

The theoretical uncertainties concern the cross section calculation both of the signal and the background processes.

Cross sections of the Higgs boson production

The Higgs boson production cross sections have been studied extensively by the LHC Higgs cross section working group. All processes for Higgs production are used, $gg \to H$, $qq \to H$ and $qq \to W/ZH$, and their uncertainties are applied to the signal samples for all mass points. The uncertainty in the production cross section due to the choice of QCD scale is $^{+12}_{-8}$ % for the gluon fusion process, and ± 1 % for the vector-boson fusion, associated WH production, and associated ZH production processes [46]. The uncertainty in the production cross section due to the parton distribution function (PDF) and α_s is ± 8 % for gluon initiated processes and ± 4 % for quark initiated processes [75–79]. Recent studies [80–82] have indicated that effects related to off-shell Higgs boson production and interference with other SM processes may become sizable at high masses ($m_H > 400$ GeV) considered in this search. In the absence of a full calculation, a conservative estimate of the possible size of such effects was included as a signal normalization systematic uncertainty following a parameterization as a function of m_H: $150\,\% \times (m_H[\mathrm{TeV}])^3$, for $m_H \geq 300$ GeV.

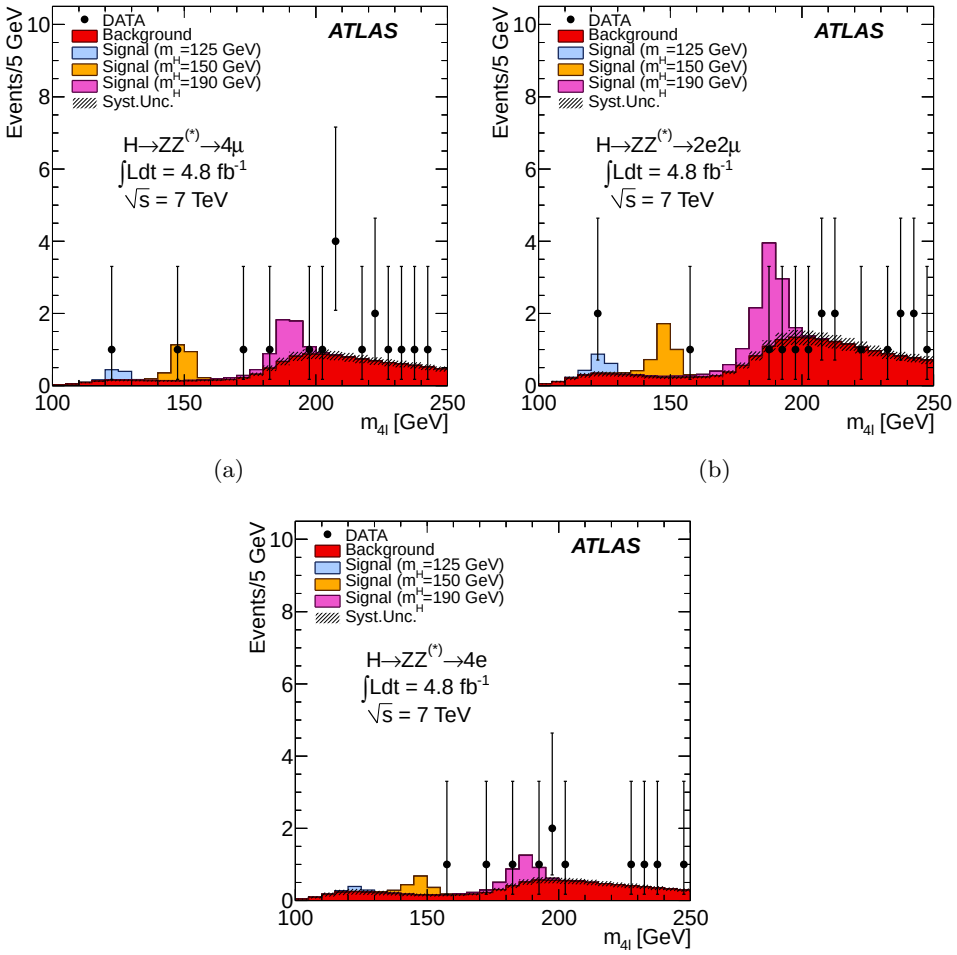

(a) (b)

(c)

Figure 5.17: The $m_{4\ell}$ distributions of the selected candidates are compared to the background expectation in the (a) 4μ, (b) $2e2\mu$ and (c) $4e$ final state channels. Error bars represent 68.3 % central confidence intervals.

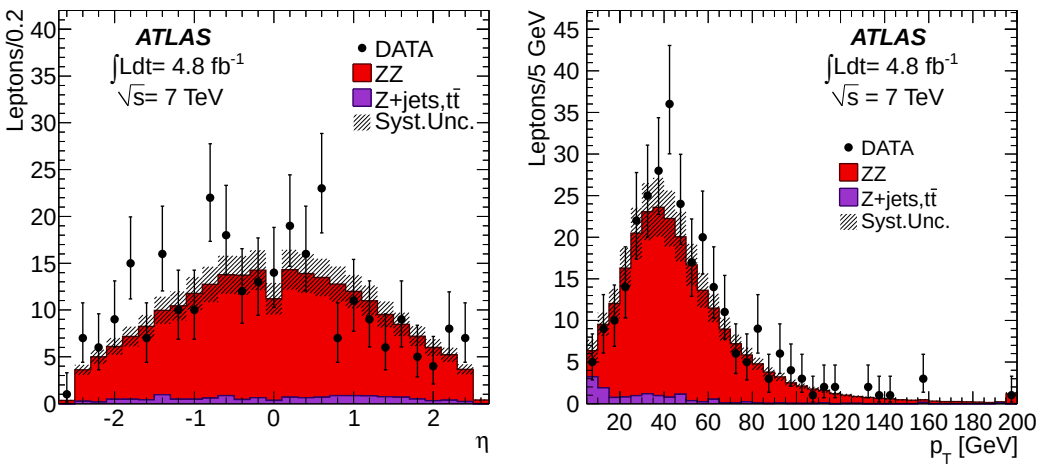

(a) (b)

Figure 5.18: The (a) η and (b) p_{T} distributions are shown for the leptons of the 71 candidates surviving the selection criteria. The expected background distributions are also shown.

Cross sections of background processes

An uncertainty of $\pm 5\,\%$ has been assigned to the $ZZ^{(*)}$ background due to the QCD scale uncertainty and $\pm 4\,\%$ ($\pm 8\,\%$) due to the PDF and α_s uncertainties for quark-initiated (gluon-initiated) processes. An additional theoretical uncertainty of $\pm 10\,\%$ on the inclusive $ZZ^{(*)}$ cross section is conservatively included due to the missing higher-order QCD corrections for the gluon-initiated process, and a correlated uncertainty on the predicted $m_{ZZ^{(*)}}$ spectrum is estimated by varying the gluon-initiated contribution by $100\,\%$ [83]. The effect of the QCD scale uncertainty on the $t\bar{t}$ cross section is $^{+4}_{-9}\,\%$, while the effect of PDF and α_s uncertainties is $\pm 7\,\%$.

5.8.2 Experimental uncertainties

The experimental uncertainties concern the calculation of the integrated luminosity, the data-driven methods used for the background estimation, lepton reconstruction and identification and trigger efficiency.

Luminosity

The integrated luminosity considered in the analysis is estimated with an overall normalization uncertainty of $3.9\,\%$. This uncertainty is only applied to MC samples for which the normalization is not obtained from the data. When it is applied, this systematic is assumed to be correlated across samples.

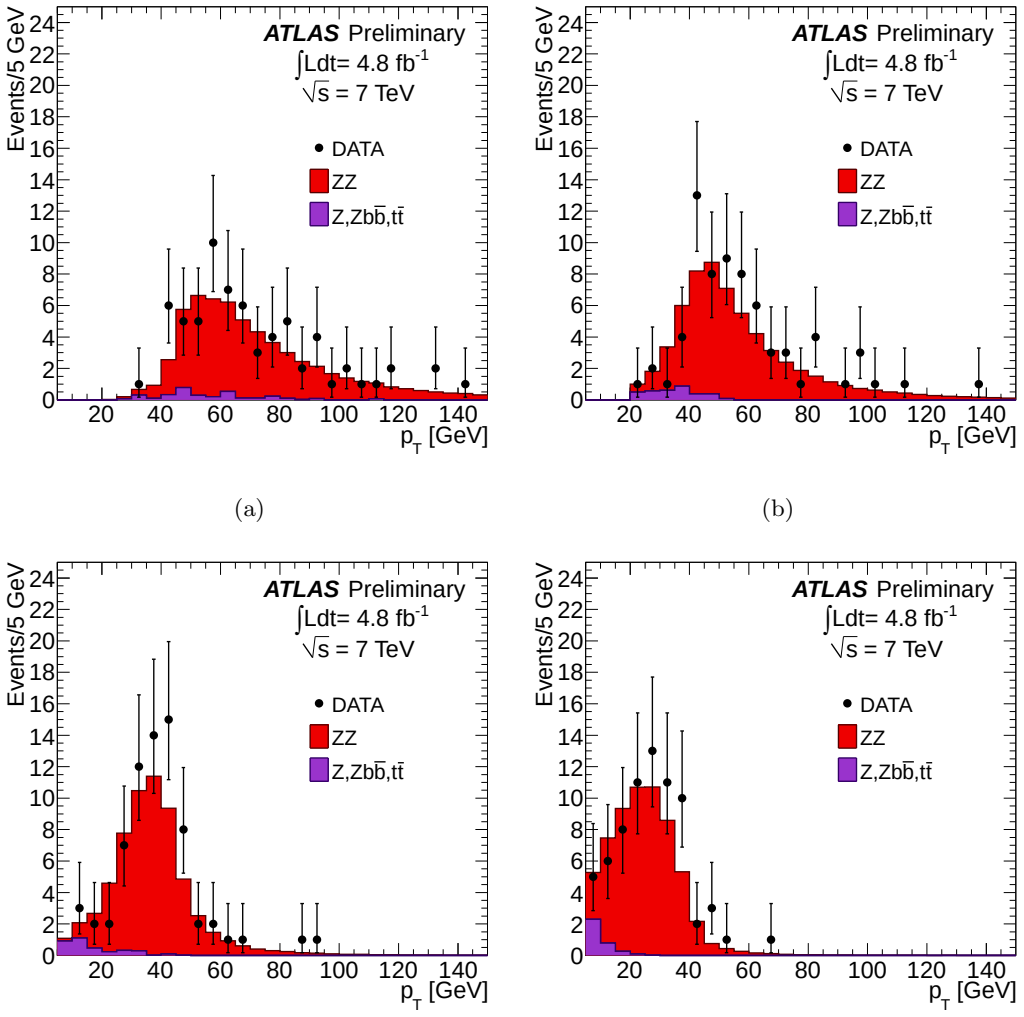

Figure 5.19: The p_T distribution is presented for the (a) highest-p_T, (b) second highest-p_T, (c) third highest-p_T and (c) lowest-p_T leptons of the 71 candidates surviving the selection criteria. The expected background distributions are also shown.

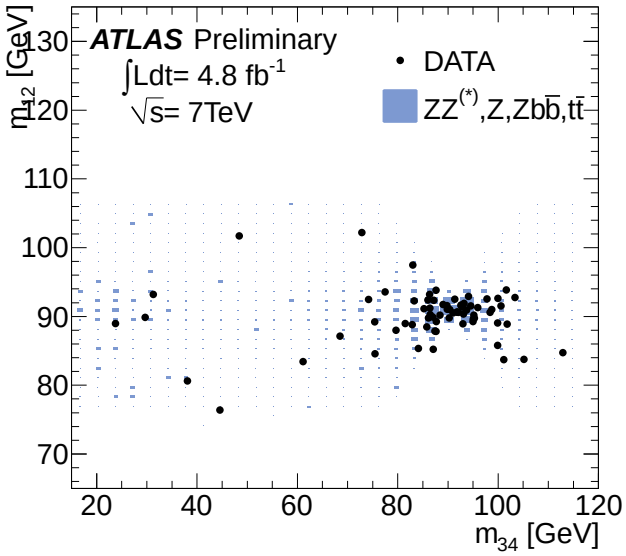

Figure 5.20: The invariant mass distribution m_{12} with respect to m_{34} for the selected candidates is presented. Comparison with background expectation is shown for the sum of the dominant $ZZ^{(*)}$, the $t\bar{t}$, the $Zb\bar{b}$ and the Z+jets processes.

Background processes

An uncertainty of 45 % and 40 % is assigned on the normalization of the Z+light-flavor-jets and $Zb\bar{b}$ samples, respectively, to account for the uncertainty on their data-driven estimation. This is coming from the statistical uncertainty in the control region yields and the extrapolation to the signal region based on the MC simulation. There is an additional uncertainty in the $t\bar{t}$ selection efficiency, estimated to be 10 %, which is negligible in comparison with the uncertainties on the main backgrounds.

Electron Reconstruction and Identification

The effect of the energy resolution in the final state is negligible, while the electron energy scale uncertainty results in an uncertainty of less than 0.6 % (0.3 %) on the mass scale of the $m_{4\ell}$ distribution for the $4e$ ($2e2\mu$) channel. The uncertainty in the electron efficiency results in a relative acceptance uncertainty of 2.3 % (1.6 %) for the $4e$ ($2e2\mu$) channel at $m_{4\ell} = 600\,\text{GeV}$ and reaches 8.0 % (4.1 %) at $m_{4\ell} = 110\,\text{GeV}$.

Muon Reconstruction and Identification

The effect of muon momentum resolution and scale uncertainties are found to be negligible. The uncertainty on the identification efficiency of muons is estimated to be between 0.5 % and 1 % for the phase space of interest.

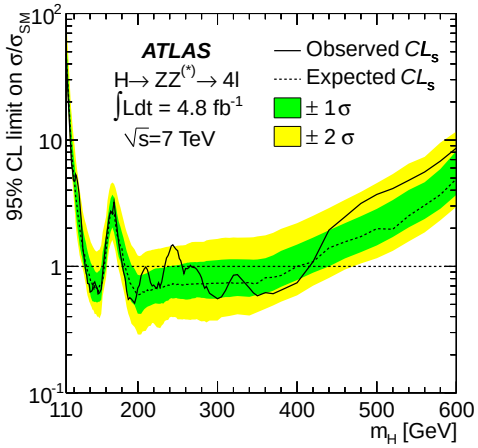

Figure 5.21: The expected and observed 95 % CL upper limits on the Standard Model Higgs boson production cross section are presented as a function of m_H, divided by the expected SM Higgs boson cross section. The 1σ and 2σ fluctuations are also included.

Trigger

Owing to the high lepton trigger efficiency and the presence of multiple high p_{T} leptons in the final state, a trigger efficiency very close to 100 % is achieved, while the corresponding uncertainties are found to be negligible.

5.9 Exclusion limits on $H \to ZZ^{(*)} \to 4\ell$ and statistical interpretation

As detailed in Section 5.7, 71 candidates were found in 2011 7 TeV data of 4.8 fb^{-1} integrated luminosity, which can be found in Tables 5.16 5.19 along with the background expectation and the expected signal for various m_H hypotheses. The corresponding total expected events from background processes are 62 ± 9.

The median expected and observed 95 % CL upper limit on the Standard Model Higgs boson production cross section as a function of the Higgs boson mass is presented in Figure 5.21 and in Figures 5.22 for the low and high Higgs mass regions separately. The dashed line corresponds to the expected and the solid line to the observed limit. The 1σ and 2σ fluctuations are also indicated. The upper limits are derived using the CL_s modified frequentist formalism [84] with the profile likelihood test statistic [85] and calculated using RooStats [86]. The test statistic is evaluated with a binned maximum-likelihood fit of signal and background models to the observed $m_{4\ell}$ distribution.

The SM Higgs boson is excluded at 95 % CL in the mass ranges $134 - 156$ GeV, $182 - 233$ GeV, $256 - 265$ GeV and $268 - 415$ GeV. The expected exclusion ranges are $136 - 157$ GeV and $184 - 400$ GeV.

The p_0-value is the probability of upward fluctuations in the background as high

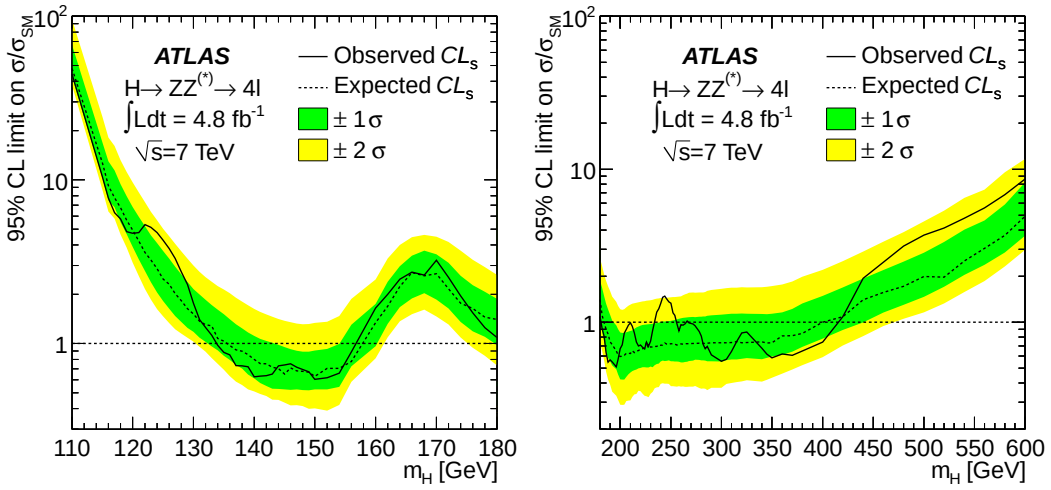

(a) (b)

Figure 5.22: The expected and observed 95 % CL upper limits on the Standard Model Higgs boson production cross section are presented in the (a) low and (b) high mass regions separately as a function of m_H, divided by the expected SM Higgs boson cross section. The 1σ and 2σ fluctuations are also included.

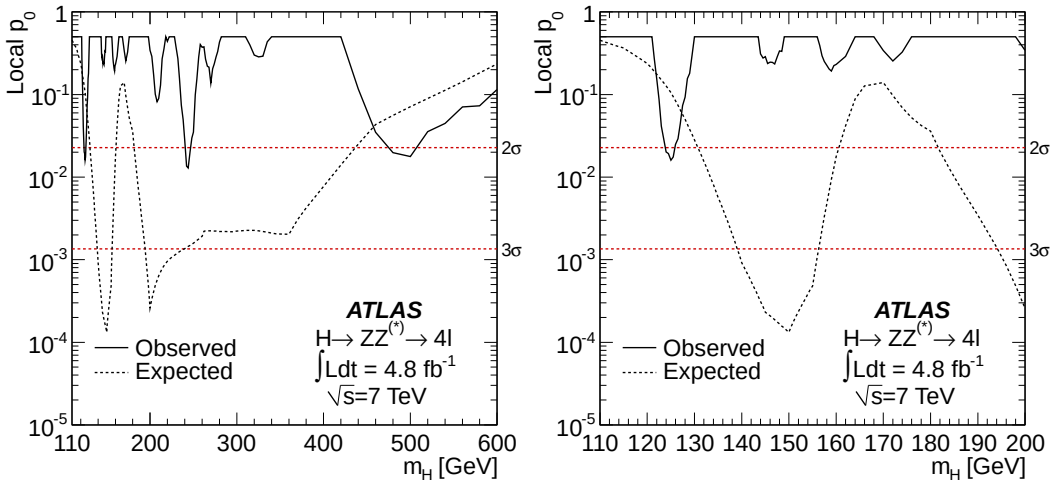

(a) (b)

Figure 5.23: The observed local p_0 and the expected median local p_0 for the signal hypothesis when tested at m_H are presented for the 5.23(a) full and 5.23(b) low mass range.

as or higher than the excesses observed in data. In Figure 6.17 the p_0-values, calculated using an ensemble of simulated pseudo-experiments, are given as a function of m_H for the full mass range of the analysis as well as in the low mass region. The observed local p_0 is shown as the solid line and the dashed curve the expected median local p_0 for the signal hypothesis when tested at the corresponding m_H. The two horizontal dashed lines indicate the p_0 values corresponding to local significance of 2σ and 3σ.

The most significant upward deviations from the background-only hypothesis are observed for $m_H = 125\,\text{GeV}$ with a local p_0 of 1.6 % (2.1 standard deviations), $m_H = 244\,\text{GeV}$ with a local p_0 of 1.3 % (2.2 standard deviations) and $m_H = 500\,\text{GeV}$ with a local p_0 of 1.8 % (2.1 standard deviations). The median expected local p_0 in the presence of a SM Higgs boson are 10.6 % (1.3 standard deviations), 0.14 % (3.0 standard deviations) and 7.1 % (1.5 standard deviations) for $m_H = 125\,\text{GeV}$, 244 GeV and 500 GeV, respectively.

These results do not account for the so-called "Look-Elsewhere" Effect (LEE) [87], which takes into account that such an excess or a larger one can appear anywhere in the search range as a result of an upward fluctuation of the background. When considering the complete mass range of this search the global p0-value for each of the three excesses becomes of O(50 %). Thus, once the look-elsewhere effect is considered, none of the observed local excesses are significant.

From the results presented above, only a hint can be extracted for the observation of a new Higgs-like particle [88]. When combining the results from the $H \to 4\ell$ search with the other Higgs searches ($H \to \gamma\gamma$, $H \to WW$, $H \to \tau^+\tau^-$ and $H \to b\bar{b}$), an excess of events is observed at Higgs boson mass hypothesis around 126 GeV with a local significance of 2.9 standard deviations [89].

Chapter 6

Optimization of the $H \to ZZ^{(*)} \to 4\ell$ analysis for a low mass Higgs

For the 2012 data taking, an optimization of the analysis selection was performed to maximize the expected signal significance for a low mass Higgs boson, owing to the results in Chapter 5. The focus was brought to the low mass region between 120 and 130 GeV which is more challenging and where changes in the kinematic requirements have a large impact on both the signal and the background processes. The optimization was performed on MC samples and signal-free control regions.

6.1 Optimization of the kinematic requirements

The optimization studies for the kinematic requirements were focused on the invariant mass of the leading (m_{12}) and the subleading dilepton (m_{34}), and the transverse momenta of the four leptons. The criterion for the selected optimized values was the signal sensitivity and the statistical variable used was the local expected p_0 which is the probability that the observed number of events are as large or larger than the expected background. To estimate the expected number of signal and background events a window of ± 6 GeV around the Higgs mass hypothesis is used. The probability is expressed as the equivalent number of standard deviations Z_0 for a Gaussian probability density function

$$Z_0 = \sqrt{2\left((s+b)\ln\left(1+\frac{s}{b}\right)-s\right)} \tag{6.1}$$

where s is the number of signal and b the number of background events. In general if small dependency of the expected Z_0 is observed, the cut selection has moved towards a more conservative value with respect to the reducible background contribution.

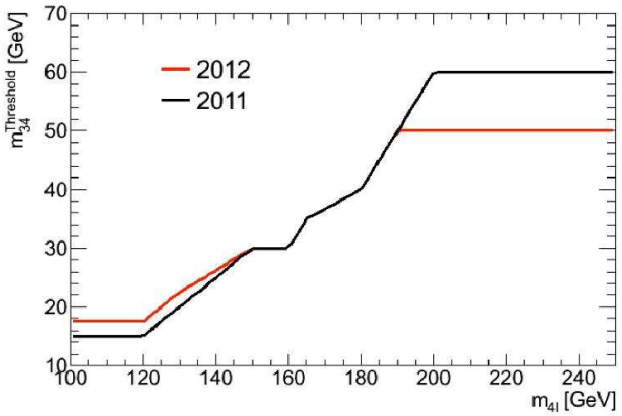

Figure 6.1: The minimum m_{34} requirement in the optimized analysis has been tightened in the low $m_{4\ell}$ and relaxed for the high masses with respect to the 2011 analysis.

6.1.1 $\ell\ell + \mu\mu$ final state channels

The selected cut value for the minimum m_{12} is selected to be 50 GeV, much relaxed compared to the $m_Z - 15$ GeV described in Section 5.3.5. For the m_{34}, the minimum requirement is chosen to be 20 GeV for $m_{4\ell} = 125$ GeV which is more tight than in the 2011 analysis selection. As presented in Figure 6.1, the m_{34} requirement is tightened for low $m_{4\ell}$ and relaxed for high $m_{4\ell}$.

Concerning the transverse momenta of the muons, the second highest-p_{T} and lowest-p_{T} muons show more sensitivity. So it has been decided to relax them to 15 GeV instead of 20 GeV for the second highest-p_{T} muon and to 6 GeV instead of 7 GeV for the lowest-p_{T} one. In contrary, the p_{T} requirement for the third highest-p_{T} muon is tightened to the more conservative 10 GeV due to lack of sensitivity.

6.1.2 $\ell\ell + ee$ final state channels

Since the $4e$ and $2\mu 2e$ final state channels share similar background composition, the optimization study for the kinematic requirements is performed for both at the same time. The minimum p_{T} required for the electrons is 7 GeV due to the availability of reliable efficiency scale factors only above this value. The selection criteria which were considered for optimization were the m_{12} invariant mass, the lower-p_{T} lepton in the leading dilepton, denoted as $p_{\mathrm{T}2}$, and the highest-p_{T} lepton in the subleading dilepton, denoted as $p_{\mathrm{T}3}$.

Concerning the m_{12} requirement, it is noted that the efficiency increases for lower values of the m_{12} cut especially for $m_H = 120$ GeV. The selection at 50 GeV is accepted since below this value the significance reaches a plateau. For $p_{\mathrm{T}2} > 15$ GeV there is a clear increase in the significance in comparison to the 20 GeV cut of the 2011 analysis. Finally, for $p_{\mathrm{T}3}$, a stricter requirement at 10 GeV has offered a good rejection of the reducible background processes with a very small impact on the signal events, compared to 7 GeV used in the 2011 analysis.

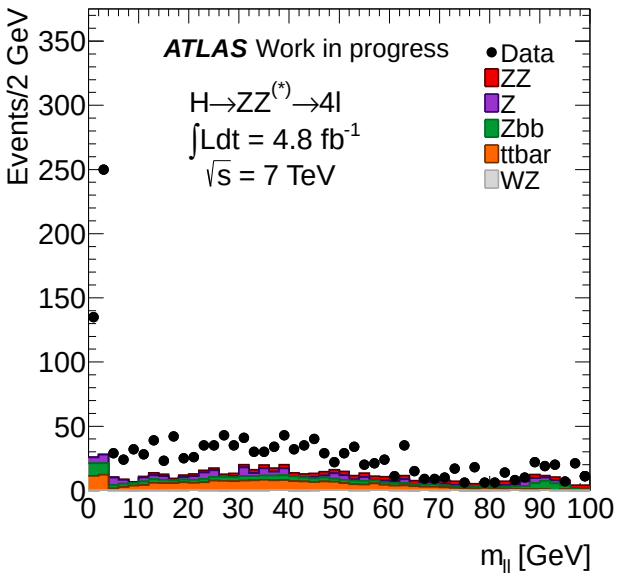

Figure 6.2: The invariant mass distribution for the cross-pairings is presented, exhibiting a clear peak at the J/ψ invariant mass range for the data. Quadruplets have been considered fulfilling the analysis selection with the exception of the lepton isolation and impact parameter requirements.

6.2 Further optimization on the $H \to ZZ^{(*)} \to 4\ell$ analysis

In addition to the kinematic requirements, the inclusion of other type of muons apart from the combined and the segment-tagged, described in Section 4.2, is studied. More specifically, the inclusion of calorimeter-tagged muons for $|\eta| < 0.1$ and standalone muons for $2.5 < |\eta| < 2.7$ has been considered which extends the muon acceptance. For $m_H = 125\,\text{GeV}$ the signal efficiency is improved by 9 % in the optimized kinematic region when including the calorimeter-tagged and standalone muons.

The muon calorimetric isolation ($\sum p_{\text{T}}$) used in the analysis had been added a correction according to the pileup. This correction has showed a decrease in sensitivity due to increase of the reducible background. So, during the optimization of the analysis this correction is removed, following a more conservative approach. Moreover, the relative calorimetric isolation for standalone muons, which have no Inner Detector track, is required to be less than 0.15.

The additional selection criteria concerning the impact parameter significance is also revised. For the 2011 analysis, the requirement has only been applied to the two lowest-p_{T} leptons of the quadruplet. Due to slight improvement in the sensitivity, in the optimized analysis this selection is applied to all four leptons. The impact parameter significance for the electron is broader due to Bremsstrahlung and is relaxed a little to 6.5 instead of 6.

The possibility of mispairing is also considered. In order to study this, cross-

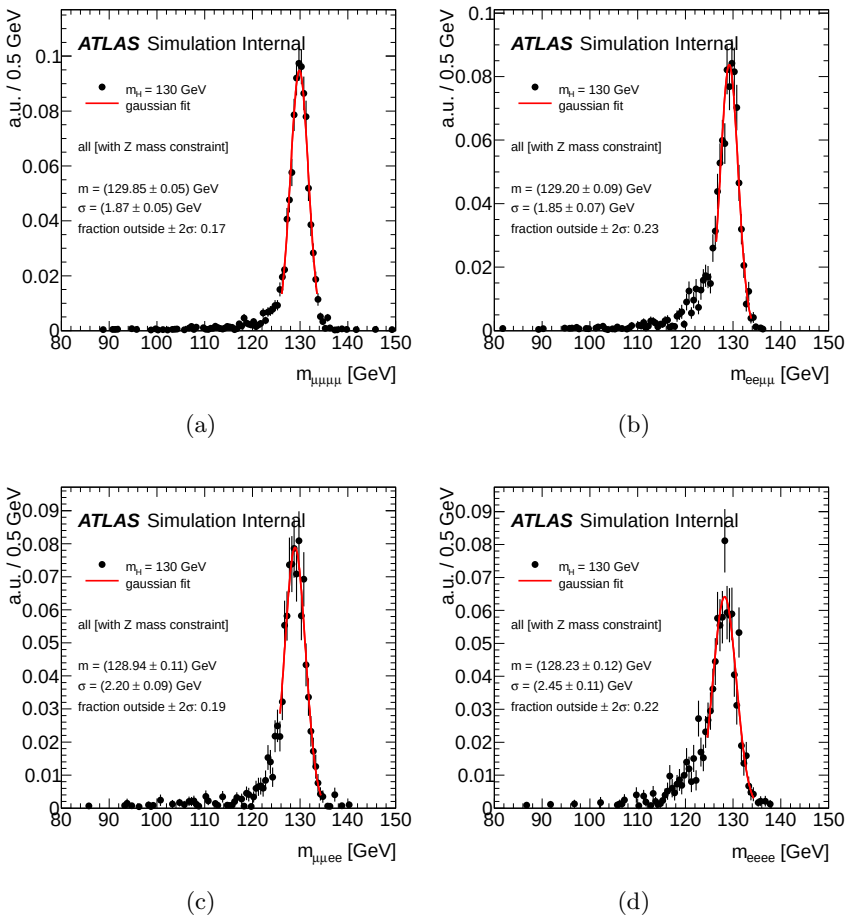

Figure 6.3: The invariant mass distribution for a simulated MC sample with $m_H = 130\,\text{GeV}$, in the (a) 4μ, (b) $2e2\mu$, (c) $2\mu2e$ and (d) $4e$ final state channels is presented. The Z mass constraint is applied. The Gaussian fit to the $m_{4\ell}$ peak is superimposed (red line).

pairing is checked by selecting the remaining combination of opposite charge and same flavor lepton pairs within the selected quadruplets. In Figure 6.2 the $m_{\ell\ell}$ invariant mass for the cross-pairs in the 4μ and $4e$ final states is presented for data and MC simulation. The analysis selection is applied for these quadruplets but no lepton isolation and impact parameters requirements. A peak at the low mass range at about 3 GeV can be clearly seen in data. Part of this is considered to arise from production of a prompt J/ψ in association with a Z boson [90,91]. As a consequence, it has been decided to reject such events by requiring that the cross-pairing invariant mass of opposite charge and same flavor leptons in the quadruplet, is larger than 5 GeV. The effect of this selection on the signal is very small.

Finally, in order to enhance the mass resolution in the low mass region where the width of the signal peak is dominated by the detector resolution, the Z mass constraint method is used. This method adjusts the lepton momenta according

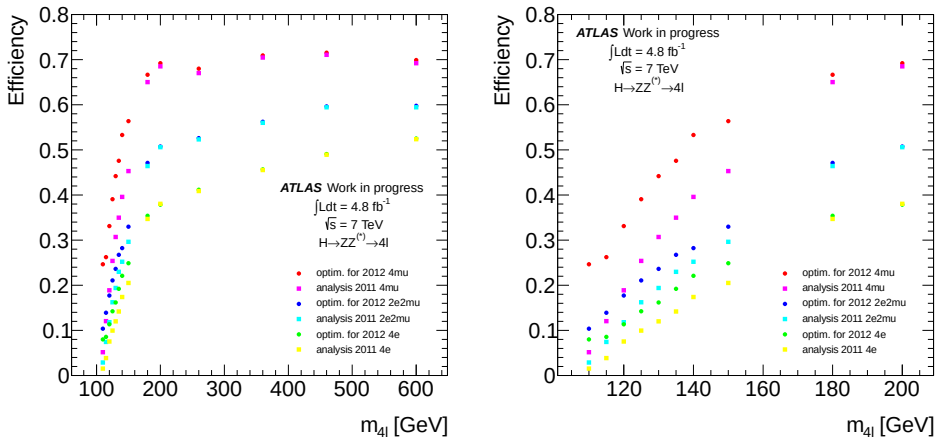

Figure 6.4: The signal reconstruction efficiency is presented as a function of m_H for the 2011 and the new analysis selection. The efficiency for each final state is shown separately.

to their uncertainties so that the invariant mass of the leading dilepton equals a constraint mass m_c. Due to the non-negligible mass width of the Z boson the m_c is estimated by maximizing the likelihood consisting of the product of the Z lineshape and the detector mass resolution. In Figures 6.3 the invariant mass distribution considering $m_H = 130\,\text{GeV}$ is shown for the four final states applying the Z mass constraint. The resolution is obtained from an unbinned maximum likelihood fit of a Gaussian model to the $m_{4\ell}$ distribution. The improvement on the resolution is 9 % for the 4μ, 16 % for the $2e2\mu$, 5 % for the $2\mu 2e$ and 0.4 % for the $4e$ final state.

Taking into account the optimized analysis selection on $m_H = 125\,\text{GeV}$ signal sample, there has been an increase in the significance of 29 % for the 4μ final state channel, 24 % for $2\mu 2e$ and $2e2\mu$, and 19 % for $4e$. In Figures 6.4 the effect of the optimized selection is reflected on the signal. The signal efficiency with respect to truth is depicted as a function of m_H for the two analysis selection sets and for every final state channel separately.

6.3 Background estimation for the optimized analysis

In the optimization procedure, an important check was to study the effect of the new selection on the background processes and the comparison of data and simulation in the control regions.

6.3.1 QCD multijet background

The event yields in the QCD multijet control region in the optimized analysis are summarized in Table 6.1 where the MC includes $ZZ^{(*)}$, Z+jets and $t\bar{t}$. Applying the track isolation to the leading leptons rejects most QCD multijet events. For

Table 6.1: The number of events in the QCD multijet control region are shown at different levels of the analysis.

Selection	4μ		$2e2\mu$		$4e$	
	Data	MC	Data	MC	Data	MC
Lepton quadruplet, kinematic req., charge requirement, dilepton mass requirements, $\Delta R(\ell, \ell') > 0.10$	37	23.1	26	10.3	12	8.8
Application of additional requirements independently						
Tracking isolation on leading dilepton	2	2.4	10	3.3	8	5.6
Tracking and calorimeter isolation on leading dilepton	1	1.4	8	2.6	7	5.0
Tracking isolation on all leptons	0	0.3	4	0.8	6	3.8
Tracking and calorimeter isolation on all dileptons	0	0.2	3	0.7	4	3.1
Isolation on all leptons and d_0 significance	0	0.0	1	0.6	3	1.7

example, in the $4e$ final state we are left with three surviving events in the data which is generally in agreement with the expectation from $ZZ^{(*)}$, Z+jets and $t\bar{t}$ due to charge misidentification. Thus, no significant QCD multijet contribution is expected after the application of the full analysis selection.

6.3.2 Control plots for the $t\bar{t}$ background contribution

For the $t\bar{t}$ control region, an $e\mu$ opposite charge dilepton pair with an invariant mass within 20 GeV from m_Z and two additional same flavor, opposite charge leptons are selected. The analysis selection is followed but isolation requirements are only applied on the $e\mu$ pair and no impact parameter criteria are required. The invariant mass distributions with the yields using the new analysis are presented in Figures 6.5 and 6.6. In the results for the subleading dimuon, data and MC simulation are in very good agreement while in the subleading dielectron case the relatively small difference is deduced to the larger QCD multijet contribution.

6.3.3 Control plots for the total background

For Figures 6.7 and 6.8 the relaxed control region is used, where the analysis selection is applied but the charge and isolation requirement on the subleading dilepton as well as the impact parameter requirement on all leptons are relaxed. In 6.7 the invariant mass distributions for the four final states correspond to the opposite charge combinations for the subleading dilepton while in 6.8 to the same charge combinations. Some disagreement is noted in the subleading dimuon final states.

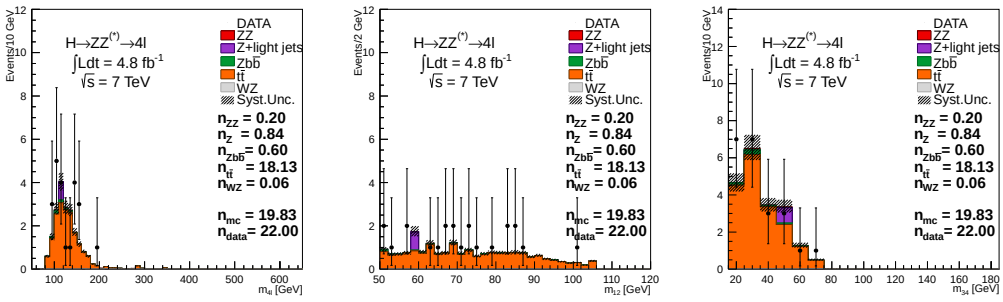

(a) (b) (c)

Figure 6.5: The invariant mass distribution of (a) $m_{4\ell}$, (b) m_{12} and (c) m_{34} are presented for the measured and expected events in the $t\bar{t}$ control region reconstructing $e\mu+\mu\mu$ events. Only isolation and no impact parameter requirements are applied on the $e\mu$ pair. On the additional lepton pair no isolation or impact parameter criteria are required.

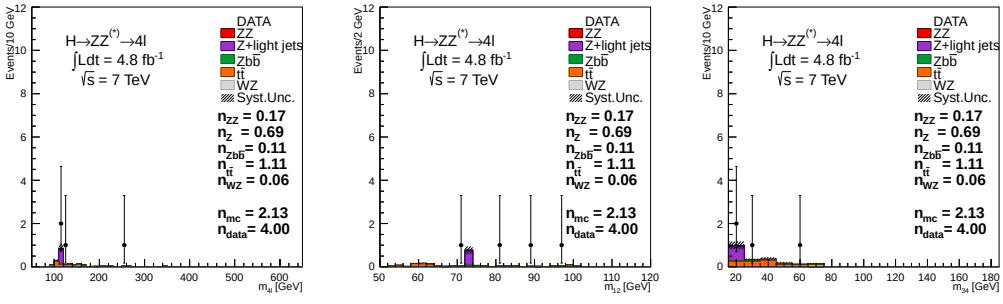

(a) (b) (c)

Figure 6.6: The invariant mass distribution of (a) $m_{4\ell}$, (b) m_{12} and (c) m_{34} are presented for the measured and expected events in the $t\bar{t}$ control region reconstructing $e\mu+ee$ events. Only isolation and no impact parameter requirements are applied on the $e\mu$ pair. On the additional lepton pair no isolation or impact parameter criteria are required. Multijet QCD background is not included.

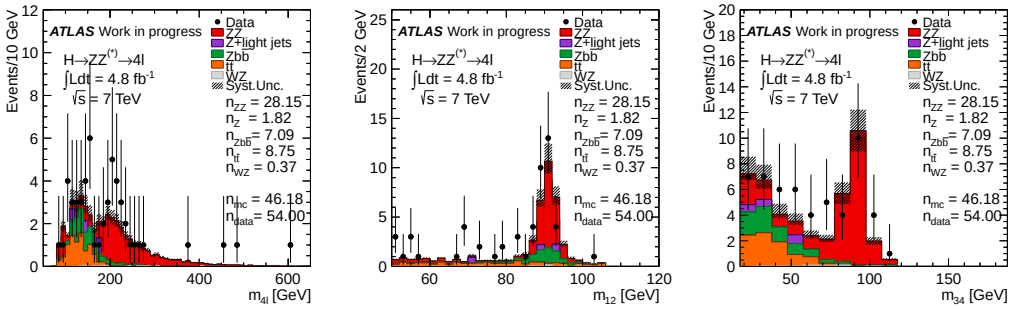

(a) $Z(\to \mu\mu) + \mu\mu \quad m_{4\ell}$ (b) $Z(\to \mu\mu) + \mu\mu \quad m_{12}$ (c) $Z(\to \mu\mu) + \mu\mu \quad m_{34}$

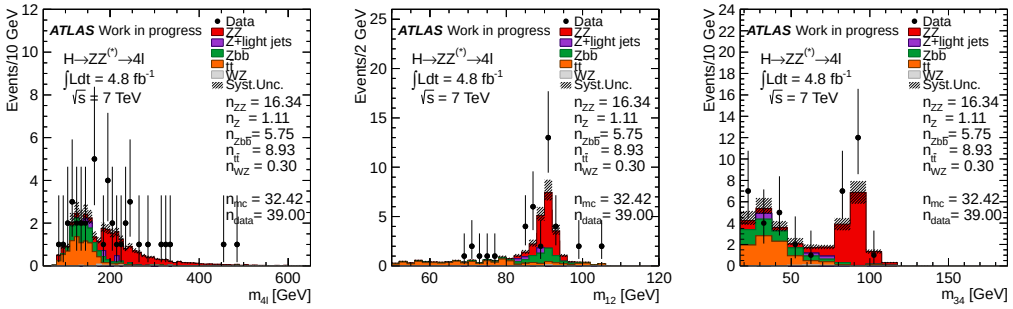

(d) $Z(\to ee) + \mu\mu \quad m_{4\ell}$ (e) $Z(\to ee) + \mu\mu \quad m_{12}$ (f) $Z(\to ee) + \mu\mu \quad m_{34}$

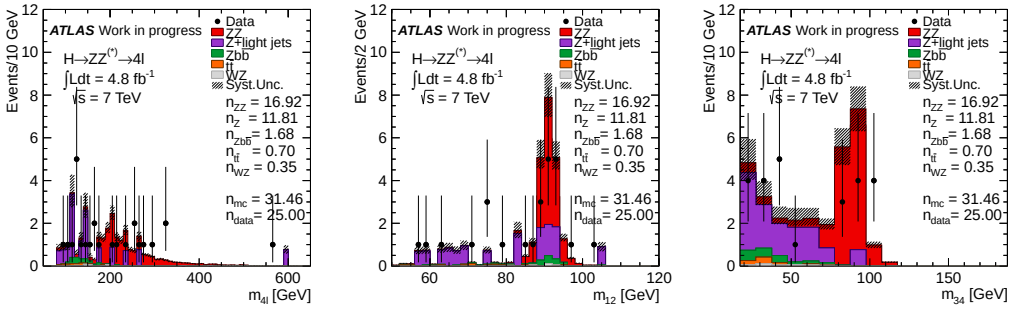

(g) $Z(\to \mu\mu) + ee \quad m_{4\ell}$ (h) $Z(\to \mu\mu) + ee \quad m_{12}$ (i) $Z(\to \mu\mu) + ee \quad m_{34}$

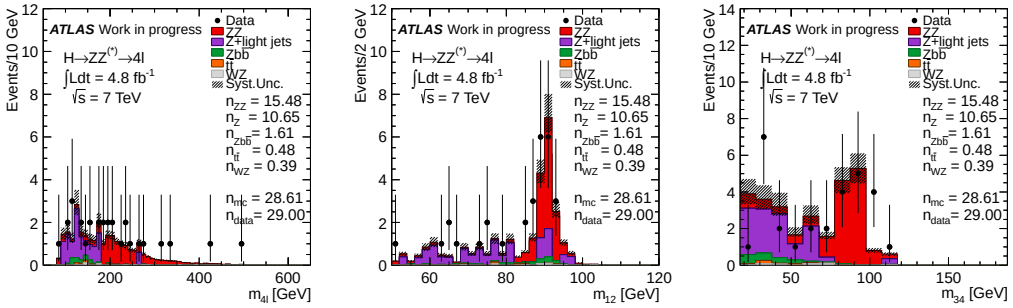

(j) $Z(\to ee) + ee \quad m_{4\ell}$ (k) $Z(\to ee) + ee \quad m_{12}$ (l) $Z(\to ee) + ee \quad m_{34}$

Figure 6.7: The invariant mass distributions are shown when applying the analysis selection but relaxing the isolation and impact parameter requirements on the subleading dilepton. Only opposite charge combinations for the subleading muons are considered.

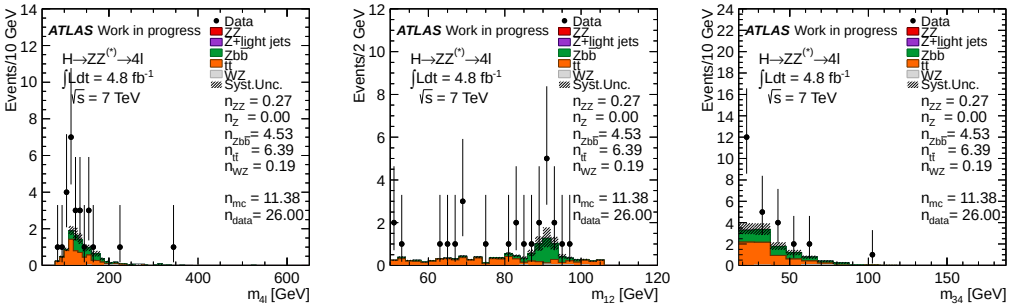

(a) $Z(\to \mu\mu) + \mu\mu \quad m_{4\ell}$ (b) $Z(\to \mu\mu) + \mu\mu \quad m_{12}$ (c) $Z(\to \mu\mu) + \mu\mu \quad m_{34}$

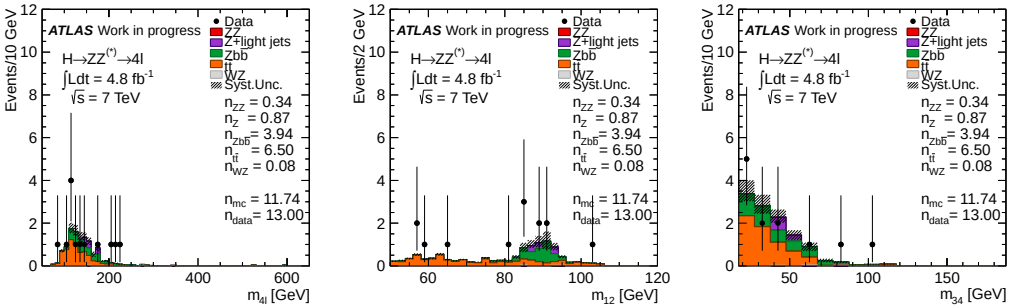

(d) $Z(\to ee) + \mu\mu \quad m_{4\ell}$ (e) $Z(\to ee) + \mu\mu \quad m_{12}$ (f) $Z(\to ee) + \mu\mu \quad m_{34}$

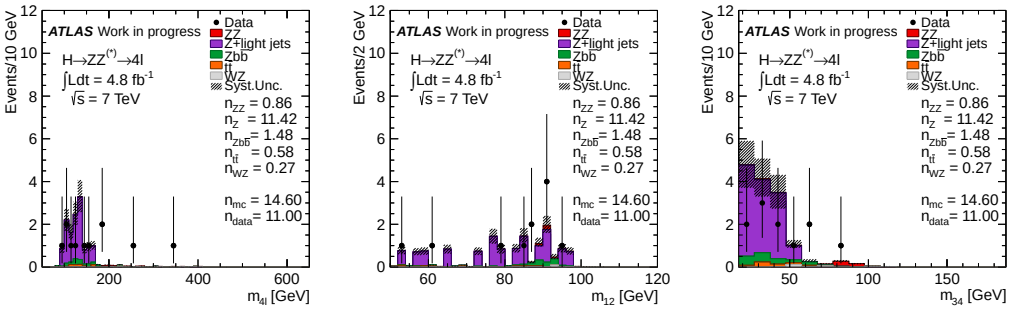

(g) $Z(\to \mu\mu) + ee \quad m_{4\ell}$ (h) $Z(\to \mu\mu) + ee \quad m_{12}$ (i) $Z(\to \mu\mu) + ee \quad m_{34}$

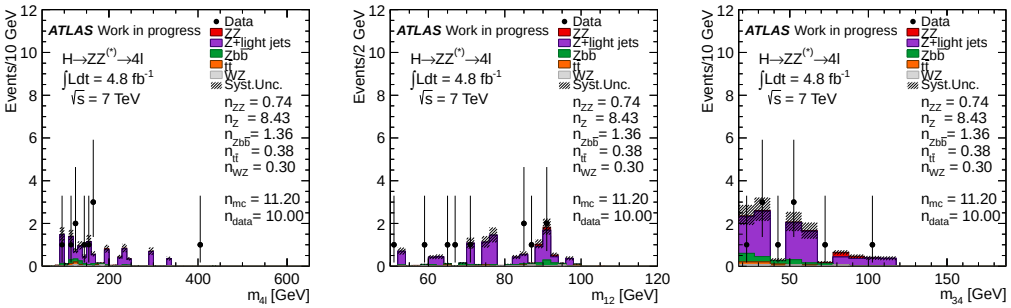

(j) $Z(\to ee) + ee \quad m_{4\ell}$ (k) $Z(\to ee) + ee \quad m_{12}$ (l) $Z(\to ee) + ee \quad m_{34}$

Figure 6.8: The invariant mass distributions are shown when applying the analysis selection but relaxing the isolation and impact parameter requirements on the subleading dilepton. Only same charge combinations for the subleading muons are considered.

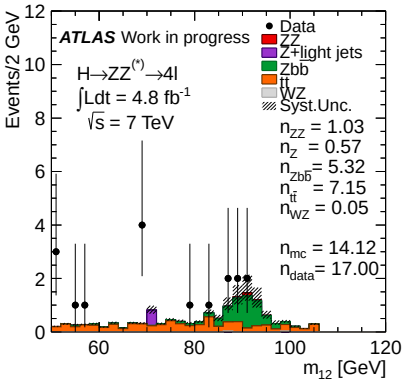

(a) $Z(\to \mu\mu) + \mu\mu \quad m_{12}$

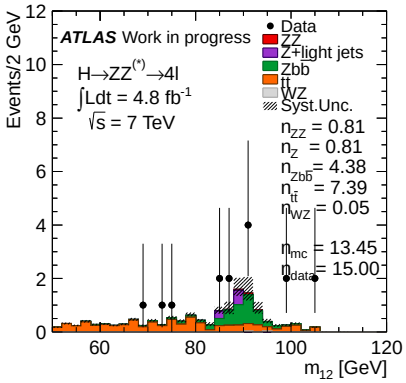

(b) $Z(\to ee) + \mu\mu \quad m_{12}$

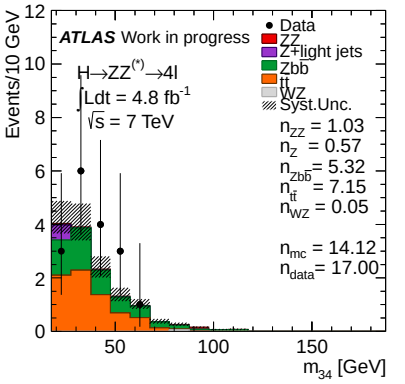

(c) $Z(\to \mu\mu) + \mu\mu \quad m_{34}$

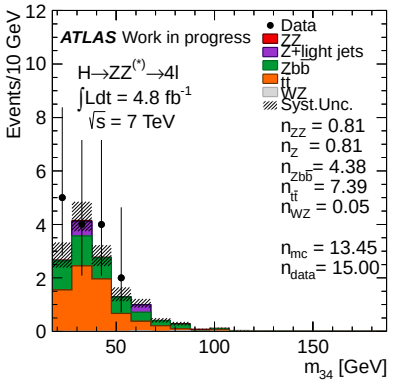

(d) $Z(\to ee) + \mu\mu \quad m_{34}$

Figure 6.9: The invariant mass distributions are shown for $Z(\to ee) + \mu\mu$ and $Z(\to \mu\mu) + \mu\mu$ when applying the analysis selection but relaxing the charge and isolation requirements while inverting the impact parameter requirement on at least one of the leptons in the subleading pair. Only opposite charge combinations for the subleading muons are considered.

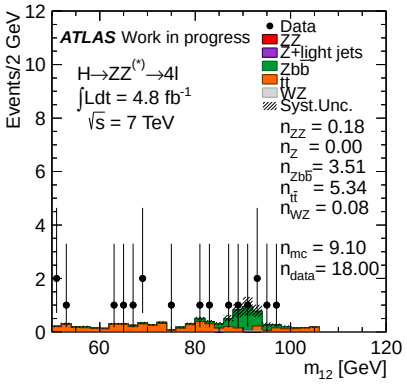

(a) $Z(\rightarrow \mu\mu) + \mu\mu \quad m_{12}$

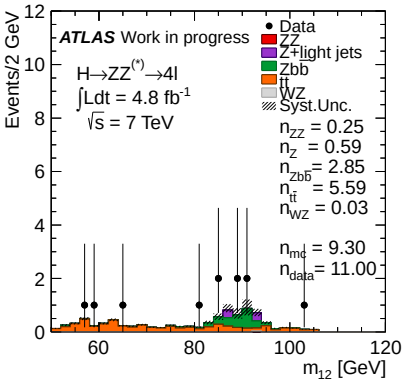

(b) $Z(\rightarrow ee) + \mu\mu \quad m_{12}$

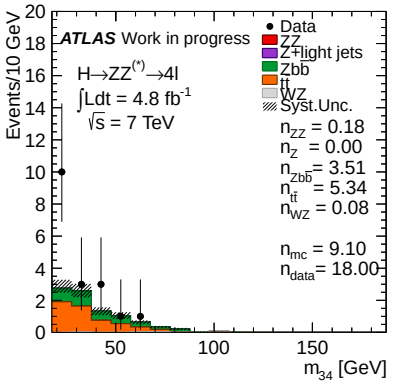

(c) $Z(\rightarrow \mu\mu) + \mu\mu \quad m_{34}$

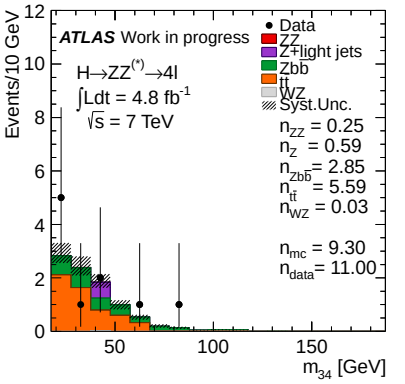

(d) $Z(\rightarrow ee) + \mu\mu \quad m_{34}$

Figure 6.10: The invariant mass distributions are shown for $Z(\rightarrow ee) + \mu\mu$ and $Z(\rightarrow \mu\mu) + \mu\mu$ when applying the analysis selection but relaxing the charge and isolation requirements while inverting the impact parameter requirement on at least one of the leptons in the subleading pair. Only same charge combinations for the subleading muons are considered.

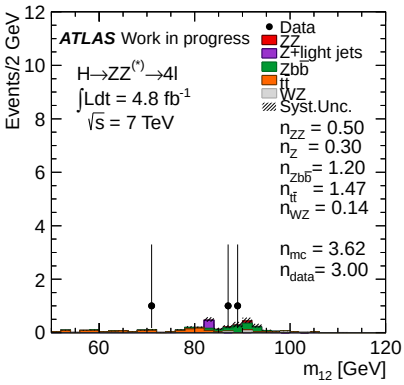

(a) $Z(\to ee) + \mu\mu \quad m_{12}$

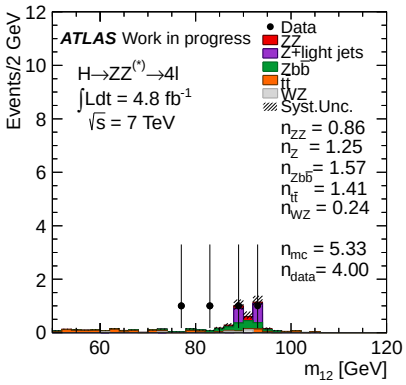

(b) $Z(\to \mu\mu) + \mu\mu \quad m_{12}$

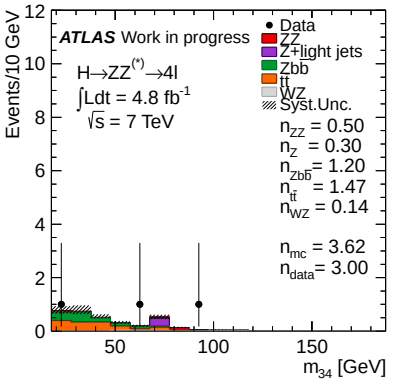

(c) $Z(\to ee) + \mu\mu \quad m_{34}$

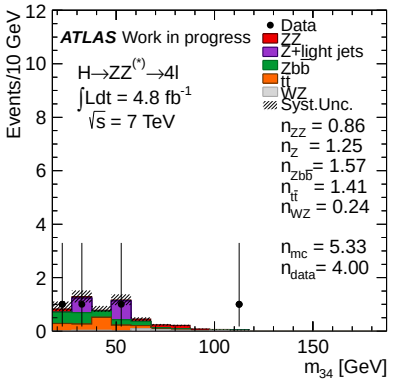

(d) $Z(\to \mu\mu) + \mu\mu \quad m_{34}$

Figure 6.11: The invariant mass distributions are shown for $Z(\to ee) + \mu\mu$ and $Z(\to \mu\mu) + \mu\mu$ when applying the analysis selection but relaxing the charge requirement while inverting the tracking isolation requirement on the subleading dileptons. The impact parameter requirements are only applied on the subleading dilepton. Only opposite charge combinations for the subleading electrons are considered.

The background contribution of the subleading dimuon final states is further investigated using the inverted impact parameter and inverted isolation control regions described in Section 5.6. In Figures 6.9 and 6.10 the invariant mass distributions are shown in the inverted impact parameter control region for the opposite- and same-charge combination, respectively. Isolation is required only for the leading dilepton while the impact parameter requirement is inverted for the subleading dimuon. At this level, agreement of the observed with the expected yields is noted in the opposite charge combination.

In Figures 6.11 and 6.12 the inverted isolation control region is applied for the opposite- and same-charge combination, respectively. Isolation requirements are applied in the leading dilepton and tracking isolation is inverted for at least one muon in the subleading pair. The impact parameter requirement is only applied in

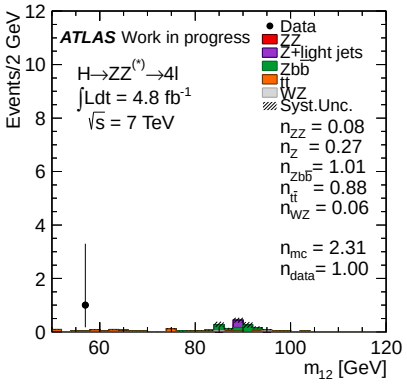

(a) $Z(\rightarrow ee) + \mu\mu \quad m_{12}$

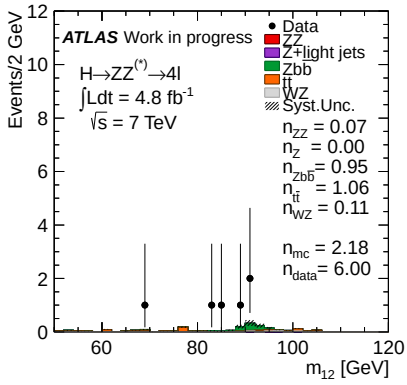

(b) $Z(\rightarrow \mu\mu) + \mu\mu \quad m_{12}$

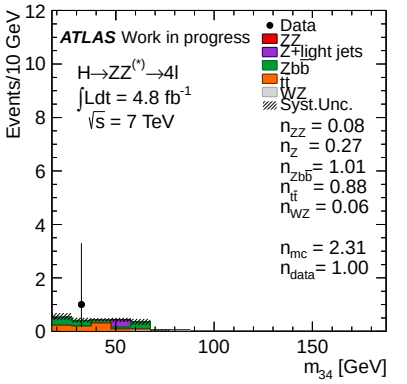

(c) $Z(\rightarrow ee) + \mu\mu \quad m_{34}$

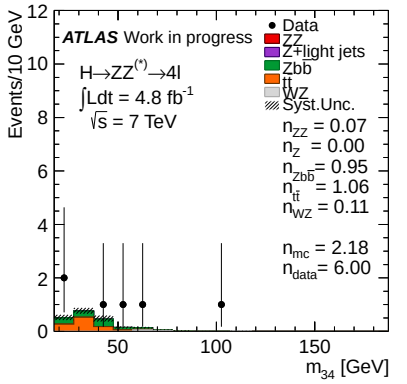

(d) $Z(\rightarrow \mu\mu) + \mu\mu \quad m_{34}$

Figure 6.12: The invariant mass distributions are shown for $Z(\rightarrow ee) + \mu\mu$ and $Z(\rightarrow \mu\mu) + \mu\mu$ when applying the analysis selection but relaxing the charge requirement while inverting the tracking isolation requirement on the subleading dileptons. The impact parameter requirements are only applied on the subleading dilepton. Only same charge combinations for the subleading electrons are considered.

Table 6.2: Same charge subleading candidates found in data after the full analysis selection. For the 4μ and $2e2\mu$ final states no candidates were found.

Type	Run Number	Event Number	$m_{4\ell}$ [GeV]	m_{12} [GeV]	m_{34} [GeV]
$4e$	183391	22157502	161.5	84.0	39.5
$4e$	189719	41739189	145.6	71.8	51.7
$4e$	190343	498361	96.8	58.1	33.1
$4e$	190618	46965700	150.3	91.0	34.5
$2\mu 2e$	183407	126937239	97.6	53.3	41.4
$2\mu 2e$	186721	140569735	185.8	90.5	87.1

Table 6.3: The transfer factors from the $t\bar{t}$ and $Z + b\bar{b}$ control regions to the signal region are quoted along with their statistical and systematic uncertainties.

[%]	$Zb\bar{b}$	$t\bar{t}$
$\mu\mu/ee + \mu\mu$	$3.3 \pm 0.3 \pm 1.0$	$0.2 \pm 0.1 \pm 0.1$
$\mu\mu/ee + ee$	$26.1 \pm 3.6 \pm 18.6$	$4.2 \pm 12.7 \pm 24.8$

the subleading dimuon. In this control region there is general agreement between the expected and the observed yields.

After applying the full analysis selection on the same charge subleading dileptons, as can be seen in Table 6.2, no events survive for the 4μ and $2e2\mu$ final state.

6.3.4 Background data-driven estimation

The expected background yield in the signal region is estimated using MC simulation normalized to the theoretical cross section for the $ZZ^{(*)}$ production while for the Z+jets and $t\bar{t}$ processes the yield and and its composition is extracted by data-driven methods.

For the subleading dimuon cases, dominated by $Z+b\bar{b}$ and $t\bar{t}$, the m_{12}-fit method is used. According to this method, the relaxed control region where no additional requirements are applied on the subleading dimuon is used but it is required that at least one of the subleading muons fails the impact parameter significance requirement. This removes $ZZ^{(*)}$ contribution with small effect on the $Z + b\bar{b}$ and $t\bar{t}$ ones. The m_{12} distribution, shown in Figure 6.13, is then fitted using a second order Chebychev polynomial for the $t\bar{t}$ component and a Breit-Wigner line-shape convoluted with a Crystal-Ball resolution function for the Z+jets one. The yields are afterwards extrapolated to the signal region using transfer factors, quoted in Table 6.3, from simulation. The transfer factors are based on the calculated efficiency for the isolation and impact parameter requirement. The systematic errors associated to the extrapolation from the control region to the signal region are comparable with the statistical errors of the fit. The expected background yields are quoted in

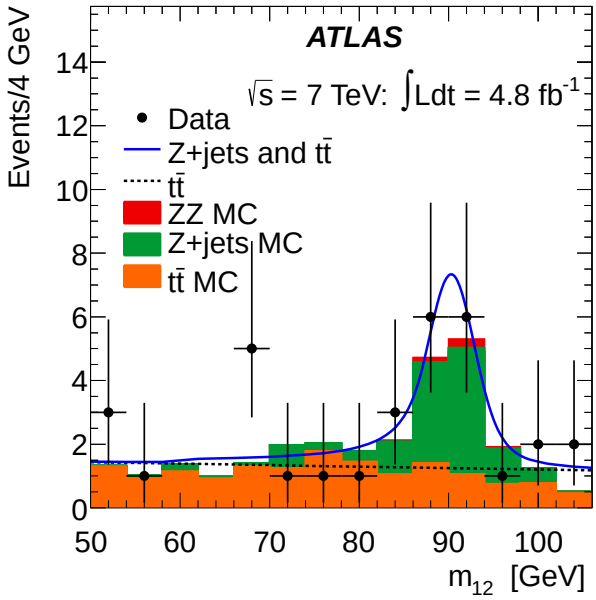

Figure 6.13: Distribution of m_{12} in the control region where the isolation requirements are not applied to the two subleading muons, and at least one of these muons fails the impact parameter significance requirement. The fit used to obtain the yields for $t\bar{t}$ and Z+jets is presented.

Table 6.4.

The reconstructed electron objects contain apart from true isolated electrons, electrons from heavy flavor semileptonic decays, electrons from photon conversions, and light jets misidentified as electrons, denoted as fake electrons. Therefore, in the subleading dielectron final states, a control region with $\mu\mu/ee + ee$ events is selected where the selection criteria for the subleading dielectron are relaxed. The events are then separated into reconstruction categories which are electron-like (E), conversion-like (C) and fake-like (F), using discriminating variables that are not used in the electron identification [92] performed in the analysis and are based on the number of B-layer hits, the fraction of high threshold hits in the TRT, the energy in the first layer of the electromagnetic calorimeter and the lateral containment of the cluster along ϕ in the second layer of the electromagnetic calorimeter. The number of observed and expected events in each category are shown in Table 6.5. For each reconstructed category, the expected truth composition is estimated, and based on the electron candidate truth origin and the efficiency of the truth category to satisfy the remaining analysis selection, the expected yield in the signal region is extracted. This method estimates the sum of Z+jets and $t\bar{t}$ background contributions. The estimations are presented in Table 6.4.

A cross-check method developed for the subleading dielectron final states is the $3\ell + \ell$. Quadruplets are built as in the analysis and all the cuts are applied to the three highest p_{T} leptons while for the least energetic electron only a certain number

Table 6.4: The estimation for the reducible background is presented. The first uncertainty is statistical, while the second one is systematic.

Method	Estimated number of events
4μ	
m_{12} fit: $Z+$jets contribution	0.25±0.10±0.08
m_{12} fit: $t\bar{t}$ contribution	0.02±0.01±0.01
$2e2\mu$	
m_{12} fit: $Z+$jets contribution	0.20±0.08±0.06
m_{12} fit: $t\bar{t}$ contribution	0.02±0.01±0.01
$2\mu 2e$	
$\ell\ell + e^{\pm}e^{\mp}$	2.6± 0.4 ±0.4
$\ell\ell + e^{\pm}e^{\pm}$ (check)	3.7± 0.9 ±0.6
$3\ell + \ell$ (check)	2.0± 0.5 ±0.3
$4e$	
$\ell\ell + e^{\pm}e^{\mp}$	3.1± 0.6 ±0.5
$\ell\ell + e^{\pm}e^{\pm}$ (check)	3.2± 0.6 ±0.5
$3\ell + \ell$ (check)	2.2± 0.5 ±0.3

Table 6.5: The observed and expected yields of $\mu\mu/ee+ee$ events are quoted for the subleading dielectron categories in the control region where the electron requirements on the subleading dielectron are relaxed.

	$4e$		$2\mu 2e$	
	Data	MC	Data	MC
EE	11	14.61	8	17.82
EC	4	2.431	3	1.768
EF	6	10.34	5	5.358
CE	5	1.592	6	3.059
CC	2	1.378	2	0.774
CF	7	4.68	10	5.282
FE	5	3.529	4	3.733
FC	5	2.784	4	4.048
FF	12	10.11	17	9.149
Total	57	51.46	59	50.99

Table 6.6: New candidates, in addition to those in Tables 5.16 to 5.18, passing the full analysis with the optimized selections for the 4.9 fb^{-1} 2011 data.

N	Run Number	Event Number	LB	$m_{4\ell}$ [GeV]	m_{12} [GeV]	m_{34} [GeV]
			4μ			
1	182747	136528490	615	157.3	66.5	65.5
2	186721	22103472	186	89.8	51.9	29.8
3	187219	24256525	199	178.8	75.2	52.0
4	187219	34502707	241	118.9	72.4	32.6
5	190256	56600537	490	114.0	86.6	21.0
6	191920	7775570	281	187.4	64.6	61.2
			$4e$			
1	183045	28329677	311	105.2	79.5	17.9
2	183081	121479214	634	213.6	89.1	97.7
3	186361	29706533	201	193.0	91.2	89.4
4	187811	40399631	361	115.7	53.7	53.2
5	189561	48300215	250	102.9	72.4	23.0
6	190116	63457816	355	156.5	73.2	44.1
7	190256	175308437	1093	122.0	55.7	53.0
8	190643	23010890	226	217.9	87.0	58.8
9	191190	9522152	244	199.9	92.0	74.5
10	191513	9086448	245	141.2	54.3	44.0
11	191635	48018112	720	142.4	66.9	65.4
			$2e2\mu$			
1	182486	21528951	236	335.8	90.1	88.4
2	190300	121067450	653	92.8	71.6	19.3
3	190878	14892058	85	103.1	59.3	30.8

of hits ($n_{Si} > 7$ and $n_{Pix} > 0$) is required, and the electron identification, isolation and impact parameter selection criteria are not applied. As the composition problem is simplified in this method, a two-dimensional fit is used to to obtain the yields for the different components. The variables used to discriminate between hadrons and conversions are: the number of B-layer hits, and the fraction of high-threshold hits in the TRT, in the barrel region and the energy in the first layer of the EM calorimeter, in the endcaps. The expected background in the signal region, is obtained applying the electron selection efficiency estimated from simulation. Following, a data-MC comparison in the Z+X control region, a systematic uncertainty of 5 % on those efficiencies is assigned. The results of this method are quoted in Table 6.4.

Table 6.7: The observed numbers of events and the final estimate for the expected backgrounds, separated into "Low mass" ($m_{4\ell} < 160\,\text{GeV}$) and "High mass" ($m_{4\ell} \geq 160\,\text{GeV}$) regions. The expected numbers of signal events is also shown for various Higgs boson mass hypotheses. For signal and background estimates, the corresponding total uncertainty is given.

	4μ		$2e2\mu/2\mu2e$		$4e$	
Int. Luminosity	$4.8\,\text{fb}^{-1}$		$4.8\,\text{fb}^{-1}$		$4.9\,\text{fb}^{-1}$	
	Low mass	High mass	Low mass	High mass	Low mass	High mass
$ZZ(*)$	4.9±0.2	18.1±1.3	3.1±0.2	27.3±2.0	1.6±0.2	10.2±0.8
Z+jets and $t\bar{t}$	0.2±0.1	0.07±0.03	2.1±0.5	0.7±0.2	2.3±0.6	0.8±0.2
Total Background	5.1±0.2	18.2±1.3	5.1±0.5	28.0±2.0	3.9±0.6	11.0±0.8
Data	8	25	5	28	4	18
$m_H = 125\,\text{GeV}$	1.0±0.1		1.0±0.1		0.37±0.05	
$m_H = 150\,\text{GeV}$	3.0±0.4		3.4±0.5		1.4±0.2	
$m_H = 190\,\text{GeV}$	5.1±0.6		7.4±1.0		2.8±0.4	
$m_H = 400\,\text{GeV}$	2.3±0.3		3.8±0.5		1.6±0.2	

Table 6.8: Candidates from Tables 5.16 to 5.18 failing the new analysis. The reason of their removal is also added.

N	Run Number	Event Number	LB	$m_{4\ell}$ [GeV]	m_{12} [GeV]	m_{34} [GeV]	Reason
			4μ				
1	189207	81313827	338	171.9	83.9	62.1	J/ψ veto
2	190300	60554334	325	145.8	94.3	29.7	J/ψ veto
			$4e$				
1	186216	36894463	176	157.6	81.3	36.1	J/ψ veto

6.4 Impact of the optimization on 4.8 fb^{-1} of 7 TeV data

By applying the optimized analysis selection on the 2011 7 TeV data, 88 candidates are found; 33 in the 4μ channel, 21 in the $2e2\mu$ channel, 12 in the $2\mu2e$ channel and 22 in the $4e$ channel. The new candidates found are quoted in Table 6.6 and the lost candidates in Table 6.8. The three events failing the new analysis were removed by the J/ψ veto. The expected events from the background processes are 71.3 ± 2.6. In Table 6.7, the observed numbers of events passing the optimized analysis requirements in each final state are summarized and compared to the expected backgrounds, separately for $m_{4\ell} < 160$ GeV and $m_{4\ell} \geq 160$ GeV, and to the expected signal for various m_H hypotheses.

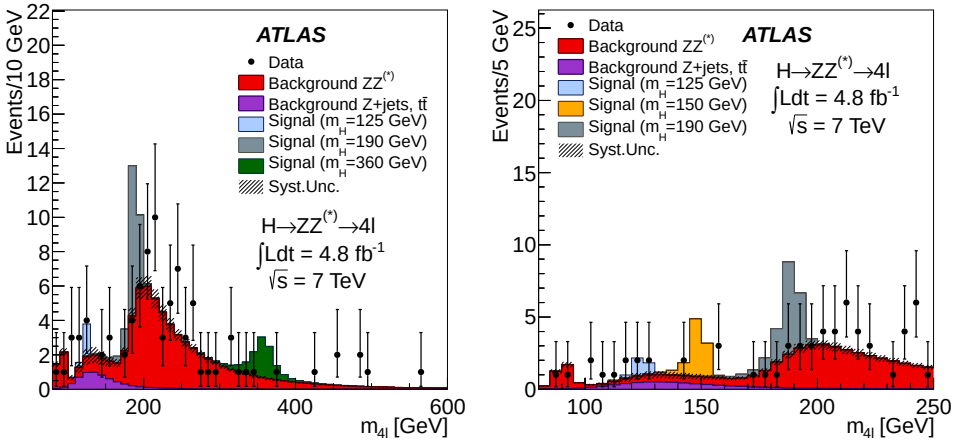

(a) (b)

Figure 6.14: The distribution of the four lepton invariant mass, $m_{4\ell}$, for the selected candidates is compared to the background expectation (a) in the range $80-600$ GeV and (b) in the $80-250$ GeV mass range. The error bars represent the 68.3% central confidence intervals. The signal expectation for several m_H hypotheses is also shown.

In Figures 7.9 the $m_{4\ell}$ distributions are presented for data, compared to the

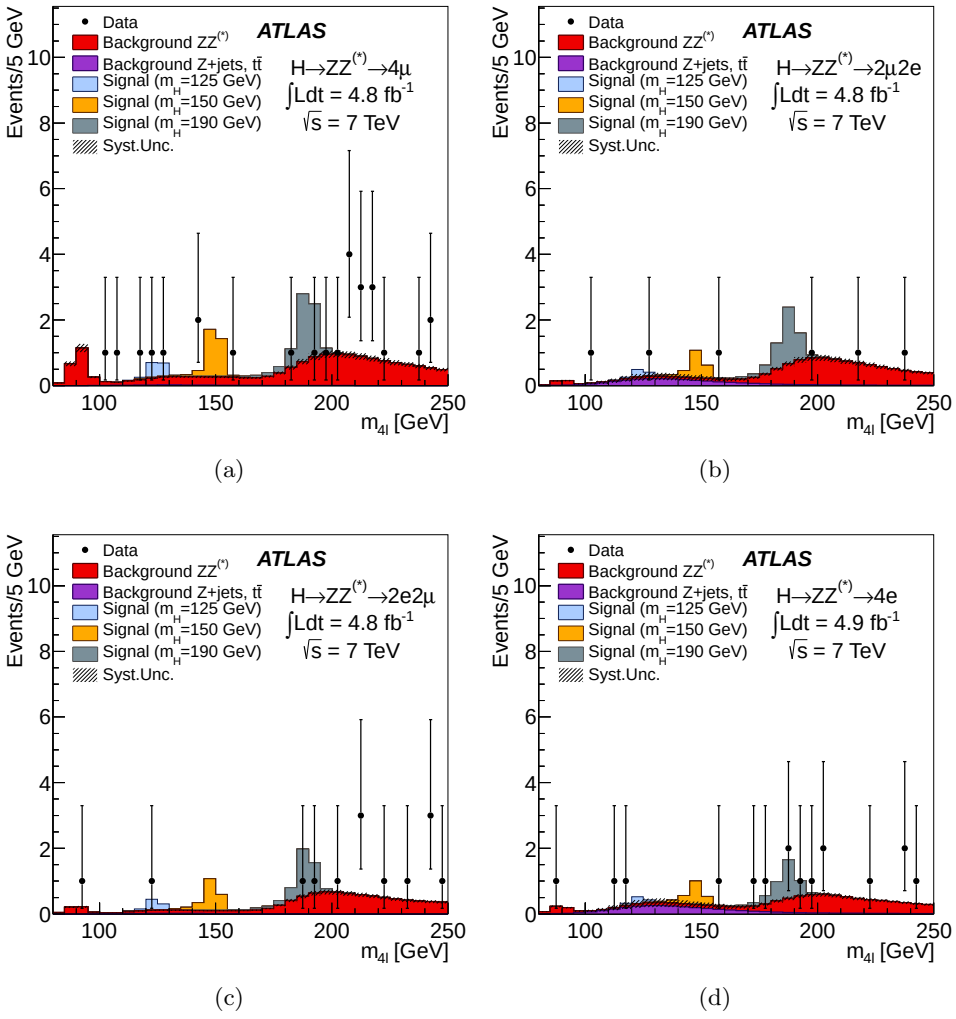

Figure 6.15: The distribution of the $m_{4\ell}$ is presented for the selected candidates for the various sub-channels: (a) 4μ, (b) $2\mu 2e$, (c) $2e2\mu$ and (d) $4e$, compared to the background expectation for the 80−250 GeV mass range. Error bars represent 68.3 % central confidence intervals. The signal expectation for several m_H hypotheses is also shown.

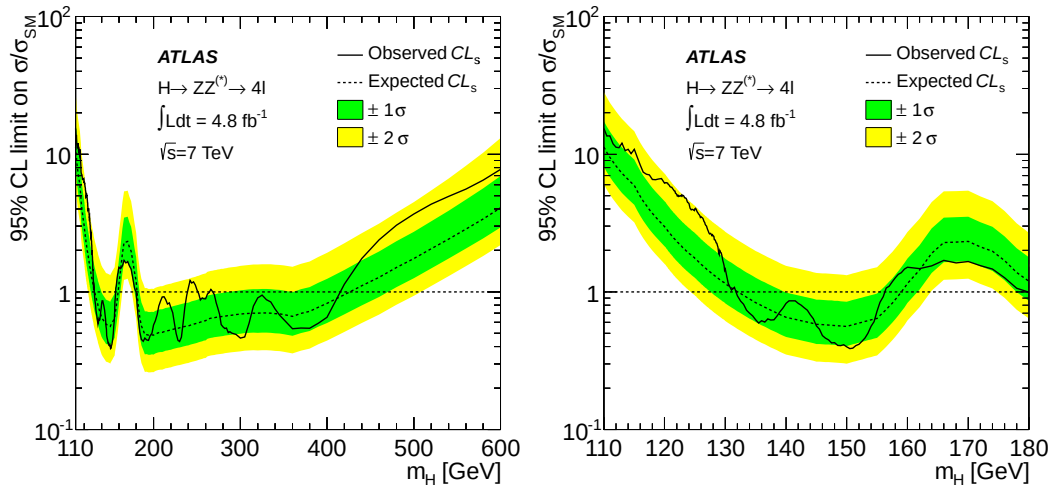

(a) (b)

Figure 6.16: The expected (dashed) and observed (full line) 95 % CL upper limits on the SM Higgs boson production cross section as a function of m_H, divided by the expected SM Higgs boson cross section is presented (a) in the full range under consideration and (b) in the low mass region. The dark (green) and light (yellow) bands indicate the expected limits with $\pm 1\sigma$ and $\pm 2\sigma$ fluctuations, respectively.

expected for the total background and several signal hypotheses in the whole mass range and in the low mass region. In Figures 7.10 the $m_{4\ell}$ mass distributions for each sub-channel, 4μ, $2\mu 2e$, $2e2\mu$ and $4e$ are shown, respectively.

The systematic uncertainties remain at the same level as described in Section 5.8. However, systematics for the background estimation have changed due to the new methods applied. For the m_{12}-fit method, an uncertainty of 50 % has been applied to the $t\bar{t}$ estimation and 30 % to the Z+jets contribution. In the $\mu\mu/ee + ee$ estimation a systematic uncertainty of 15 % has been used.

Upper limits are set on the Higgs boson production cross section at 95 % CL, using the CL_s modified frequentist formalism with the profile likelihood ratio test statistic. The test statistic is evaluated using a binned maximum-likelihood fit of signal and background models to the observed $m_{4\ell}$ distribution. Figures 6.16 show the observed and expected 95 % CL cross section upper limits, as a function of m_H. The SM Higgs boson is excluded at 95 % CL in the mass ranges $132 - 156$ GeV, $180 - 239$ GeV, $251 - 264$ GeV and $268 - 414$ GeV. The expected exclusion mass ranges are $132 - 159$ GeV and $181 - 426$ GeV.

In Figure 6.17 the local p_0 is presented as a function of the m_H hypothesis for each analysis subchannel. The most significant upward deviations from the background-only hypothesis in data are observed for $m_H = 125$ GeV with a local p_0 of 0.6 % (2.5 standard deviations), for $m_H = 242$ GeV with a local p_0 of 0.9 % (2.4 standard deviations) and for $m_H = 480$ with a local p_0 of 1.3 % (2.2 standard deviations). The increase on the signal significance for $m_H = 125$ GeV in the new analysis with respect to the 2011 one is 19 %.

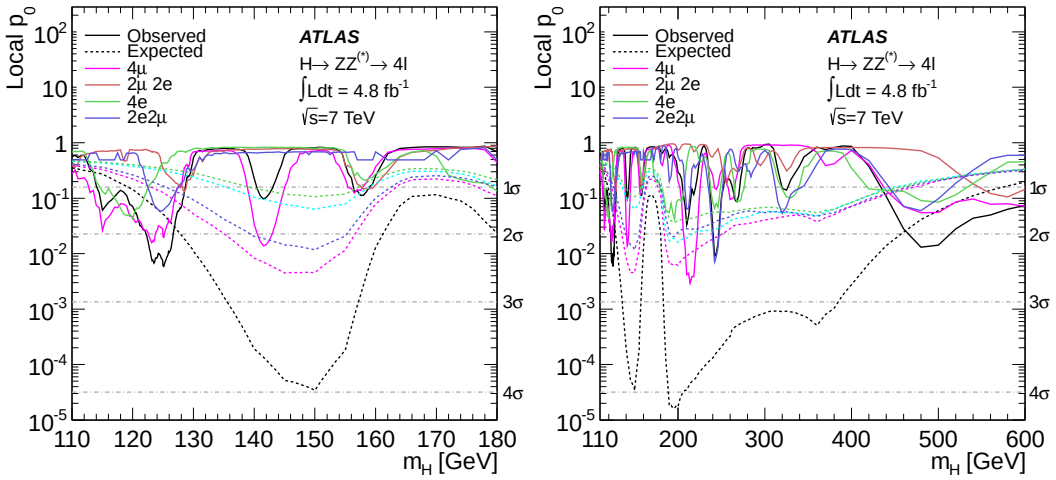

(a) (b)

Figure 6.17: The observed local p_0, the probability that the background fluctuates to the observed number of events or higher, is shown (a) in the low mass region and (b) in the full mass range for each analysis subchannel and their combination. Dashed curves show the expected median local p_0 for the signal hypothesis when tested at m_H.

Chapter 7

Search for the $H \to ZZ^{(*)} \to 4\ell$ using 5.8 fb^{-1} of 8 TeV data and 4.8 fb^{-1} of 7 TeV data

For 2012 data taking, the LHC centre-of-mass energy was increased to 8 TeV. This results in an increase in both the signal cross section, of about 30 %, and the background ones, depending on the process and reaching up to 68.5 % for $t\bar{t}$ production.

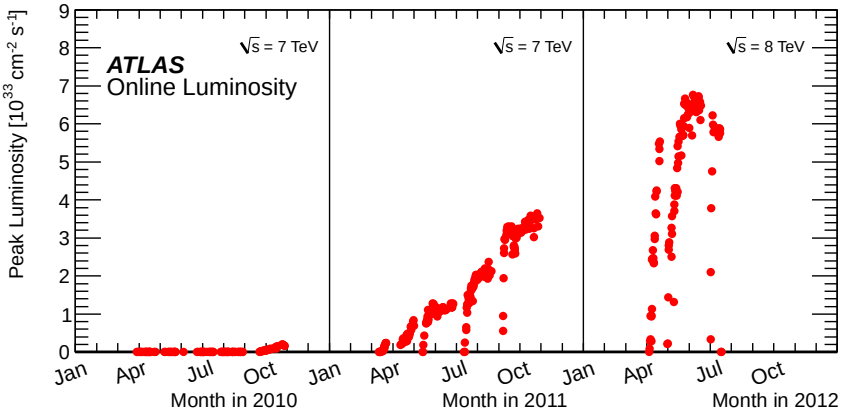

Figure 7.1: The peak instantaneous luminosity delivered to ATLAS per day is presented versus time during the $p-p$ runs of 2010, 2011 and 2012.

The LHC parameters during 2012 data taking have resulted to a relative increase on the instantaneous luminosity delivered to ATLAS with respect to 2011 data taking. In Figure 7.1 the peak instantaneous luminosity delivered to ATLAS per day is presented versus time during the pp runs of 2010, 2011 and 2012. A peak luminosity record of $6.8 \times 10^{33}\,\mathrm{cm}^{-2}\mathrm{s}^{-1}$ has been reached. As a result, the mean number of interactions per bunch crossing has increased by approximately a factor of two as shown in Figure 2.4. In Figure 2.3 the cumulative integrated luminosity per day during stable beams is presented for the three years of data taking.

Table 7.1: Higgs boson production cross sections are quoted for gluon fusion, vector-boson fusion and associated production with a vector boson in pp collisions at $\sqrt{s} = 8\,\text{TeV}$. The quoted uncertainties correspond to the total theoretical systematic uncertainty. The branching ratio of $H \to 4\ell$, with $\ell = e, \mu$, is reported in the last column.

m_H [GeV]	$\sigma(gg \to H)$ [pb]	$\sigma(qq \to Hqq)$ [pb]	$\sigma(qq \to WH)$ [pb]	$\sigma(qq \to ZH)$ [pb]	$\text{BR}(H \to 4\ell)$ $\times 10^{-3}$
125	19.5 ± 2.9	$1.56^{+0.04}_{-0.05}$	0.70 ± 0.03	0.39 ± 0.02	0.13
130	18.1 ± 2.6	1.49 ± 0.04	0.61 ± 0.03	0.35 ± 0.02	0.19
190	7.9 ± 1.1	$0.91^{+0.03}_{-0.02}$	0.156 ± 0.007	0.094 ± 0.006	0.94
400	2.9 ± 0.4	0.25 ± 0.01	–	–	1.21
600	0.5 ± 0.1	0.097 ± 0.004	–	–	1.23

In this Chapter, the results of the analysis on $5.8\,\text{fb}^{-1}$ of 8 TeV data are presented along with the results of the combination with $4.8\,\text{fb}^{-1}$ of 7 TeV data and other Higgs searches. These results have been published in Phys. Lett. B716.

7.1 Data samples and event selection

Both $H \to ZZ^{(*)} \to 4\ell$ signal and background samples have been modeled using the same MC event generators as in the 7 TeV data described in Section 5.2. The cross sections for the exclusive production mechanisms and the branching ratios for some generated m_H are listed in Table 7.1 for pp collisions at $\sqrt{s} = 8\,\text{TeV}$.

Data are selected using single lepton and dilepton unprescaled triggers as in 2011 data taking but the p_T thresholds have been increased a bit. For the single muon trigger the threshold is raised to 24 GeV, while for the single electron to 25 GeV. For the dimuon triggers the thresholds are $p_\text{T} = 13\,\text{GeV}$ for each muon or $p_{\text{T}1} = 18\,\text{GeV}$, $p_{\text{T}2} = 8\,\text{GeV}$ in the case of the asymmetric trigger, while for the dielectron triggers the thresholds are $E_{\text{T}1} = 12\,\text{GeV}$ for each electron.

For the 2012 LHC data taking, the electron reconstruction algorithm is improved with respect to 2011, improving the performance at low p_T. The ATLAS track pattern recognition and fit procedure were updated to account for energy losses due to bremsstrahlung, and the track-to-cluster matching algorithm was improved to be less sensitive to bremsstrahlung losses. All tracks associated to electromagnetic clusters are re-fitted using a Gaussian-Sum Filter [34], as in the 2011 analysis, which allows for bremsstrahlung energy losses.

The requirements applied in the analysis follow the event selection in 2011, described in Section 5.3 with the exception of the electron calorimetric isolation. The calorimetric isolation for the electrons in the 2012 analysis is topological-cluster based [93] rather than cell based. The algorithm for topological clustering suppresses noise by keeping cells with a significant energy deposit and their neighbours.

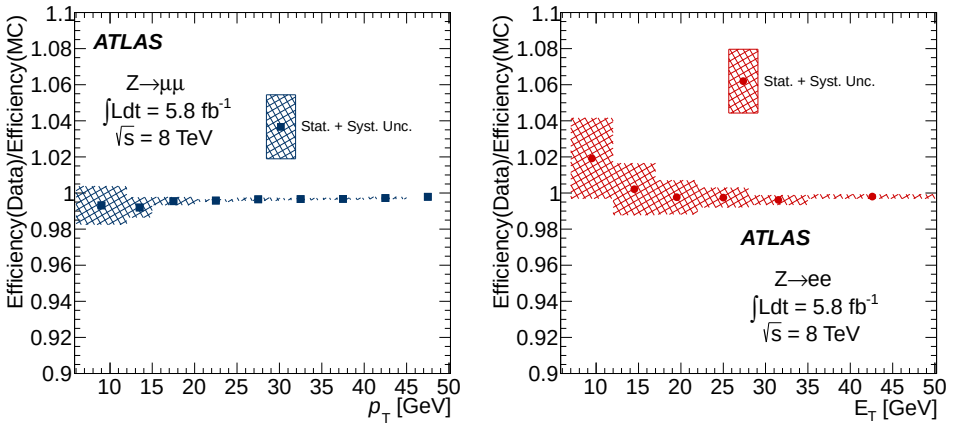

(a) (b)

Figure 7.2: The ratio of the isolation and impact parameter efficiencies between data and simulation, estimated with the Tag and Probe method, using (a) $Z \to \mu\mu$ and (b) $Z \to ee$ events.

The ambient energy deposition in the event from pileup and the underlying event is also accounted for using a calculation of the median transverse energy density from low-pT jets [94, 95]. The normalized calorimetric isolation for electrons is required to be less than 0.20, instead of 0.30 in 2011 analysis.

The efficiency of the isolation and impact parameter requirements on signal-like muons and electrons has been revised using the Tag and Probe method. It is found to be greater than 92 % even in the low energy leptons. The efficiency ratio between data and MC simulation is shown in Figure 7.2.

The combined signal reconstruction and selection efficiencies for a SM Higgs with $m_H = 125\,\text{GeV}(m_H = 130\,\text{GeV})$ are 36 %(41 %) for the 4μ channel, 22 %(27 %) for the $2e2\mu/2\mu2e$ channels and 20 %(23 %) for the $4e$ channel.

7.2 Background estimation

The expected background yield and its composition is estimated using MC simulation normalized to the theoretical cross section for $ZZ^{(*)}$ production and using data-driven methods for the Z+jets and $t\bar{t}$ processes and the background composition depends on the flavor of the subleading dilepton. Following the methods described in Section 6.3.4, the expected background yields in the signal region are summarized in Table 7.2 for all the final states.

For the estimation of the $Z+b\bar{b}$ and $t\bar{t}$ background processes, the m_{12}-fit method is used in the subleading dimuon final states, described in Section 6.3.4. The m_{12} distribution for this control region is shown in Figure 7.3 and the transfer factors for the extrapolation of the yields to the signal region are calculated to be $3.3 \pm 0.3 \pm 1.0$ for $Zb\bar{b}$ and $0.3 \pm 0.1 \pm 0.1$ for $t\bar{t}$.

For the background contribution of the subleading electron final states the method

Table 7.2: The estimation for the reducible background is presented. The first uncertainty is statistical, while the second one is systematic.

Method	Estimated number of events
4μ	
m_{12} fit: $Z+$jets contribution	0.51±0.13±0.16
m_{12} fit: $t\bar{t}$ contribution	0.04±0.02±0.02
$2e2\mu$	
m_{12} fit: $Z+$jets contribution	0.41±0.10±0.13
m_{12} fit: $t\bar{t}$ contribution	0.04±0.01±0.01
$2\mu 2e$	
$\ell\ell + e^{\pm}e^{\mp}$	4.9± 0.8 ±0.7
$\ell\ell + e^{\pm}e^{\pm}$ (check)	4.1± 0.6 ±0.8
$3\ell + \ell$ (check)	3.5± 0.5 ±0.5
$4e$	
$\ell\ell + e^{\pm}e^{\mp}$	3.9± 0.7 ±0.8
$\ell\ell + e^{\pm}e^{\pm}$ (check)	3.1± 0.5 ±0.6
$3\ell + \ell$ (check)	3.0± 0.4 ±0.4

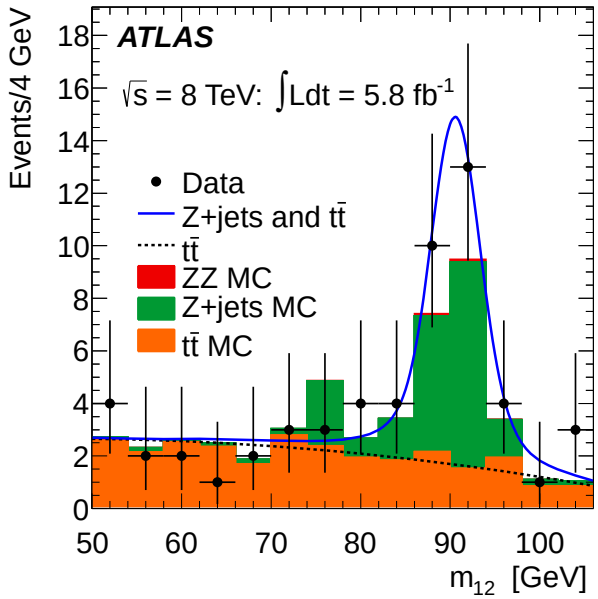

Figure 7.3: Distribution of m_{12} in the control region where the isolation requirements are not applied to the two subleading muons, and at least one of these muons fails the impact parameter significance requirement. The fit used to obtain the yields for $t\bar{t}$ and Z+jets is presented.

Table 7.3: The observed and expected yields of $\mu\mu/ee+ee$ events are quoted for the subleading dielectron categories in the control region where the electron requirements on the subleading dielectron are relaxed.

	$4e$		$2\mu 2e$	
	Data	MC	Data	MC
EE	11	14.61	8	17.82
EC	4	2.431	3	1.768
EF	6	10.34	5	5.358
CE	5	1.592	6	3.059
CC	2	1.378	2	0.774
CF	7	4.68	10	5.282
FE	5	3.529	4	3.733
FC	5	2.784	4	4.048
FF	12	10.11	17	9.149
Total	57	51.46	59	50.99

used in the 2011 analysis is applied. The subleading electrons in the relaxed electron identification control region are classified into electron-like (E), conversion-like (C) and fake-like (F), based on the B-layer, TRT and calorimeter measurement. The numbers of observed events in each category are presented in Table 7.3. Extrapolation is then performed to the signal region based on the truth based efficiencies of the remaining selection. The final background estimation is quoted in Table 7.2.

The m_{12} and m_{34} distributions for events selected by the analysis when relaxing the isolation and impact parameter requirements for the subleading dilepton are presented in Figure 7.4. The events are divided according to the flavor of the subleading lepton pair into $\ell\ell+\mu\mu$ and $\ell\ell+ee$ events. The MC is normalized to the data driven background estimations given in Table 7.2. The shape and normalization of the backgrounds are in good agreement with data. This is observed both for large values of m_{34}, where the $ZZ^{(*)}$ background dominates, and for low m_{34} values. When combining with the 2011 data, Figures 7.5 are extracted dividing the distributions according to the subleading dilepton flavor and in Figures 7.6 the distributions are combined for all flavors, including the contribution of the $m_H = 125\,\text{GeV}$ signal.

The shapes for the background are based on the MC simulation. The MC shape templates are checked with data in a Z+jets and $t\bar{t}$ enhanced control region where the subleading dilepton fails either the isolation or the impact parameter requirements. The comparison is shown in Figure 7.7 where the MC template is shown to be in good agreement within statistics with the data.

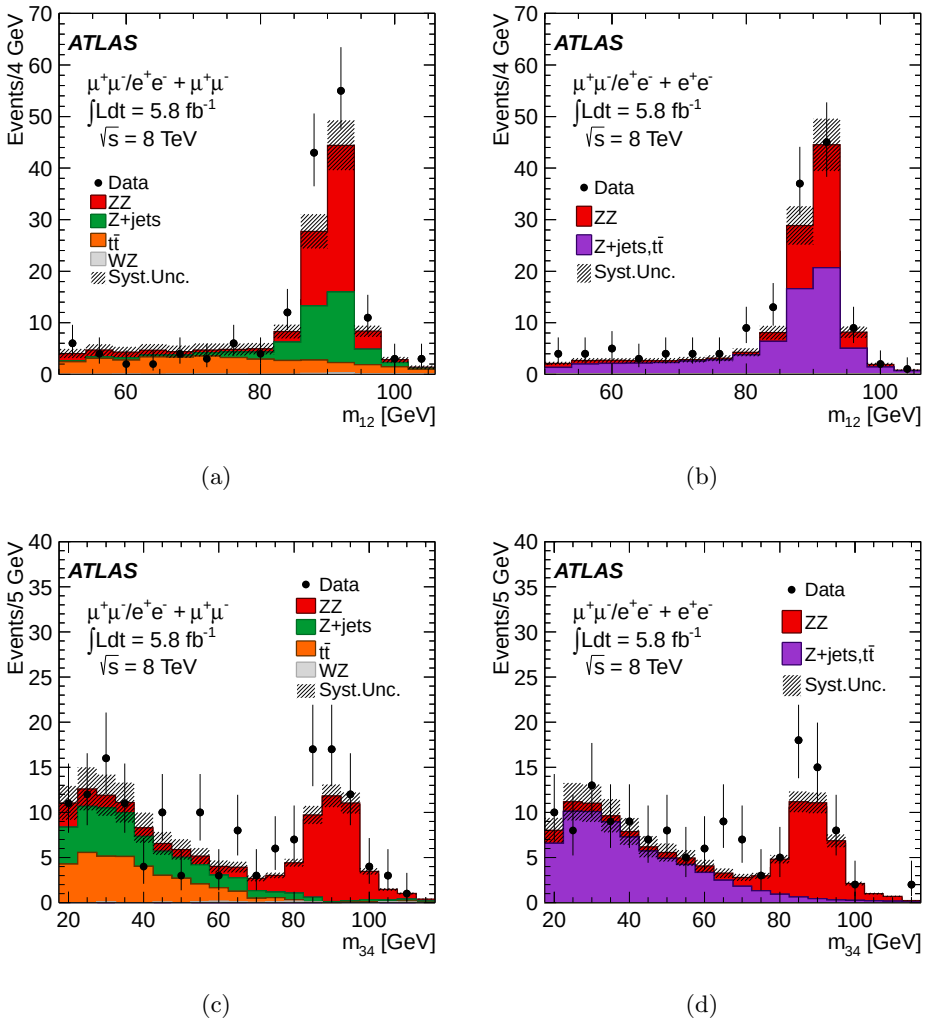

Figure 7.4: The invariant mass distributions of the lepton pairs in the control sample defined by a Z boson candidate and an additional same-flavor lepton pair are presented divided according to the flavor of the additional lepton pair. In (a) the m_{12} and in (c) the m_{34} distributions are presented for $\ell\ell\,(\mu^+\mu^-/e^+e^-)+\mu^+\mu^-$ events. In (b) the m_{12} and in (d) the m_{34} distributions are presented for $\ell\ell\,(\mu^+\mu^-/e^+e^-)+e^+e^-$ events. The kinematic selection of the analysis is applied. Isolation and impact parameter significance requirements are applied to the first lepton pair only.

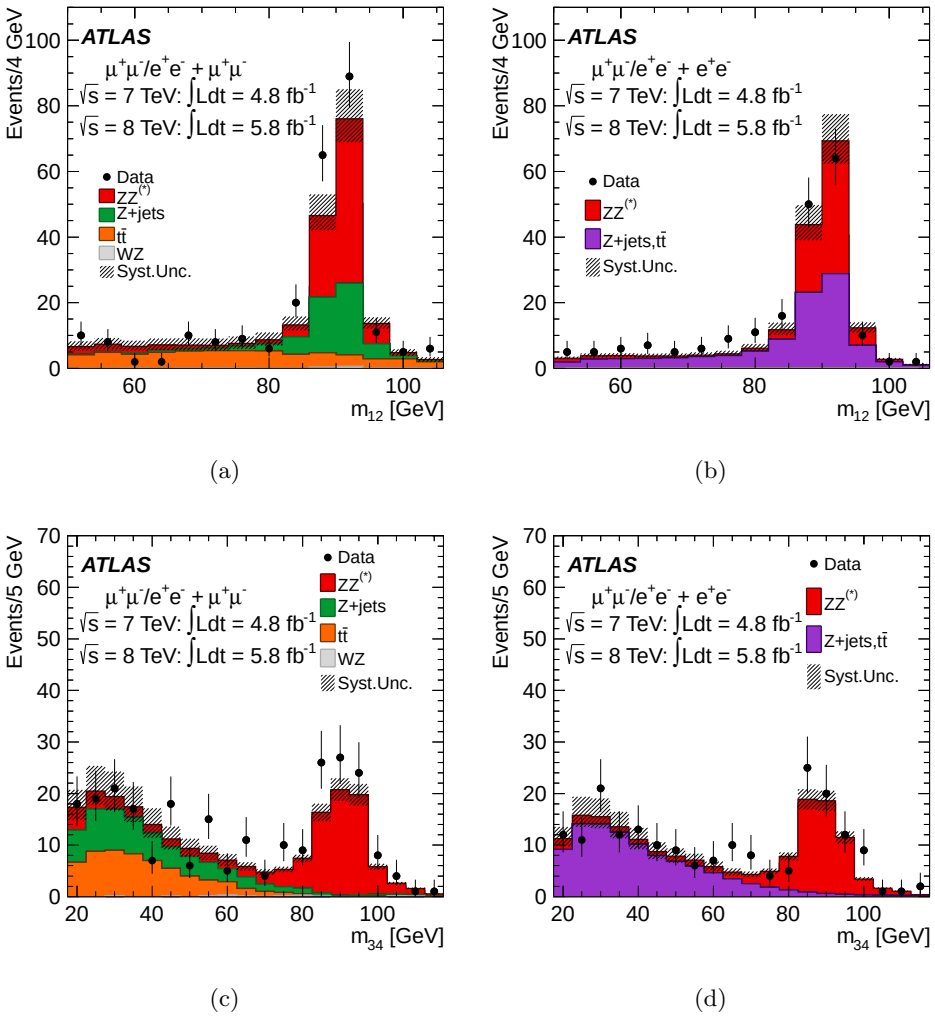

Figure 7.5: The invariant mass distributions of the lepton pairs in the relaxed control region are presented divided according to the flavor of the subleading dilepton after the combination of the 2011 and 2012 data. In (a) the m_{12} and in (c) the m_{34} distributions are presented for $\ell\ell\,(\mu^+\mu^-/e^+e^-) + \mu^+\mu^-$ events. In (b) the m_{12} and in (d) the m_{34} distributions are presented for $\ell\ell\,(\mu^+\mu^-/e^+e^-) + e^+e^-$ events. The kinematic selection of the analysis is applied. Isolation and impact parameter significance requirements are applied to the first lepton pair only.

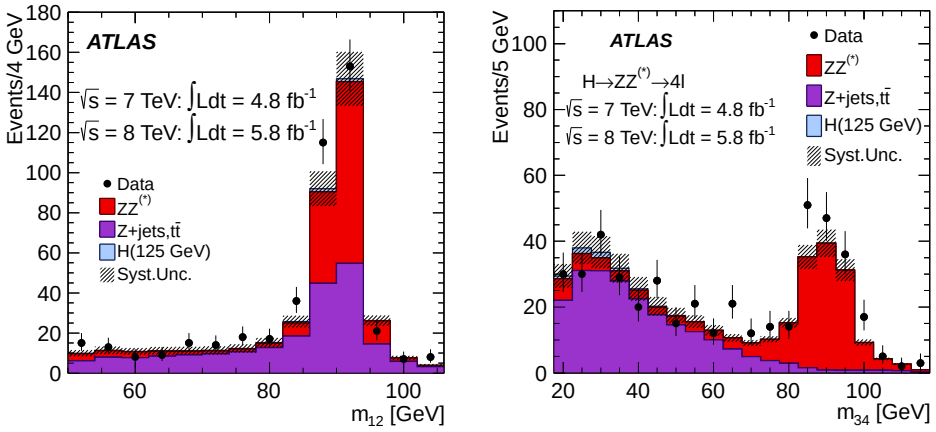

(a) (b)

Figure 7.6: The (a) m_{12} and (b) m_{34} invariant mass distributions of the lepton pairs in the relaxed control region are presented after the combination of the 2011 and 2012 data. The kinematic selection of the analysis is applied. Isolation and impact parameter significance requirements are applied to the first lepton pair only.

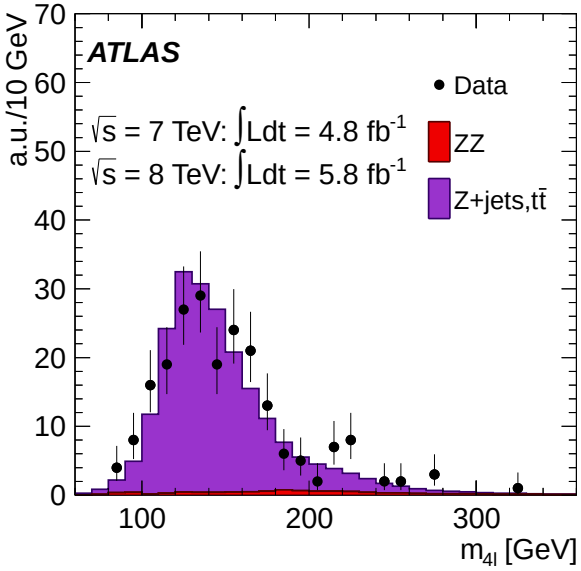

Figure 7.7: Shape comparison of the $m_{4\ell}$ distribution used for the contributions contributions in a control region where the subleading dilepton fails either the isolation or the impact parameter significance requirements of the analysis. Both $\sqrt{s} = 7\,\text{TeV}$ and $\sqrt{s} = 8\,\text{TeV}$ data samples are used.

Table 7.4: List of the $4e$ candidates passing the full selection using $5.9\,\text{fb}^{-1}$ of $8\,\text{TeV}$ data.

N	Run Number	Event Number	LB	$m_{4\ell}$ [GeV]	m_{12} [GeV]	m_{34} [GeV]
1	201113	36934150	399	307.39	83.88	75.14
2	202991	29492591	418	209.61	91.38	76.64
3	203335	44927851	250	211.11	96.00	85.55
4	203432	58320601	456	162.20	76.45	52.73
5	203524	64340754	365	188.74	90.64	92.83
6	203602	82614360	429	124.49	70.63	44.66
7	203602	99681996	532	174.60	79.83	70.22
8	203602	106701658	578	296.57	92.42	113.69
9	203636	95484441	546	399.18	87.43	101.72
10	203680	44088690	548	229.24	89.02	94.45
11	203719	20441551	149	264.36	91.14	88.69
12	203739	73042609	864	220.25	89.80	79.23
13	203934	89714329	997	87.38	51.22	30.05
14	203934	91585470	1005	160.06	72.78	47.13
15	204240	29054747	685	195.52	90.85	86.37
16	204265	11531490	170	201.28	89.15	88.61
17	204265	15870479	185	193.92	90.74	93.34
18	204564	72798274	843	143.80	84.63	31.64
19	204564	76786292	858	114.14	57.28	49.05
20	204564	193961472	1290	192.23	91.11	87.19
21	204564	228171673	1464	301.72	88.80	87.78
22	204633	4809722	171	193.42	87.37	84.98
23	204668	60678687	252	202.59	87.72	86.36
24	204726	20583917	203	105.06	51.41	31.21
25	204910	22993546	376	125.52	88.93	22.28
26	204932	53150539	301	187.78	91.69	64.28
27	204932	60690285	335	261.82	89.36	88.08
28	204954	19454464	152	378.19	84.48	83.41
29	204955	90366740	412	114.55	77.26	35.82
30	205055	13546817	348	208.81	90.76	89.33
31	205071	193422310	1106	549.31	91.93	93.05
32	205112	46981864	434	280.77	91.04	89.70

Table 7.5: List of the 4μ candidates passing the full selection using $5.8\,\text{fb}^{-1}$ of 8 TeV data.

N	Run Number	Event Number	LB	$m_{4\ell}$ [GeV]	m_{12} [GeV]	m_{34} [GeV]
1	200926	17712380	418	300.17	90.39	94.42
2	201494	26817712	140	273.60	91.85	85.11
3	202668	26299894	221	384.08	90.82	83.75
4	203195	5763465	109	255.93	86.05	83.46
5	203258	59505222	399	228.83	92.53	86.64
6	203277	22949094	269	191.04	89.44	88.84
7	203353	26647061	384	242.54	91.53	86.98
8	203432	46880033	391	213.27	91.09	92.56
9	203456	24914034	119	187.57	91.35	74.74
10	203524	62321499	355	237.94	91.01	90.39
11	203602	80248134	415	376.59	91.94	92.41
12	203636	34504484	215	337.53	88.57	86.26
13	203745	63994592	371	227.42	91.39	91.59
14	203779	46710128	499	344.23	93.90	80.11
15	203876	9282788	483	326.67	87.46	85.90
16	203934	100600041	1050	210.74	91.83	89.81
17	204026	87732822	472	189.95	89.98	93.54
18	204071	30963264	476	261.35	88.98	77.71
19	204073	18405446	203	278.84	91.02	87.11
20	204153	22992989	146	120.99	54.55	20.85
21	204153	32436165	180	574.78	88.08	82.53
22	204158	108769641	783	231.71	91.24	90.90
23	204240	52902065	786	209.05	94.36	85.81
24	204416	20491680	88	295.18	93.47	72.17
25	204564	25416035	663	128.72	90.94	27.48
26	204564	149682166	1125	281.83	88.34	86.99
27	204763	64671324	313	220.33	93.95	61.55
28	204763	198344978	956	361.78	92.19	85.51
29	204769	71902630	398	124.09	86.34	31.57
30	204769	82599793	447	123.25	84.01	34.21
31	204769	84802829	457	422.79	91.59	89.21
32	204976	52368897	312	191.49	90.87	96.97
33	205016	37425673	144	513.24	92.28	97.61
34	205017	7255669	33	196.20	89.54	89.34
35	205071	55053974	414	264.86	88.06	94.68
36	205071	222074238	1245	303.05	91.87	91.94
37	205112	29305779	362	213.82	89.97	85.84
38	205112	58173349	479	319.11	100.19	74.51

Table 7.6: List of the $2e2\mu$ candidates passing the full selection using 4.8 fb^{-1} of 8 TeV data.

N	Run Number	Event Number	LB	$m_{4\ell}$ [GeV]	m_{12} [GeV]	m_{34} [GeV]
1	200987	50726675	356	246.36	87.17	110.04
2	201113	29045106	344	202.32	91.60	90.37
3	201113	34945963	383	264.99	87.92	94.89
4	201138	27887257	407	212.80	89.58	86.61
5	201190	13200815	151	236.30	87.75	106.78
6	202798	43736485	699	161.04	74.92	61.78
7	203027	71454016	782	193.62	91.34	92.81
8	203195	25217284	227	361.43	91.93	89.71
9	203228	15214720	173	233.75	90.67	87.77
10	203258	105740575	742	129.92	86.24	25.44
11	203353	79978481	686	373.72	83.38	56.36
12	203432	20659622	238	448.87	90.88	96.62
13	203523	13350735	295	206.62	93.23	84.79
14	203636	10916804	109	319.08	89.70	93.70
15	203636	69879354	396	432.08	91.88	89.35
16	203739	67630085	839	259.21	88.51	94.43
17	203876	96963848	750	341.25	87.45	64.44
18	204153	33235991	183	193.27	90.30	89.83
19	204158	18242755	397	264.46	91.06	96.38
20	204240	31409138	695	228.96	90.43	79.30
21	204240	151358568	1230	193.69	90.50	89.85
22	204265	72546153	406	198.86	87.64	86.98
23	204416	42212637	172	193.05	88.24	97.09
24	204474	56451245	335	266.04	85.50	84.23
25	204474	89082513	490	184.28	95.22	78.48
26	204763	5630931	75	89.05	51.36	17.89
27	204763	67344918	325	214.16	89.94	88.42
28	204910	95498501	722	266.89	89.57	64.92
29	204955	16392574	70	325.42	83.81	101.79
30	204955	72469686	322	181.39	91.20	89.27
31	205112	25095415	346	168.15	89.44	71.57
32	205113	12611816	632	122.65	87.96	19.63

Table 7.7: List of the $2\mu 2e$ candidates passing the full selection using $4.8\,\text{fb}^{-1}$ of 8 TeV data.

N	Run Number	Event Number	LB	$m_{4\ell}$ [GeV]	m_{12} [GeV]	m_{34} [GeV]
1	201113	55604596	559	222.15	92.54	88.27
2	201257	21308431	430	188.00	89.26	86.16
3	201257	121862343	980	353.11	90.95	93.62
4	201289	10043905	131	219.11	88.86	82.33
5	201556	6395332	436	177.52	88.82	86.04
6	201556	10787809	453	212.54	80.22	77.61
7	202798	7203716	466	241.14	87.05	63.69
8	203258	114413312	804	185.53	88.12	95.26
9	203335	49048571	273	283.14	93.03	88.84
10	203353	7225045	288	162.04	83.70	52.13
11	203353	28661403	394	200.93	93.95	87.55
12	203524	28303221	183	198.44	89.66	82.69
13	203636	65210779	369	211.00	89.77	84.61
14	203680	10638148	388	175.39	84.76	79.99
15	203719	12262192	124	251.36	86.80	85.88
16	203745	75039428	433	230.74	96.53	69.92
17	203745	90860257	524	310.81	90.47	83.83
18	203876	36135200	578	287.43	89.83	78.60
19	203876	60324400	653	209.61	90.15	88.41
20	203934	70728810	914	148.80	88.45	49.51
21	203934	98492930	1038	254.36	90.95	90.17
22	204071	32311568	481	293.63	92.93	88.38
23	204073	38389153	276	190.56	89.54	88.83
24	204153	26755807	159	225.19	83.50	83.32
25	204265	223273173	1213	368.63	91.69	112.88
26	204474	131005091	707	230.69	84.44	59.88
27	204474	134814016	725	93.44	56.20	25.35
28	204564	68230882	825	896.52	90.97	92.87
29	204564	198222712	1308	219.26	92.57	62.45
30	204668	141229289	617	201.90	92.44	94.04
31	204763	95056361	457	118.83	89.23	27.26
32	204769	38987331	252	242.53	92.15	86.66
33	204772	81936527	384	85.48	56.16	27.93
34	204932	57770438	323	265.12	90.25	87.58
35	204954	36015359	211	154.04	93.01	48.18
36	205017	18590216	79	152.11	95.92	47.39
37	205055	201414970	1178	272.84	91.28	86.12
38	205071	36046056	346	128.19	89.68	31.91
39	205112	5259842	277	113.60	88.22	20.79
40	205113	28375316	689	247.80	92.50	89.12

Table 7.8: The observed numbers of events and the final estimate for the expected backgrounds, separated into "Low mass" ($m_{4\ell} < 160\,\text{GeV}$) and "High mass" ($m_{4\ell} \geq 160\,\text{GeV}$) regions. The expected numbers of signal events is also shown for various Higgs boson mass hypotheses. For signal and background estimates, the corresponding total uncertainty is given.

	4μ		$2e2\mu/2\mu2e$		$4e$	
Int. Luminosity	$5.8\,\text{fb}^{-1}$		$5.8\,\text{fb}^{-1}$		$5.9\,\text{fb}^{-1}$	
	Low mass	High mass	Low mass	High mass	Low mass	High mass
$ZZ(*)$	6.3±0.3	27.5±1.9	3.7±0.2	41.7±3.0	2.9±0.3	17.7±1.4
Z+jets and $t\bar{t}$	0.4±0.2	0.15±0.07	3.9±0.9	1.4±0.3	2.9±0.8	1.0±0.3
Total Background	6.7±0.3	27.6±1.9	7.6±1.0	43.1±3.0	5.7±0.8	18.8±1.4
Data	4	34	11	61	7	25
$m_H = 125\,\text{GeV}$	1.4±0.2		1.7±0.2		0.8±0.1	
$m_H = 150\,\text{GeV}$	4.5±0.6		5.9±0.8		2.7±0.4	
$m_H = 190\,\text{GeV}$	8.2±1.0		12.5±1.7		5.3±0.8	
$m_H = 400\,\text{GeV}$	3.9±0.5		6.6±0.9		2.9±0.4	

Table 7.9: The numbers of expected signal and background events together with the number of observed events, in a window of $\pm 5\,\text{GeV}$ around the hypothesized Higgs boson mass for the $5.8\,\text{fb}^{-1}$ at $\sqrt{s} = 8\,\text{TeV}$ and the $4.8\,\text{fb}^{-1}$ at $\sqrt{s} = 7\,\text{TeV}$ datasets as well as for their combination.

	$\sqrt{s} = 8\,\text{TeV}$			$\sqrt{s} = 7\,\text{TeV}$			$\sqrt{s} = 8\,\text{TeV}$ and $\sqrt{s} = 7\,\text{TeV}$		
				4μ					
m_H	exp. signal	exp. bkg	obs	exp. signal	exp. bkg	obs	exp. signal	exp. bkg	obs
120	0.68±0.09	0.61± 0.04	2	0.48±0.06	0.46± 0.03	2	1.16± 0.15	1.07± 0.07	4
125	1.25±0.17	0.74± 0.05	4	0.84±0.11	0.56± 0.03	2	2.09± 0.28	1.30± 0.08	6
130	1.88±0.25	0.81± 0.05	2	1.38±0.18	0.63± 0.03	1	3.26± 0.43	1.44± 0.08	3
				$2e2\mu/2\mu2e$					
m_H	exp. signal	exp. bkg	obs	exp. signal	exp. bkg	obs	exp. signal	exp. bkg	obs
120	0.81±0.12	1.15± 0.17	2	0.48±0.07	0.78± 0.10	1	1.29± 0.19	1.93± 0.18	3
125	1.45±0.20	1.30± 0.19	3	0.83±0.11	0.89± 0.11	2	2.28± 0.31	2.19± 0.21	5
130	2.24±0.32	1.34± 0.20	2	1.27±0.17	0.94± 0.11	1	3.51± 0.49	2.28± 0.21	3
				$4e$					
m_H	exp. signal	exp. bkg	obs	exp. signal	exp. bkg	obs	exp. signal	exp. bkg	obs
120	0.35±0.05	0.79±0.15	1	0.15±0.02	0.60±0.12	1	0.50±0.07	1.39±0.19	2
125	0.61±0.09	0.90±0.17	2	0.28±0.04	0.69±0.13	0	0.89±0.13	1.59±0.22	2
130	0.91±0.15	0.96±0.17	1	0.42±0.06	0.74±0.14	0	1.33±0.21	1.70±0.22	1

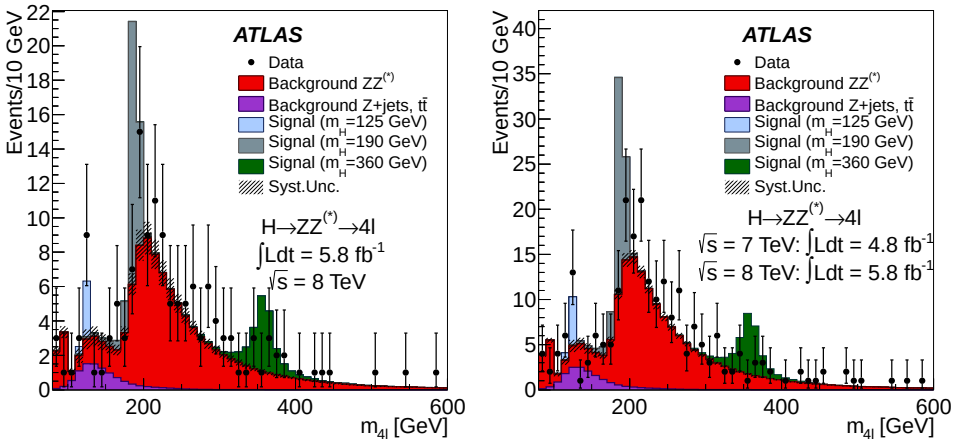

(a) (b)

Figure 7.8: The $m_{4\ell}$ invariant mass is presented for the selected candidates compared to the background expectation in the range $80 - 600\,\text{GeV}$ for the (a) $\sqrt{s} = 8\,\text{TeV}$ and (b) $\sqrt{s} = 7\,\text{TeV}$ datasets. The error bars represent the 68.3% central confidence intervals. The signal expectation for several m_H hypotheses is also shown.

7.3 Results of event selection

Using $5.8\,\text{fb}^{-1}$ of 8 TeV data 142 candidates events survive the analysis. The details on these events are presented in Tables 7.4 to 7.7. In Table 7.8, the numbers of events observed in each final state are summarized and compared to the expected backgrounds, separately for $m_{4\ell} < 160\,\text{GeV}$ and $m_{4\ell} \geq 160\,\text{GeV}$, and to the expected signal for various m_H hypotheses. Table 7.9 presents the observed and expected events, in a window of $\pm 5\,\text{GeV}$ around various hypothesized Higgs boson masses, for the $5.8\,\text{fb}^{-1}$ at $\sqrt{s} = 8\,\text{TeV}$ and the $4.8\,\text{fb}^{-1}$ at $\sqrt{s} = 7\,\text{TeV}$ datasets as well as for their combination.

The expected $m_{4\ell}$ distributions for the total background and several signal hypotheses are compared to the data in Figure 7.8. Figure 7.9 presents the same distributions only for the low mass range $80 - 250\,\text{GeV}$. In Figures 7.10 and 7.11 the $m_{4\ell}$ mass distributions for each sub-channel (4μ, $2\mu 2e$, $2e2\mu$, $4e$) are shown for the data at $\sqrt{s} = 8\,\text{TeV}$ and the combination of 2011 and 2012, respectively. In Figure 7.12 the m_{34} invariant mass with respect to m_{12} is presented. The expected distribution for $m_H = 125\,\text{GeV}$ is superimposed, with the size of the boxes indicating the relative density, as well as the expected distribution for the total background, with the intensity of the shading indicating the relative density. The distribution does not depict results from the Z-mass constrained kinematic fit.

High-p_{T} photon emissions from final state radiation (FSR), although occurring at a low rate, are not taken into account explicitly in the lepton reconstruction, and affect the reconstructed invariant mass in rare cases. In MC, QED corrections are fully considered and accounted for in the templates used for the mass distributions. All candidates selected have been checked and no appreciable FSR activity has been

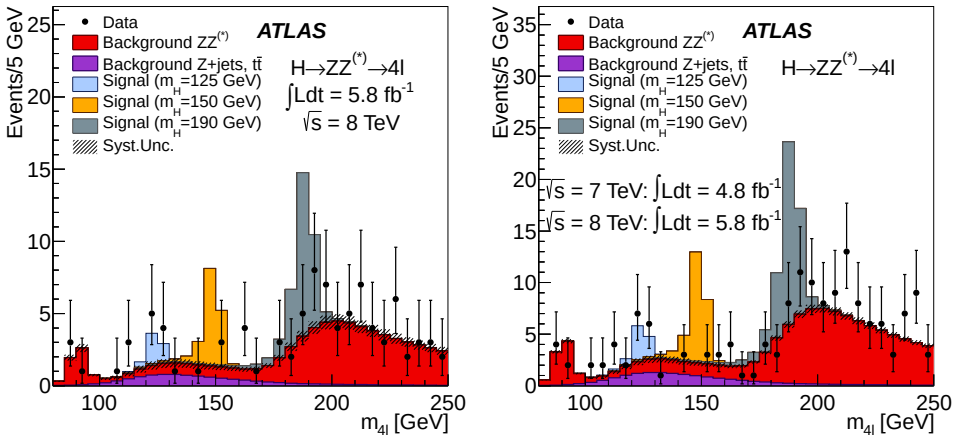

(a) (b)

Figure 7.9: The $m_{4\ell}$ invariant mass is presented for the selected candidates compared to the background expectation in the $80 - 250\,\text{GeV}$ mass range for the (a) $\sqrt{s} = 8\,\text{TeV}$ and (b) $\sqrt{s} = 7\,\text{TeV}$ datasets. Error bars represent 68.3% central confidence intervals. The signal expectation for several m_H hypotheses is also shown.

found for the candidates below 160 GeV.

7.4 Systematic uncertainties

The theoretical uncertainties have been studied extensively by the LHC Higgs cross section working group [12]. The QCD scale uncertainties for $m_H = 125\,\text{GeV}$ amount to $^{+7}_{-8}\,\%$ for the gluon-fusion process and $\pm 1\,\%$ for the vector-boson fusion and associated WH/ZH production processes. The uncertainty of the production cross section due to uncertainties of the parton distribution function (PDF) and α_s is $\pm 8\,\%$ for gluon-initiated processes and $\pm 4\,\%$ for quark-initiated processes, estimated by following the prescription in Reference [75] and by using the PDF sets of CTEQ [77], MSTW [78] and NNPDF [79]. The PDF uncertainties are assumed to be 100 % correlated among processes with identical initial states, regardless of these being signal or background [75–79]. The uncertainties on the predicted branching ratios amount to $\pm 5\,\%$.

For the SM $ZZ^{(*)}$ background, which is estimated from MC simulation, the uncertainty on the total yield due to the QCD scale uncertainty is $\pm 5\,\%$, while the effect of the PDF and α_s uncertainties is $\pm 4\,\%$ and $\pm 8\,\%$ for processes initiated by quarks and gluons, respectively [13]. In addition, the dependence of these uncertainties on the four-lepton invariant mass spectrum has been taken into account. Though a small excess of events is observed for $m_{4\ell} > 180\,\text{GeV}$, the measured $ZZ^{(b)} \to 4\ell$ cross section [96] is consistent with the SM theoretical prediction. The impact of not using the theoretical constraints on the $ZZ^{(b)}$ yield on the search for a Higgs boson with $m_H < 2m_Z$ has been studied [97] and has been found to be negligible. The impact of the interference between a Higgs signal and the non-resonant $gg \to ZZ^{(b)}$

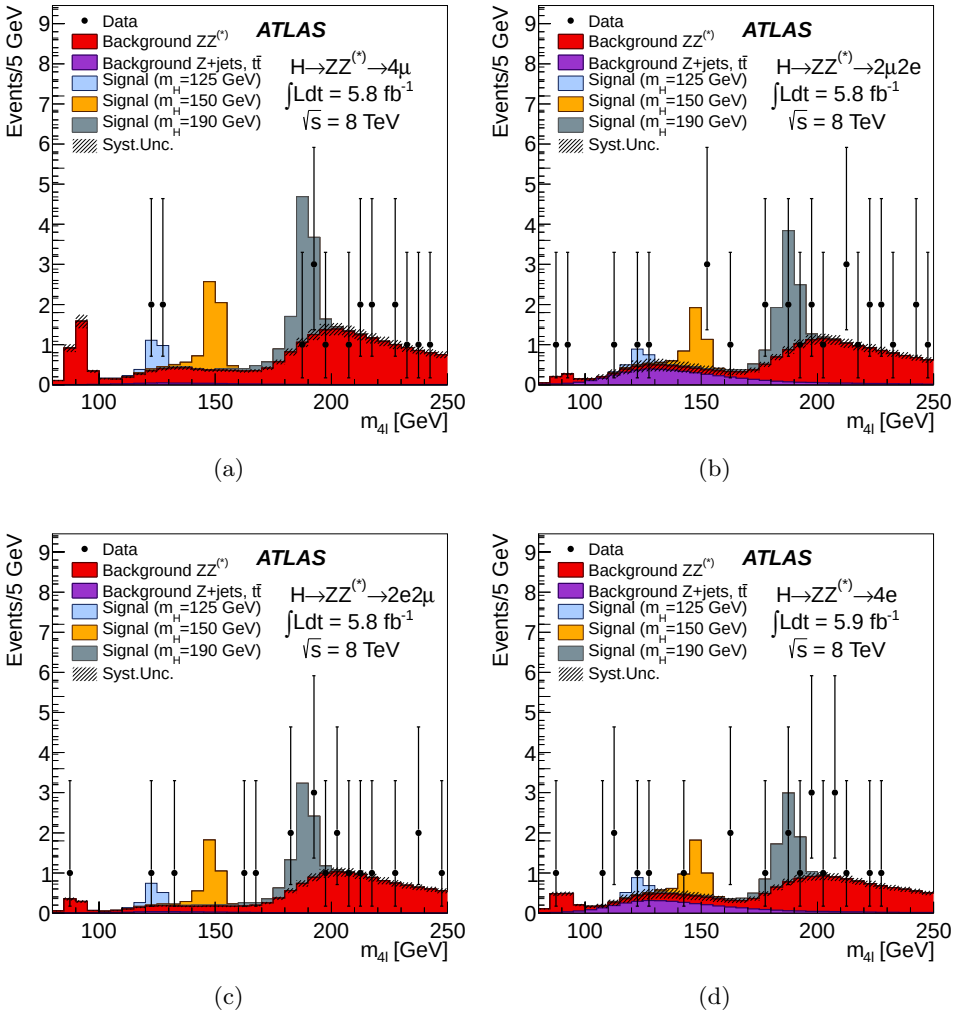

Figure 7.10: The $m_{4\ell}$ distributions are shown for the selected candidates for the $\sqrt{s} = 8\,\text{TeV}$ analysis, for the various sub-channels (a) 4μ, (b) $2\mu 2e$, (c) $2e2\mu$ and (d) $4e$, compared to the background expectation for the $80 - 250\,\text{GeV}$ mass range. Error bars represent 68.3% central confidence intervals. The signal expectation for several m_H hypotheses is also shown.

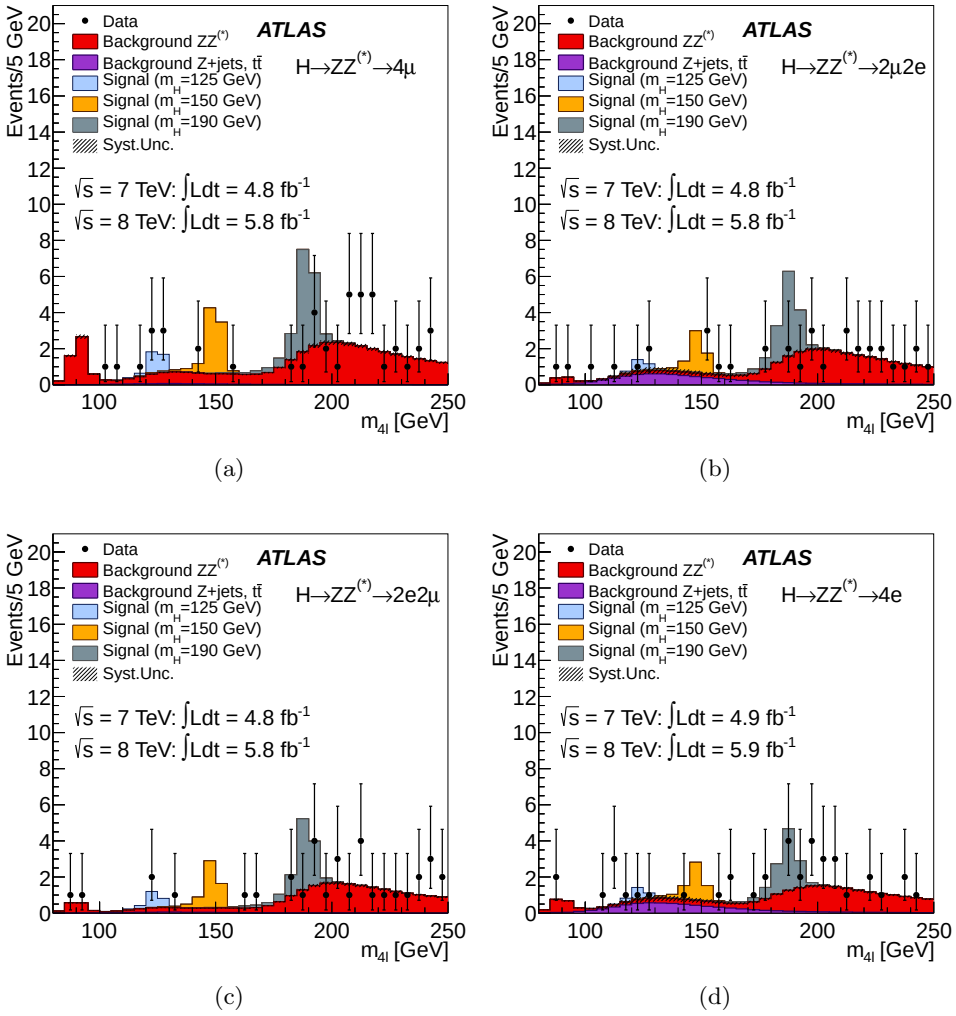

Figure 7.11: The $m_{4\ell}$ distributions are shown for the selected candidates for the $\sqrt{s} = 8\,\text{TeV}$ analysis, for the various sub-channels (a) 4μ, (b) $2\mu 2e$, (c) $2e2\mu$ and (d) $4e$, compared to the background expectation for the $80 - 250\,\text{GeV}$ mass range. Error bars represent 68.3% central confidence intervals. The signal expectation for several m_H hypotheses is also shown.

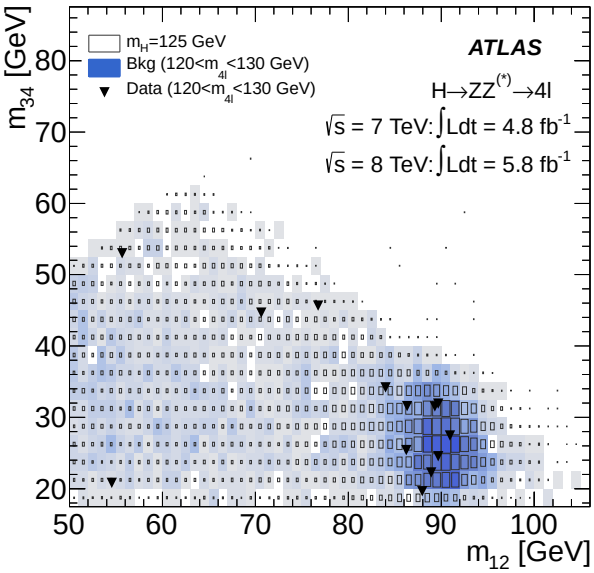

Figure 7.12: The distribution of the m_{34} versus the m_{12} invariant mass is presented, before the application of the Z-mass constrained kinematic fit, for the selected candidates in the $m_{4\ell}$ range 120 to 130 GeV. The expected distributions for a SM Higgs with $m_H = 125$ GeV (the sizes of the boxes indicate the relative density) and for the total background (the intensity of the shading indicates the relative density) are also shown.

background is small and becomes negligible for $m_H < 2m_Z$ [98].

The uncertainties on the integrated luminosity are determined to be 1.8 % for the 7 TeV data and 3.6 % for the 8 TeV data. The improved evaluation of the 7 TeV luminosity has been accomplished through comparisons of the long-term stability and accuracy of the calibration applied to the pp collisions at $\sqrt{s} = 7$ TeV [99].

The uncertainties on the lepton reconstruction and identification efficiencies and on the momentum scale and resolution are determined using samples of Z and J/ψ decays [30, 100]. The relative uncertainty on the signal acceptance due to the uncertainty on the muon reconstruction and identification efficiency is ± 0.7 % (± 0.5 %/± 0.5 %) for the 4μ ($2e2\mu/2\mu2e$) channel for $m_{4\ell} = 600$ GeV and increases to ± 0.9 % (± 0.8 %/± 0.5 %) for $m_{4\ell} = 115$ GeV. Similarly, the relative uncertainty on the signal acceptance due to the uncertainty on the electron reconstruction and identification efficiency is ± 2.6 % (± 1.7 %/± 1.8 %) for the $4e$ ($2e2\mu/2\mu2e$) channel for $m_{4\ell} = 600$ GeV and reaches ± 8.0 % (± 2.3 %/± 7.6 %) for $m_{4\ell} = 115$ GeV. The uncertainty on the electron energy scale results in an uncertainty of ± 0.7 % (± 0.5 %/± 0.2 %) on the mass scale of the $m_{4\ell}$ distribution for the $4e$ ($2e2\mu/2\mu2e$) channel. The impact of the uncertainties on the electron energy resolution and on the muon momentum resolution and scale are found to be negligible.

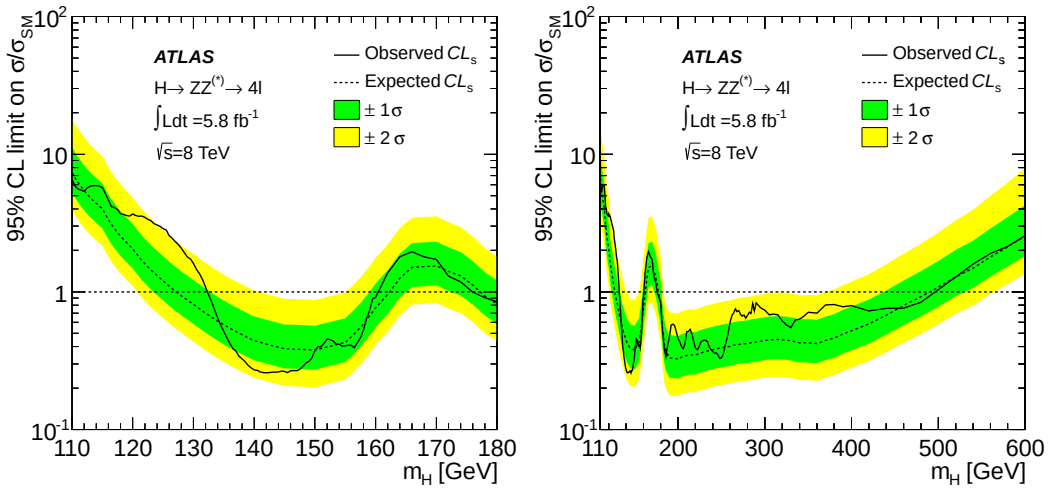

Figure 7.13: The expected (dashed) and observed (full line) 95 % CL upper limits on the Standard Model Higgs boson production cross section as a function of m_H, divided by the expected SM Higgs boson cross section, for the $\sqrt{s} = 8\,\text{TeV}$ data sample in the (a) low mass range and (b) the full range under consideration. The dark (green) and light (yellow) bands indicate the expected limits with $\pm 1\sigma$ and $\pm 2\sigma$ fluctuations, respectively.

7.5 Exclusion limits and statistical interpretation

Figures 7.13 and 7.14 show the observed and expected 95 % CL cross section upper limits, as a function of m_H, for the 2012 $\sqrt{s} = 8\,\text{TeV}$ data and for the combination of the 2011 and 2012 data. Combining the two datasets, the SM Higgs boson is excluded at 95 % CL in the mass ranges $131 - 162\,\text{GeV}$ and $170 - 460\,\text{GeV}$. The expected exclusion ranges are $124 - 164\,\text{GeV}$ and $176 - 500\,\text{GeV}$.

The significance of an excess is given by the probability, p_0, that a background-only experiment is more signal-like in terms of the test statistic than the observed data. In Figure 7.15 the local p_0 is presented as a function of the m_H hypothesis for the 2011, 2012 data and their combination.

In the $\sqrt{s} = 8\,\text{TeV}$ data, the most significant upward deviations from the background-only hypothesis are observed at $m_H = 125.5\,\text{GeV}$ with a local p_0 of 0.4 % (2.7 standard deviations), and for $m_H = 266\,\text{GeV}$ with a local p_0 of 3.5 % (1.8 standard deviations). In the combined analysis of the two datasets, the lowest local p_0 value is 0.029 % (3.4 standard deviations), at $m_H = 125\,\text{GeV}$.

The probability that such an excess occurs anywhere in the full mass range considered in this search, applying the "Look-Elsewhere" Effect, is evaluated [87], using the mass range between 110 GeV and 141 GeV (*i.e.*, the mass range not previously excluded at the 95 % C.L. by the LHC experiments [101]). The global p_0 of the excess located at $m_H = 125\,\text{GeV}$ is 0.65 %, or 2.5 standard deviations. In the high mass region ($m_H > 160\,\text{GeV}$), the lowest p_0 is at 1.9 % (2.1 standard deviations), at

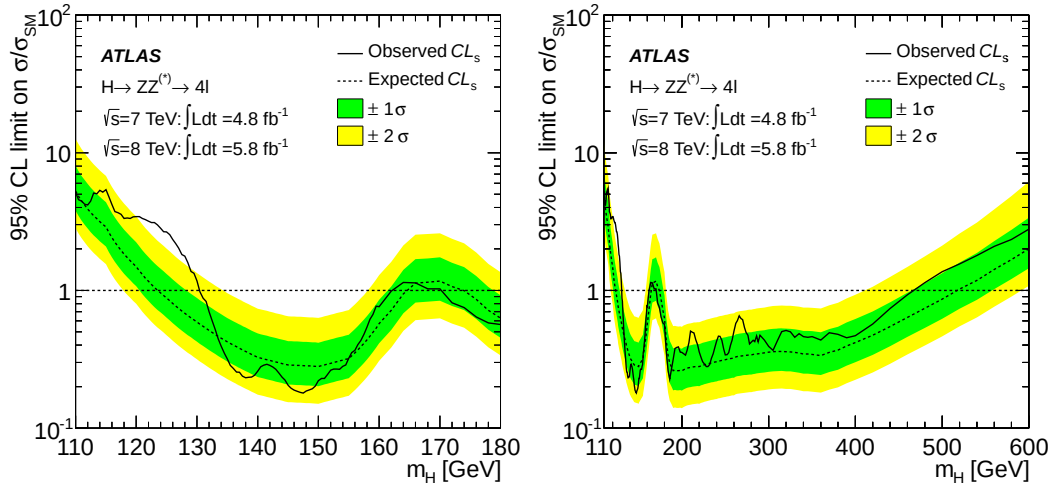

(a) (b)

Figure 7.14: The expected (dashed) and observed (full line) 95 % CL upper limits on the Standard Model Higgs boson production cross section as a function of m_H, divided by the expected SM Higgs boson cross section, for the combination of the 2011 and 2012 data in (a) the low mass range and (b) the full range under consideration. The dark (green) and light (yellow) bands indicate the expected limits with $\pm 1\sigma$ and $\pm 2\sigma$ fluctuations, respectively.

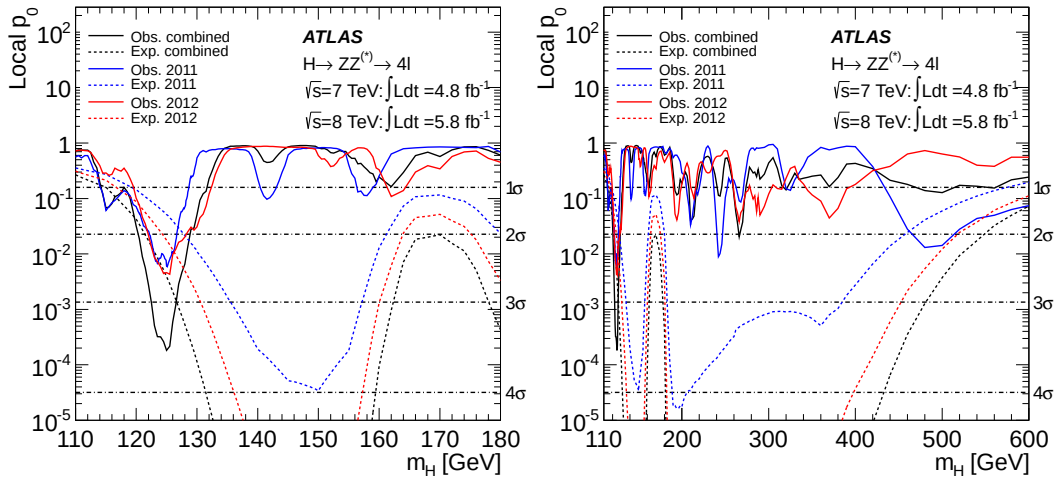

(a) (b)

Figure 7.15: The observed local p_0 for the combination of the 2011 and 2012 datasets (solid black line); the $\sqrt{s} = 7\,\text{TeV}$ and $\sqrt{s} = 8\,\text{TeV}$ data results are shown in solid lines (blue and red, respectively). The dashed curves show the expected median local p_0 for the signal hypothesis when tested at the corresponding m_H. The horizontal dashed lines indicate the p_0 values corresponding to local significance of 1σ, 2σ, 3σ and 4σ.

$m_H = 266\,\text{GeV}$.

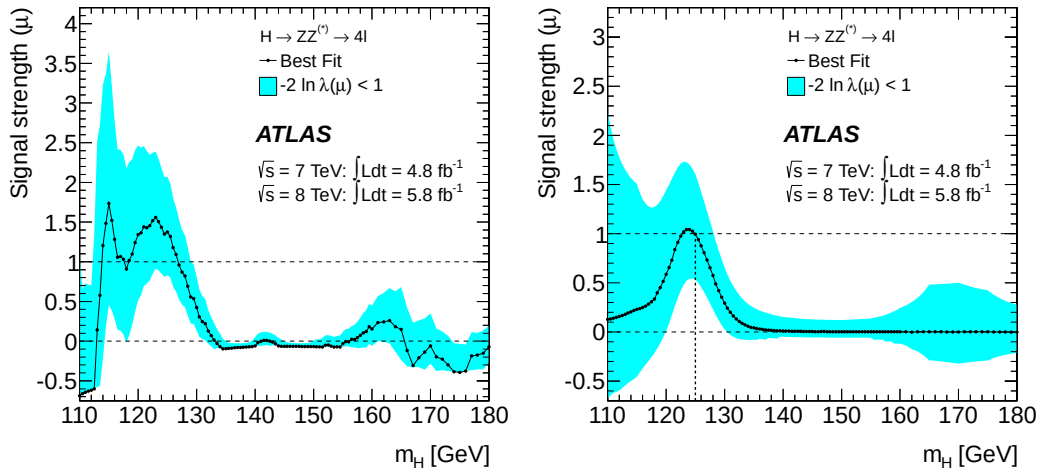

Figure 7.16: The signal strength parameter $\mu = \sigma/\sigma_{SM}$ obtained from a fit to the data is presented (a) for the combined fit to the 2011 and 2012 data samples and (b) for the expected value of μ as a function of m_H when a SM Higgs signal with $m_H = 125$ GeV is injected.

In Figure 7.16(a) the signal strength parameter $\mu = \sigma/\sigma_{SM}$ is presented as a function of m_H for the combination of the two data samples. The corresponding result in the case where a SM Higgs signal of $m_H = 125\,\text{GeV}$ is injected is shown in Figure 7.16(b). The bands illustrate the μ interval corresponding to $-2\ln\lambda(\mu) < 1$, where λ is the profile likelihood ratio test statistic, and represent an approximate $\pm 1\sigma$ variation. The fitted signal strength divided by the expected SM rate is denoted with $\hat{\mu}$. The expected $\hat{\mu}$ has an asymmetric shape and because the expected SM rate rises rapidly with m_H in the low mass region, the expected $\hat{\mu}$ is increased below the injected signal mass and slightly exceeds one for a small mass range.

Combining the 2011 and 2012 datasets recorded by ATLAS, an excess of events is observed around $m_H = 125\,\text{GeV}$, whose p_0 value is 0.029 % (3.4 standard deviations) and the SM Higgs boson is excluded at 95 % CL in the mass ranges $131 - 162\,\text{GeV}$ and $170 - 460\,\text{GeV}$ [97].

7.6 Combination with other Higgs boson searches

The conclusion of the Higgs searches in the $H \to 4\ell$ channel has been supported by other channels, too. More specifically, the $H \to ZZ^{(*)} \to 4\ell$ search was combined with the results of the $H \to \gamma\gamma$ and $H \to WW^{(*)} \to e\nu\mu\nu$ searches in the 8 TeV data, with previously published results of searches for $H \to ZZ^{(*)}$, $H \to WW^{(*)}$, $H \to b\bar{b}$ and $H \to \tau\tau$ in the 7 TeV data, and results from improved analyses of the $H \to ZZ^{(*)} \to 4\ell$ and $H \to \gamma\gamma$ channels in the 7 TeV data [102]. In Figure 7.17 the

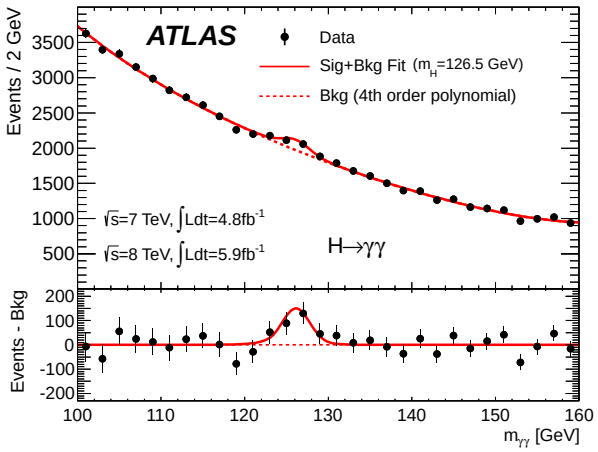

Figure 7.17: The invariant mass distribution of the diphoton candidates is presented for the combined $\sqrt{s} = 7\,\text{TeV}$ and $\sqrt{s} = 8\,\text{TeV}$ data samples. The result of a fit to the data of the sum of a signal component fixed to $m_H = 126.5\,\text{GeV}$ and a background component described by a fourth-order Bernstein polynomial is superimposed. The bottom inset displays the residuals of the data with respect to the fitted background component.

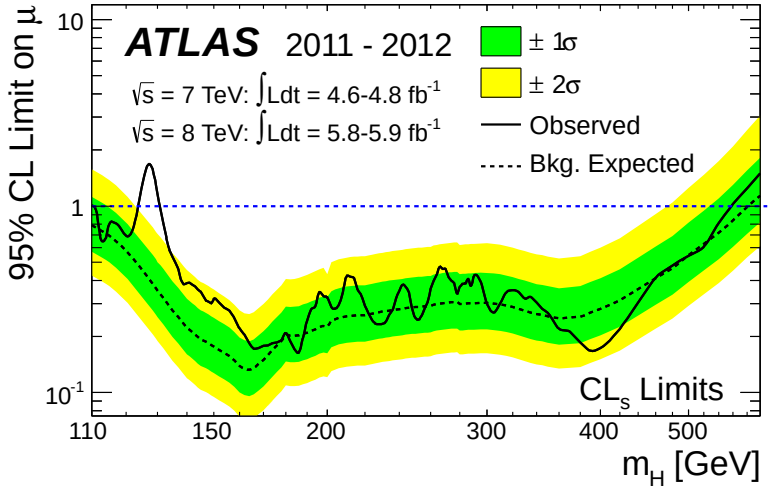

Figure 7.18: The observed (solid) 95 % CL upper limit on the signal strength as a function of m_H and the expectation (dashed) under the background-only hypothesis. The dark and light shaded bands show the $\pm 1\sigma$ and $\pm 2\sigma$ uncertainties on the background-only expectation.

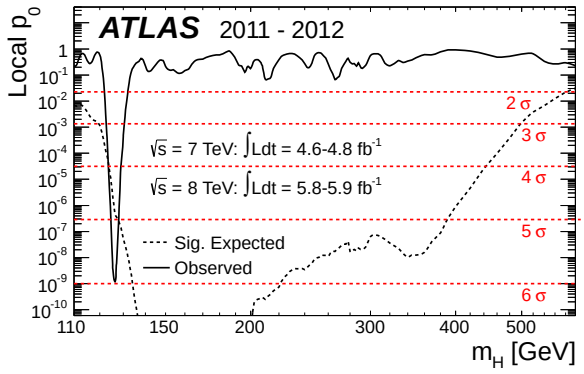

(a)

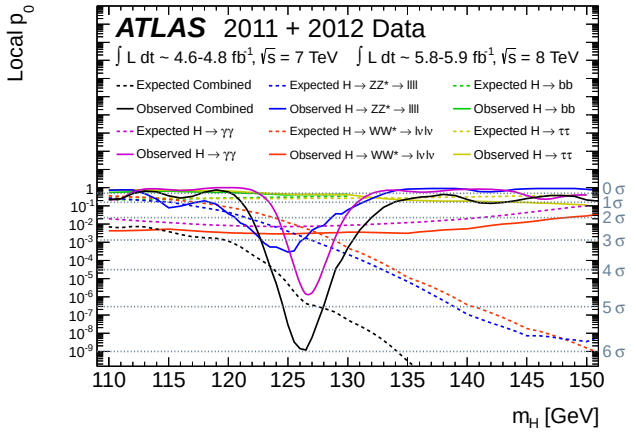

(b)

Figure 7.19: The local probability p_0 for a background-only experiment to be more signal-like than the observation is presented (a) in the full mass range of this analysis and (b) in the low mass range including the p_0 for individual channels, as a function of m_H. The dashed curves show the median expected local p_0 under the hypothesis of a Standard Model Higgs boson production signal at that mass. The horizontal dashed lines indicate the p-values corresponding to significance of 1σ to 6σ.

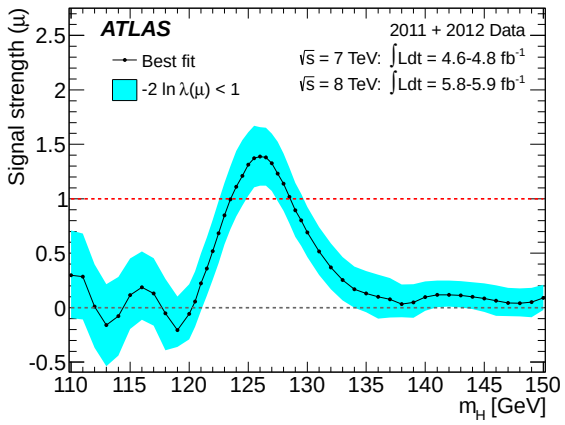

Figure 7.20: The best-fit signal strength is presented as a function of the Higgs boson mass hypothesis for the full combination of the 2011 and 2012 data.

diphoton invariant mass is presented. The distribution is fitted with the sum of a signal component fixed to $m_H = 126.5\,\text{GeV}$ and a background component described by a fourth-order Bernstein polynomial.

In Figure 7.18 the combined search results are presented. The combined 95 % CL exclusion limits on the production of the SM Higgs boson, expressed in terms of the signal strength parameter μ, are shown as a function of m_H. The expected 95 % CL exclusion region covers the m_H range from 110 GeV to 582 GeV. The observed 95 % CL exclusion regions are $111 - 122\,\text{GeV}$ and $131 - 559\,\text{GeV}$. The mass regions excluded at 99 % CL are the $113 - 114$, $117 - 121$ and $132 - 527\,\text{GeV}$, while the expected excluded mass region at 99 % CL is the $113 - 532\,\text{GeV}$.

In Figure 7.19 the local p_0 is presented as a function of the m_H hypothesis for the combination of the two analyses using both the 2011 and 2012 data. The largest local significance for the combination of the 7 and 8 TeV data is found for a SM Higgs boson mass hypothesis of $m_H = 126.5\,\text{GeV}$, where it reaches $6.0\,\sigma$, with an expected value in the presence of a SM Higgs boson signal at that mass of $4.9\,\sigma$.

The mass of the observed new particle is estimated using the profile likelihood ratio $\lambda(m_H)$ for $H \to ZZ^{(*)} \to 4\ell$ and $H \to \gamma\gamma$, the two channels with the highest mass resolution. The resulting estimate for the mass of the observed particle is $126.0 \pm 0.4\,(\text{stat}) \pm 0.4\,(\text{sys})\,\text{GeV}$.

The best-fit signal strength, $\hat{\mu}$, is shown in Figure 7.20 as a function of m_H. The interval around mu-hat corresponds to a variation of -2ln$\lambda(\mu) < 1$ that, in the asymptotic limit, corresponds to the 68 % confidence interval. The observed excess corresponds to $\hat{\mu} = 1.4 \pm 0.3$ for $m_H = 126\,\text{GeV}$, which is consistent with the SM Higgs boson hypothesis $\mu = 1$.

Chapter 8

Conclusions

ATLAS is one of the experiments at the CERN LHC, the world's largest and highest-energy particle accelerator and collider. It is a general purpose detector with a wide physics program from Standard Model precision tests to search for exotic processes. The size and complexity of the detector requires a powerful system for the control and monitoring of its various components. This has been accomplished, as shown in this thesis, by using the SCADA framework, PVSS, to perform essential actions such as operation and alarming. Due to the fine granularity of the detectors, a Finite State Machine has been added to complement the PVSS with an efficient hierarchy-based structure of the detector.

One of the main goals of the physics program of ATLAS is the search for the Higgs boson. The Higgs boson is a postulated particle by the Standard Model but had not been experimentally observed up to the latest experiments. Its mass is a free parameter of the theory but it can be constrained using theoretical arguments, direct searches performed in LEP and Tevatron, and indirect searches involving precision measurements of the electroweak observables in connection with their theoretical predictions.

The Higgs in the LHC is produced mainly through gluon fusion, but also through vector boson fusion and in association with a vector boson or a $t\bar{t}$ pair. The subject of this thesis is the search for the SM Higgs boson in the decay channel $H \to ZZ^{(*)} \to 4\ell$. In this channel only muons and electrons are considered in the final state. Electrons are reconstructed and identified by combining inner tracking detector and calorimeter information whereas for the muons, the inner tracking detector and the muon spectrometer are used. Muon isolation has been studied for various pileup conditions as well as the muon fake rate from kaon and pion decays-in-flight. In addition, the efficiency of the isolation and transverse impact parameter significance requirements has been measured in data using the Tag and Probe technique while the simulation was found to be in agreement.

The search for the SM Higgs boson through the decay $H \to ZZ^{(*)} \to 4\ell$ is sensitive in the mass range $110 - 600\,\text{GeV}$. The main background contribution to this final state is the irreducible $ZZ^{(*)}$ production. However, the reducible background processes depend on the subleading dilepton flavor, with $Z+$ light quark jets dominating in electron final states and $Zb\bar{b}$ and the $t\bar{t}$ production, in muon final states.

The control and estimation of the background contribution are vital for the Higgs boson searches. In this thesis, it is shown that the background processes are well understood and various methods are used for the estimation of their contribution in the signal region.

The Higgs boson search in the $H \to ZZ^{(*)} \to 4\ell$ channel is performed using $4.8\,\text{fb}^{-1}$ of 7 TeV and $5.8\,\text{fb}^{-1}$ of 8 TeV data, leading to the observation of an excess of events around $m_H = 126.5\,\text{GeV}$. This observation is supported by $H \to \gamma\gamma$ and $H \to WW^{(*)} \to e\nu\mu\nu$ searches. Combination of the Higgs searches using 7 TeV and 8 TeV data has led to clear evidence for the production of a neutral boson with a measured mass of $126.0 \pm 0.4\,(\text{stat}) \pm 0.4\,(\text{sys})\,\text{GeV}$. This observation, which has a local statistical significance of 5.9 standard deviations, corresponding to a background fluctuation probability of 1.7×10^{-9}, is compatible with the production and decay of the Standard Model Higgs boson.

Bibliography

[1] J. B. et al. (Particle Data Group), *The Review of Particle Physics*, Phys. Rev. D **86** (2012) 010001.

[2] S. Choudhury, G. C. Joshi, S. Mahajan, and B. H. McKellar, *Probing large distance higher dimensional gravity from lensing data*, Astropart.Phys. **21** (2004) 559–563, `arXiv:hep-ph/0204161 [hep-ph]`.

[3] P. W. Higgs, *Spontaneous Symmetry Breakdown without Massless Bosons*, Phys. Rev. **145** (May, 1966) 1156–1163.

[4] B. W. Lee, C. Quigg, and H. B. Thacker, *Weak interactions at very high energies: The role of the Higgs-boson mass*, Phys. Rev. D **16** (Sep, 1977) 1519–1531.

[5] U. M. Heller, M. Klomfass, H. Neuberger, and P. M. Vranas, *Numerical analysis of the Higgs mass triviality bound*, Nucl.Phys. **B405** (1993) 555–573, `arXiv:hep-ph/9303215 [hep-ph]`.

[6] T. Hambye and K. Riesselmann, *Matching conditions and Higgs boson mass upper bounds reexamined*, Phys. Rev. D **55** (Jun, 1997) 7255–7262.

[7] C. F. Kolda and H. Murayama, *The Higgs mass and new physics scales in the minimal standard model*, JHEP **0007** (2000) 035, `arXiv:hep-ph/0003170 [hep-ph]`.

[8] *Search for the Standard Model Higgs boson at LEP*, Physics Letters B **565** (2003) no. 0, 61 – 75.

[9] Tevatron New Physics Higgs Working Group, CDF Collaboration, D0 Collaboration Collaboration, C. Group, D. Collaborations, the Tevatron New Physics, and H. Working, *Updated Combination of CDF and D0 Searches for Standard Model Higgs Boson Production with up to 10.0 fb^{-1} of Data*, `arXiv:1207.0449 [hep-ex]`.

[10] H. Flacher, M. Goebel, J. Haller, A. Hocker, K. Monig, et al., *Revisiting the Global Electroweak Fit of the Standard Model and Beyond with Gfitter*, Eur.Phys.J. **C60** (2009) 543–583, `arXiv:0811.0009 [hep-ph]`. Version accepted for publication in EPJ-C and corrected for erratum, 66 pages, 14 figures, Gfitter web: http://www.cern.ch/Gfitter.

[11] M. Baak, M. Goebel, J. Haller, A. Hoecker, D. Ludwig, et al., *Updated Status of the Global Electroweak Fit and Constraints on New Physics*, arXiv:1107.0975 [hep-ph].

[12] LHC Higgs Cross Section Working Group, S. Dittmaier, C. Mariotti, G. Passarino, and R. Tanaka (Eds.), *Handbook of LHC Higgs Cross Sections: 1. Inclusive Observables*, CERN-2011-002 (CERN, Geneva, 2011) , arXiv:1101.0593 [hep-ph].

[13] LHC Higgs Cross Section Working Group, S. Dittmaier, C. Mariotti, G. Passarino, and R. Tanaka (Eds.), *Handbook of LHC Higgs Cross Sections: 2. Differential Distributions*, CERN-2012-002 (CERN, Geneva, 2012) , arXiv:1201.3084 [hep-ph].

[14] M. Spira, *QCD effects in Higgs physics*, Fortsch.Phys. **46** (1998) 203–284, arXiv:hep-ph/9705337 [hep-ph].

[15] A. Pak, M. Rogal, and M. Steinhauser, *Finite top quark mass effects in NNLO Higgs boson production at LHC*, JHEP **1002** (2010) 025, arXiv:0911.4662 [hep-ph]. 15 pages.

[16] R. V. Harlander, H. Mantler, S. Marzani, and K. J. Ozeren, *Higgs production in gluon fusion at next-to-next-to-leading order QCD for finite top mass*, Eur.Phys.J. **C66** (2010) 359–372, arXiv:0912.2104 [hep-ph].

[17] *HDECAY: a program for Higgs boson decays in the Standard Model and its supersymmetric extension*, Computer Physics Communications **108** (1998) no. 1, 56 – 74.

[18] A. Bredenstein, A. Denner, S. Dittmaier, and M. Weber, *Radiative corrections to the semileptonic and hadronic Higgs-boson decays $H \to WW/ZZ \to 4$ fermions*, JHEP **0702** (2007) 080, arXiv:hep-ph/0611234 [hep-ph]. 29 pages, LaTeX, 30 postscript figures.

[19] L. Evans and P. Bryant, *LHC Machine*, Journal of Instrumentation **3** no. 08, S08001.

[20] J. Blewett, *200 GeV intersecting storage accelerators*, Proceedings of the 8th International Conference on High-Energy Accelerators .

[21] E. Bleser, *Superconducting magnets for the CBA project*, Nucl. Instrum. Meth. A **235** 435.

[22] O. S. BrG'Oning, P. Collier, P. Lebrun, S. Myers, R. Ostojic, J. Poole, and P. Proudlock, *LHC Design Report*. CERN, Geneva, 2004.

[23] ATLAS Collaboration, G. Aad et al., *The ATLAS Experiment at the CERN Large Hadron Collider*, Journal of Instrumentation **3** no. 08, S08003.

[24] ATLAS Collaboration, G. Aad et al., *Expected performance of the ATLAS experiment: Detector, Trigger and Physics*. 2009. `arXiv:0901.0512 [hep-ex]`.

[25] ATLAS Collaboration, G. Aad et al., *ATLAS muon spectrometer: Technical Design Report*. No. ATLAS-TDR-010. CERN, Geneva, 1997.

[26] H. L. Groenstege, *The RASNIK/CCD 3D alignment system*, Tech. Rep. ATL-MUON-94-063. ATL-M-PN-63, CERN, Geneva, Dec, 1994.

[27] D. R. Myers, *The LHC Experiments' Joint Controls Project, JCOP*, .

[28] B. Franek and C. Gaspar, *SMI++ object oriented framework used for automation and error recovery in the LHC experiments*, J. Phys.: Conf. Ser. **219** (2010) 022031. 10 p.

[29] T. Alexopoulos, E. Gazis, G. Iakovidis, S. Leontsinis, E. Mountricha, G. Tsipolitis, and S. Vlachos, *MDT PS Developers Documentation*, Tech. Rep. ATL-COM-MUON-2011-012, CERN, Geneva, May, 2011.

[30] ATLAS Collaboration, G. Aad et al., *Electron performance measurements with the ATLAS detector using the 2010 LHC proton-proton collision data*, Eur.Phys.J. **C72** (2012) 1909, `arXiv:1110.3174 [hep-ex]`.

[31] ATLAS Collaboration, *Expected electron performance in the ATLAS experiment*, Tech. Rep. ATL-PHYS-PUB-2011-006, CERN, Geneva, Apr, 2011.

[32] R. E. Kalman, *A New Approach to Linear Filtering and Prediction Problems*, Transactions of the ASME - Journal of Basic Engineering no. 82 (Series D), 35–45.

[33] *Track fitting with non-Gaussian noise*, Computer Physics Communications **100** (1997) no. 1-2, 1 – 16.

[34] ATLAS Collaboration, *Improved electron reconstruction in ATLAS using the Gaussian Sum Filter-based model for bremsstrahlung*, Tech. Rep. ATLAS-CONF-2012-047, CERN, Geneva, May, 2012.

[35] *A muon identification and combined reconstruction procedure for the ATLAS detector at the LHC using the (MUONBOY, STACO, MuTag) reconstruction packages*, Nuclear Instruments and Methods in Physics Research Section A: Accelerators, Spectrometers, Detectors and Associated Equipment **572** (2007) no. 1, 77 – 79.

[36] D. Adams, K. A. Assamagan, M. Biglietti, G. Carlino, G. Cataldi, F. Conventi, A. Farilla, Y. Fisyak, S. Goldfarb, E. Gorini, T. Lagouri, K. Mair, L. Merola, A. Nairz, A. Poppleton, M. Primavera, S. Rosati, J. T. Shank, S. Spagnolo, L. Spogli, G. D. Stavropoulos, M. Verducci, and T. Wenaus, *Track reconstruction in the ATLAS Muon Spectrometer with*

MOORE 007, Tech. Rep. ATL-SOFT-2003-007, CERN, Geneva, May, 2003. revised version number 1 submitted on 2003-10-13 13:51:39.

[37] K. Nakamura and P. D. Group, *Review of Particle Physics*, Journal of Physics G: Nuclear and Particle Physics **37** no. 7A, 075021.

[38] T. Sjostrand, S. Mrenna, and P. Z. Skands, *PYTHIA 6.4 Physics and Manual*, JHEP **05** (2006) 026, arXiv:hep-ph/0603175.

[39] ATLAS Collaboration, *D^* mesons reconstruction in pp collisions at $\sqrt{s} = 7$ TeV*, Tech. Rep. ATLAS-CONF-2010-034, CERN, Geneva, Jul, 2010.

[40] M. Pivk and F. R. Le Diberder, *sPlot: a statistical tool to unfold data distributions*, Tech. Rep. physics/0402083. LAL-2004-07, Paris 11. Lab. Accél. Linéaire, Orsay, Feb, 2004.

[41] S. Alioli, P. Nason, C. Oleari, and E. Re, *NLO Higgs boson production via gluon fusion matched with shower in POWHEG*, JHEP **04** (2009) 002, arXiv:0812.0578 [hep-ph].

[42] P. Nason and C. Oleari, *NLO Higgs boson production via vector-boson fusion matched with shower in POWHEG*, JHEP **02** (2010) 037, arXiv:0911.5299 [hep-ph].

[43] D. de Florian, G. Ferrera, M. Grazzini, and D. Tommasini, *Transverse-momentum resummation: Higgs boson production at the Tevatron and the LHC*, JHEP **1111** (2011) 064, arXiv:1109.2109 [hep-ph].

[44] P. Golonka and Z. Was, *PHOTOS Monte Carlo: A Precision tool for QED corrections in Z and W decays*, Eur. Phys. J. **C45** (2006) 97–107, arXiv:hep-ph/0506026.

[45] Z. Was, *TAUOLA the library for tau lepton decay, and KKMC/KORALB/KORALZ/... status report*, Nucl. Phys. Proc. Suppl. **98** (2001) 96–102, arXiv:hep-ph/0011305.

[46] LHC Higgs Cross Section Working Group, S. Dittmaier, C. Mariotti, G. Passarino, and R. Tanaka (Eds.), *Handbook of LHC Higgs cross sections: 1. Inclusive observables*, CERN, Geneva, 2011. CERN-2011-002 (CERN, Geneva, 2011) , arXiv:1101.0593 [hep-ph].

[47] R. V. Harlander and W. B. Kilgore, *Next-to-next-to-leading order Higgs production at hadron colliders*, Phys. Rev. Lett. **88** (2002) 201801, arXiv:hep-ph/0201206.

[48] C. Anastasiou and K. Melnikov, *Higgs boson production at hadron colliders in NNLO QCD*, Nucl. Phys. **B646** (2002) 220–256, arXiv:hep-ph/0207004.

[49] V. Ravindran, J. Smith, and W. L. van Neerven, *NNLO corrections to the total cross section for Higgs boson production in hadron hadron collisions*, Nucl. Phys. **B665** (2003) 325–366, arXiv:hep-ph/0302135.

[50] C. Anastasiou, R. Boughezal, and F. Petriello, *Mixed QCD-electroweak corrections to Higgs boson production in gluon fusion*, JHEP **04** (2009) 003, arXiv:0811.3458 [hep-ph].

[51] D. de Florian and M. Grazzini, *Higgs production through gluon fusion: updated cross sections at the Tevatron and the LHC*, Phys. Lett. **B674** (2009) 291–294, arXiv:0901.2427 [hep-ph].

[52] J. Baglio and A. Djouadi, *Higgs production at the lHC*, JHEP **1103** (2011) 055.

[53] P. Bolzoni, F. Maltoni, S.-O. Moch, and M. Zaro, *Higgs production via vector-boson fusion at NNLO in QCD*, Phys. Rev. Lett. **105** (2010) 011801, arXiv:arXiv:1003.4451 [hep-ph].

[54] O. Brein, A. Djouadi, and R. Harlander, *NNLO QCD corrections to the Higgs-strahlung processes at hadron colliders*, Phys.Lett. **B579** (2004) 149–156, arXiv:hep-ph/0307206 [hep-ph].

[55] S. Catani, D. de Florian, M. Grazzini, and P. Nason, *Soft-gluon resummation for Higgs boson production at hadron colliders*, JHEP **07** (2003) 028, arXiv:hep-ph/0306211.

[56] U. Aglietti, R. Bonciani, G. Degrassi, and A. Vicini, *Two-loop light fermion contribution to Higgs production and decays*, Phys. Lett. **B595** (2004) 432–441, arXiv:hep-ph/0404071.

[57] S. Actis, G. Passarino, C. Sturm, and S. Uccirati, *NLO Electroweak Corrections to Higgs Boson Production at Hadron Colliders*, Phys. Lett. **B670** (2008) 12–17, arXiv:0809.1301 [hep-ph].

[58] M. Ciccolini, A. Denner, and S. Dittmaier, *Strong and electroweak corrections to the production of Higgs+2jets via weak interactions at the LHC*, Phys. Rev. Lett. **99** (2007) 161803, arXiv:0707.0381 [hep-ph].

[59] M. Ciccolini, A. Denner, and S. Dittmaier, *Electroweak and QCD corrections to Higgs production via vector-boson fusion at the LHC*, Phys. Rev. **D77** (2008) 013002, arXiv:0710.4749 [hep-ph].

[60] M. L. Ciccolini, S. Dittmaier, and M. Kramer, *Electroweak radiative corrections to associated WH and ZH production at hadron colliders*, Phys. Rev. **D 68** (2003) 073003, arXiv:hep-ph/0306234.

[61] A. Bredenstein, A. Denner, S. Dittmaier, and M. M. Weber, *Precise predictions for the Higgs-boson decay $H \to WW/ZZ \to 4leptons$*, Phys. Rev. **D74** (2006) 013004, arXiv:hep-ph/0604011.

[62] J. M. Campbell and R. K. Ellis, *An update on vector boson pair production at hadron colliders*, Phys. Rev. **D60** (1999) 113006, arXiv:hep-ph/9905386.

[63] J. M. Campbell, R. K. Ellis, and C. Williams, *Vector boson pair production at the LHC*, JHEP **07** (2011) 018, arXiv:1105.0020 [hep-ph].

[64] M. L. Mangano et al., *ALPGEN, a generator for hard multiparton processes in hadronic collisions*, JHEP **07** (2003) 001, arXiv:hep-ph/0206293.

[65] S. Frixione and B. R. Webber, *The MC@NLO event generator*, arXiv:hep-ph/0207182.

[66] S. Frixione and B. R. Webber, *Matching NLO QCD computations and parton shower simulations*, JHEP **06** (2002) 029, arXiv:hep-ph/0204244.

[67] S. Frixione, P. Nason, and B. R. Webber, *Matching NLO QCD and parton showers in heavy flavour production*, JHEP **08** (2003) 007, arXiv:hep-ph/0305252.

[68] G. Corcella et al., *HERWIG 6.5 release note*, arXiv:hep-ph/0210213.

[69] J. M. Butterworth, J. R. Forshaw, and M. H. Seymour, *Multiparton interactions in photoproduction at HERA*, Z. Phys. **C72** (1996) 637–646, arXiv:hep-ph/9601371.

[70] K. Melnikov and F. Petriello, *Electroweak gauge boson production at hadron colliders through $O(\alpha_s^2)$*, Phys. Rev. **D74** (2006) 114017, arXiv:hep-ph/0609070.

[71] C. Anastasiou, L. J. Dixon, K. Melnikov, and F. Petriello, *High precision QCD at hadron colliders: Electroweak gauge boson rapidity distributions at NNLO*, Phys. Rev. **D69** (2004) 094008, arXiv:hep-ph/0312266.

[72] M. Aliev et al., *HATHOR: HAdronic Top and Heavy quarks crOss section calculatoR*, Comp. Phys. Comm. **182** (2011) 1034, arXiv:1007.1327 [hep-ph].

[73] ATLAS Collaboration, *Muon Reconstruction Performance*, ATLAS-CONF-2010-064 (2010) .

[74] C. Anastopoulos, N. Kerschen, and S. Paganis, *A technique for measuring the pp to $Z + X$ background to the $H \to 4l$ channel for the discovery of the Higgs Boson at the LHC*, Tech. Rep. ATL-COM-PHYS-2009-400, CERN, Sep, 2009.

[75] M. Botje, J. Butterworth, A. Cooper-Sarkar, A. de Roeck, J. Feltesse, et al., *The PDF4LHC Working Group Interim Recommendations*, arXiv:1101.0538 [hep-ph].

[76] S. Alekhin, S. Alioli, R. D. Ball, V. Bertone, J. Blumlein, et al., *The PDF4LHC Working Group Interim Report*, arXiv:1101.0536 [hep-ph].

[77] H.-L. Lai, M. Guzzi, J. Huston, Z. Li, P. M. Nadolsky, et al., *New parton distributions for collider physics*, Phys.Rev. **D82** (2010) 074024, arXiv:1007.2241 [hep-ph].

[78] A. Martin, W. Stirling, R. Thorne, and G. Watt, *Parton distributions for the LHC*, Eur.Phys.J. **C63** (2009) 189–285, arXiv:0901.0002 [hep-ph].

[79] R. D. Ball, V. Bertone, F. Cerutti, L. Del Debbio, S. Forte, et al., *Impact of Heavy Quark Masses on Parton Distributions and LHC Phenomenology*, Nucl.Phys. **B849** (2011) 296–363, arXiv:1101.1300 [hep-ph].

[80] G. Passarino, C. Sturm, and S. Uccirati, *Higgs Pseudo-Observables, Second Riemann Sheet and All That*, Nucl.Phys. **B834** (2010) 77–115, arXiv:1001.3360 [hep-ph].

[81] C. Anastasiou, S. Buehler, F. Herzog, and A. Lazopoulos, *Total cross-section for Higgs boson hadroproduction with anomalous Standard Model interactions*, JHEP **1112** (2011) 058, arXiv:1107.0683 [hep-ph].

[82] J. Campbell, R. Ellis, and C. Williams, *Gluon-gluon contributions to W^+W^- production and Higgs interference effects*, JHEP **1110** (2011) 005, arXiv:1107.5569 [hep-ph].

[83] J. Campbell, E. Castaneda-Miranda, Y. Fang, N. Kauer, B. Mellado, et al., *Normalizing Weak Boson Pair Production at the Large Hadron Collider*, Phys.Rev. **D80** (2009) 054023, arXiv:0906.2500 [hep-ph].

[84] A. L. Read, *Presentation of search results: The CL(s) technique*, J. Phys. G **28** (2002) 2693–2704.

[85] G. Cowan, K. Cranmer, E. Gross, and O. Vitells, *Asymptotic formulae for likelihood-based tests of new physics*, Eur.Phys.J. **C71** (2011) 1554, arXiv:1007.1727 [physics.data-an].

[86] L. Moneta et al., *The RooStats Project*, PoS **ACAT2010** (2010) 057, arXiv:1009.1003 [physics.data-an].

[87] E. Gross and O. Vitells, *Trial factors for the look elsewhere effect in high energy physics*, Eur. Phys. J. **C70** (2010) 525–530, arXiv:1005.1891 [physics.data-an].

[88] ATLAS Collaboration, G. Aad et al., *Search for the Standard Model Higgs boson in the decay channel $H \to ZZ^{(*)} \to 4l$ with $4.8\,fb^{-1}$ of pp collision data at $\sqrt{s} = 7$ TeV with ATLAS*, Phys.Lett. **B710** (2012) 383–402, arXiv:1202.1415 [hep-ex].

[89] ATLAS Collaboration, G. Aad et al., *Combined search for the Standard Model Higgs boson in pp collisions at $\sqrt{s} = 7$ TeV with the ATLAS detector*, Phys.Rev. **D86** (2012) 032003, arXiv:1207.0319 [hep-ex].

[90] S. Mao, M. Wen-Gan, L. Gang, Z. Ren-You, and G. Lei, *QCD corrections to J/ψ plus Z^0-boson production at the LHC*, JHEP **1102** (2011) 071, arXiv:1102.0398 [hep-ph].

[91] E. Braaten, J. Lee, and S. Fleming, *Associated production of Υ and weak gauge bosons in hadron colliders*, Phys. Rev. D **60** (Oct, 1999) 091501.

[92] ATLAS Collaboration, G. Aad et al., *Measurements of the electron and muon inclusive cross-sections in proton-proton collisions at $\sqrt{s} = 7$ TeV with the ATLAS detector*, Phys. Lett. **B707** (2012) 438–458, arXiv:1109.0525 [hep-ex].

[93] W. Lampl, S. Laplace, D. Lelas, P. Loch, H. Ma, S. Menke, S. Rajagopalan, D. Rousseau, S. Snyder, and G. Unal, *Calorimeter Clustering Algorithms: Description and Performance*, Tech. Rep. ATL-LARG-PUB-2008-002. ATL-COM-LARG-2008-003, CERN, Geneva, Apr, 2008.

[94] *Pileup subtraction using jet areas*, Physics Letters B **659** (2008) no. 1-2, 119 – 126.

[95] M. Cacciari, G. P. Salam, and G. Soyez, *FastJet User Manual*, Eur.Phys.J. **C72** (2012) 1896, arXiv:1111.6097 [hep-ph].

[96] ATLAS Collaboration, *Measurement of the total ZZ production cross section in the four-lepton channel using 5.8 fb^{-1} of ATLAS data at $\sqrt{s} = 8$ TeV*, Tech. Rep. ATLAS-CONF-2012-090, CERN, Geneva, Jul, 2012.

[97] ATLAS Collaboration, *Observation of an excess of events in the search for the Standard Model Higgs boson in the $H \to ZZ^{(*)} \to 4\ell$ channel with the ATLAS detector.*, Tech. Rep. ATLAS-CONF-2012-092, CERN, Geneva, Jul, 2012.

[98] N. Kauer and G. Passarino, *Inadequacy of zero-width approximation for a light Higgs boson signal*, JHEP **1208** (2012) 116, arXiv:1206.4803 [hep-ph].

[99] ATLAS Collaboration, *Improved Luminosity Determination in pp Collisions at $\sqrt{s} = 7$ TeV using the ATLAS Detector at the LHC*, Tech. Rep. ATLAS-CONF-2012-080, CERN, Geneva, Jul, 2012.

[100] ATLAS Collaboration, *Muon reconstruction efficiency in reprocessed 2010 LHC proton-proton collision data recorded with the ATLAS detector*, Tech. Rep. ATLAS-CONF-2011-063, CERN, Geneva, Apr, 2011.

[101] ATLAS Collaboration, ATLAS and C. Collaborations, *Combined Standard Model Higgs boson searches with up to 2.3 fb^{-1} of pp collisions at $\sqrt{s} = 7$ TeV at the LHC*, ATLAS-CONF-2011-157 (2011) .

[102] ATLAS Collaboration Collaboration, G. Aad et al., *Observation of a new particle in the search for the Standard Model Higgs boson with the ATLAS detector at the LHC*, Phys.Lett. **B716** (2012) 1–29, `arXiv:1207.7214 [hep-ex]`.

Appendices

Appendix A

Additional results on muon efficiencies

The efficiencies for muon isolation and impact parameter cuts for $Z \rightarrow \mu\mu$ muons are derived using a Tag and Probe approach as described in 4.3.3. The selection criteria under study are $\Sigma p_T/p_T < 0.15$ (tracking isolation), $\Sigma E_T/E_T < 0.3$ (calorimeter isolation) and $d_0/\sigma_{d_0} < 3.5$ (transverse impact parameter significance). For both the tracking and calorimetric isolation a cone of 0.2 around the muon is used. This study is performed on $4.8\,\text{fb}^{-1}$ 7 TeV data and several Monte Carlo samples both for the signal and the backgrounds.

The results of the fits on the opposite and same charge combination invariant mass distributions are presented for all probe p_{T} bins in the Figures A.1 to A.9 in the case of the tracking isolation cut ($4.8\,\text{fb}^{-1}$). The blue dashed line corresponds to the QCD estimation using the same charge templates from the data. The red dashed line corresponds to the estimated $Z \rightarrow \tau^+\tau^-$ and the green one to the $t\bar{t}$ contribution. The combination of all the templates is shown with the continuous blue line. The combination of the templates is in agreement with the data in all probe p_{T} bins.

In Figures A.10 to A.18 the $Z \rightarrow \mu\mu$ invariant mass distributions are presented using MC simulation for the probe p_{T} bins. The distributions are shown for both before and after applying the tracking isolation selection.

In order to estimate the systematics, larger ranges are considered for the calculation of the efficiency (5 GeV and 8 GeV around the Z peak), a broader fitting range is used (56-126 GeV) and a Pythia generated $Z \rightarrow \mu^+\mu^-$ Monte Carlo sample is taken into account. The results from these systematics studies are summarized in Tables A.1 to A.4.

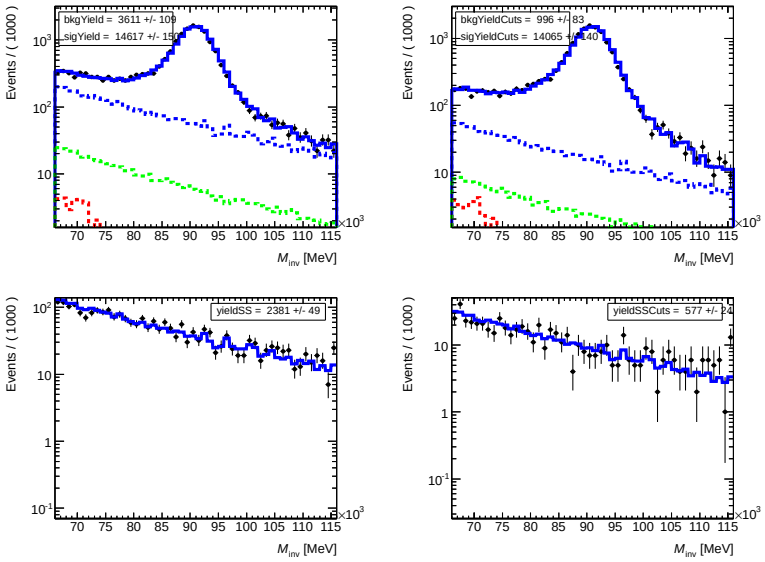

Figure A.1: Invariant mass distributions for the opposite sign muon pairs (top plots) and same sign ones (bottom plots) before (left plots) and after (right plots) applying the tracking isolation cut, using the Tag and Probe method for the probe p_{T} bin 6 to 12 GeV ($4.8\,\mathrm{fb}^{-1}$).

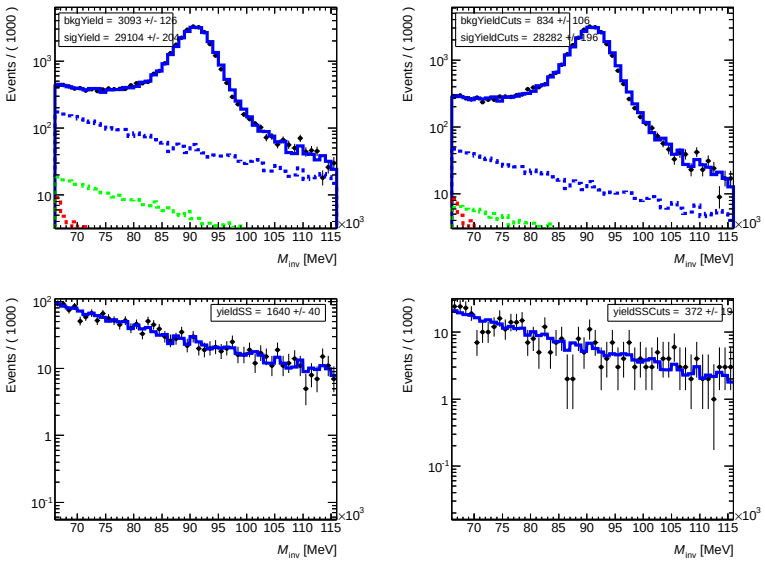

Figure A.2: Invariant mass distributions for the opposite sign muon pairs (top plots) and same sign ones (bottom plots) before (left plots) and after (right plots) applying the tracking isolation cut, using the Tag and Probe method for the probe p_{T} bin 12 to 15 GeV ($4.8\,\mathrm{fb}^{-1}$).

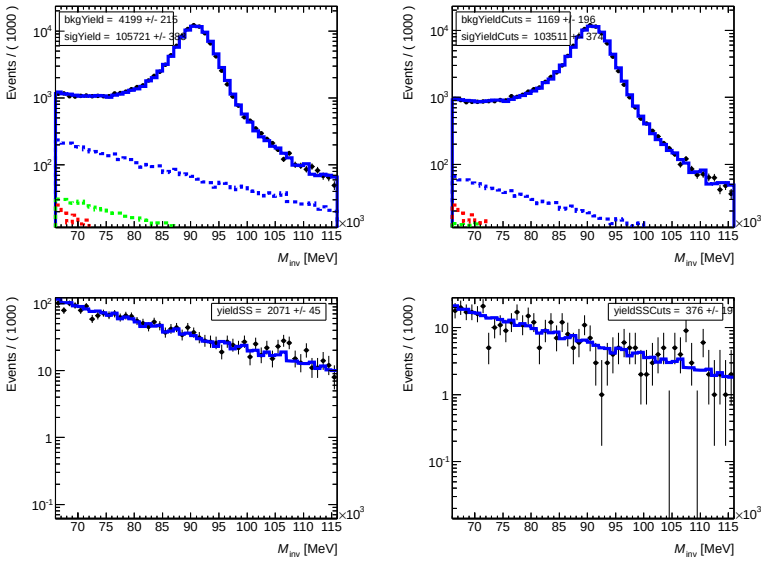

Figure A.3: Invariant mass distributions for the opposite sign muon pairs (top plots) and same sign ones (bottom plots) before (left plots) and after (right plots) applying the tracking isolation cut, using the Tag and Probe method for the probe p_{T} bin 15 to 20 GeV ($4.8\,\mathrm{fb}^{-1}$).

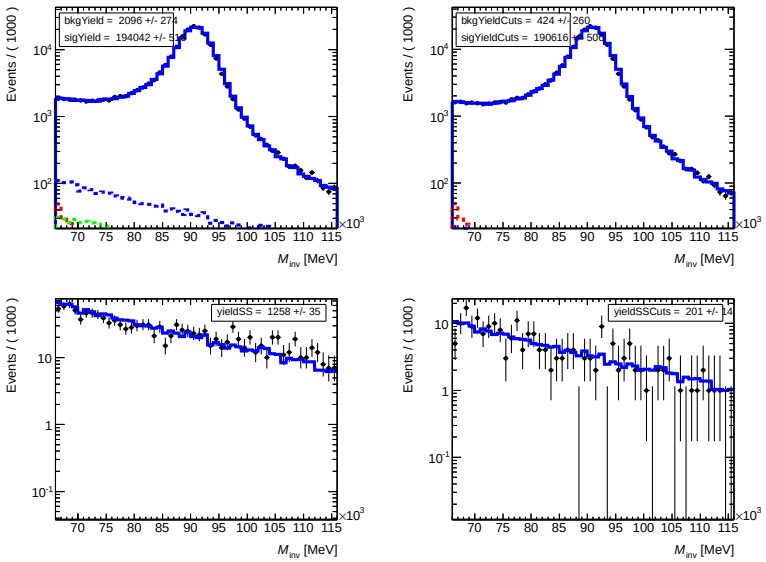

Figure A.4: Invariant mass distributions for the opposite sign muon pairs (top plots) and same sign ones (bottom plots) before (left plots) and after (right plots) applying the tracking isolation cut, using the Tag and Probe method for the probe p_{T} bin 20 to 25 GeV ($4.8\,\mathrm{fb}^{-1}$).

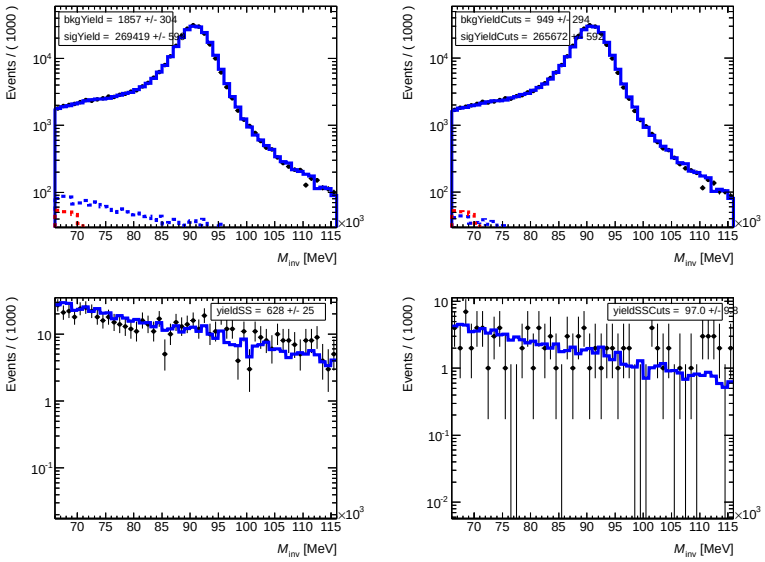

Figure A.5: Invariant mass distributions for the opposite sign muon pairs (top plots) and same sign ones (bottom plots) before (left plots) and after (right plots) applying the tracking isolation cut, using the Tag and Probe method for the probe p_{T} bin 25 to 30 GeV ($4.8\,\mathrm{fb}^{-1}$).

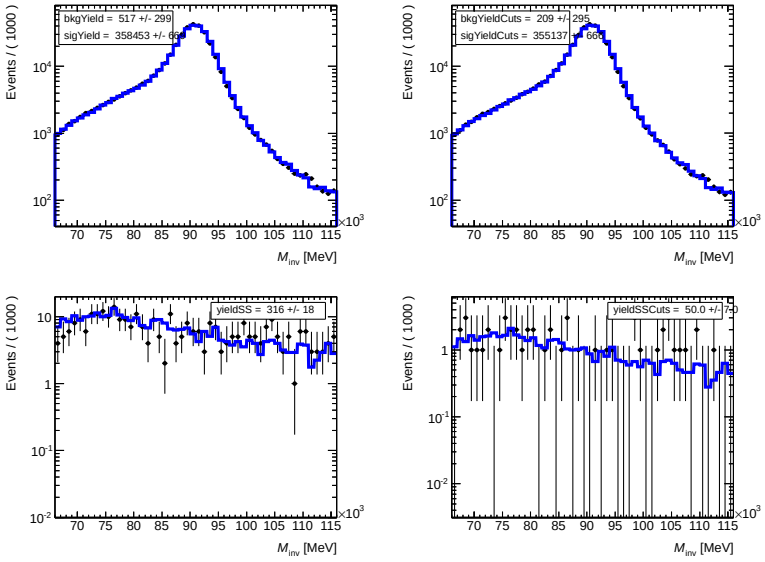

Figure A.6: Invariant mass distributions for the opposite sign muon pairs (top plots) and same sign ones (bottom plots) before (left plots) and after (right plots) applying the tracking isolation cut, using the Tag and Probe method for the probe p_{T} bin 30 to 35 GeV ($4.8\,\mathrm{fb}^{-1}$).

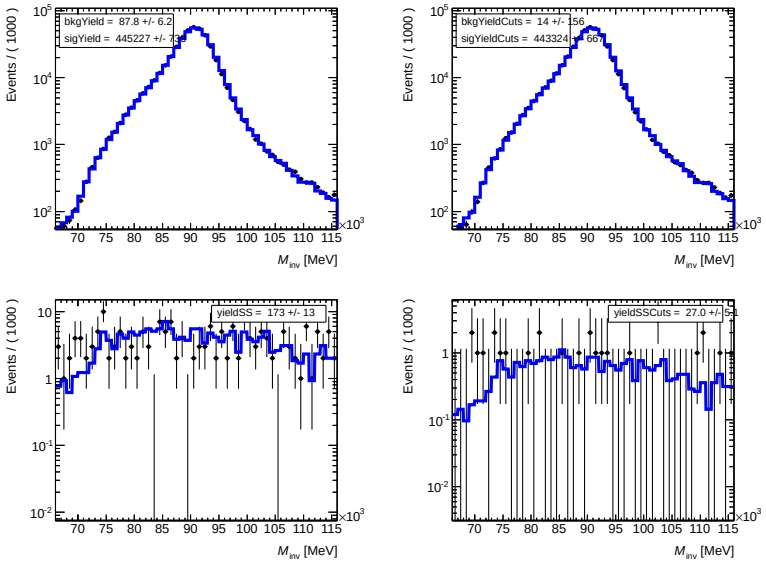

Figure A.7: Invariant mass distributions for the opposite sign muon pairs (top plots) and same sign ones (bottom plots) before (left plots) and after (right plots) applying the tracking isolation cut, using the Tag and Probe method for the probe p_{T} bin 35 to 40 GeV ($4.8\,\mathrm{fb}^{-1}$).

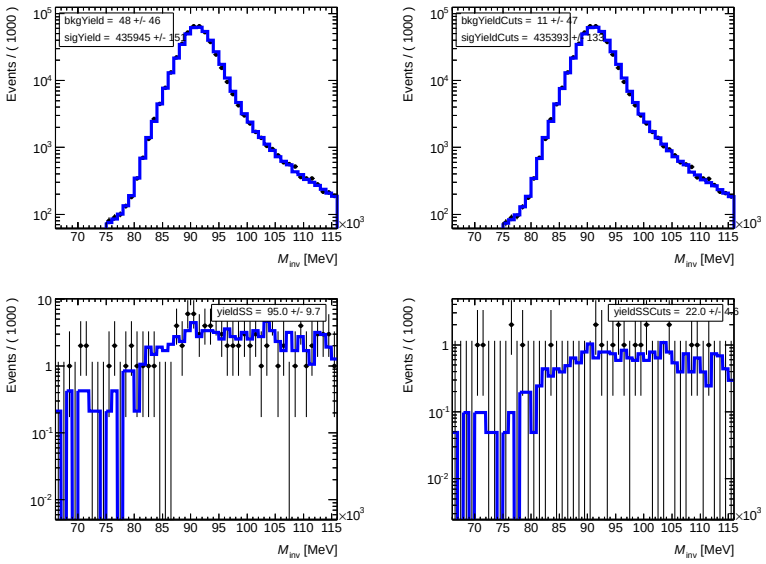

Figure A.8: Invariant mass distributions for the opposite sign muon pairs (top plots) and same sign ones (bottom plots) before (left plots) and after (right plots) applying the tracking isolation cut, using the Tag and Probe method for the probe p_{T} bin 40 to 45 GeV ($4.8\,\mathrm{fb}^{-1}$).

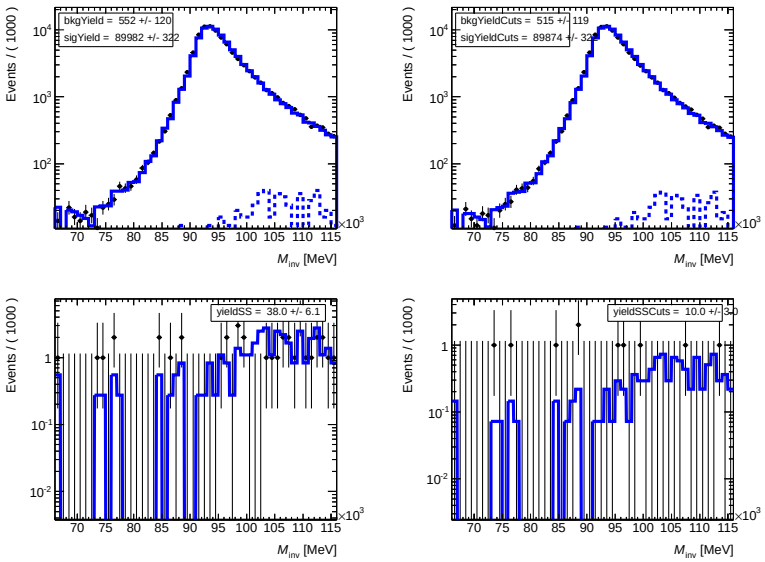

Figure A.9: Invariant mass distributions for the opposite sign muon pairs (top plots) and same sign ones (bottom plots) before (left plots) and after (right plots) applying the tracking isolation cut, using the Tag and Probe method for the probe p_{T} bin 45 to 50 GeV ($4.8\,\mathrm{fb}^{-1}$).

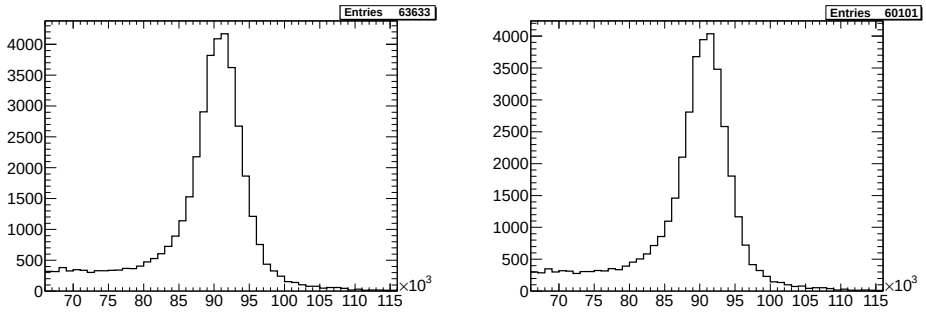

(a) (b)

Figure A.10: Invariant mass distributions for $Z \to \mu\mu$ using MC simulation (a) before and (a) after applying the tracking isolation cut in the probe p_{T} bin 7 to 12 GeV.

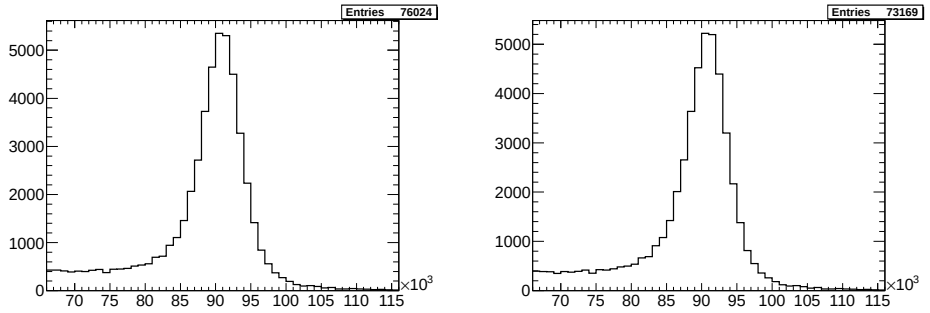

(a) (b)

Figure A.11: Invariant mass distributions for $Z \rightarrow \mu\mu$ using MC simulation (a) before and (a) after applying the tracking isolation cut in the probe p_{T} bin 12 to 15 GeV.

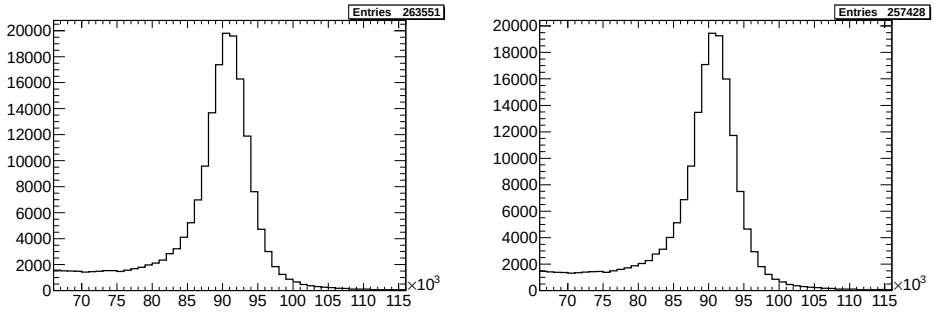

(a) (b)

Figure A.12: Invariant mass distributions for $Z \rightarrow \mu\mu$ using MC simulation (a) before and (a) after applying the tracking isolation cut in the probe p_{T} bin 15 to 20 GeV.

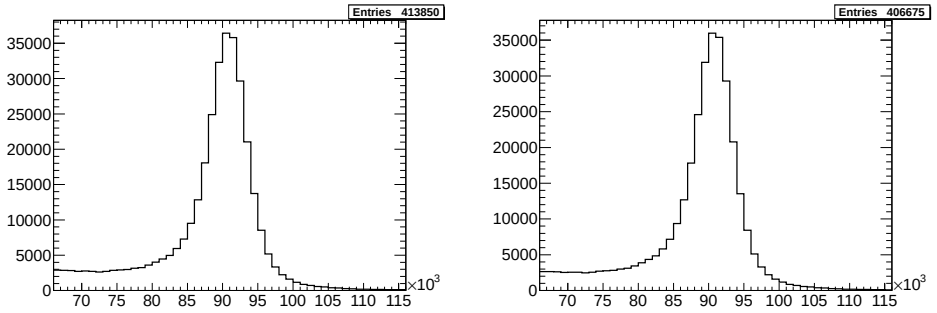

(a) (b)

Figure A.13: Invariant mass distributions for $Z \rightarrow \mu\mu$ using MC simulation (a) before and (a) after applying the tracking isolation cut in the probe p_{T} bin 20 to 25 GeV.

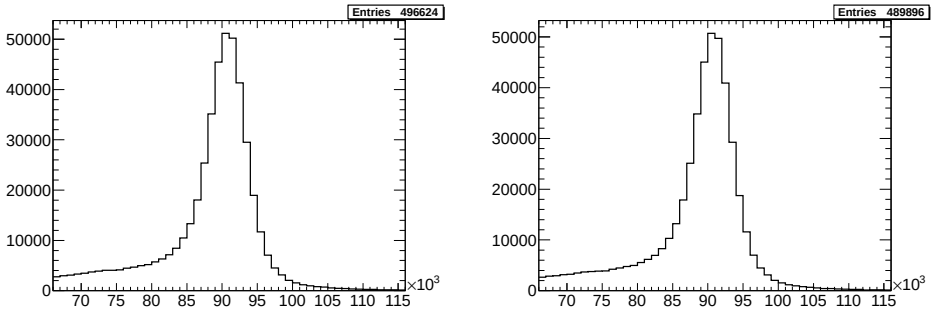

(a) (b)

Figure A.14: Invariant mass distributions for $Z \rightarrow \mu\mu$ using MC simulation (a) before and (a) after applying the tracking isolation cut in the probe p_{T} bin 25 to 30 GeV.

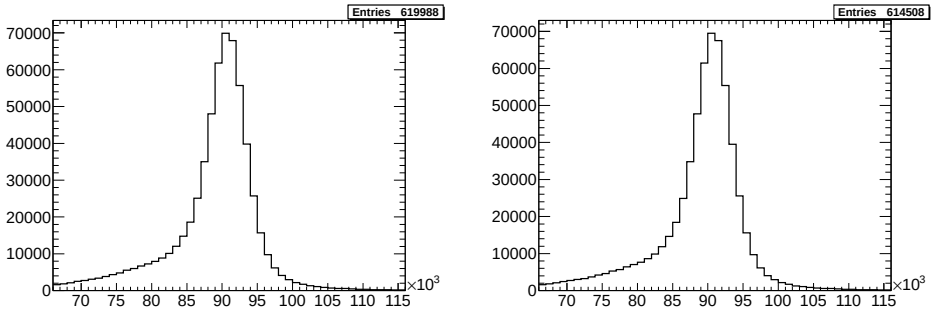

(a) (b)

Figure A.15: Invariant mass distributions for $Z \rightarrow \mu\mu$ using MC simulation (a) before and (a) after applying the tracking isolation cut in the probe p_{T} bin 30 to 35 GeV.

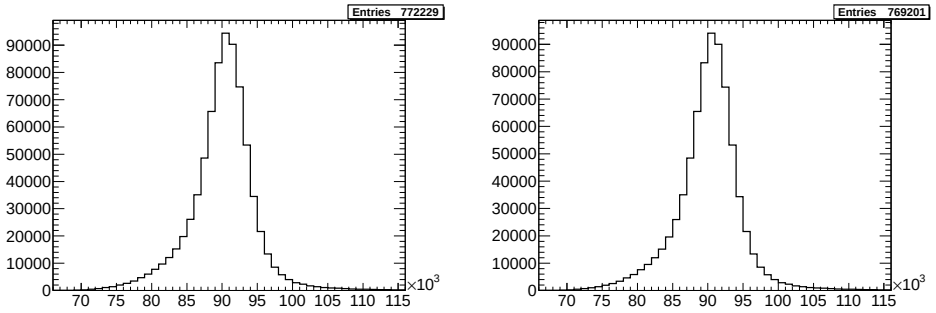

(a) (b)

Figure A.16: Invariant mass distributions for $Z \rightarrow \mu\mu$ using MC simulation (a) before and (a) after applying the tracking isolation cut in the probe p_{T} bin 35 to 40 GeV.

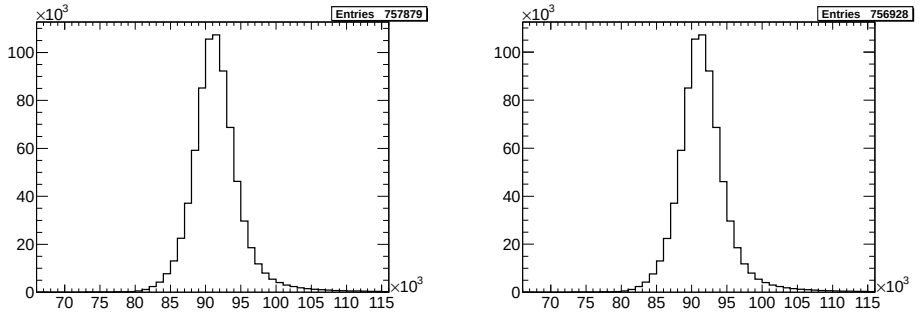

(a) (b)

Figure A.17: Invariant mass distributions for $Z \rightarrow \mu\mu$ using MC simulation (a) before and (a) after applying the tracking isolation cut in the probe p_{T} bin 40 to 45 GeV.

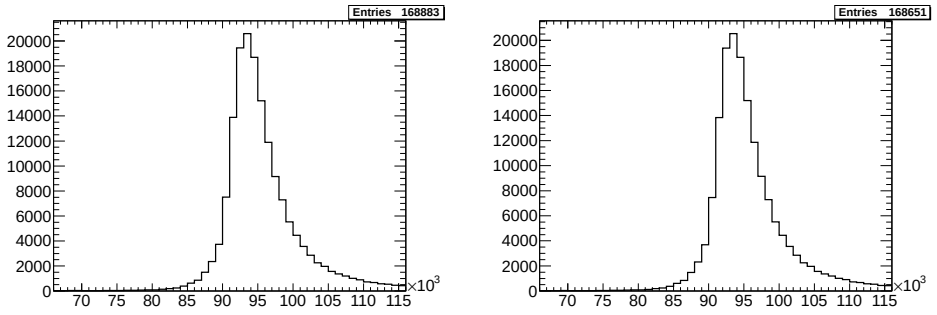

(a) (b)

Figure A.18: Invariant mass distributions for $Z \rightarrow \mu\mu$ using MC simulation (a) before and (a) after applying the tracking isolation cut in the probe p_{T} bin 45 to 50 GeV.

Table A.1: Selection criteria efficiencies and their ratio between data ($4.8\,\mathrm{fb}^{-1}$) and Monte Carlo when using a $\pm 5\,\mathrm{GeV}$ range around the m_Z for the efficiency calculation.

probe p_T	Track Isolation			Calorimeter Isolation			d_0 significance			all three		
(GeV)	Data	MC	ratio	Data	MC	ratio	Data	MC	ratio	Data	MC	ratio
7 - 12	0.968	0.964	1.004	0.988	0.983	1.006	0.994	0.988	1.007	0.957	0.951	1.007
12 - 15	0.977	0.975	1.001	0.992	0.987	1.005	0.992	0.988	1.004	0.966	0.965	1.002
15 - 20	0.985	0.983	1.002	0.995	0.991	1.004	0.991	0.991	1.000	0.975	0.975	1.000
20 - 25	0.989	0.987	1.002	0.996	0.993	1.003	0.993	0.992	1.001	0.981	0.980	1.000
25 - 30	0.992	0.991	1.002	0.998	0.995	1.002	0.993	0.993	1.000	0.984	0.985	1.000
30 - 35	0.995	0.994	1.001	0.999	0.997	1.001	0.993	0.993	1.000	0.988	0.988	1.000
35 - 40	0.998	0.996	1.001	1.000	0.998	1.001	0.993	0.994	0.999	0.990	0.991	0.999
40 - 45	0.999	0.998	1.001	1.000	0.999	1.001	0.993	0.994	0.999	0.992	0.993	0.999
45 - 50	0.999	0.997	1.003	1.000	0.997	1.003	0.994	0.993	1.001	0.993	0.992	1.001

Table A.2: Selection criteria efficiencies and their ratio between data ($4.8\,\mathrm{fb}^{-1}$) and Monte Carlo when using a $\pm 8\,\mathrm{GeV}$ range around the m_Z for the efficiency calculation.

probe p_T	Track Isolation			Calorimeter Isolation			d_0 significance			all three		
(GeV)	Data	MC	ratio	Data	MC	ratio	Data	MC	ratio	Data	MC	ratio
7 - 12	0.968	0.964	1.004	0.990	0.982	1.008	0.994	0.987	1.007	0.957	0.950	1.007
12 - 15	0.977	0.975	1.001	0.991	0.987	1.004	0.991	0.988	1.003	0.966	0.964	1.001
15 - 20	0.985	0.983	1.002	0.994	0.991	1.004	0.991	0.990	1.000	0.974	0.974	1.000
20 - 25	0.989	0.987	1.002	0.996	0.993	1.003	0.992	0.992	1.001	0.980	0.980	1.000
25 - 30	0.992	0.990	1.002	0.997	0.995	1.002	0.992	0.992	1.000	0.983	0.984	0.999
30 - 35	0.994	0.993	1.001	0.999	0.997	1.002	0.993	0.993	1.000	0.987	0.987	1.000
35 - 40	0.997	0.996	1.001	0.999	0.998	1.001	0.992	0.993	0.999	0.989	0.990	0.999
40 - 45	0.999	0.998	1.001	1.000	0.999	1.001	0.993	0.994	0.999	0.992	0.993	0.999
45 - 50	0.999	0.997	1.002	1.000	0.997	1.003	0.993	0.993	1.000	0.992	0.992	1.000

Table A.3: Selection criteria efficiencies and their ratio between data ($4.8\,\mathrm{fb}^{-1}$) and Monte Carlo when using a wider fitting range ($56 - 126\,\mathrm{GeV}$).

probe p_T	Track Isolation			Calorimeter Isolation			d_0 significance			all three		
(GeV)	Data	MC	ratio	Data	MC	ratio	Data	MC	ratio	Data	MC	ratio
6 - 12	0.972	0.965	1.007	0.990	0.983	1.007	0.993	0.988	1.006	0.960	0.952	1.009
12 - 15	0.977	0.976	1.001	0.991	0.987	1.004	0.992	0.988	1.004	0.966	0.965	1.001
15 - 20	0.985	0.983	1.002	0.994	0.991	1.003	0.991	0.991	1.000	0.975	0.975	0.999
20 - 25	0.989	0.987	1.002	0.996	0.994	1.003	0.993	0.992	1.001	0.981	0.981	1.001
25 - 30	0.993	0.991	1.002	0.998	0.996	1.002	0.993	0.993	1.000	0.985	0.985	1.000
30 - 35	0.995	0.994	1.001	0.999	0.997	1.002	0.993	0.993	1.000	0.988	0.988	1.000
35 - 40	0.998	0.997	1.001	1.000	0.998	1.001	0.993	0.994	0.999	0.991	0.991	0.999
40 - 45	0.999	0.998	1.001	1.000	0.999	1.001	0.993	0.994	0.999	0.992	0.993	0.999
45 - 50	0.999	0.996	1.003	1.000	0.997	1.003	0.994	0.993	1.001	0.993	0.992	1.001

Table A.4: Selection criteria efficiencies and their ratio between data ($4.8\,\mathrm{fb}^{-1}$) and Monte Carlo when using the PYTHIA generated MC.

probe p_T	Track Isolation			Calorimeter Isolation			d_0 significance			all three		
(GeV)	Data	MC	ratio	Data	MC	ratio	Data	MC	ratio	Data	MC	ratio
6 - 12	0.972	0.972	1.000	0.991	0.991	1.000	0.993	0.989	1.004	0.961	0.957	1.004
12 - 15	0.977	0.983	0.995	0.992	0.995	0.997	0.991	0.990	1.001	0.966	0.971	0.995
15 - 20	0.985	0.987	0.999	0.995	0.995	0.999	0.991	0.992	0.999	0.975	0.977	0.998
20 - 25	0.989	0.991	0.997	0.996	0.997	1.000	0.993	0.993	1.000	0.981	0.983	0.998
25 - 30	0.993	0.993	1.000	0.998	0.998	1.000	0.993	0.994	0.999	0.985	0.986	0.999
30 - 35	0.995	0.995	1.000	0.999	0.999	1.000	0.993	0.994	1.000	0.988	0.989	0.999
35 - 40	0.998	0.998	1.000	1.000	1.000	1.000	0.993	0.994	0.999	0.991	0.992	0.999
40 - 45	0.999	0.999	1.000	1.000	1.000	1.000	0.993	0.995	0.999	0.992	0.994	0.999
45 - 50	0.999	0.999	1.000	1.000	1.000	1.000	0.994	0.995	0.999	0.993	0.994	0.999

OK, cool!

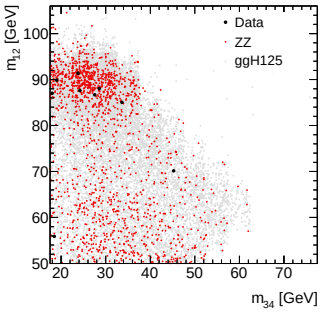

(a) 2012 07 01

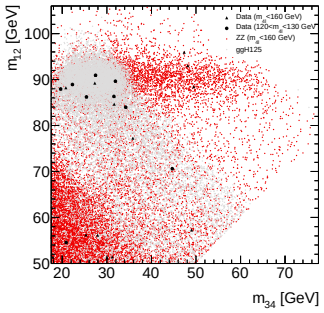

(b) 2012 07 06

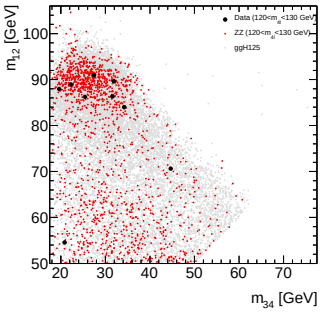

(c) 2012 07 06, fine binning

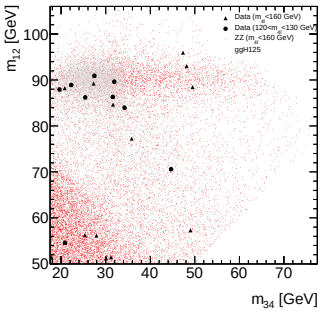

(d) 2012 07 11

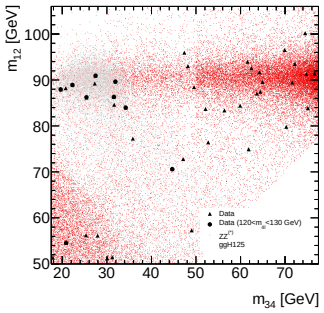

(e) 2012 07 11

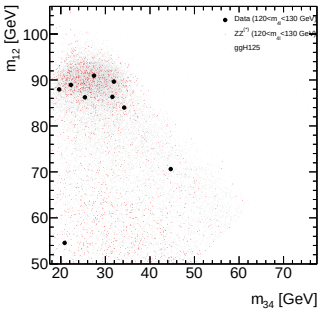

(f) 2012 07 11

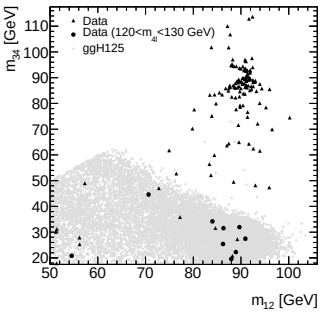

(g) 2012 07 13, no ZZ

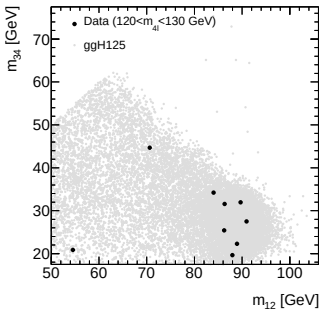

(h) 2012 07 13, no ZZ

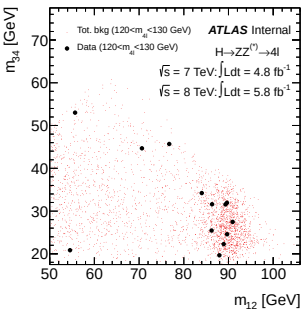

(i) 2012 07 14, 19:09

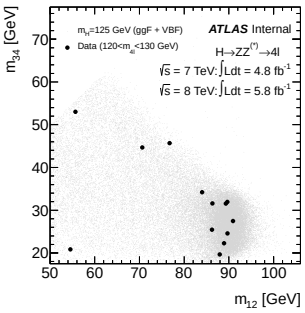

(j) 2012 07 14, 19:09, VBF

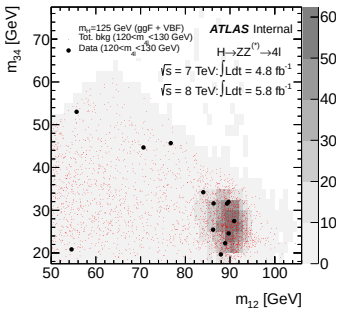

(k) 2012 07 14, 19:09, colz

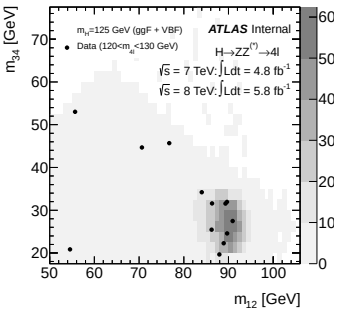

(l) 2012 07 14, 19:09, no ZZ

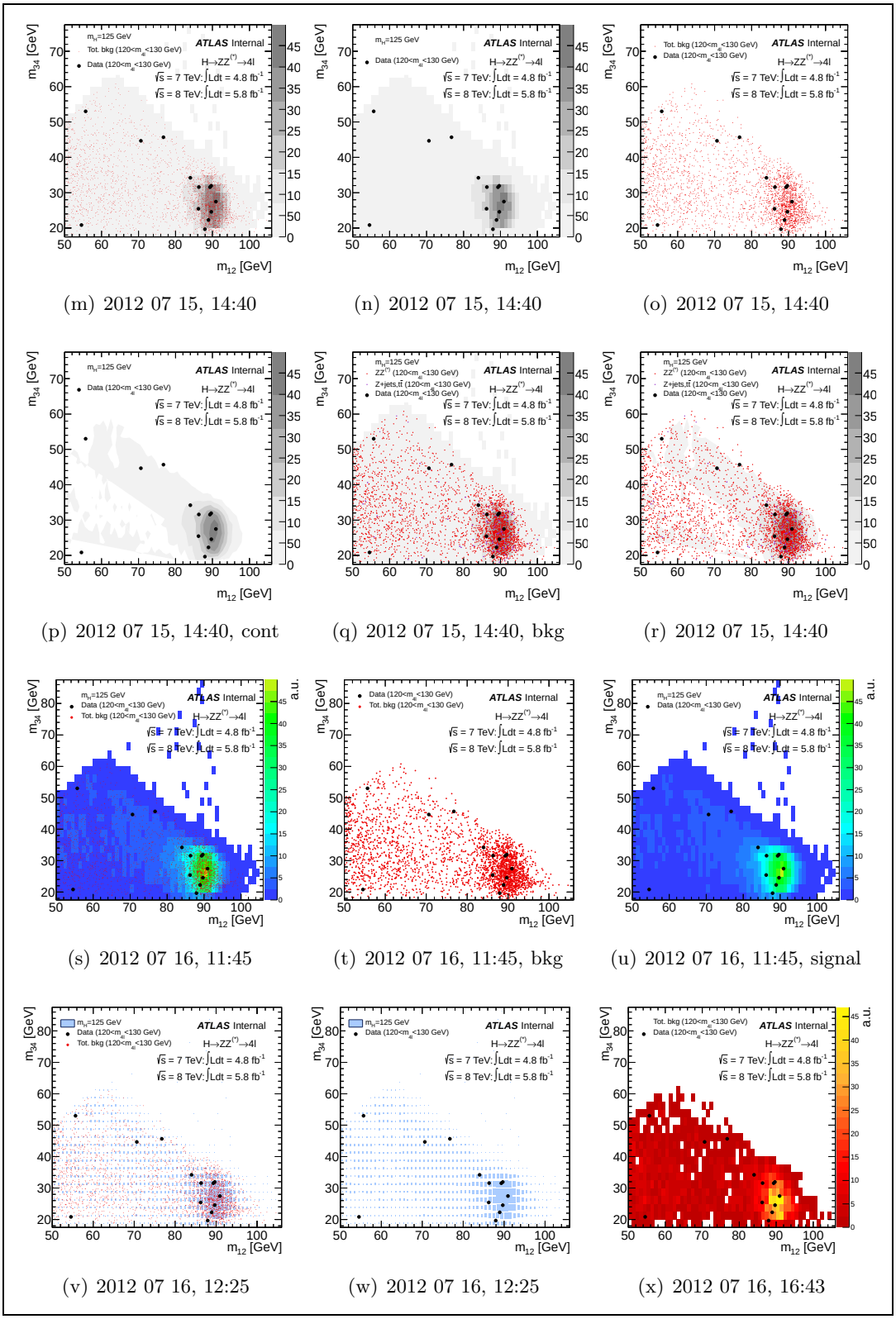

(m) 2012 07 15, 14:40 (n) 2012 07 15, 14:40 (o) 2012 07 15, 14:40

(p) 2012 07 15, 14:40, cont (q) 2012 07 15, 14:40, bkg (r) 2012 07 15, 14:40

(s) 2012 07 16, 11:45 (t) 2012 07 16, 11:45, bkg (u) 2012 07 16, 11:45, signal

(v) 2012 07 16, 12:25 (w) 2012 07 16, 12:25 (x) 2012 07 16, 16:43

Figure 8.19:

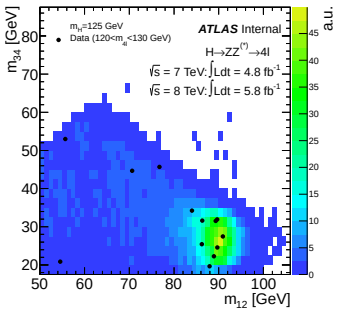

(a) 2012 07 16, 17:51, clean

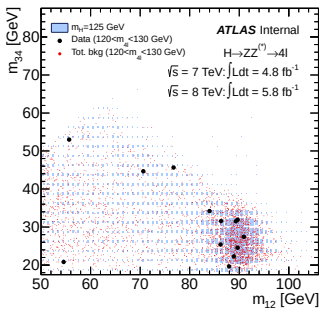

(b) 2012 07 20, 09:47

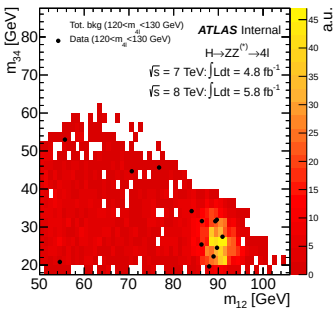

(c) 2012 07 20, 09:47

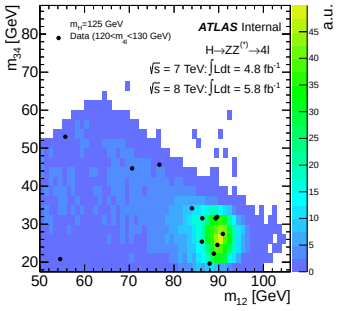

(d) 2012 07 20, 09:47

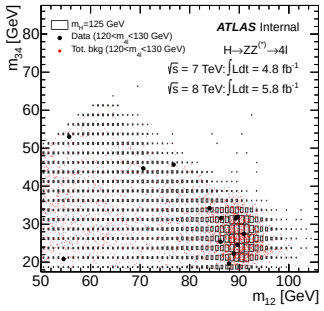

(e) 2012 07 20, 15:07

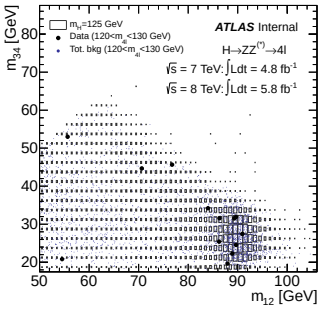

(f) 2012 07 20, 16:33

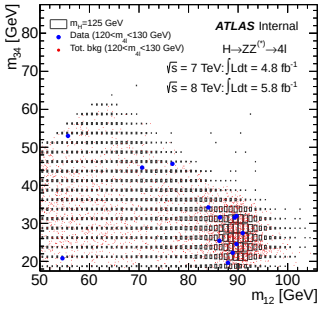

(g) 2012 07 20, 16:51

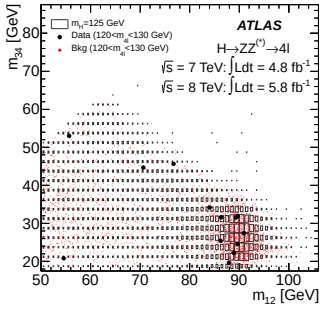

(h) 2012 07 24, 23:15

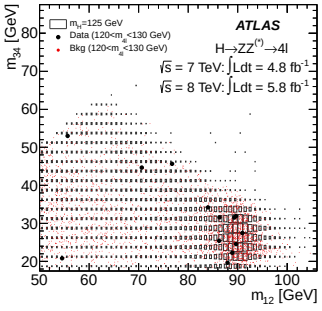

(i) 2012 07 25, 22:37

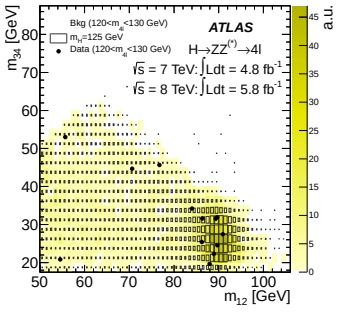

(j) 2012 07 26, 00:02

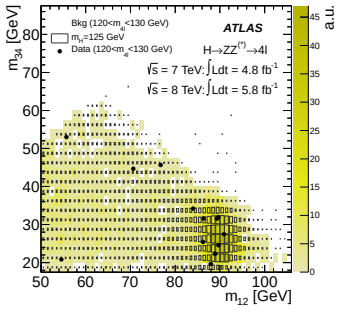

(k) 2012 07 26, 01:07

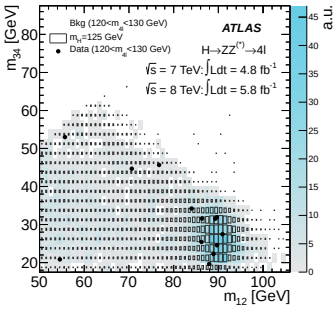

(l) 2012 07 26, 01:26

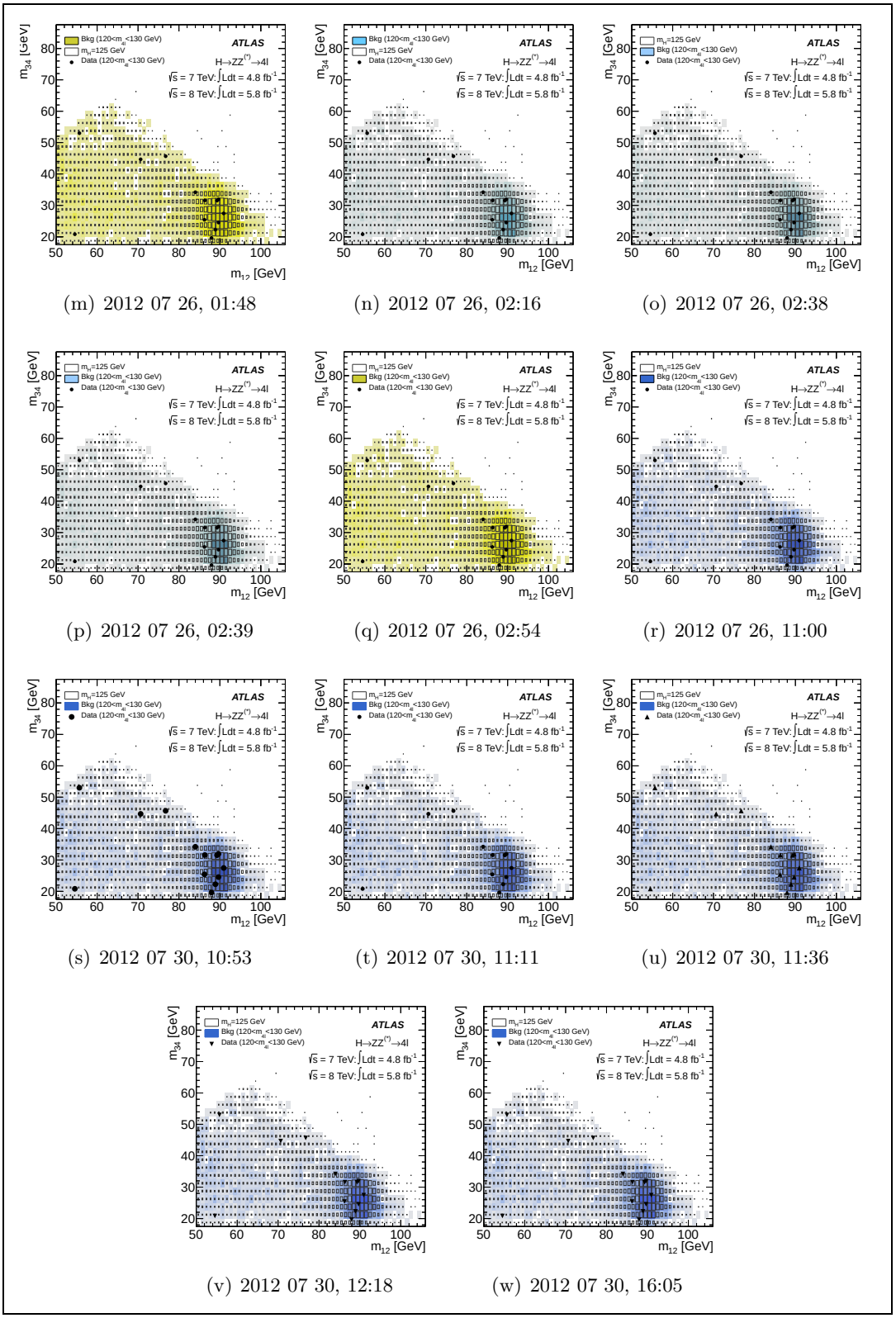

(m) 2012 07 26, 01:48 (n) 2012 07 26, 02:16 (o) 2012 07 26, 02:38

(p) 2012 07 26, 02:39 (q) 2012 07 26, 02:54 (r) 2012 07 26, 11:00

(s) 2012 07 30, 10:53 (t) 2012 07 30, 11:11 (u) 2012 07 30, 11:36

(v) 2012 07 30, 12:18 (w) 2012 07 30, 16:05

Figure 8.20: